
Ultra-high-energy neutrinos and cosmic rays from gamma-ray bursts: exploring and updating the connection

Mauricio Bustamante



Würzburg, 2014

Ultra-high-energy neutrinos and cosmic rays from gamma-ray bursts: exploring and updating the connection

Mauricio Bustamante

Dissertation zur Erlangung
des naturwissenschaftlichen Doktorgrades
der Julius–Maximilians–Universität Würzburg

vorgelegt von
Mauricio Bustamante
aus Würzburg

Würzburg, 2014

Eingereicht am: 20.08.2014
bei der Fakultät für Physik und Astronomie

1. Gutachter: Priv.-Doz. Dr. Walter Winter
2. Gutachter: Prof. Dr. Karl Mannheim
3. Gutachter:
der Dissertation

1. Prüfer: Priv.-Doz. Dr. Walter Winter
2. Prüfer: Prof. Dr. Karl Mannheim
3. Prüfer: Prof. Dr. Raimund Ströhmer
der Promotionskolloquium

Tag der Promotionskolloquium: 22.09.2014

Doktorurkunde ausgehändigt am:

Contents

Acknowledgements	viii
List of publications	xi
Kurzzusammenfassung	xii
Abstract	xiv
1 Introduction: gamma-ray bursts and the UHE messengers	1
1.1 Motivation: the big (multi-messenger) picture	1
1.2 Historical perspectives	3
1.2.1 Gamma-ray bursts	3
1.2.2 Cosmic rays	6
1.2.3 Ultra-high-energy neutrinos	9
1.3 The UHE multi-messenger picture within the GRB fireball model	12
1.4 Implementation of the GRB fireball model	14
2 A two-component model of UHECR emission	19
2.1 Neutron and direct proton escape from an expanding shell	19
2.2 Parameter space study of the cosmic ray-neutrino connection	24
2.3 Application to specific GRBs	27
3 UHECR propagation	31
3.1 Introduction	31
3.2 The CR transport equation in detail	32
3.2.1 Cosmological expansion	32
3.2.2 Energy loss rate due to $p\gamma$ interactions	33
3.2.3 Energy loss rate due to e^+e^- pair production	34
3.2.4 Scaling of the cosmological photon backgrounds	36

3.2.5	CR injection rate	39
3.2.6	Solving the transport equation under adiabatic expansion only	40
3.2.7	Cosmogenic neutrinos	41
3.2.8	Energy density of electromagnetic cascades	43
3.3	Selected results	44
3.3.1	The UHE proton flux at Earth	44
3.3.2	Modification factor	45
3.3.3	The cosmogenic neutrino flux at Earth	49
3.4	The effect of the CIB on cosmogenic neutrinos	50
3.4.1	Adding an extra component to the CIB photon spectrum	52
3.4.2	A simple model of the CIB injection function	57
4	Constraining joint UHECR-neutrino production in GRBs	63
4.1	Introduction	63
4.2	Cosmic energy budget and observables for GRBs	64
4.3	Combined production and propagation model	68
4.3.1	Ankle model for cosmic ray transition	68
4.3.2	Dip model for cosmic ray transition	71
4.4	Statistical analysis of the cosmic ray ankle model	73
4.4.1	Impact of cosmic ray escape model	73
4.4.2	Effect of cosmological source evolution	79
4.5	Limitations of the analysis	81
5	A dynamical GRB evolution model	83
5.1	Fireball evolution and collision model	83
5.1.1	General description and fireball parameters	83
5.1.2	Fireball initialisation	84
5.1.3	Fireball evolution	87
5.2	A few results and correlations	91
5.3	Light curves and burst duration	96
5.3.1	Normalising the photon spectrum	99
5.4	Detailed study of a simulated burst	102
6	UHE astrophysical neutrino decay	113
6.1	Introduction	113
6.2	Decay framework for cosmological neutrinos	115
6.3	Decay of neutrinos from GRBs	118

7	Summary and conclusions	125
8	Outlook	129
A	Description and numerical implementation of the UHECR propagation	133
A.1	Assumptions	133
A.2	Inputs	134
A.3	Limitations	135
A.4	Numerical implementation	135
A.4.1	Discretised transport equation	135
A.4.2	Electromagnetic cascade energy density	137
A.4.3	Tricks for speed-up	137
B	The UHECR energy budget from GRBs	139
B.0.4	Observation of prompt gamma-rays, and local GRB rate	139
B.0.5	Cosmic ray injection and observation	140
B.0.6	Neutrinos and multi-messenger physics with GRBs	141
C	Details of the statistical analysis	143
D	Algorithms for the dynamical GRB model	145
E	Calculation of the pair creation cut-off for photons	151
F	Photodisintegration of nuclei	155

Acknowledgements

Needless to say, a PhD is hard work, but my fellow students at the Institut für Physik und Astrophysik at Uni-Würzburg made it a lot of fun. Particularly stress-relieving were the daily afternoon coffee pauses, with a especially-composed jingle of their own (thanks to Eliel), during which conversation topics seamlessly spanned the range from metastable Higgs vacua and computer coding problems to linguistic quirks, the love life of ewoks, and the convenience of having a pet sheep. To Ben, Eliel, Martin, Lukas, Manuel, Debottam, and, more recently, Thomas and Timon, my thanks for letting me blow steam in the best way that I know: by letting the tangents dominate the conversation.

For two years, since the start of my PhD in March of 2012, I shared an office with Philipp Baerwald. Special thanks go to Philipp for helping me settle in the university, for numerous translations from German to English and help with the finer subtleties of German bureaucracy, and for the most fulfilling, close collaboration in science and programming that I have so far had. My thanks also go to Svenja Hümmer, another member of my research group, who, together with Philipp, developed the core of the NeuCosmA software which is integral to the neutrino calculations in my work. To Stefano Morisi, postdoc within my group, my thanks for showing me that thinking outside the box works more often than expected. To Walter Winter, my supervisor, goes my deep gratitude: first, for taking me as his student; second, for always being so eager to work on interesting projects, and to include us in them; and, third, for the vast amount of career advice that he has provided over the years. At this point, I would also like to thank Werner Porod, the speaker of the research training group DFG Graduiertenkolleg GRK1147 “Theoretische Astrophysik und Teilchenphysik”, for accepting me as a member of the GRK and for providing funding for the first two years of my PhD. Equally, I would like to thank Ansgar Denner, chair of the Lehrstuhl für Theoretische Physik II “Theoretische Elementarteilchenphysik” for taking me in under his chair.

For the last six months of my PhD, from March to September of 2014, Walter and I moved to DESY (Deutsches Elektronen-Synchrotron) in Zeuthen, where we joined the astroparticle physics theory group led by Martin Pohl. I would like to thank Martin, Johannes Knapp –head of the astroparticle group at DESY– and the whole theory group there and in Universität Potsdam, where half of the group sits, for a smooth transition.

During my two and a half years of PhD I had the fortune of being able to travel quite a lot in order to work with different collaborators. First and foremost I would like to thank John Beacom for hosting me in September and October of 2013 in the Center for Cosmology and Astroparticle Physics (CCAPP) of the Ohio State University; CCAPP has a rarely-found stimulating and friendly atmosphere and I greatly enjoyed my weeks there. In September 2013 I also visited the Wisconsin IceCube Particle Astrophysics Center (WIPAC), invited by Markus Ahlers. In October of the same year, I spent a few days at the Institute for Advanced Study in Princeton, visiting Kohta Murase. My appreciation to Markus and Kohta for their hospitality, and for interesting scientific

discussion and collaboration. In this regard, I also thank Julia Tjus Becker, from the Ruhr-Universität Bochum, and Francis Halzen, from WIPAC, for input and advice at different points over these years. In March and May of 2014 I visited Uppsala Universitet, in Sweden, and I would like to acknowledge the hospitality of the group there, especially of Olga Botner, Allan Hallgren, and Carlos de los Heros. In June, I was invited to the Instituto de Física Corpuscular in Valencia, Spain, by my good friend Joel Jones; a week of interesting work, and beautiful Valencian sights, was extremely appreciated.

I would also like to express my appreciation to a few other friends and collaborators (the line blurs): Julia Schmid, from the Erlangen Center for Astroparticle Physics, with whom we worked on several occasions on GRB neutrino predictions for the ANTARES telescope; Bruny Baret, from the AstroParticule et Cosmologie (APC) lab, who was an excellent host during the “Gamma-ray bursts in the multi-messenger era” workshop in Paris in June of 2014; Carlos Argüelles and Jordi Salvadó, from WIPAC, with whom the exchange of exciting ideas is never lacking; and Alberto Gago, who was the supervisor of my master’s work and with whom I am glad to continue to collaborate.

There is some people who deserve a special mention, given the presence that they have had in my life over these past years. Interactions with them have, at different times, fallen into either the “keeping me sane” or the “pushing me towards insanity” categories. However, they have invariably made my life richer, and, for better or worse, are partially responsible for who I have come to be. The list includes María Inés Ortiz, my closest friend for over twenty-three years, who would make transatlantic phone calls just because she needed to tell me about something that she thought I would find funny (she was always right); Maga, for reasons that are too many to mention here and that, as is usual with her, become hardly expressible in words, but very much clear in gestures; Michael, Claudia, Charlie, Fiorella M., Jaime, and Fiorella C., for the immensely generous act of sharing with me their weddings, kids, and lives; Ingrid, for visiting Würzburg twice in a year, for her many attempts to cheer me up, her awesome photos, for helping me many times with the Physics colloquia at PUCP, in Lima, and for generally being an orchestra-woman; Sandra, for assuring me that I will most likely not get a heart attack soon, for letting me show her what little of Berlin I have come to know, but mainly for being always one of the most caring, fun, honest, and intense persons that I have had the chance to meet; and Lisa, who has her own, unique way to live life, and that rocks.

Finally, there is my family. My mother and father have been the one constant, not only during my PhD years, but always. I have no words to express my enormous gratitude towards them. This PhD is the end of a long, long road, one that started as far back as I can remember. They have been there all the way, first leading me on, and afterwards providing support when support was needed. For valuing an education that gave me the freedom to choose what to do with my life, for love and care that exceeded words, and for their continuing support, I am forever indebted to them.

List of publications

In connection to the present thesis, the following papers were published.

Peer-reviewed publications:

- *Neutrino and cosmic-ray emission from multiple internal shocks of gamma-ray bursts*
Mauricio Bustamante, Philipp Baerwald, Kohta Murase, and Walter Winter
Nat. Commun. **6**, 6783 (2015) [arXiv:1409.2874]
- *Are gamma-ray bursts the sources of ultra-high energy cosmic rays?*
Philipp Baerwald, Mauricio Bustamante, and Walter Winter
Astropart. Phys. **62**, 66 (2015) [arXiv:1401.1820]
- *UHECR escape mechanisms for protons and neutrons from GRBs, and the cosmic ray-neutrino connection*
Philipp Baerwald, Mauricio Bustamante, and Walter Winter
Astrophys. J. **768**, 186 (2013) [arXiv:1301.6163]
- *Neutrino decays over cosmological distances and the implications for neutrino telescopes*
Philipp Baerwald, Mauricio Bustamante, and Walter Winter
JCAP **120**, 020 (2012) [arXiv:1208.4600]

Conference proceedings:

- *UHE neutrino and cosmic ray emission from GRBs: revising the models and clarifying the cosmic ray-neutrino connection*
Mauricio Bustamante, Philipp Baerwald, and Walter Winter
Published as part of the proceedings of the 6th Very Large Volume Neutrino Telescope Workshop (VLVnT13), Stockholm, Sweden, 5–7 August, 2013 [arXiv:1402.1497]
- *Escape and propagation of UHECR protons and neutrons from GRBs, and the cosmic ray-neutrino connection*
Mauricio Bustamante, Philipp Baerwald, and Walter Winter
Published as part of the proceedings of the 33rd International Cosmic Ray Conference (ICRC2013), Rio de Janeiro, Brazil, 2-9 July, 2013 [arXiv:1306.2755]

Kurzzusammenfassung

Es ist eine natürliche Annahme, dass die energiereichsten beobachteten Teilchen ($> 10^{18}$ eV), die ultra-hochenergetische Kosmische Strahlung (UHECRs), möglicherweise in Verbindung mit den leuchtkräftigsten zeitlich beschränkten Ereignissen ($> 10^{52}$ erg s $^{-1}$), sogenannten Gammablitz (GRBs), stehen. Als Folge der Wechselwirkungen zwischen den extrem beschleunigten, in Magnetfeldern gefangenen Protonen und Ionen und den Photonfeldern im Inneren der Gammablitz werden sowohl Neutronen als auch UHE Neutrinos erwartet. Erstere können die Quelle verlassen und zerfallen zu Protonen via β -Zerfall, welche zur Erde propagieren und dort als UHECR detektiert werden können, während Letztere, wenn detektiert, den eindeutigen Beweis für die Beschleunigung von Hadronen in besagten Quellen erbringen würden.

Vor Kurzem haben km 3 -große Neutrinoobservatorien, wie IceCube, endlich die benötigte Sensitivität erreicht, um die Neutrinovorhersagen für einige existierende GRB-Modelle zu testen. In diesem Zusammenhang präsentieren wir hier ein überarbeitetes, selbstkonsistentes Modell der gemeinsamen Produktion von UHE Protonen und Neutrinos in GRBs. Dieses enthält eine hochmoderne, verbesserte numerische Kalkulation des Neutrinoflusses (NeuCosmA), ein verallgemeinertes Emissionsmodell für UHECR, welches darauf beruht, dass einige Protonen direkt aus den Magnetfeldern innerhalb der Quelle entkommen können ohne wechselzuwirken, und bezieht die Energieverluste der Protonen auf ihrem Weg zur Erde mit ein. Wir nutzen unsere Voraussagen, um einen genaueren Blick auf die Verbindung zwischen Kosmischer Strahlung und Neutrinos zu werfen, und stellen fest, dass aktuelle UHECR Beobachtungen mittels gigantischen Luftschauerdetektoren zusammen mit den oberen Schranken auf den Neutrinofluss von GRBs bereits ausreichen, um Widersprüche zu einigen Emissions- und Propagationsmodellen aufzuzeigen, und deuten uns in die Richtung einiger Voraussetzungen, die von GRBs erfüllt sein müssen, sollten diese die Quellen der UHECRs sein. Des Weiteren verfeinern wir unsere Analyse, indem wir ein dynamisches Explosionsmodell studieren, mittels welcher wir herausfinden, dass unterschiedliche Teilchen von bestimmten Phasen des expandierenden GRBs stammen, welche durch unterschiedliche Bedingungen charakterisiert sind. Zum Schluss betrachten wir die Möglichkeit von "neuer Physik", den Zerfall von UHE Neutrinos im Neutrinofluss von GRBs. Im Großen und Ganzen zeigen unsere Ergebnisse, dass selbstkonsistente Modelle mittlerweile ein integraler Bestandteil für den Fortschritt dieses Feldes geworden sind, wenn man berücksichtigt, dass der Gesamtzusammenhang des UHE Universums erst sichtbar wird, wenn man den Himmel in unterschiedlichen Kanälen betrachtet, genauer gesagt gleichzeitig in Gammastrahlung, in Kosmischer Strahlung und in Neutrinos.

Abstract

It is natural to consider the possibility that the most energetic particles detected ($> 10^{18}$ eV), ultra-high-energy cosmic rays (UHECRs), are originated at the most luminous transient events observed ($> 10^{52}$ erg s $^{-1}$), gamma-ray bursts (GRBs). As a result of the interaction of highly-accelerated, magnetically-confined protons and ions with the photon field inside the burst, both neutrons and UHE neutrinos are expected to be created: the former escape the source and β -decay into protons which propagate to Earth, where they are detected as UHECRs, while the latter, if detected, would constitute the smoking gun of hadronic acceleration in the sources.

Recently, km-scale neutrino telescopes such as IceCube have finally reached the sensitivities required to probe the neutrino predictions of some of the existing GRB models. On that account, we present here a revised, self-consistent model of joint UHE proton and neutrino production at GRBs that includes a state-of-the-art, improved numerical calculation of the neutrino flux (NeuCosmA); that uses a generalised UHECR emission model where some of the protons in the sources are able to "leak out" of their magnetic confinement before having interacted; and that takes into account the energy losses of the protons during their propagation to Earth. We use our predictions to take a close look at the cosmic ray-neutrino connection and find that the current UHECR observations by giant air shower detectors, together with the upper bounds on the flux of neutrinos from GRBs, are already sufficient to put tension on several possibilities of particle emission and propagation, and to point us towards some requirements that should be fulfilled by GRBs if they are to be the sources of the UHECRs. We further refine our analysis by studying a dynamical burst model, where we find that the different particle species originate at distinct stages of the expanding GRB, each under particular conditions. Finally, we consider a possibility of new physics: the effect of neutrino decay in the flux of UHE neutrinos from GRBs. On the whole, our results demonstrate that self-consistent models of particle production are now integral to the advancement of the field, given that the full picture of the UHE Universe will only emerge as a result of looking at the multi-messenger sky, *i.e.*, at gamma-rays, cosmic rays, and neutrinos simultaneously.

Life is to be lived, not controlled;
and humanity is won by continuing to play
in face of certain defeat.
Invisible Man, by Ralph Ellison

A little flesh, a little breath,
and a Reason to rule all – that is myself.
Meditations, by Marcus Aurelius

Chapter 1

Introduction: gamma-ray bursts and the UHE messengers

1.1 Motivation: the big (multi-messenger) picture

Since the 1960s, intense bursts of gamma-ray radiation have been detected; these gamma-ray bursts (GRBs) are the most luminous transient events in the observed Universe. Fifty years of study have revealed that they are distributed isotropically, that they are extragalactic objects (GRBs with redshifts of up to ~ 8.2 have been observed, corresponding to ~ 4 Gpc, the size of the observable Universe), and that they come in, at least, two populations, depending on whether they last for a short or a long time. Gamma-ray luminosities of GRBs are of the order of 10^{52} erg s^{-1} , a magnitude that should be compared to the 10^{33} erg s^{-1} emitted by the Sun, 10^{41} erg s^{-1} by a supernova, and 10^{45} erg s^{-1} by a whole galaxy. Concentrated in burst episodes that last from less than one second to a few hundreds of seconds, it is easy to see that GRBs are able to outshine a galaxy while they last. Lacking direct observation of the mechanism driving the source, however, we can only hypothesise how the gamma-ray emission is generated. There are two competing possibilities: theories of leptonic origin of the emission postulate that the gamma-rays are the synchrotron radiation of highly-accelerated electrons, while the hadronic origin theories postulate that there is a sizable amount of baryons (protons and ions) in the source, which get accelerated to very high energies due to the presence of intense magnetic fields at the source, and show synchrotron radiation and interaction products are responsible for the observed gamma-rays.

In parallel, since 1962 we have been detecting cosmic rays –charged particles from outside the terrestrial atmosphere– of the highest energies, $\gtrsim 10^{18}$ eV. These ultra-high-energy cosmic rays (UHECRs) are the most energetic particles observed so far. One of the most energetic cosmic rays was detected by the Fly’s Eye Experiment, in Utah, in 1991 [1]: the event, baptised as the “oh-my-God particle”, had an energy of $\sim 3 \cdot 10^{20}$ eV, or about 50 J, which is approximately 40 million times higher than a 7 TeV proton in the LHC. To put this in context, this is equivalent to the energy carried by a baseball (142 g) traveling at 94 km h^{-1} or by a football (410 g) traveling at 55 km h^{-1} , but concentrated in a volume of radius of roughly 1 fm = 10^{-15} m. At this energy, the deviation of the particle’s speed relative to the speed of light is about 5 parts in 10^{24} . Thus, UHECRs are extremely energetic particles, and they are so rare that only a few dozen have been detected in the fifty years following their discovery.

It is only natural to wonder whether the most energetic particles seen –UHECRs– could be gen-

erated in the most luminous events – GRBs. Under the assumption of a hadronic origin of the gamma-ray emission, there would be a highly energetic population of protons and nuclei in the source. Let us take protons for concreteness, which will actually be our working assumption throughout the bulk of this thesis. Because of the intense magnetic fields, they would remain trapped inside the sources. Due to the high photon densities expected to exist in the source – GRBs are, after all, extremely luminous *in gamma-rays*–, it is expected that proton-photon ($p\gamma$) interactions occur often. In these, neutrons would be produced, *e.g.*, via the creation and decay of the Δ^+ (1232) resonance: $p\gamma \rightarrow \Delta^+$ (1232), followed by the Δ^+ (1232) decay into either π^+n or π^0p . The neutrons are no longer magnetically confined within the source: they escape from it, and β -decay into protons, which propagate over cosmological baselines from the high redshift of the source to the local Universe, to be detected at Earth as UHECRs. The π^0 decays into two gamma-ray photons, which contribute to the electromagnetic emission of the GRB.

What is the distinct signature of this hadronic acceleration scenario? The smoking gun is provided by the UHE neutrinos created in the decay of the charged pions: $\pi^+ \rightarrow \mu^+\nu_\mu \rightarrow \bar{\nu}_\mu\nu_e e^+\nu_\mu$. Therefore, within the hadronic acceleration scenario, there should be a flux of UHE neutrinos accompanying the UHECR and gamma-ray fluxes from GRBs. While this prediction has been known for several decades, no evidence of these neutrinos had been seen so far, on account of the insufficient size of the Čerenkov detectors used to search for the neutrinos. The situation has recently changed, when in 2012, the IceCube neutrino telescope, a 1 km³-scale detector that uses the pure Antarctic ice as target for the UHE neutrinos, attained enough sensitivity to finally reach the level of the neutrino flux predictions of an analytical, basic version of the neutron-escape model outlined above [2]: IceCube failed to detect any neutrinos in coincidence with more than two hundred observed GRBs, and the predicted added flux from all of them exceeded the corresponding upper bound [3]. This version of the model was hence discarded. However, more refined, numerical recalculations yield predictions that still lie one order of magnitude below the upper bound; see, *e.g.*, Refs. [4, 5].

Furthermore, in 2013, IceCube reported the first detection of UHE neutrinos, with energies in the range 30 TeV to 2 PeV, and a highly probable astrophysical origin [6, 7, 8]. This is a milestone, since the detection of the long-sought UHE astrophysical neutrinos marks the beginning of the neutrino astronomy era and the first strong hint of the validity of the hadronic acceleration scenarios as their origin. Hence, we now know that the UHE neutrinos exist, but we have not yet identified their origin.

The work contained in this thesis constitutes a step in that direction. We present refinements of the UHECR-neutrino connection in GRBs, in the form of a source model where protons are able to leak out of their magnetic confinement and the neutrino emission is altered, the use of UHECR observations and neutrino upper bounds to constrain the parameter space of this joint production model, and a dynamical burst model, where we discard the assumption that all of the different particles species in the source are emitted under identical conditions. We also explore the possibility of testing a particular form of new physics, neutrino decay, in the GRB neutrino flux.

The present era of larger and more sensitive gamma-ray, cosmic-ray, and neutrino detectors, has granted us, first, high-statistics catalogues of GRBs, second, a more precise and extended determination of the UHECR flux over several energy decades, and, third, the knowledge that UHE neutrinos do exist. In this context, and in light of the latest bounds on GRB neutrinos by IceCube, it has become necessary to go beyond the initial predictions, an aim which, we believe, our work helps to achieve.

1.2 Historical perspectives

1.2.1 Gamma-ray bursts

In 1963, the Partial Nuclear Test Ban Treaty was signed by the Soviet Union, the United Kingdom, and the United States of America, to prevent test detonations of nuclear weapons in the atmosphere, outer space, and underwater. In order to enforce the treaty, the U.S.A. developed and launched a series of six pairs of satellites named *Vela*, which carried X-ray, gamma-ray, and neutron detectors. While the first four pairs of satellites, *Vela* 1 through 4, lacked the spatial resolution capabilities to pinpoint the source of the emission, the fifth iteration had it. While intense gamma-ray emission from a nuclear explosion was expected to last 10^{-6} s or less, longer-lasting bursts of gamma-ray, of order 10 s or more, were unexpectedly detected. The first burst was detected, by inspecting archival data, by *Vela* 3 and 4, on July 2nd, 1967, at 14:19 UTC. By 1973, the satellites had detected sixteen of these events [9], in the energy range 0.2–1.5 MeV, with durations shorter than ~ 1 s to 30 s, and fluences between $\sim 10^{-5}$ erg cm $^{-2}$ to $\sim 2 \cdot 10^{-4}$ erg cm $^{-2}$. The directional capabilities of *Vela* 5a and 5b allowed to eliminate the Earth and solar flares as sources. In addition, no supernova was reported in coincidence with the detections. Furthermore, already at this low level of statistics, the bursts seemed to be distributed isotropically on the sky, thus hinting at a possible cosmic origin. The publication of these first results in 1973 by Klebesadel, Strong, and Olson in Ref. [9] marks the beginning of the study of gamma-ray bursts (GRBs).

Already in the discovery paper, it was claimed that “significant time structure within bursts was observed” [9]. Indeed, the light curves of GRBs (*i.e.*, photon count vs. time) exhibit small-scale structure (see Fig. 1.1), of the order of 1 ms or shorter, that suggests that whatever process is responsible for the gamma-ray emission, it has to take place with a maximum length scale of $(1 \text{ ms}) \cdot c / (1 + z)$ at the source, assuming it is located at a redshift z . This observation has been incorporated in the so-called fireball model, the current paradigm of how the GRB emission occurs; see section 1.3. Fig. 1.1 shows a few sample GRB light curves recorded by the BATSE detector [10]. A large variation in curve shape is evident, a fact that has made building a single underlying model of GRBs a challenging task. However, the small-scale structure, in the form of “noise-like” peaks, is clearly visible in all of the light curves, which hints at a common underlying emission mechanism.

Interest in GRBs and their nature grew. Starting from 1978, the 1st Inter-Planetary Network of satellites, which included the *Vela* satellites, was used to determine the position of GRBs with an accuracy of a few minutes of arc [12]. From 1991 to 2000, the Burst and Transient Source Explorer (BATSE) instrument onboard the Compton Gamma Ray Observatory detected 2704 bursts of different luminosity. BATSE provided strong confirmation of the isotropic distribution of GRBs [13] by calculating dipole and quadrupole moments of the GRB arrival directions and showing that the bursts are not concentrated around the Galactic plane, which would have been the most likely scenario had the bursts originated inside the Milky Way; see Fig. 1.2.

Additionally, BATSE revealed that GRBs can be classified in two populations [15], depending on the duration of the gamma-ray emission: short-duration bursts, which last up to 2 s and account for about 30% of the bursts detected, and long-duration bursts, which last beyond 2 s, up to tens or, rarely, hundreds of seconds; see Fig. 1.3. The gamma-ray spectrum of the short-duration bursts is typically harder than that of the long-duration bursts. Currently, it is believed that short-duration bursts occur as a result of the merger of a binary neutron star, or of a binary star and black hole [16]. On account of the higher statistics (70% of the total bursts), long-duration bursts haven been more widely studied: they have been observed to occur in association with

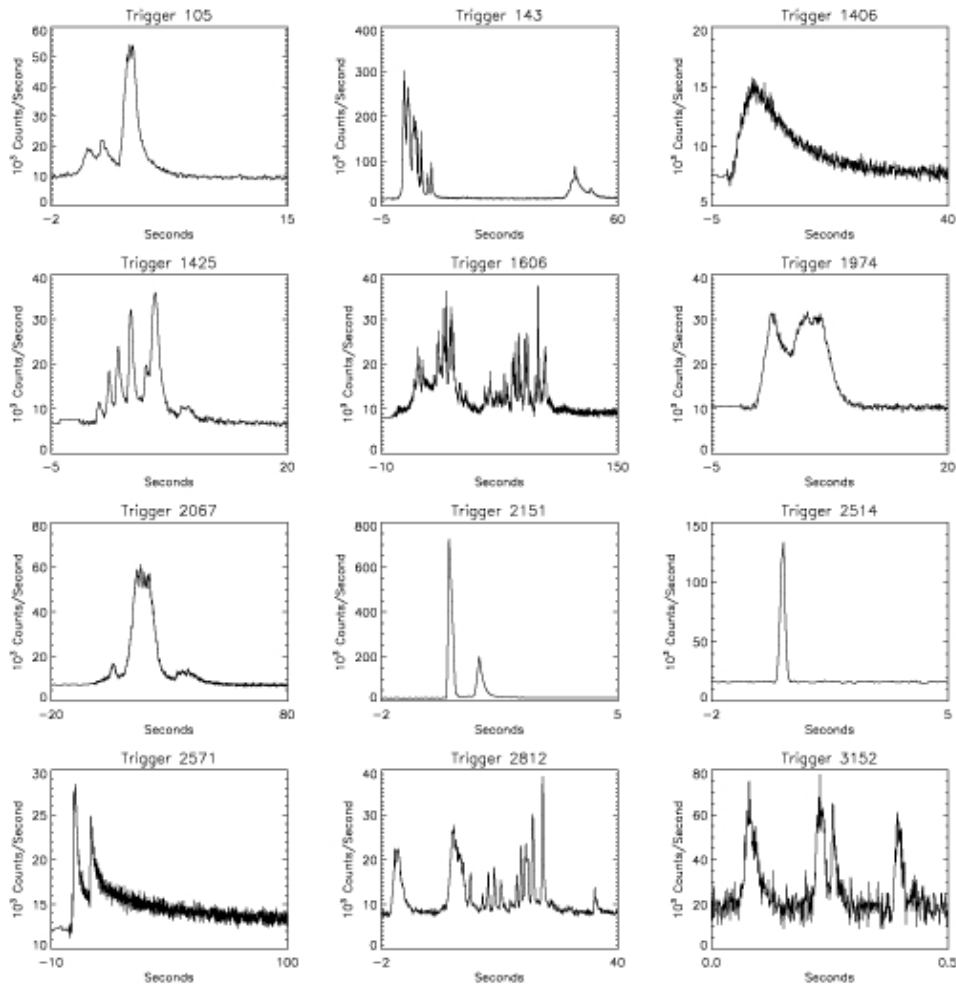


Figure 1.1: A few sample GRB light curves recorded by the BATSE detector. Taken from Ref. [10].

core-collapse supernovae [17]. A possibly third population of GRBs, lasting for more than 10000 s, was discovered in 2009 (see, *e.g.*, Refs. [18, 19]): while only few of them have been so far observed, it is believed that they might result from the collapse of a blue supergiant star.

After BATSE, a host of satellite missions were flown, notably: BeppoSAX (1996–2003), the first X-ray instrument capable of simultaneously observing in three energy decades (0.1 to 300 keV), which played a key role in confirming the extragalactic nature of GRBs in 1997 [20]; the Konus-WIND (1994–) gamma-ray instrument onboard the WIND satellite, sensitive in the range 10 keV to 10 MeV [21]; the INTERNATIONAL Gamma-Ray Astrophysics Laboratory (INTEGRAL, 2002–), capable of observing GRBs in the gamma-ray, X-ray, and visible wavelengths simultaneously (15 keV to 10 MeV) [22]; the Swift Gamma-Ray Burst Mission (2004–), or *Swift*, which observed for the first time the afterglow of short-duration GRBs [23]; and the Fermi Gamma-ray Space Telescope (2008–), or *Fermi*, which carries two onboard instruments for GRB studies, the Gamma-ray Burst Monitor (GBM), sensitive in the range 150 keV–30 MeV, and the Large Area Telescope (LAT), sensitive in the range 30 MeV–300 GeV [24]. As of February of 2014, *Fermi*-GBM had detected 1310 bursts, while LAT had detected 73. In April of 2013, *Fermi* detected GRB130427A [25] (also seen by *Swift* [26] and Konus-WIND [27]), a nearby ($z = 0.34$) burst with the highest energy

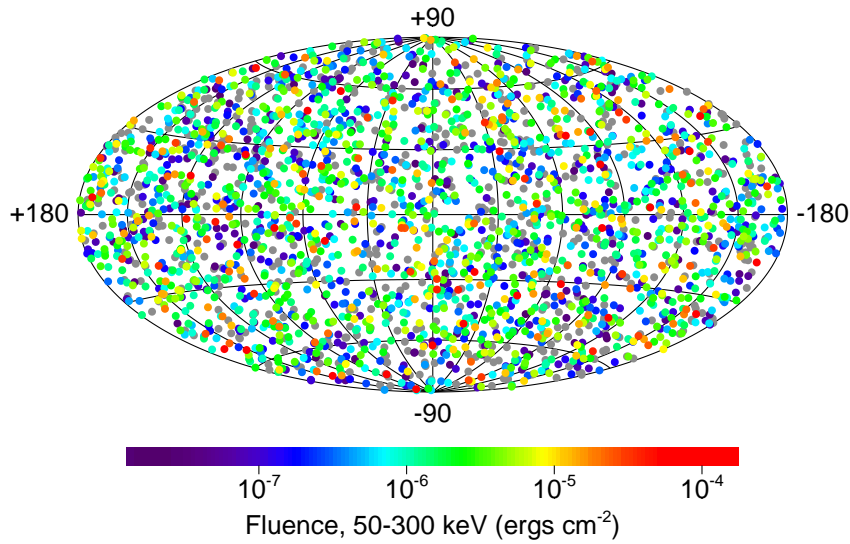


Figure 1.2: Distribution of the 2704 GRBs with varying fluence detected by BATSE in the period 1991–2000. Taken from Ref. [11].

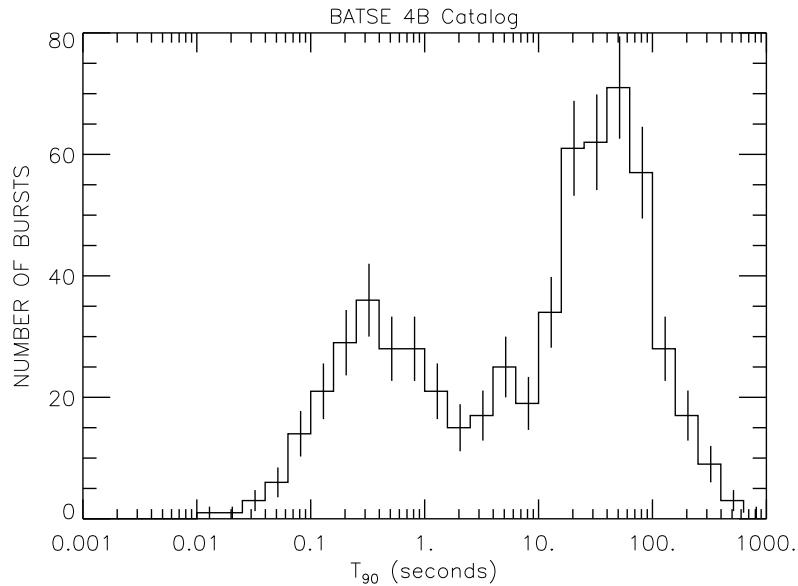


Figure 1.3: Distribution of the duration of the GRBs in the BATSE 4B catalogue. Taken from Ref. [14].

output seen ($\sim 3 \cdot 10^{53}$ erg s $^{-1}$), including the detection of the most energetic photon so far, with 94 GeV [28].

Swift and *Fermi* continue to monitor the sky for GRBs. New missions, like the upcoming joint Chinese-French satellite SVOM [29], seem to guarantee a steady rise of the size of GRB samples in the coming years, and with it, a better chance of testing theoretical predictions.

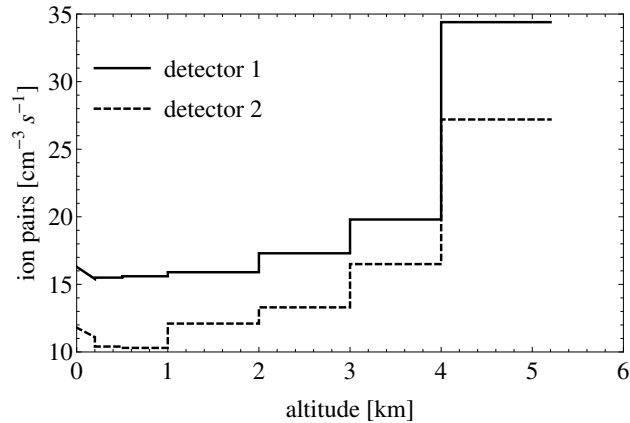


Figure 1.4: Average values of the results obtained by Hess during his 1912 balloon flights. Data plotted from Ref. [32].

1.2.2 Cosmic rays

After the discovery of X-rays in 1895 by Wilhelm Röntgen and of radioactivity in 1896 by Henri Becquerel, followed by the work of Ernest Rutherford, Paul Villard –who discovered gamma-rays in 1900–, and Pierre and Marie Curie, it was widely believed that all of the environmental ionising radiation had as a source the radioactive elements in the Earth’s crust and atmosphere. However, early experiments cast doubt over this belief: in 1909, Theodor Wulf used an electrometer to show the ionisation rate at the top of the Eiffel Tower was higher than at its base [30], while in 1911, Domenico Pacini performed measurements at different locations, including at mountains of different heights and at 3 m deep under the sea (which resulted in a 20% reduction of the ionisation rate), and reached the conclusion that at least part of the ionising radiation had to have an origin other than the radioactivity of the Earth [31].

In order to settle the issue, in 1912 Victor Hess performed seven high-altitude balloon flights, up to 5.3 km, and used three electrometers to measure the ionisation rate at different altitudes. He found that it initially decreased, up to a height of about 1 km, and then increased by a factor of up to ~ 3.5 compared to the value at ground level [32]; see Fig. 1.4. Thus, Hess observed that, in fact, close to the ground the ionisation rate did seem to depend on the ground radioactivity, since the rate initially went down with altitude. However, a new source of ionising radiation seemed to set in at altitudes above 1 km. By performing a flight during a near-total eclipse, Hess ruled out the Sun as the source of the rising radiation. Later balloon flights performed by Werner Kolhörster in 1913 and 1914 up to an altitude of 9 km confirmed these observations. Hess therefore concluded that the most likely explanation was that powerful radiation from beyond the atmosphere was responsible for the ionisation, a discovery for which he was awarded the Nobel Prize for Physics in 1936.

The term “cosmic rays” was coined by Robert Millikan in 1920, who believed that they were mainly energetic photons. Later, however, in 1927, J. Clay found that the intensity of cosmic rays varies with latitude (from Java to Genova and later from Java to Amsterdam), an indication that they were being deflected by the Earth’s magnetic field, and so they had to be charged particles [33, 34]. Bruno Rossi in 1930 predicted that a difference in the cosmic rays intensities coming from the east and the west, depending on their charge [35]. The confirmation of this effect

by three experiments, and further work carried out between 1930 and 1945, proved that cosmic rays were mostly positively charged, *i.e.*, that they were mainly protons. Later on, Homi Bhabha and Walther Heitler would go on to develop a theory of how the secondary particles produced by the interaction of a cosmic ray electron with the atoms in the atmosphere cascade down to the ground [36], a theory that has been extended to include other types of primary cosmic rays and which serves as the basis of the modern understanding of atmospheric particle showers initiated by cosmic rays, also known as **air showers**.

Up to cosmic ray energies of $\sim 10^{14}$ eV, direct detection of the cosmic rays remains feasible. However, the abundance of cosmic rays with higher energies drops rapidly –as a power law in the energy, as we will see– and so direct detection of the primary becomes impractical, due to limited detector sizes and exposure times. At these energies, indirect observation of cosmic rays becomes the main detection method: instead of detecting the primary cosmic ray, experiments focus on detecting the shower of secondary particles that is produced in the many interactions of the primary and its secondaries as they travel downwards in the atmosphere. Bruno Rossi was one of the first to experimentally study air showers, in 1934 [37]: he realised that, since groups of different particles seen at ground level were detected simultaneously, they must have been generated by a common interaction due to a primary cosmic ray in the atmosphere. In order to detect these showers, an array of detectors was spread over a large area to sample the particle densities at different locations and to use the reconstructed energy and multiplicities at each of them to infer the energy of the primary cosmic ray. However, it is Pierre Auger who is credited for the discovery, in 1939, of extensive air showers, *i.e.*, showers of secondary particles extending over an area of several km^2 , and initiated by particularly energetic primary cosmic rays [38]. Auger estimated that the energy of the primary cosmic ray of an extensive air shower had to be larger than 10^{15} eV.

The next step in cosmic ray history is especially relevant for our work: the Volcano Ranch experiment, led by John Linsley in New Mexico, consisted of nineteen plastic scintillator surface detectors that covered an area of 9 km^2 . Plastic scintillators have the property of luminescence: when excited by the ionising radiation of the impinging particles, they will radiate visible light, which is then amplified by photomultipliers and detected. On February 22, 1962, the experiment detected the first ultra-high-energy cosmic ray (UHECR), a single cosmic ray with energy above 10^{20} eV [39]. Later observations confirmed that these are extremely rare events: at these energies, the flux of cosmic rays that reach the ground is only ~ 1 particle per km^2 per century. Hence, it is unfeasible to detect them except by indirect means, and the larger the area covered by the detectors, the higher the chance of collecting the secondaries of these most energetic of cosmic rays. The use of plastic scintillators popularised, and several other extensive air shower detectors made use of them, notably, the Haverah Park experiment in England [40], Yakutsk in Russia [41], the Sydney University Giant Airshower Recorder (SUGAR) in Australia [42], and the Akeno Giant Air Shower Array (AGASA) in Japan, the latter with about 100 km^2 [43].

A different cosmic ray detection method consists in seeing the Čerenkov light generated by the particles of the air showers at ground level. For this, just as for the scintillator detectors, arrays of water tanks fitted with photomultipliers are spread to cover a large area. When an energetic particle of the air shower enters the tank, it will travel faster than the speed of light in the water, and hence emit a Čerenkov light front that is recorded and used to reconstruct the energy of the particle. Yet another method consists in detecting the fluorescence light generated during the longitudinal development of the air shower in the atmosphere: the high-energy photons from the air shower excite N_2 molecules in the atmosphere, which emit a lower-energy, ultraviolet photon when they de-excite. This fluorescence light can be observed, on Moonless nights, at distances

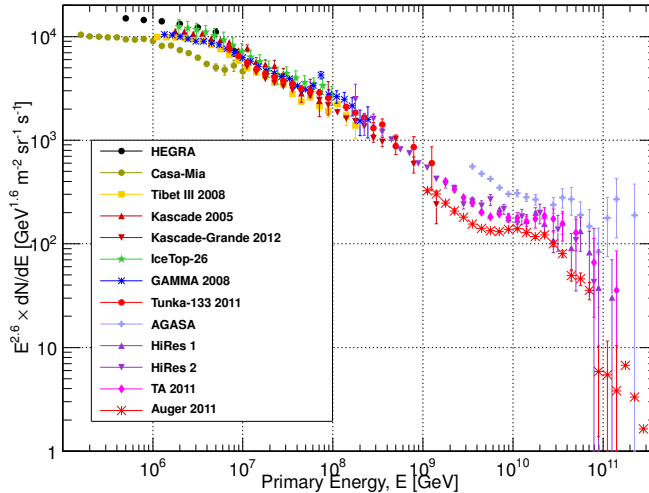


Figure 1.5: All-particle cosmic-ray spectrum from a variety of experiments. Taken from Ref. [54].

of up to 20 km from the shower core by photomultipliers located at the focus of a concentrating mirror.

Currently, the largest cosmic-ray detection experiment is the Pierre Auger Observatory (PAO), in Malargüe, Argentina. It is the first hybrid detector of its kind, employing 1600 water tanks as surface Čerenkov detectors, covering an area of 3000 km², and four air fluorescence detectors. The PAO has now accumulated enough data to be able to probe the absolute highest tail of the UHECR spectrum and to confirm the existence of a suppression of the flux at $\sim 5 \cdot 10^{19}$ eV [44], which likely corresponds to the cut-off predicted by Greisen, Zatsepin, and Kuzmin (GZK) in 1966 due to the interactions of the UHECRs with the photons from the cosmic microwave background [45, 46] (see section 3.2.4). The existence of the **GZK cut-off** was afterward confirmed by the Telescope Array [47], another hybrid detector (see below), and the Fly’s Eye experiment [48], an air fluorescence detector. In addition, the PAO has also published correlation results between the arrival directions UHECRs and the positions of known, close-by (< 75 Mpc) active galactic nuclei [49], albeit only at a low significance level, and on the apparent change of composition of the UHECRs from protons to nuclei at higher energies [50, 51]. The latter is inferred mainly by studying the lateral development of the showers via its fluorescence emissions: showers initiated by protons tend to contain fewer particles than those initiated by nuclei of the same energy, and the maximum number of secondary particles for proton primaries is reached at a later stage in the shower development than for nuclei primaries, *i.e.*, deeper in the atmosphere.

Another kind of hybrid extensive air shower detector is the Telescope Array (TA), which uses plastic scintillator surface detectors and fluorescence detectors, and covers an area of 762 km², making it smaller than PAO. In contrast to it, TA has not found evidence of a heavier UHECR composition at higher energies [52]. In fact, the issue of the possible change towards heavier composition with energy is controversial and ongoing; for a recent review, see Ref. [53].

After 102 years of study, we now know that the cosmic ray spectrum spans twelve orders of magnitude and that it follows a power-law behaviour, with several features marking important physical transitions. Fig. 1.5 shows a compilation of data from all the main cosmic ray detection

experiments, extracted from Ref. [54]. Two suppressed regions are evident: the first one, at $\sim 10^{9.5}$ GeV, is due to the energy losses from electron-positron pair creation via the process $p\gamma_{\text{CMB}} \rightarrow pe^+e^-$, on photons of the cosmic microwave background and is known as the **pair-production dip**; the second suppression is the GZK cut-off mentioned above, starting at $\sim 5 \cdot 10^{11}$ GeV. The position of the GZK cut-off is determined by the energy threshold of the photohadronic interaction processes $p\gamma_{\text{CMB}} \rightarrow n\pi^+/p\pi^0$, which can be calculated, from the kinematics, to be $\sim 5 \cdot 10^{11}$ GeV. The mean free path associated to this interaction is around 50 Mpc, *i.e.*, it is very unlikely that a proton with an energy higher than $5 \cdot 10^{11}$ GeV reaches the Earth from a distance larger than 50 Mpc. Hence, this distance is also known as the **GZK horizon**: all of the most extreme UHECRs are expected to be generated in source within this horizon.

The power-law behaviour shown in Fig. 1.5 is broken at three points, where it changes the value of the spectral index: at the *knee*, $\sim 10^{6.5}$ GeV, where it changes from $E^{-2.7}$ to $E^{-3.1}$; at the *second knee*, $\sim 10^{8.7}$ GeV, where it changes to $E^{-3.2}$; and at the *ankle*, $\sim 10^{9.5}$ GeV, where it becomes harder again, $E^{-2.7}$. Each kink in the power law corresponds to a transition. The knee might correspond to the point at which Galactic cosmic rays, believed to be created by supernovae, reach energies high enough that their gyroradius –proportional to the energy– has grown beyond the containment size of the Galaxy and, therefore, they escape, thus depleting the population of more energetic Galactic cosmic rays. Protons seem to dominate the spectrum down to $\sim 10^{18}$ GeV, and the second knee might mark the energy above which the low-energy component of Galactic heavy nuclei becomes negligible, although it might also signal the transition from Galactic to extragalactic cosmic rays [55]. Finally, the ankle is widely thought to mark the transition from Galactic to more energetic extragalactic cosmic rays. Throughout the twelve orders of magnitude, the cosmic ray spectrum varies greatly: at 100 GeV, the flux is ~ 1 particle $\text{m}^{-2} \text{s}^{-1}$; at the knee, it has fallen to ~ 1 particle $\text{m}^{-2} \text{yr}^{-1}$; at the ankle, ~ 1 particle $\text{km}^2 \text{yr}^{-1}$; and at GZK cut-off, as we mentioned earlier, it is very low, ~ 1 particle $\text{km}^{-2} \text{century}^{-1}$. Finally, notice that while the normalisation of the spectrum is different for different experiments in Fig. 1.5, they can all be made to coincide by a shift of the energy scale, within the energy uncertainty of each distinct experiment, with the goal of making them all coincide at the pair-production dip.

Thus, we see that, while a century after the discovery of cosmic rays, and fifty years after the discovery of UHECRs, we know much more about them, their origin and their composition still elude us. Thanks to large-area detectors of the current generation, however, we are finally able to start giving meaningful answers to these questions.

1.2.3 Ultra-high-energy neutrinos

Neutrinos were postulated in 1930 by Wolfgang Pauli as a last resort to ensure the conservation of energy, momentum, and spin in β decay: they were to be electrically neutral, light fermions (particles with spin 1/2) that were emitted together with the proton and the electron, *i.e.*, $n \rightarrow pe\bar{\nu}_e$. Their existence remained as hypothetical until 1956, when Clyde Cowan, Frederick Reines, F. B. Harrison, H. W. Kruse, and A. D. McGuire reported their discovery via inverse β decay [57]: in the process $\bar{\nu}_ep \rightarrow ne^+$, the positron will quickly annihilate with a neighbouring electron, and the two resulting gamma-rays are detectable, while the neutron can be captured by a nucleus and emit another gamma-ray. The coincidence of both emissions constitutes a signature of a neutrino interaction. Later, the other two flavours of (active) neutrinos¹, the muon-neutrino and

¹Motivated by several experimental anomalies, *e.g.*, in short-baseline neutrino oscillation experiments, it is possible that a different type of neutrinos exists: sterile neutrinos, which do not interact with the other particles of the Standard Model, but whose existence might be inferred by their mixing with the active neutrinos [58, 59].

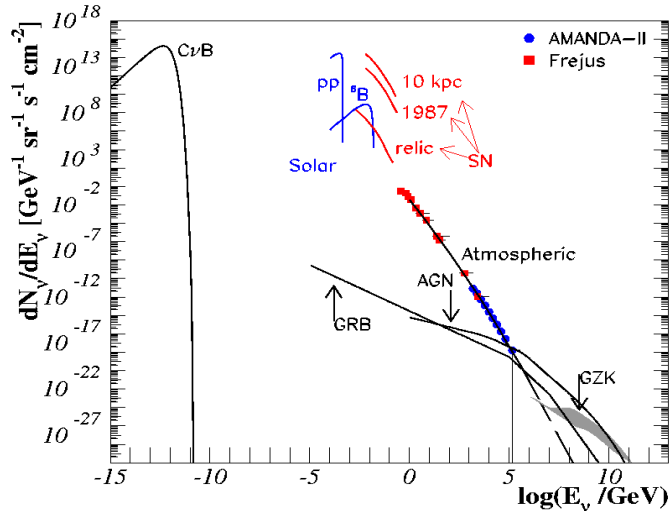


Figure 1.6: Astrophysical and cosmic neutrino spectra. Taken from Ref. [56].

tau-neutrino, were discovered, respectively, in 1962, by Leon M. Lederman, Melvin Schwartz and Jack Steinberger [60], and by the DONUT Collaboration, in 2000 [61].

Since then, neutrinos have been detected in a wide range of energies and from a variety of sources, both natural, like the cosmic ray interactions in the atmosphere ($\gtrsim 100$ GeV) [62], the Sun (0.1–18 MeV) [63], supernovae ($\lesssim 60$ MeV) [64], and geoneutrinos from the decay of radioactive elements in the Earth’s interior ($\lesssim 4$ MeV) [65]; and manmade, including neutrinos from accelerators ($\lesssim 10$ GeV) [66] and nuclear reactors ($\lesssim 10$ MeV) [67].

The fact that neutrinos are subject only to weak interactions, via either W or Z bosons, makes them notoriously difficult to detect. Point in case: the typical weak cross section of 10^{-42} cm² results in an extraordinarily long mean free path of neutrinos of more than one light year of lead. Hence, neutrino detector must be either very dense or very large; ideally, they should be both. One of the most widely used detection method is through the observation of Čerenkov radiation, in much the same way as for cosmic rays (see previous section). Čerenkov experiments typically consist large tanks of ultra-pure water, or of water doped with specific dopants, and instrumented with photomultipliers. To reduce the background of cosmic rays, which might be mistakenly reconstructed as neutrinos, the detectors are placed deep underground, typically a kilometer or more below a mountain. The Super-Kamiokande detector, for instance –the descendent of the Kamiokande-II detector– is located 1 km below the Mozumi Mine in Kamioka, Japan, and consists in a tank that holds fifty thousand tons of water, the inner walls lined up with photomultipliers. The observation of a neutrino in a Čerenkov detector is akin to the observation of a cosmic ray in surface detectors that we mentioned in the previous section: in the rare occasions when a neutrino impinges on a nucleon of the water and creates a fast, charged lepton (either an electron or a muon, since tau-neutrinos are rare), the latter, moving at a speed higher than the speed of light in water will create a Čerenkov light front that will leave a ring-like imprint on the wall of photomultipliers.

Up until 2013, the only extraterrestrial neutrinos that had been observed were neutrinos (ν_e) from the Sun, with a flux of $\sim 7 \cdot 10^{10}$ neutrinos cm⁻² s⁻¹, and a handful of neutrinos attributed to the supernova SN1987A, detected by the Kamiokande II (11 anti-neutrinos detected), the IrvineMichiganBrookhaven (IMB) detector (8 anti-neutrinos), and the Baksan detector (5 antineutrinos), all

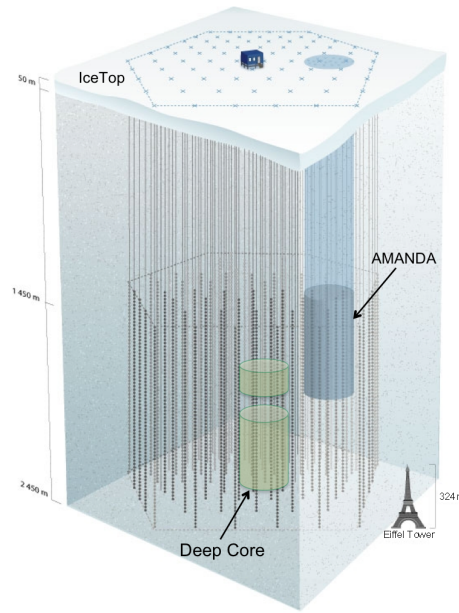


Figure 1.7: The IceCube neutrino detector, showing also the DeepCore sub-array and the former AMANDA array. Taken from Ref. [56].

of them Čerenkov detectors. In 2013, the IceCube neutrino experiment reported the detection –with more than 5σ statistical significance– of the first UHE neutrinos, very likely of astrophysical and even extragalactic origin, with energies between 30 TeV and 2 PeV [6, 7, 8]. IceCube is also a Čerenkov detector. However, it differs from other such detectors in two ways: first, instead of water, it uses pure, Antarctic ice as target and, second, when it was completed, in late 2010, it became the largest neutrino Čerenkov detector, with an instrumented volume of 1 km^3 . Digital optical modules (DOMs) containing photomultipliers are arranged in strings of sixty units, and buried in ice at depths from 1450 m to 2450 m; see Fig. 1.7. Within the main instrumental array, strings are separated by 125 m, while DOMs on a string have a separation of 17 m between them. A section of the ice located in the center of the array, dubbed DeepCore, has been more densely instrumented, in order to achieve a lower neutrino energy threshold for detection ($\sim 100 \text{ GeV}$). As seen in Fig. 1.7, IceCube was built on a predeceasing array, the Antarctic Muon And Neutrino Detector Array (AMANDA), which served as a proof of principle for the technique from 1996 to 2009.

There are two main event topologies in IceCube associated to neutrinos: cascades and muon tracks. Cascades can be created by the neutral-current interaction of any flavour of neutrinos ($\nu_x N \rightarrow \nu_x N'$), which generates a hadronic cascade, or by the charged-current interaction of electron-neutrinos ($\nu_e N \rightarrow e N'$), which generates an electromagnetic cascade, *i.e.*, one with more electron and photon content. In both cases, cascades are seen as localised and sometimes approximately spherical regions of light emission. Since all of the event is likely to be contained within the detector, the uncertainty in the energy reconstruction is low ($\sim 15\%$ above 10 TeV [68]), but, due to the approximately point-like shape (on the length scale of the strings and the DOMs), their uncertainty in the reconstruction of their arrival direction is high, ranging from 10° to 40° . On the other hand, muon tracks are created as a result of the charged-current interaction of a muon-neutrino ($\nu_\mu N \rightarrow \mu N'$): the highly energetic muon exits the region of the interaction vertex

and, while propagating, leaves a path of photons that can be used to reconstruct its direction with high accuracy ($\lesssim 1^\circ$). In this case, due to the large muon mean free path in ice, it is common for only part of the muon track to be contained within the detector, which is why the uncertainty in the energy reconstruction of the muon is high, and depends on what fraction of the track is contained [68]. Furthermore, it is expected that tau-neutrinos with energies around PeV can sometimes be identified via two distinct event topologies [69]: a “double bang”, where both the hadronic shower at the $\nu_\tau N$ interaction vertex where a tau lepton is created and the vertex where it decays again into a ν_τ are contained within the detector, and a “lollipop”, when only the latter is.

In 2013 and 2014, IceCube reported the detection of UHE neutrinos in data collected in the period 2010–2012: 37 events in the range 30 TeV–2 PeV [8], 8 of which are muon tracks, 28 are cascades, and 1 is likely to be a background muon event² Even with these low numbers, it appears that the signal is isotropic, that it does not show any time clustering, nor is it coincident with the occurrence of GRBs. The signal is consistent with a flux of 10^{-8} GeV cm⁻² s⁻¹ sr⁻¹ per flavour. Given the proximity of this value to the original prediction by Waxman and Bahcall [70] for the magnitude of a cosmic flux of neutrinos, it can be interpreted as a mild hint of its potential extragalactic origin. On the other hand, no events have so far been detected above 2 PeV. Whether this is a limitation of the detector size, exposure time, or the search algorithms, or whether this is a physical cut-off, is still an open question. With the current level of statistics, the neutrino spectrum can be fitted either by a E^{-2} power law with an exponential cut-off at 2 PeV, or with a steeper power law, closer to $E^{-2.3}$, without a cut-off.

Clearly, the era of neutrino astronomy has begun and we need only wait for the accumulation of more data in order to start probing the theoretical predictions rigorously.

1.3 The UHE multi-messenger picture within the GRB fireball model

Cosmic ray observations tell us that particles with energies higher than 10^{19} eV hit the Earth, which are expected to be of extragalactic origin. The search for the sources of these ultra-high energy cosmic rays (UHECRs) is therefore one of the main objectives in high-energy astrophysics. It can be either performed directly, by cosmic ray observations, or indirectly, by looking for the neutrinos accompanying the cosmic ray emission. So far, no evidence for a correlation between specific UHECR sources and cosmic ray measurements has been found.

One class of potential UHECR sources are gamma-ray burst (GRB) fireballs (see Refs. [71, 72] for reviews), where the cosmic rays are expected to be accelerated to the highest energies by collisions with the interstellar medium [73], or by internal collisions inside the ejected material [74, 75]. The general fireball model describes a GRB as a catastrophic release of energy, during which matter of the order of a solar rest mass is ejected from a compact object. These ejecta are then first accelerated to ultra-relativistic speeds, and are then assumed to coast at constant velocity while expanding into interstellar space. It is assumed that the bursts can also lose energy via radiation at higher radii during the expansion of the fireball. The expansion ends when the ejecta hit the interstellar medium and are decelerated. The observations in several energy bands have shown that GRBs have several distinct phases of emission, with the prompt emission phase being the most

²This is suspected, since the signal within the detector was correlated with a signal at IceCube’s own surface Čerenkov detector, IceTop, which is used as a veto to eliminate atmospheric muon events.

energetic one. During this phase, the burst is mainly visible in gamma-rays, and the emission is assumed to originate from the coasting phase of the fireball. The high variability and non-thermal properties of the observed gamma-ray spectra give rise to the notion that the prompt emission might be due to the collision of internal shells, leading to Fermi shock acceleration of the charged particles such as electrons or protons (internal shock model). While recent observations point towards a heavier composition at the highest energies [50], we focus on protons as candidates for the UHECRs in this study, for which plausible models for the particle acceleration and emission from GRBs exist. Especially the idea of indirect escape of protons, via neutrons, from the shells has been a very popular extension of the internal shock model in the literature. However, there are also several other alternative models for GRB emission which describe certain aspects of the observed emission well, such as magnetic reconnection models [76, 77, 78] or photospheric emission models [79, 80, 81, 82, 83, 84, 85].

Because of the high photon densities, it is expected that the protons accelerated in the colliding shocks dissipate energy into pion production. In the standard picture, this can be described by the $\Delta(1232)$ -resonance

$$p + \gamma \rightarrow \Delta^+ \rightarrow \begin{cases} n + \pi^+ & \frac{1}{3} \text{ of all cases} \\ p + \pi^0 & \frac{2}{3} \text{ of all cases} \end{cases} . \quad (1.1)$$

A substantial neutrino flux then originates from π^+ decays via the decay chain

$$\begin{aligned} \pi^+ &\rightarrow \mu^+ + \nu_\mu, \\ \mu^+ &\rightarrow e^+ + \nu_e + \bar{\nu}_\mu, \end{aligned} \quad (1.2)$$

where $\nu_e : \nu_\mu : \nu_\tau$ are produced in the ratio 1 : 2 : 0. On the other hand, the neutrons decay via

$$n \rightarrow p + e^- + \bar{\nu}_e, \quad (1.3)$$

typically outside the source, which leads to a cosmic ray (proton) flux even if the protons themselves are magnetically confined (“neutron model”), as discussed in, *e.g.*, [86]. Highly energetic gamma-rays originating from the π^0 decays are injected into the electromagnetic cascade, which leads to constraints from the *Fermi*-LAT diffuse GRB measurement; see, *e.g.*, [87] or [88].

The neutrino flux has been predicted for the standard internal shock model in [89], assuming that GRBs are the sources of the UHECRs. If one assumes that the observed gamma-ray spectrum represents the photon density within the source in the prompt phase, one can calculate the expected neutrino fluence from the observed gamma-ray fluence; corresponding analytical methods have been developed in [2], [90], and [91]. Recently, the IceCube collaboration has however strongly constrained the neutrino flux from GRBs, see [3, 92], with the conclusion that these simple approaches are already severely constrained. Nonetheless, it is known that additional photomeson production processes somewhat harden the neutrino spectra, and that the cooling of the secondaries and flavor mixing change the spectral shape and flavor composition, see [93], [94], [95], [96], and [97]. In addition, the predicted normalization is significantly reduced if spectral effects on the pion production efficiency, the energy dependence of the mean free path of the protons, and the impact of the secondary cooling on the energy budget are taken into account, see [4], [98], and [5]. If one extrapolates a quasi-diffuse flux from a few GRBs, the low statistics of the stacking sample will lead to a systematical error [99]. Given the astrophysical and systematical uncertainties of the model in [89], the current neutrino observations just start to enter the predicted neutrino flux range, and the full-scale IceCube experiment should find neutrinos after ten years of operation if

the baryonic loading of the jets is as high as anticipated in [4]. Note, however, that if the prompt emission comes from larger radii, no neutrinos may be found, see [5]. Additionally, there have been recent efforts to calculate the neutrino emission from GRBs in the dissipative photospheric models [84], as well as efforts for model-independent calculations [78].

As far as the direct connection between neutrinos and cosmic rays is concerned, Eq. (1.1) suggests roughly one muon neutrino per cosmic ray after flavor mixing, which changes the $\nu_e : \nu_\mu : \nu_\tau$ from $1 : 2 : 0$ to $1 : 1 : 1$. This hypothesis has been tested in [100] and [92], with the conclusion that GRBs cannot be the sole source of the UHECR protons. In a more general framework, the authors of [101] conclude that the protons resulting from photopion processes are not sufficient to explain the cosmic-ray measurements. Therefore, we discuss the validity of the assumptions going into the “one neutrino per cosmic ray” paradigm, henceforth called “the standard case”:

1. The protons are magnetically confined, and cosmic rays can only escape as neutrons.
2. The protons interact only once, at most, and the produced neutrons can escape from the source (source optically thin to neutron escape).

If one of these assumptions is violated, the consequences are obvious: protons “leaking” are not accompanied by neutrino production. On the other hand, multiple interactions will enhance the neutrino flux compared to the standard picture, while only neutrons from the boundaries can escape. In this study, we will explore these two regimes in addition to the standard picture, and we will demonstrate that, for high proton acceleration efficiencies, which are required to describe the observed UHECR spectrum, the standard case only occupies a very small region of the parameter space.

1.4 Implementation of the GRB fireball model

We use a simplified description of the relativistically expanding fireball, based on [102], to illustrate our main points. Primed quantities refer to the shock rest frame (SRF), and unprimed quantities to the observer’s or source (cosmologically co-moving) frame, which we clearly indicate. GRB observations exhibit a strong time variability over a scale t_v (defined in the observer’s frame), which can be related to a basic length scale $r_0 = ct_v/(1+z)$ in the source frame. We assume that the central engine of the GRB emits shells of thickness $\Delta r \simeq c \cdot t_v/(1+z) = r_0$ in the source frame, since causality implies that variations of the timescale t_v can only propagate over a distance scale Δr . The time evolution of the fireball can be divided into different zones. In the first zone, the shell gets accelerated, powered by the energy transfer from the thermal photons to the baryons in the shell. The Lorentz factor of the shell grows with the radius until a maximum value Γ is reached, which is, in principle, given by $\Gamma = E_{\text{tot}}/(Mc^2)$, where M is the total mass of baryons and E_{tot} , the total energy of the fireball. This transition is complete at a radius $r \approx \Gamma r_0$. Here the second zone is considered to start: since the shell is accelerated to its maximal velocity, it coasts with constant Γ , while the expansion of the width of the shell itself is still negligible. However, when the shell reaches the radius $r \approx \Gamma^2 r_0$, the growth of the shell width can no longer be neglected, since $\delta\Delta r \simeq r/\Gamma^2 \simeq r_0$. We will come back to this later when we discuss the effects of an expanding shell. For now, we assume that the shell width in the SRF is roughly given by

$$\Delta r' \simeq \Gamma c \frac{t_v}{1+z} \quad (1.4)$$

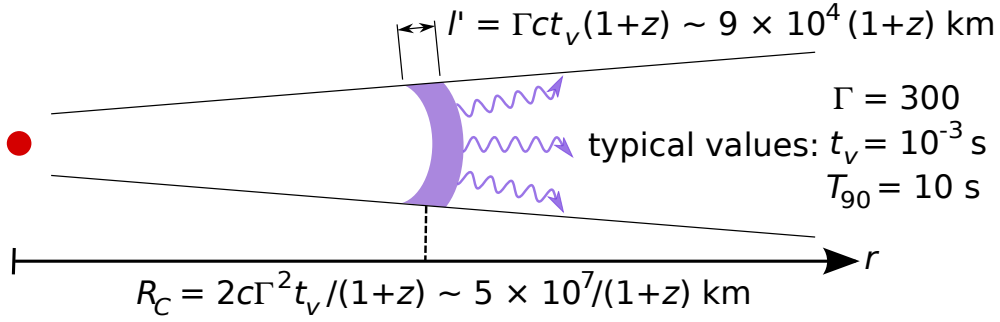


Figure 1.8: Diagram of a static gamma-ray burst.

at the indicated radius. At roughly the same radii,

$$R_C \simeq 2\Gamma^2 r_0 = 2\Gamma^2 c \frac{t_v}{1+z}, \quad (1.5)$$

the collisions of the different shells start, based on the assumed fluctuations of the shells Lorentz factors of the order of $\Delta\Gamma/\Gamma \sim 1$. External collisions with the interstellar medium can also lead to efficient proton acceleration, which we do not consider since the typical photon densities are orders of magnitude lower than in the internal collision zone.

We focus on the description of the prompt phase, which is associated with the collisions of the shells. Since a relativistically expanding fireball may undergo different phases in its expansion, with varying parameters, we describe the physics of one collision, following [99], [4], and [103] and consistent with [89] and [2]. If one assumes that the collisions occur at the same radius r_C , as it is implied in all of the state-of-the-art neutrino analyses [3, 92], the total fluences can be obtained by summing over $N \simeq T_{90}/t_v$ such collisions, where T_{90} is the time during which 90% of the total energy is observed. Our shell-dependent approach has the advantage that the conventional results can be easily retrieved, and that in addition the relation to collision radius-dependent models can be established. Fig. 1.8 illustrates a fundamental assumption of our calculation: that all of the collisions are identical and occur at the same radius R_C . This averaged picture of the burst is already useful to make predictions of the UHECR and neutrino fluxes; however, later, in chapter 5, we will move beyond this **static burst approximation** and consider instead a dynamical burst in which collisions occur at different radii and under different conditions of particle densities.

For the photohadronic interactions, the secondary (such as pion) injection $Q'(E')$ (in units of $\text{GeV}^{-1} \text{cm}^{-3} \text{s}^{-1}$) can be computed from the proper photon $N'_\gamma(\varepsilon')$ and proton $N'_p(E'_p)$ densities (SRF, in units of $\text{GeV}^{-1} \text{cm}^{-3}$) as

$$Q'(E') = \int_{E'}^{\infty} \frac{dE'_p}{E'_p} N'_p(E'_p) \int_0^{\infty} c d\varepsilon' N'_\gamma(\varepsilon') R(x, y). \quad (1.6)$$

Here, $x \equiv E'/E'_p$ is the fraction of energy going into the secondary particles, $y \equiv (E'_p \varepsilon')/m_p c^2$, and $R(x, y)$ is a “response function”. If many interaction types are considered, this response function can be quite complicated. Nevertheless, if it is known from particle physics, Eq. (1.6) can be used to compute the secondary injection for arbitrary proton and photon spectra; see [96]. Note that the secondary injection depends on the product normalization of the proton density $N'_p(E'_p)$ and the target photon density $N'_\gamma(\varepsilon')$. Once the proper proton and photon densities (including the spectral shapes) are known, as well as the magnetic field B' , the secondary meson and neutron

production is just a straightforward particle physics consequence. We use the method from [96], based on the physics of SOPHIA [104], for the computation of the photohadronic interactions. For the secondary meson decays (including the helicity dependence of the muon decays), see, *e.g.*, [95]. The magnetic field effects and flavor mixing are included as in [99] and [4]. Below, we will describe how to determine the relevant input $N'_p(E'_p)$, $N'_\gamma(\varepsilon')$, and B' from the observables.

In Eq. (1.6), two types of spectra are present: the injection/ejection spectrum Q' and the steady spectrum N' . For a specific particle species, these are related to each other by a kinetic equation describing energy losses and escape. If the energy losses can be neglected, they are, for one species of particles, related by

$$N'(E') = Q'(E') t'_{\text{esc}}, \quad (1.7)$$

where t'_{esc} is the escape time. For example, the observed gamma-ray spectrum can be obtained from Q'_γ , whereas the spectrum relevant for the photohadronic interactions in Eq. (1.6) is N'_γ . Typically, one establishes a relationship between observed gamma-ray fluence and target photon density by implying that the gamma-rays escape over $t'_{\text{esc}} = t'_{\text{dyn}} \simeq \Delta r'/c$, which means that Eq. (1.7) can be used. However, if the optical thickness to pair production or other processes is of order unity, this assumption does not apply, and the observed spectrum is not representative for the density in the source anymore.

For $N'_\gamma(\varepsilon')$, a broken power law is normally assumed, parameterized as

$$N'_\gamma(\varepsilon') \propto \begin{cases} \left(\frac{\varepsilon'}{\varepsilon'_{\gamma,\text{break}}}\right)^{-\alpha_\gamma} & \varepsilon'_{\gamma,\text{min}} \leq \varepsilon' < \varepsilon'_{\gamma,\text{break}} \\ \left(\frac{\varepsilon'}{\varepsilon'_{\gamma,\text{break}}}\right)^{-\beta_\gamma} & \varepsilon'_{\gamma,\text{break}} \leq \varepsilon' < \varepsilon'_{\gamma,\text{max}} \\ 0 & \text{else} \end{cases} \quad (1.8)$$

with $\varepsilon'_{\gamma,\text{break}} = \mathcal{O}(\text{keV})$ the break energy of the photon spectrum in the SRF. Typical values for the spectral indices are $\alpha_\gamma \approx 1$ and $\beta_\gamma \approx 2$. The minimal and the maximal photon energies are chosen to be $\varepsilon'_{\gamma,\text{min}} = 0.2 \text{ eV}$ and $\varepsilon'_{\gamma,\text{max}} = 300 \cdot \varepsilon'_{\gamma,\text{break}}$ in our calculations, if the highest energetic photons can escape (see below). These values are far enough away from the break energy to have no visible effect on the predicted neutrino spectra [95, 99], though they can somewhat affect the neutron escape spectra; see Sec. 2.3 for a more detailed discussion. In addition, the energy partition is hardly affected by the maximal photon energy for a spectral index $\beta_\gamma \gtrsim 2$, since the energy in photons then depends only logarithmically on the maximal photon energy, at most. Note that high-energy photons will not be able to escape above the pair production threshold. In this case, we choose $\varepsilon'_{\gamma,\text{max}}$ consistent with the pair production threshold.³

In case of the internal collisions, it is generally assumed that Fermi shock acceleration leads to a non-thermal particle spectrum of the form

$$N'_p(E'_p) \propto (E'_p)^{-\alpha_p} \cdot \exp\left(-\left(\frac{E'_p}{E'_{p,\text{max}}}\right)^k\right) \quad (1.9)$$

with the spectral index $\alpha_p \approx 2$. For the exponential cutoff, we choose $k \simeq 2$ unless noted otherwise. The maximal proton energy $E'_{p,\text{max}}$ can be obtained by comparing the acceleration timescale to the dominant loss timescale

$$t'_{\text{acc}}(E'_{p,\text{max}}) = \min [t'_{\text{dyn}}, t'_{\text{syn}}(E'_{p,\text{max}}), t'_{p\gamma}(E'_{p,\text{max}})] \quad (1.10)$$

³ We use Eq. (6) from [89] to estimate that, applicable for the ε^{-2} -spectra (above the break), assuming that the photon spectrum extends to infinitely high energies. This is only a rough estimate, since gamma-rays may interact by additional processes. The impact on $\varepsilon'_{\gamma,\text{max}}$ is, however, typically small.

Here we assume that the acceleration time (in Gaussian cgs units) is given by

$$t'_{\text{acc}}(E') = \frac{E'}{\eta c e B'} , \quad (1.11)$$

with the elementary charge $e \simeq 4.803 \cdot 10^{-10}$ Fr and η the acceleration efficiency (η is defined here so that large values mean efficient acceleration). It is generally assumed that the dominant loss mechanism is either the adiabatic loss due to the expansion of the shell or the synchrotron loss of the protons due to the magnetic fields present in the shells. We do not consider the adiabatic loss timescale explicitly, since we assume that it is of the same order as the dynamical timescale $t'_{\text{dyn}}(E')$. The synchrotron loss time is given by

$$t'_{\text{syn}}(E') = \frac{9 m^4}{4 c e^4 B'^2 E'} , \quad (1.12)$$

with the particle mass m being in erg, using the relation $1 \text{ erg} = 624.15 \text{ GeV}$. Moreover, the photohadronic timescale $t'_{p\gamma}$ is numerically computed from the interaction rate as given in [96].

Let us now derive $N'_\gamma(\varepsilon')$ and $N'_p(E'_p)$ from the observables. Frequently used observables are the (bolometrically corrected) gamma-ray fluence of a detected GRB, S_{bol} (in units of erg cm^{-2}), or the radiative flux F_γ (in units of $\text{GeV cm}^{-2} \text{ s}^{-1}$). Here we focus on a momentary picture of the fireball, described by (a possibly bolometrically corrected) F_γ , which leads to the isotropic equivalent energy per shell (or collision)

$$E_{\text{iso}}^{\text{sh}} \simeq \frac{4\pi d_L^2}{(1+z)} F_\gamma t_v \quad , \quad (1.13)$$

where d_L is the luminosity distance. One has $E_{\text{iso}}^{\text{sh}} = E_{\text{iso}}^{\text{sh}}/\Gamma$ in the SRF, and $L_{\gamma,\text{iso}} = E_{\text{iso}}^{\text{sh}} \cdot (1+z)/t_v$. Assuming energy equipartition between photons and electrons, the photons carry a fraction ϵ_e (fraction of energy in electrons) of the total energy $E_{\text{iso,tot}}^{\text{sh}}$, and

$$E_{\text{iso,tot}}^{\text{sh}} = \epsilon_e^{-1} \cdot E_{\text{iso}}^{\text{sh}} . \quad (1.14)$$

In order to compute the photon and proton densities in the SRF, it turns out to be useful to define an ‘‘isotropic volume’’ $V'_{\text{iso}} = 4\pi R_C^2 \Delta r' \propto \Gamma^5$, where the latter relationship can be easily read off from Eqs. (1.4) and (1.5). Here V'_{iso} can be interpreted as the volume of the interaction region assuming isotropic emission by the source.⁴ If the characteristics of all collisions are alike, $S_{\text{bol}} \simeq F_\gamma T_{90}$.

Now one can determine the normalization of the photon density in Eq. (1.8) and the proton density in Eq. (1.9) from

$$\int \varepsilon' N'_\gamma(\varepsilon') d\varepsilon' = \frac{E_{\text{iso}}^{\text{sh}}}{V'_{\text{iso}}} , \quad \int E'_p N'_p(E'_p) dE'_p = \frac{1}{f_e} \frac{E_{\text{iso}}^{\text{sh}}}{V'_{\text{iso}}} . \quad (1.15)$$

Here f_e is the ratio between energy in electrons and protons (f_e^{-1} is the baryonic loading). Assuming that the magnetic field carries a fraction ϵ_B of $E_{\text{iso}}^{\text{sh}}$, one has in addition

$$U'_B = \frac{\epsilon_B}{\epsilon_e} \cdot \frac{E_{\text{iso}}^{\text{sh}}}{V'_{\text{iso}}} \quad \text{or} \quad B' = \sqrt{8\pi \frac{\epsilon_B}{\epsilon_e} \cdot \frac{E_{\text{iso}}^{\text{sh}}}{V'_{\text{iso}}}} . \quad (1.16)$$

⁴Since both the energy and the volume of the source need to be, in principle, corrected by a beaming factor, this beaming factor cancels in the computation of the energy densities.

After photohadronic interactions and weak decays, one obtains the injection spectrum of secondary neutrinos or neutrons Q' , which is to be translated into the observable neutrino or neutron fluence \mathcal{F}^{sh} (in units of $\text{GeV}^{-1} \text{cm}^{-2}$) per shell:

$$\mathcal{F}^{\text{sh}} = t_v V'_{\text{iso}} \frac{(1+z)^2}{4\pi d_L^2} Q', \quad E = \frac{\Gamma}{1+z} E'. \quad (1.17)$$

In chapter 3, however, we discuss the impact on UHECR observations including pair production and photohadronic losses during the UHECR proton propagation. Additionally, we assume that neutrinos are subject to flavor mixing using the mixing angles $\theta_{12} = 0.587$, $\theta_{13} = 0.156$, $\theta_{23} = 0.670$, and $\delta_{\text{CP}} = 1.08\pi$, taken from [105] for the normal (mass) hierarchy, unless noted otherwise. For reference, later on, in chapters 2 and 4 it will be also illustrative to show the cosmic ray proton fluence if all protons were allowed to escape over t'_{dyn} , which represents the maximal possible “leakage” from the source. This fluence can be obtained from Eq. (1.17) using $Q'_p = N'_p/t'_{\text{dyn}}$.

There are three important features of our approach. First of all, we relate everything to the prompt phase, which is implied by using the flux during that phase in Eq. (1.13). The proper densities in Eq. (5.38) describe the (steady) proton and photon densities in that phase. We do not specify the origin of the target photons, such as synchrotron emission of co-accelerated electrons or inverse Compton scattering. Second, we consider emitted neutrino and cosmic ray fluences instead of fluxes, which implies that we do not need to resolve the time-dependence of the emissions. For instance, the cosmic ray protons emitted with a different escape mechanism may not be emitted at the same time as the gamma-rays. And, third, we compute the fluences per shell, which may seem a bit peculiar, but has the advantage that our approach can describe dynamical changes of the fireball parameters over time, such as collisions at different radii. If all collisions are alike, as it is often assumed, one can easily obtain the result by summing over $N \simeq T_{90}/t_v$ such collisions.

Chapter 2

A two-component model of UHECR emission

It is common for predictions of the UHECRs and UHE neutrino signals from GRBs to be made using a so-called “neutron model”, where protons are magnetically confined inside the source, where they create neutrons and neutrinos via $p\gamma$ interactions; the neutrons are able to escape the source and β -decay into protons outside the source. The lack of observation by IceCube of neutrinos in correlation with GRBs has recently put tension on the validity of the neutron model [3]. Motivated by these results, and following a trend towards building more realistic models of UHECR and neutrino emission, in this chapter, we discuss “direct escape” as a second UHECR escape mechanism: high-energy protons are no longer perfectly confined within the source, but those that lie close to the outer edges of the matter shells can directly escape from them, without undergoing photohadronic interactions, and, hence, without producing neutrinos. While this contribution may be generically expected to be small, we will demonstrate that it is an energy-dependent fraction of protons which can directly escape, and that the direct escape can dominate over the escape of neutrons produced in photohadronic interactions in regions of the parameter space.

2.1 Neutron and direct proton escape from an expanding shell

If the particles are isotropically distributed inside an expanding matter shell, then the fraction of directly escaping particles is proportional to the escape volume, which is defined as the thin shell of thickness λ'_{mfp} from within which particles can escape without interacting. The mean free path λ'_{mfp} will be defined in Eq. (2.3). The fraction of escaping particles f_{esc} after a collision can then be estimated from the ratio between escape volume and isotropic volume as

$$f_{\text{esc}} \equiv \frac{V'_{\text{direct}}}{V'_{\text{iso}}} \simeq \frac{1}{2} \cdot \frac{4\pi (r^2 + (r - \Delta r')^2) \lambda'_{\text{mfp}}}{4\pi r^2 \Delta r'} \simeq \frac{\lambda'_{\text{mfp}}}{\Delta r'} . \quad (2.1)$$

Here it is taken into account that there are in fact two escape regions in each shell (inner and outer edge), and that only half of the particles along the mean free path propagate in the outwards direction. The fluence of directly escaping protons can then be computed from Eq. (1.17) using

$$Q'_p = \frac{N'_p}{t'_{\text{dyn}}} \cdot f_{\text{esc}} = \frac{N'_p}{t'_{\text{dyn}}} \cdot \frac{\lambda'_{\text{mfp}}}{\Delta r'} = \frac{N'_p}{t'_{\text{eff,dir}}} , \quad (2.2)$$

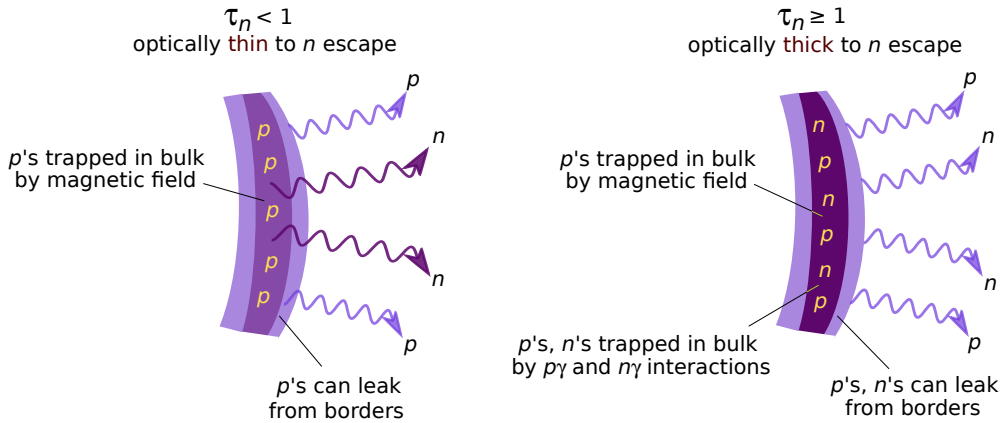


Figure 2.1: Two-component UHECR emission from an internal collision. Figure taken from Ref. [106].

with an effective direct escape timescale $t'_{\text{eff,dir}} \equiv t'_{\text{dyn}} \Delta r' / \lambda'_{\text{mfp}}$. A schematic illustration of the two-component model is shown in Fig. 2.1; we will see that direct proton escape dominates when the shell is optically thin to neutron escape, *i.e.*, $\tau_n < 1$, whereas for optically thick sources the protons remain magnetically trapped in the bulk of the shell.

The mean free paths for protons and neutrons, respectively, are given by

$$\begin{aligned} \lambda'_{p,\text{mfp}}(E') &= \min [\Delta r', R'_L(E'), ct'_{p\gamma}(E')] , \\ \lambda'_{n,\text{mfp}}(E') &= \min [\Delta r', ct'_{p\gamma}(E')] . \end{aligned} \quad (2.3)$$

The first term, $\Delta r'$, ensures that $f_{\text{esc}} \leq 1$. The photohadronic interaction length $ct'_{p\gamma}$, calculated by NeuCosmA after Ref. [96], will become relevant especially when the proton and photon densities are high enough. Protons are confined inside the source by magnetic fields, and the Larmor radius is defined as

$$R'_L = \frac{E'_p}{e B'} \simeq 33.3 \text{ cm} \cdot \left(\frac{E'_p}{\text{GeV}} \right) \cdot \left(\frac{10^5 \text{ G}}{B'} \right) . \quad (2.4)$$

Under conditions of low particle densities, effectively everything within a distance R'_L of the edges will eventually escape from the shells, which we call “direct escape”¹. Within this region, the particles can escape without being scattered at all, and without having lost energy. Now, R'_L is proportional to E'_p , and $R'_L = ct'_{\text{acc}}$ for $\eta = 1$ (see Eq. (1.11)). Therefore, it is easy to see that all protons will directly escape at the highest energy if $\eta = 1$ and the maximal proton energy is limited by the dynamical timescale, where $ct'_{\text{acc}} = \Delta r'$. This is the region where direct escape of UHECR dominates. For lower acceleration efficiencies, or synchrotron- or photohadronic-loss limited maximal proton energies, the direct escape component will be smaller, and the question of what kind of escape dominates will be more complicated. Like for protons, to obtain the fluence of directly escaping neutrons, we multiply the neutron injection Q'_n by f_{esc} from Eq. (2.1). By computing neutrino and proton fluences (instead of fluxes), we do not need to identify when the particles actually escape, we just compute the fraction of escaping particles f_{esc} . This means that

¹Note that the results in this section can be only interpreted as rough estimates, and there may be additional escape components compared to the ones discussed here, *e.g.*, diffusion may play a role. We discuss the possible impact of diffusion in appendix A of Ref. [106], where we demonstrate that it does not affect our qualitative conclusions. However, we also point out that a dedicated treatment of diffusion requires a model-dependent solution of the transport equations, which goes beyond the scope of this study, whereas direct escape can be regarded as a guaranteed contribution to the cosmic ray injection.

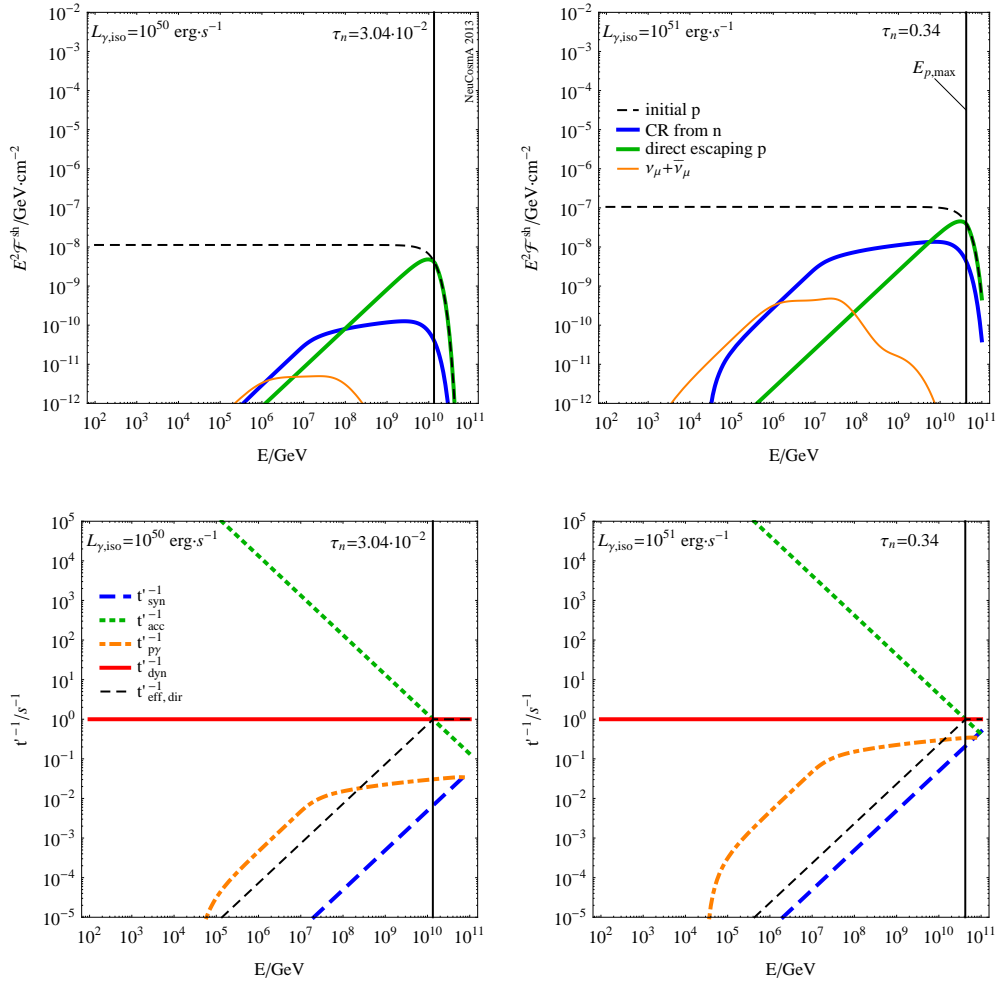


Figure 2.2: Particle fluences per shell (upper row) and inverse timescales of different processes (in SRF, lower row) as a function of E in the observer’s frame. The figure shows two different parameter values for $L_{\gamma,\text{iso}}$ in the different columns, where the other burst parameters are fixed to $\Gamma = 300$, $t_v = 0.01 \text{ s}$, $\eta = 1$, $\epsilon_e/\epsilon_B = 1$, $f_e = 0.1$, $\alpha_\gamma = 1$, $\beta_\gamma = 2$, $\epsilon'_{\gamma,b} = 1 \text{ keV}$, and $z = 2$. Both examples are for the **optically thin (to neutron escape)** case, where the optical thickness τ_n is given in the panels. For the cosmic rays, only adiabatic energy losses are taken into account for the propagation. See main text for details. Figure taken from Ref. [106].

we can evaluate Eq. (2.1) in the collision phase using $r \simeq R_C$ with the corresponding proton density.

We define the optical thickness to neutron escape as

$$\tau_n \equiv \left. \frac{t'_{p\gamma}{}^{-1}}{t'_{\text{dyn}}{}^{-1}} \right|_{E_{p,\text{max}}} \quad (2.5)$$

at the maximal proton energy. Thus, if $\tau_n \gtrsim 1$, neutrons at the maximal proton energy will rather interact than escape, and will therefore be confined. Since $t'_{p\gamma}{}^{-1}$ increases with energy (see, *e.g.*, Fig. 2.2, lower panels), this optical thickness is typically at its maximum at the maximal proton energy. That is, it applies to the UHECR part of the emission, whereas neutrons at lower energies

may escape more easily. Of course, not only the neutrons will interact rather than leave the region, but also the protons; hence, τ_n is also a measure of the optical thickness to *proton* escape in the source.

Two examples of optically-thin, direct escape-dominated bursts can be found in the different columns of Fig. 2.2 for the parameter sets given in the plot; the two columns differ in the isotropic luminosity: 10^{50} erg s⁻¹ (left) and 10^{51} erg s⁻¹ (right). The upper row shows the particle fluences, where “initial p” stands for the case if all protons were able to escape over the dynamical timescale, “CR from n” represents the cosmic rays through neutron escape from photohadronic interactions, “direct escaping p” for direct proton escape, and $\nu_\mu + \bar{\nu}_\mu$ for the muon-neutrino fluence including flavor mixing.² In the lower panels, the acceleration timescale and the considered energy loss/escape timescales are shown, where the direct escape effective timescale is defined in Eq. (2.2). It can be read off from these panels that in both cases the dynamical timescale limits the maximal proton energy. In the upper left panel, the direct escape clearly dominates. Since the acceleration efficiency $\eta = 1$, practically all protons escape at the highest energy, which is where the dynamical timescale, acceleration timescale, and direct escape timescale meet. However, in that case hardly any neutrinos are produced due to the low photohadronic interaction rate. The upper right panel represents the typical case for the optically thin (to neutron escape) source, where both substantial neutrino and neutron fluxes are produced. The additional component from direct escape still dominates at the highest energies, while for energies below $10^{9.5}$ GeV, the neutron flux dominates the cosmic ray production. This can be also read off from the corresponding timescales in the lower panel. Note that direct escape strongly depends on the acceleration efficiency: if $\eta \ll 1$, the Larmor radius will be much smaller than $\Delta r'$ at the maximal proton energy, and the direct component becomes suppressed.

In contrast, we show two examples for the optically thick case in the columns of Fig. 2.3. In both cases (see lower panels), the photohadronic interaction rate exceeds the dynamical escape rate by a factor of τ_n at the highest energies. It also limits the maximal proton energy in both cases. The neutron production is therefore very efficient; see upper panels. However, only the neutrons from the edges can escape, which implies that the dashed curves (corresponding to the escape of all protons over the dynamical timescale) cannot be exceeded, and a level of about 50% of the dashed curves is reached (since the baryon system contains about 50% protons and neutrons each in the optically thick limit). In contrast, the neutrinos from interactions everywhere within the shell can escape, which means that the neutrino fluence becomes relatively enhanced, and the “one neutrino per cosmic ray” paradigm does not hold anymore. This can be especially seen in the upper right panel. Note however that the neutrino fluence is typically lower than the cosmic ray fluence, because the neutrons obtain a higher fraction of energy in the interaction. In none of the discussed cases the direct escape of protons substantially contributes, which is characteristic for the optically thick regime.

Our approach has several limitations. First, one may argue that the protons and neutrons trapped by photohadronic interactions may escape later in a relativistically expanding fireball. Indeed, since the photon density drops as the burst expands, the injection of neutrons ceases and the confinement by photohadronic interactions will come to an end at a certain radius (the “neutronsphere”), and all remaining neutrons may escape. In this direction, in chapter 5 we will study a dynamical burst model, in which the individual matter shells expand and collide at different radii, where different

²Note that for the sake of comparability, the CR spectra shown here are “at the observer” assuming that the CRs receive the same boost and losses as the neutrinos. In particular, the spectra here are without any losses during propagation apart from the adiabatic losses due to the cosmic expansion. In chapter 3 we will introduce propagation effects.

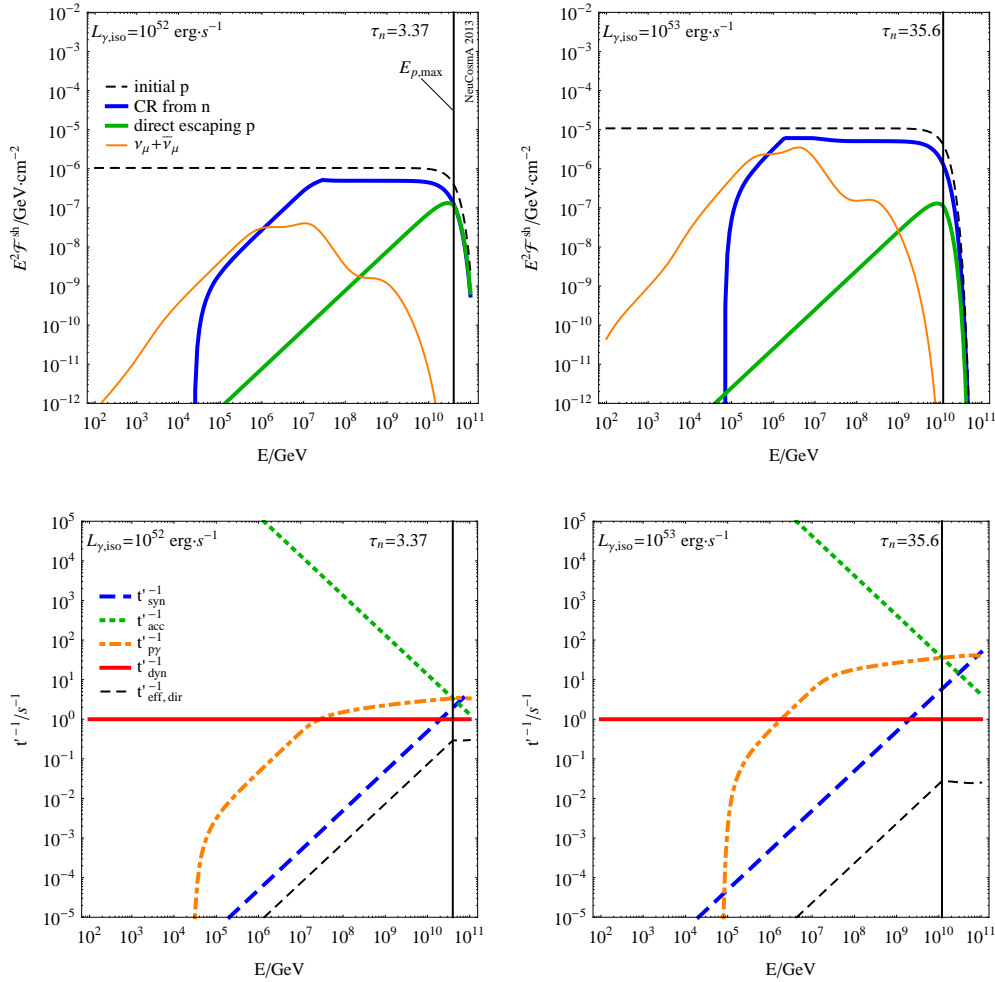


Figure 2.3: Particle fluences per shell (upper row) and inverse timescales of different processes (in SRF, lower row) as a function of E in the observer’s frame. The figure shows two different parameter values for $L_{\gamma, \text{iso}}$ in the different columns, where the other burst parameters are fixed to the same values as in Fig. 2.2. Both examples are for the **optically thick (to neutron escape) case**, where the optical thickness τ_n is given in the panels. See main text for details. Figure taken from Ref. [106].

particle densities exist: we will find that, whereas neutron escape dominates at lower radii, due to a higher rate of photohadronic interactions, direct proton escape dominates at larger radii. Another limitation is that the energy partition fractions may be different than the ones assumed in the optically thick regime. We also do not consider the effects of muon re-acceleration [107, 108, 109, 110], or interactions of pions and kaons [111], which have however much smaller interaction rates than the protons.

There are several subtleties in the optically thick case, which are best illustrated with the pion production efficiency f_{π} relevant for neutrino production. As we show in detail analytically in appendix B of Ref. [106], these lead to an underestimation of the neutrino production in the optically thick case if the current IceCube method for the computation of f_{π} from Ref. [91] is used, which is the foundation for all state-of-the-art GRB stacking analyses, as in Ref. [92]. In fact, it turns out that the original formula for f_{π} from Ref. [2] also applies to the optically thick case if

the energy partition is defined with respect to the particle densities within the source, even though it was not derived for that limit. Current state-of-the-art numerical predictions, such as Ref. [4], take this into account automatically.

2.2 Parameter space study of the cosmic ray-neutrino connection

Depending on the values of the GRB parameters (luminosity, redshift, Lorentz factor of the matter shells, *etc.*), the UHECR emission can fall in one of three regimes:

Optically thin to neutron escape regime. This is the usual scenario discussed in the literature: the cosmic rays are produced as neutrons and can escape the source (“neutron model”). Additional escape components are negligible, and the “one (muon-) neutrino per cosmic ray” paradigm applies.

Direct escape regime. Here the cosmic rays from direct escape dominate at least at the highest energy. Since the neutron production by photohadronic processes is sub-dominant, the one-neutrino-per-cosmic-ray relation does not hold, and more cosmic rays than neutrinos will be produced.

Optically thick to neutron escape regime. Here the protons and neutrons interact multiple times, and only protons and neutrons on the outer edges of the shells can (directly) escape. The neutrinos, however, can escape from everywhere within the shell, which leads to more neutrinos per cosmic ray than in the optically thin case.

In the optically thin to neutron escape regime, one (muon-) neutrino per cosmic ray will be produced; in case the direct escape regime, the UHECR escape will not be necessarily accompanied by neutrino production; and in the optically thick regime, the neutrino production will be enhanced compared to the optically thin regime, since the neutrinos can escape from everywhere within the shell.

In this section, we perform a scan of the GRB parameter space and identify the regions that correspond to the different emission regimes. We distinguish the dominant effect by using figures such as Fig. 2.2 and Fig. 2.3: if the fluence maximum in the spectrum comes from directly escaping protons, we assign the direct escape category, otherwise the optically thin regime. The optically thin and thick cases are distinguished by the optical thickness τ_n , as defined in Eq. (2.5), being smaller or larger than one, respectively. It turns out that either of these three categories can be uniquely assigned (neglecting minor overlap).

We show a (numerical) parameter space scan in Fig. 2.4, where we always plot $L_{\gamma,\text{iso}}$ on the horizontal axis. Let us focus on moderate acceleration efficiencies $\eta = 0.1$ first (lower row), which clearly exhibit all three regimes. The optically thin case, in light yellow (light gray), can be found close to the often-used standard parameter values. In this case, the direct escape contribution cannot reach the same level as shown in Fig. 2.2 since the maximal achievable proton energy is lower, and therefore the Larmor radius at the maximal energy cannot reach the shell width. Therefore, the escape of neutrons produced in photohadronic interactions dominates. On the other hand, in the light red (gray) regions, $\tau_n > 1$, which means that the neutrino production is enhanced. In the blue (darker) regions, the direct escape component exceeds the neutron escape at the highest energies. For efficient acceleration, $\eta = 1$, see upper row. Here the optically thin to neutron escape region almost vanishes, which is due to an enhancement of the direct escape. Remember that for

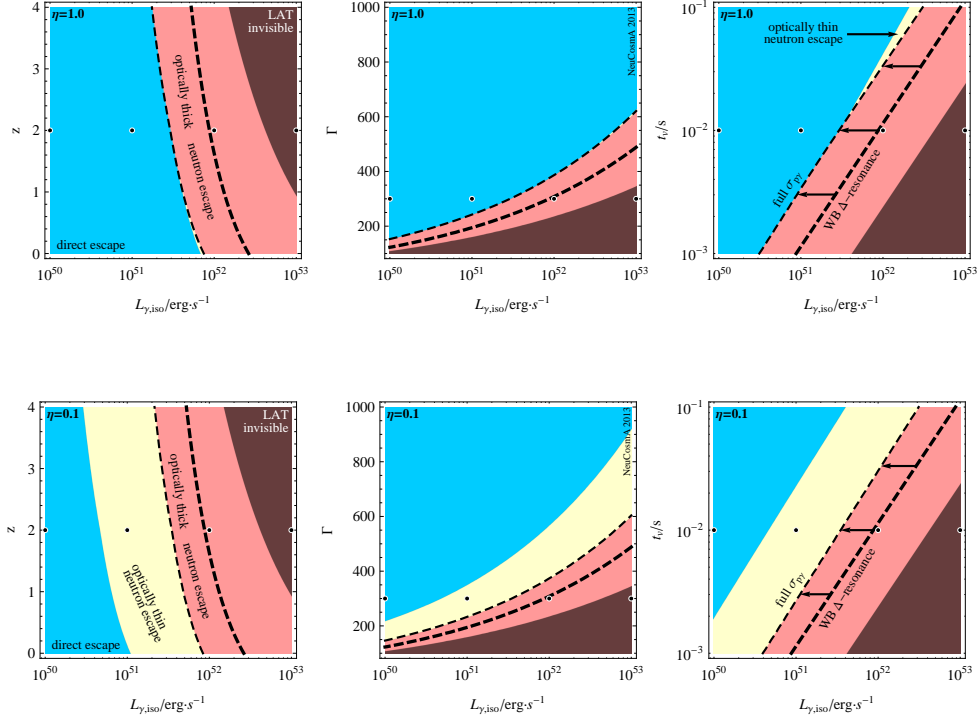


Figure 2.4: Parameter space scan of the GRB parameters for classification of regimes. The upper row corresponds to the acceleration efficiency $\eta = 1$, the lower row to $\eta = 0.1$. For the standard parameter values, see caption of Fig. 2.2. Dashed curves mark the limit between optically thin and thick regimes. The thick dashed curve represents the analytical result if the photohadronic interaction rate based on Eq. (3) of [89] is used. In the dark-shaded regions “LAT invisible”, gamma-rays above 30 MeV cannot leave the source anymore due to pair production. That is, sources left of these regions are in principle visible in the full *Fermi*-GBM range and may be even observable in LAT, whereas sources within these regions will not exhibit emission into the LAT range. The dots correspond to the parameter sets chosen in Fig. 2.2 and Fig. 2.3. Figure taken from Ref. [106].

$\eta = 1$, all protons can directly escape at the highest energy if the maximal energy is limited by the dynamical timescale. To summarise, for efficient proton acceleration, the standard case (one neutrino per cosmic ray) only applies in a very small region of the parameter space, and either fewer or more neutrinos per cosmic ray are produced, depending on the parameters.

In order to better understand the relation to earlier works, consider the Δ -resonance parameterization proposed by [89] (see Eq. (3), increased by a factor of two because we consider the photohadronic interaction rate, not the pion production rate). We show in Fig. 2.4 the separator between optically thin and thick regimes as thick dashed curves for this cross section. Obviously, in all cases the optically thin region reappears and gets enlarged. One reason is that the full numerical computation includes high-energy processes, such as multi-pion production, which enhance the interaction rate at high energies by a factor of a few, and which is not included in the shown Δ -resonance approximation. As a result, photohadronic processes become more important in the numerical result.

Let us now relate the parameter space to *Fermi*-LAT observations. We hence show in Fig. 2.4 the “LAT invisible” regions, where gamma-rays above 30 MeV cannot leave the source anymore because they exceed the pair production threshold. That is, sources to the left of these regions should be visible in the full *Fermi*-GBM range and may be even observable in LAT, while sources in the “LAT invisible” regions will not exhibit emission into the LAT range. One can clearly see that the parameter set corresponding to the rightmost dot, associated to the right column of Fig. 2.3, cannot be seen in LAT. In addition, even though the optical thicknesses τ_n (for neutrons) and $\tau_{\gamma\gamma}$ (for photons) are roughly proportional, they still have slightly different parameter dependencies.³ Note that, in practice, the LAT emission lasts longer (see, *e.g.*, [112]), which means that it may come from larger emission radii. That is, in a realistic time-dependent model, the fireball may follow a trajectory in the considered parameter space, and may actually visit more than one regime during the burst duration. We defer such an exploration to chapter 5.

Since Fig. 2.4 only shows sections through the parameter space, it is instructive to at least have approximate analytical expressions for the different regimes. The interface between the direct escape and optically thin regions can be obtained from the maximal proton energy: if it is dominated by the dynamical timescale, direct escape will dominate at the highest energies since all protons can escape (for $\eta = 1$); if it is dominated by synchrotron losses, neutron escape will take over. Taking into account η , one can estimate that

$$L_{\gamma,\text{iso}}^{\text{direct}} \lesssim 3.6 \cdot 10^{51} \text{ erg s}^{-1} \cdot \eta^{\frac{2}{3}} \cdot \left(\frac{\Gamma}{10^{2.5}} \right)^{\frac{14}{3}} \cdot \left(\frac{t_v}{0.01 \text{ s}} \right)^{\frac{2}{3}} \cdot \left(\frac{1+z}{3} \right)^{-\frac{2}{3}} \cdot \left(\frac{\epsilon_B}{\epsilon_e} \right)^{-1} \quad (2.6)$$

limits the direct escape dominated region. The interface between the optically thin and thick regimes (analytical thick dashed curves) can be obtained from $\tau_n \simeq 1$ in Eq. (2.5), using the analytical expression for $t_{p\gamma}^{\prime-1}$ from [89]. The optically thick regime is then estimated as

$$L_{\gamma,\text{iso}}^{\text{opt. thick}} \gtrsim 1.1 \cdot 10^{52} \text{ erg s}^{-1} \cdot \left(\frac{\Gamma}{10^{2.5}} \right)^5 \cdot \left(\frac{t_v}{0.01 \text{ s}} \right) \cdot \left(\frac{\epsilon'_{\gamma,\text{break}}}{1 \text{ keV}} \right) \cdot \left(\frac{1+z}{3} \right)^{-1}. \quad (2.7)$$

These formulas allow to estimate how a specific burst can be classified for arbitrary parameters. There are, however, some limitations. First of all, Eq. (2.7) underestimates the photohadronic interactions, as discussed above. And, second, some of the (numerical) parameter dependencies in Eq. (2.6) cannot be reproduced within these assumptions.

In order to describe the UHECR spectrum, it is a necessary condition that high enough proton energies can be obtained in the co-moving (source) frame. We show in Fig. 2.6 the maximal proton energy $\log_{10}(E_{p,\text{max}}/\text{GeV})$ (contours) in the co-moving frame as a function of the GRB parameters, similar to Fig. 2.4. The upper row is shown for an acceleration efficiency $\eta = 1$; the lower row, for $\eta = 0.1$. One can clearly see the symmetry around the transition curve between the optically

³This is mainly due to one important difference in the calculations, namely which frame is considered to be relevant. The maximal proton/neutron energy is calculated in the SRF during our calculation, however the calculation of $\tau_{\gamma\gamma}$ is done for an observed photon energy. Hence there is a difference in redshift z and Lorentz factor Γ . Moreover, the break energy is important for the calculation of the (energy) densities, but it is not relevant for the optical thickness of the observed gamma-rays, as this calculation refers to photons far above the break.

	SB	GRB080916C	GRB090902B	GRB091024
α_γ	1	0.91	0.61	1.01
β_γ	2	2.08	3.80	2.17
$\epsilon_{\gamma,\text{break}}$ [MeV]	1.556	0.167	0.613	0.081
Γ	$10^{2.5}$	1090	1000	195
t_v [s]	0.0045	0.1	0.053	0.032
T_{90} [s]	30	66	22	196
z	2	4.35	1.822	1.09
F_γ [erg cm $^{-2}$]	$1 \cdot 10^{-5}$	$1.6 \cdot 10^{-4}$	$3.3 \cdot 10^{-4}$	$5.1 \cdot 10^{-5}$
$L_{\gamma,\text{iso}}$ [erg s $^{-1}$]	10^{52}	$4.9 \cdot 10^{53}$	$3.6 \cdot 10^{53}$	$1.7 \cdot 10^{51}$

Table 2.1: Properties of four bursts discussed in section 2.3; see [97] for SB (“Standard Burst”, similar to [89, 113]), [114] and [115] for GRB080916C, [114] and [116] for GRB090902B, and [114] and [117] for GRB091024. The luminosity is calculated with $L_{\gamma,\text{iso}} = 4\pi d_L^2 \cdot S_{\text{bol}}/T_{90}$, with S_{bol} the fluence in the (bolometrically adjusted) energy range 1 keV – 10 MeV. Adopted from [118]. Table taken from Ref. [106].

thin (or direct escape dominated) and optically thick cases, where the proton energy is limited by photohadronic losses in the latter case. The highest proton energies can be obtained along this transition curves, but the overall dependence of the maximal proton energy on the model parameters is relatively weak. The main impact comes from the acceleration efficiency (compare upper with lower row): for $\eta = 1$, about an order of magnitude higher proton energies can be achieved than for $\eta = 0.1$.

2.3 Application to specific GRBs

So far, we have discussed the dependence of the cosmic ray escape on the theoretical parameters, such as $L_{\gamma,\text{iso}}$. However, actually the gamma-ray flux or fluence are the observables, and $L_{\gamma,\text{iso}}$ is just a function of these observables. In addition, for many bursts, the other necessary ingredients, such as redshift and time variability, have been measured. We therefore study in this section the different cosmic ray escape mechanisms for specific bursts; see table 2.1. In this case, we use the bolometric fluence as observable, and assume that it is obtained from $N = T_{90}/t_v$ identical collisions, in consistency with the approaches used in Refs. [3, 92], and Ref. [4].

The standard burst “SB” has been inspired to produce a spectrum similar to Refs. [89, 113]. The other three bursts have been actually observed, and their properties can be taken from the literature (see table caption). GRB080916C is one of the brightest bursts ever seen, although at a large redshift, and one of the best studied *Fermi*-LAT bursts. The gamma-ray spectrum of GRB090902B has a very steep photon spectral cutoff and a smaller redshift, although Γ is very high as well. GRB091024 can be regarded as a typical example representative of many *Fermi*-GBM bursts [114], except for the long duration. Note that the neutrino spectra from these GRBs have been also discussed in Refs. [103, 119].

We show in Fig. 2.5 the expected cosmic ray and neutrino fluences for the GRBs listed in table 2.1 (thick curves). In each panel, we also give the optical thickness to neutron escape and photon escape (for 30 MeV gamma-rays). Note that we use an acceleration efficiency $\eta = 0.1$ for these simulations; a higher acceleration efficiency would pronounce the direct escape component. The burst SB is a typical example for an optically thin burst with a substantial amount of neutrino

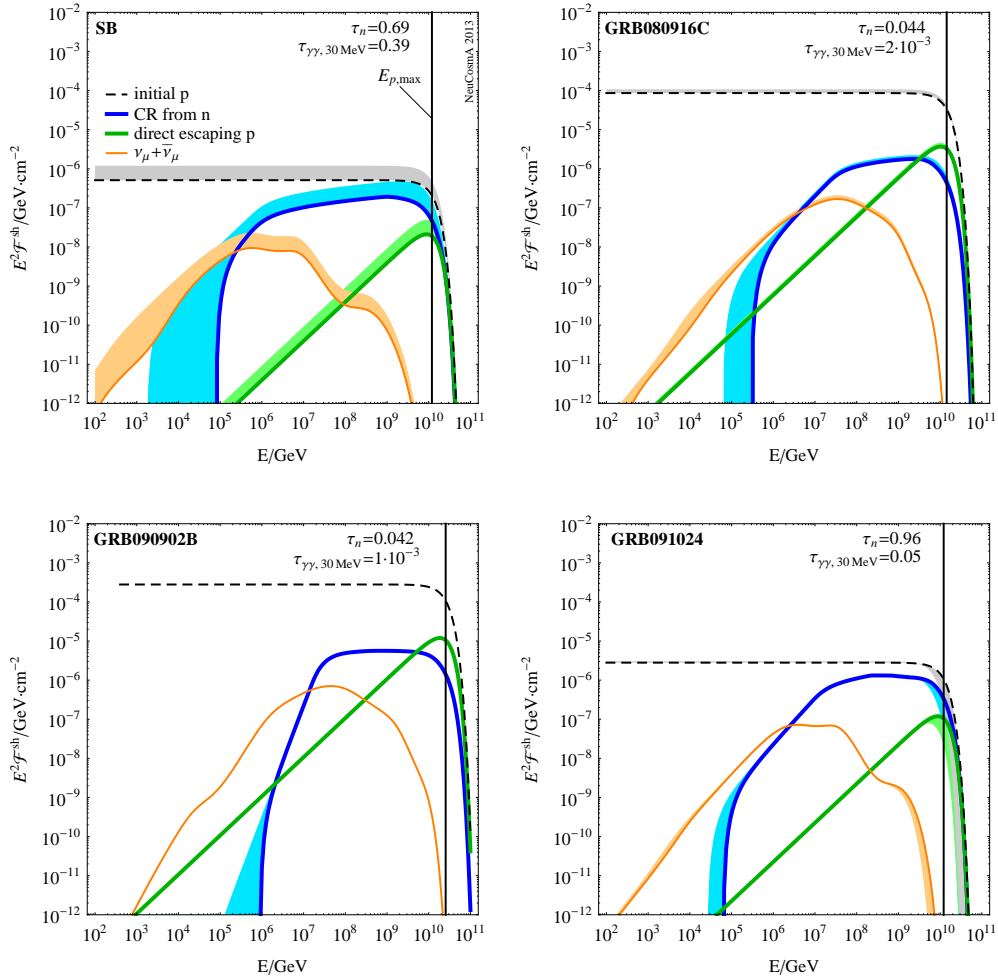


Figure 2.5: The expected cosmic ray and neutrino fluences for the GRBs listed in table 2.1. The maximal proton energy and the optical thickness are given/marked in the different panels. The thick curves correspond to the photon fluence and energy range given in the caption of table 2.1, whereas the shadings represent a bolometric correction beyond this range; see main text. In each panel, we also give the optical thickness to neutron and photon escape (the latter for 30 MeV gamma-rays). Note that we use an acceleration efficiency $\eta = 0.1$ for these simulations. Figure taken from Ref. [106].

production. The contribution of the direct escape component depends on the proton acceleration efficiency, and in this case it is suppressed. Therefore, the relation one-neutrino-per-cosmic-ray holds. On the other hand, the two high- Γ *Fermi*-LAT bursts GRB080916C and GRB090902B exhibit a clear direct escape domination, which is a feature of the large Γ ; see Fig. 2.4 (second row, second column). It is clear that GRBs will be only observed in LAT if they are to the left of the dark-shaded regions in Fig. 2.4. An even larger value of the photon energy, such as 100 MeV, will extend these regions further to the left, which means that the LAT-associated parameter space region tends to overlap the direct escape regime. Therefore, LAT-observed GRBs tend to directly emit UHECR protons at the highest energies, at least in the LAT emission phase. The situation is different for GRB091024 in the lower right panel of Fig. 2.5, which is on the edge of the optically thick regime. For this burst, again cosmic rays from escaped neutrons dominate, and the neutrino

production follows the standard assumption.

In order to illustrate the effect of the minimal and maximal photon energies in Eq. (1.8), we illustrate the impact of a “bolometric correction”⁴ as shaded areas in Fig. 2.5. This bolometric correction takes into account that the gamma-ray fluence has only been observed in a certain energy range, whereas it cannot be excluded that lower and higher energy photons are present in the source as well, either because they are outside the detection energy range, or because they cannot escape from the source.⁵ The proton density is then calculated from energy partition using the extended energy range according to Eq. (5.38). The bolometric correction increases it in all cases due to photons not accounted for in the observation, and therefore the normalisation of the spectra increases, including that of the “initial protons”. In none of the cases, the neutrino spectrum is very much affected by this bolometric correction, apart from the normalisation change.⁶ The extension of the photon energy range hardly affects the neutrino spectral shape, but the extension of the spectrum to higher energies has a significant effect on the neutron spectra at low energies. In the lower right panel, the bolometric correction even leads to a lower maximal proton energy, which is because photohadronic energy losses take over to limit the maximal proton energy. Additionally, we checked that the gamma-rays from π^0 -decays produced by the three observed bursts are below the LAT bounds or observations for these bursts.

In summary, *Fermi*-LAT observed GRBs seem to have a strong direct escape component of cosmic rays, at least during the observed emission phase, whereas the direct escape contribution of typical GBM bursts depends on the proton acceleration efficiency. Therefore, conclusions on the cosmic ray-neutrino connection will depend on the actual burst sample including the specific parameters of the fireballs, and the time evolution of the fireball properties, which we did not discuss in this chapter; see chapter 5 for such a treatment. A possible bolometric correction beyond the observed energy ranges of the gamma-rays typically has a small effect, as long as $\beta_\gamma \gtrsim 2$.

While here we have focused on the UHECR proton and neutrino emission from a single source using our two-component model, in chapter 4 we will concentrate on the emission, within this same model, from a population of GRBs that evolves with redshift. For the UHECR flux predictions at Earth, we will use the proton propagation method introduced in chapter 3, which will also generate a cosmogenic neutrino flux from the $p\gamma$ interactions on the cosmological photon backgrounds.

For efficient proton acceleration, we have demonstrated that the standard case of optically thin sources and one neutrino per cosmic ray only applies to a very narrow region of the parameter space at the highest energies, since either direct escape dominates, or the optical thickness to neutron escape is large. For less efficient proton acceleration, a significant region where optically thin emission is possible has been found, which is around the often assumed standard parameter values. However, we have illustrated that the maximal proton energies are in that case not sufficient to describe the observed UHECR spectrum for typical burst parameters. Therefore, it appears that the standard, optically thin case is in tension with the assumption that GRBs are the sources

⁴Not to be confused with the bolometric correction factor f_{bol} , related instead to UHECRs.

⁵For this correction, we fix the gamma-ray spectrum in the observed energy range from the observed fluence, and then linearly extrapolate the spectrum (on a double log plot) to the range between 0.2 eV (SRF) and 100 MeV (observer’s frame). This extended range is motivated by the fact that high energy protons then always find sufficiently many low energy photons as interaction partners, and low energy protons find enough high energy photons. The 100 MeV are chosen in the observer’s frame since they correspond to a typical *Fermi*-LAT energy.

⁶This correction depends mostly on the upper spectral index of the photon spectrum. It is ε'^{-2} in the upper left panel, which leads to a logarithmic dependence on the maximal proton energy, and steeper in the other cases, which leads to a (stronger) power law suppression.

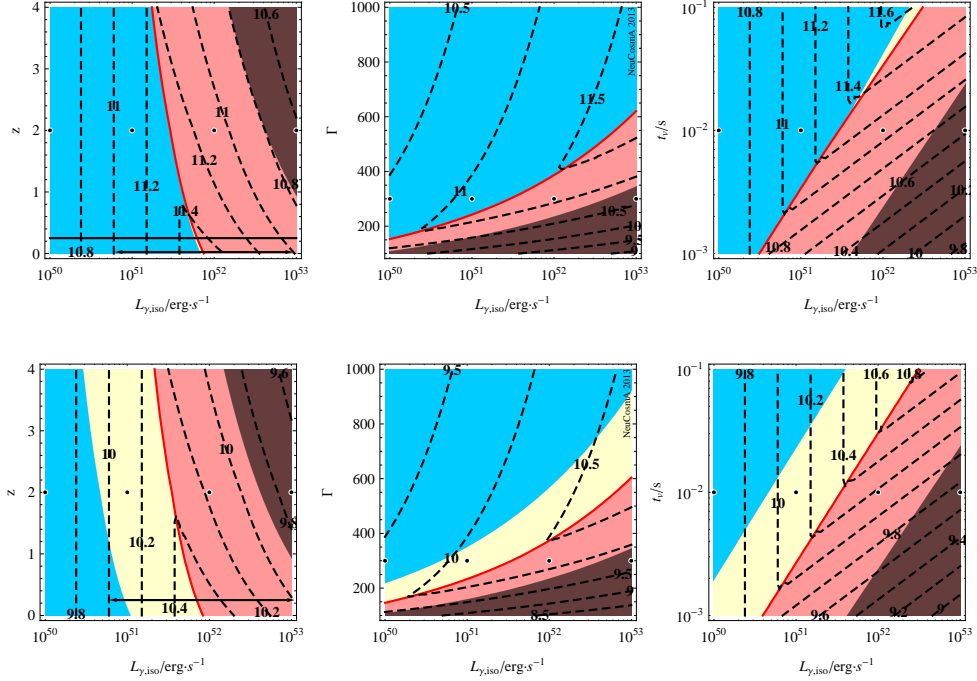


Figure 2.6: Maximal proton energy $\log_{10}(E_{p,\text{max}}/\text{GeV})$ (contours) in the source (cosmologically co-moving) frame as a function of the GRB parameters. The upper row is for $\eta = 1$; the lower row, for $\eta = 0.1$. Same regions and parameters as in Fig. 2.4. Figure taken from Ref. [106].

of the UHECRs, and specific conclusions can be only drawn on a burst-by-burst basis.

The region in which the optical thickness to neutron escape is large has been found to be larger than previous calculations suggest, because high-energy processes have been included in the photohadronic interaction rate. In this case, the neutrinos can escape from everywhere within the shell, whereas the neutrons (and protons) are trapped over the photohadronic interaction length scale and can only (directly) escape from the edges. The neutrino production can therefore be significantly enhanced. Furthermore, we have explicitly demonstrated that the formula used for the pion production efficiency in the IceCube treatment in [91, 92] in fact underestimates the neutrino production in the optically thick case, and that the original formula in [2] applies instead (which was originally developed for the optically thin case). This has consequences for individual GRBs, and is, in fact, already taken into account in the prediction by [4].

Finally, we note that the three different encountered regimes may even be present in one source, especially if collisions occur at very different radii, a possibility that we have explored via a dynamical GRB model in chapter 5. Therefore, the one neutrino per cosmic ray assumption is, in fact, not as general as one may believe. Note that some of our conclusions can be transferred to other classes of sources, such as active galactic nuclei, and to heavier nuclei accelerated in the sources. In all those cases, a substantial fraction of particles may directly leak from the sources at the highest energies, and there can be regions where the source is optically thick to baryon escape.

Chapter 3

UHECR propagation

We wish to calculate the propagation of cosmic rays (CRs) from their origin, at a cosmological source with redshift z , to Earth, taking into account the effects of energy losses en route, due to the adiabatic cosmological expansion and to the interaction with the protons of the cosmic microwave background (CMB) and the cosmic infrared background (CIB). For a selection of literature on the subject, see Refs. [45, 46, 120, 121, 122, 123, 124, 125, 126]. We will assume that CRs are composed solely of protons.

3.1 Introduction

The interactions that we will consider between protons and background photons are e^+e^- pair production, *i.e.*, $p + \gamma \rightarrow p + e^+ + e^-$, and photohadronic processes described, in a first approximation, by the resonant process $p + \gamma \rightarrow \Delta^+(1232) \rightarrow n + \pi^+$ (though the NeuCosmA code that has been used implements a larger number of photohadronic processes; see section 3.2.2). An accompanying “guaranteed” flux of cosmogenic neutrinos is predicted from the decays of the secondary neutrons and pions [127, 128]: $n \rightarrow p + e^- + \bar{\nu}_e$ and $\pi^+ \rightarrow \mu^+\nu_\mu \rightarrow \bar{\nu}_\mu e^+\nu_e + \nu_\mu$. See Refs. [127, 128, 87, 129, 130, 131, 132].

The propagation is performed through solving the Boltzmann transport equation for the comoving number density of protons ($\text{GeV}^{-1} \text{Mpc}^{-3}$),

$$Y_p(E, z) = a^3(z) n_p(E, z) = n_p(E, z) / (1+z)^3, \quad (3.1)$$

with n_p the real number density and $a(z) = (1+z)^{-1}$ the scale factor. The transport equation is (see, *e.g.*, Eq. (17) in Ref. [100]):

$$\dot{Y}_p = \partial_E(HEY_p) + \partial_E(b_{e^+e^-}Y_p) + \partial_E(b_{p\gamma}Y_p) + \mathcal{L}_{\text{CR}}, \quad (3.2)$$

with E the proton energy in the source frame (see, *e.g.*, Ref. [122]). In the r.h.s. of Eq. (3.2), the first term accounts for continuous energy losses due to the adiabatic cosmological expansion, with H the Hubble parameter. The second and third terms, respectively, account for continuous energy losses due to e^+e^- pair production and photopion ($p\gamma$) production on the photon backgrounds, with the corresponding energy-loss rates $b_{e^+e^-}$ and $b_{p\gamma}$, where $b \equiv dE/dt$ (GeV s^{-1}). The fourth term describes the CR injection rate per comoving volume. The proper density $n_p(E, z)$ at any redshift is obtained by solving for $Y_p(E, z)$ and multiplying it by $(1+z)^3$. The diffuse proton flux

J_p at Earth ($\text{GeV}^{-1} \text{ cm}^{-2} \text{ s}^{-1} \text{ sr}^{-1}$) is obtained from the local density through

$$J_p(E_0) = \frac{c}{4\pi} n_p(E, 0) . \quad (3.3)$$

Table 3.1 shows the units that we have used for the parameters in our numerical implementation. In principle, an extra term of the form $\sum_j \int dE_j \gamma_{j \rightarrow p} Y_j$ could be added to Eq. (3.2) to account for particle generation $j \rightarrow p$. However, in our code we have treated protons and neutrons as the same species (*pneutrons*); see sections 3.2.7 and A.1. Under this assumption, no new nucleons are produced en route to Earth, and we have not included such a particle-creation term for protons due to neutron decay.

Writing $Y \equiv Y_p$, Eq. (3.2) can be recast as an equation in redshift by using

$$dz = -dt (1+z) H(z) , \quad (3.4)$$

i.e.,

$$\begin{aligned} -\partial_z Y(E, z) = & \frac{1}{(1+z)H(z)} \{ \partial_E [H(z) E Y(E, z)] + \partial_E [b_{e+e^-}(E, z) Y(E, z)] \\ & + \partial_E [b_{p\gamma}(E, z) Y(E, z)] + \mathcal{L}_{\text{CR}}(E, z) \} . \end{aligned} \quad (3.5)$$

We have written original computer code to numerically solve Eq. (3.5).

Note that the implementation of a solution for Eq. (3.2) that we present here is strictly valid only for energies above $\sim 10^9$ GeV. Below this energy, diffusion effects due to the magnetic fields become important. At the other end, above a critical energy $E_c(z)$ ($\approx 4 \cdot 10^{11}$ GeV at $z=0$), the neutron interaction time, or loss time, is shorter than its decay time, so that it loses energy before decaying into high-energy neutrinos; see Fig. 5 in Ref. [124]. In sections 3.2.7 and A.1 we explain that we have accounted for this by appending a cut-off $\sim e^{-E^2/E_c^2(z)}$ to the neutron injection spectrum.

In appendix A we explicitly list the assumptions, inputs, and limitations of our UHECR propagation treatment and we describe its numerical implementation.

3.2 The CR transport equation in detail

In this section we describe each of the terms in the r.h.s. of Eq. (3.5). We also present the redshift scaling of the photon backgrounds and the associated energy loss rates due to interactions of the protons with them.

3.2.1 Cosmological expansion

The Hubble parameter is given by

$$H(z) = H_0 \sqrt{\Omega_m (1+z)^3 + \Omega_\Lambda} , \quad (3.6)$$

with the local value $H_0 = 70.5 \text{ km s}^{-1} \text{ Mpc}^{-1} = 2.28475 \cdot 10^{-18} \text{ s}^{-1}$, and the energy densities of matter and cosmological constant given by $\Omega_m = 0.27$ and $\Omega_\Lambda = 0.73$, respectively [133].

Parameter	Description	Units
Y_p	comoving number density of protons	$\text{GeV}^{-1} \text{Mpc}^{-3}$
n_p	real number density of protons	$\text{GeV}^{-1} \text{Mpc}^{-3}$
n_γ	real number density of photons (CMB or CIB)	$\text{GeV}^{-1} \text{cm}^{-3}$
N_{CIB}	number of IR/optical photons per proper volume	cm^{-3}
J_p	diffuse proton flux at Earth	$\text{GeV}^{-1} \text{cm}^{-2} \text{s}^{-1} \text{sr}^{-1}$
J_ν	diffuse cosmogenic neutrino flux at Earth	$\text{GeV}^{-1} \text{cm}^{-2} \text{s}^{-1} \text{sr}^{-1}$
E	proton energy in the source frame	GeV
H	Hubble parameter	s^{-1}
b	energy loss rate	GeV s^{-1}
\mathcal{L}_{CR}	comoving proton injection rate	$\text{GeV}^{-1} \text{Mpc}^{-3} \text{s}^{-1}$
\mathcal{L}_{CIB}	comoving IR/optical photon injection rate	$\text{GeV}^{-1} \text{Mpc}^{-3} \text{s}^{-1}$
Q_{CR}	proton injection rate at the source	$\text{GeV}^{-1} \text{Mpc}^{-3} \text{s}^{-1}$
Q_{CIB}	IR/optical photon injection rate at the source	$\text{GeV}^{-1} \text{Mpc}^{-3} \text{s}^{-1}$
\mathcal{H}_{CR}	redshift source evolution of CR sources	adimensional
\mathcal{H}_{CIB}	redshift source evolution of CIB sources	adimensional
ω_{cas}	local e.m. cascade energy density	GeV cm^{-3}

Table 3.1: Main parameters of the CR propagation and cosmogenic neutrino formalism and their units.

3.2.2 Energy loss rate due to $p\gamma$ interactions

In general, the interaction rate (probability of interaction per unit time per particle) between protons and a background photon field n_γ ($\text{GeV}^{-1} \text{cm}^{-3}$), at proton energy E , is calculated as in Eq. (3) of Ref. [96] (see also Refs. [122, 123]):

$$\Gamma_{p\gamma \rightarrow p'b}(E, z) = \frac{1}{2} \int_{-1}^{+1} dc_\theta \int d\epsilon (1 - \beta c_\theta) n_\gamma(\epsilon, z, c_\theta) \sigma_{p\gamma \rightarrow p'b}^{\text{tot}}(\epsilon_r), \quad (3.7)$$

where p' can be either a proton or a neutron, ϵ is the photon energy, and $c_\theta \equiv \cos \theta$, with θ the angle between the proton and photon momenta. The total cross section $\sigma_{p\gamma \rightarrow p'b}^{\text{tot}}$ (cm^2) considers interactions of the type $p + \gamma \rightarrow p' + b$, with the daughter particles (b), typically π^+ , π^- , π^0 , or K ; $\epsilon_r = E\epsilon/m_p(1 - c_\theta)$ is the photon energy in the rest frame of the parent nucleon in the limit $\beta \approx 1$. Based on Ref. [96], we consider the following processes, which are incorporated in NeuCosmA¹:

- **Δ -resonance:**

$$p + \gamma \xrightarrow{\Delta^{+(1232)}} \begin{cases} p + \pi^0, & 1/3 \text{ of all cases} \\ n + \pi^+, & 2/3 \text{ of all cases} \end{cases} \quad (3.8)$$

- **Higher resonances:**

$$p + \gamma \xrightarrow{\Delta, N} \Delta' + \pi, \quad \Delta' \rightarrow p' + \pi' \quad (3.9)$$

$$p + \gamma \xrightarrow{\Delta, N} \rho + p', \quad \rho \rightarrow \pi + \pi' \quad (3.10)$$

- **Direct production:** the t -channels of Eqs. (3.8) and (3.9) (since the photon can couple to the charged pion)

¹Note that, with our choice of units for n_γ and $\sigma_{p\gamma}^{\text{tot}}$, the rate $\Gamma_{p\gamma \rightarrow p'b}$ is output in cm^{-1} ; multiplication by c gives it the appropriate units, s^{-1} .

- **Multi-pion production:** processes where two or more pions are produced, as implemented in SOPHIA

Under the assumption of an isotropic photon field, the integral over c_θ in Eq. (3.7) can be transformed into an integral over ϵ_r , yielding [96]

$$\Gamma_{p\gamma \rightarrow p'b}(E, z) = \frac{1}{2} \frac{m_p^2}{E^2} \int_{\frac{\epsilon_{\text{th}} m_p}{2E}}^{\infty} d\epsilon \frac{n_\gamma(\epsilon, z)}{\epsilon^2} \int_{\epsilon_{\text{th}}}^{2E\epsilon/m_p} d\epsilon_r \epsilon_r \sigma_{p\gamma \rightarrow p'b}^{\text{tot}}(\epsilon_r) , \quad (3.11)$$

with $\epsilon_{\text{th}} = 150$ MeV the threshold photon energy, below which the cross sections are zero.

As explained in appendix B of Ref. [96], in $p\gamma$ interactions, cooling processes are those in which the primary loses energy in the interaction, such as $p + \gamma \rightarrow p + \pi^0$, while escape processes are those in which the primary disappears, such as $p + \gamma \rightarrow n + \pi^+$ (which will contribute to the cosmogenic neutrino flux). To each, there is associated an interaction time:

$$t_{\text{cool}}^{-1}(E) = -\frac{1}{E} \frac{dE}{dt} = -\frac{1}{E} b_{p\gamma}(E) , \quad (3.12)$$

$$t_{\text{esc}}^{-1} = -\frac{1}{n_p} \frac{dn_p}{dt} . \quad (3.13)$$

Recall that, in our calculation, we assume that all neutrons have already decayed into protons and have been re-injected, so we consider only the cooling of the protons. NeuCosmA calculates the cooling time through (Eq. (B1) in Ref. [96])

$$t_{\text{cool}}^{-1}(E, z) = \sum_i \Gamma_{p \rightarrow p}^i(E, z) K^i , \quad (3.14)$$

where the sum is over all interactions that conserve the primary p and $K^i E$ is the loss of energy per interaction, with the ‘‘inelasticity’’ K^i a constant for each channel, calculated in Ref. [96].

For a given photon background (CMB, CIB), NeuCosmA computes² the cooling time, t_{cool}^{-1} , in units of s^{-1} . The cooling rate that appears in Eq. (3.5), $b_{p\gamma} = dE/dt$, can then be calculated as

$$b_{p\gamma}(E, z) = -E t_{\text{cool}}^{-1}(E, z) , \quad (3.15)$$

directly in units of GeV s^{-1} , as needed.

3.2.3 Energy loss rate due to e^+e^- pair production

The energy loss rate $b_{e^+e^-}$ due to e^+e^- pair production in the interaction $A + \gamma \rightarrow A + e^+ + e^-$ between very energetic nuclei with charge Z (for which the Lorentz factor $\gamma \gg 1$ and $\beta \equiv v/c$ is taken to be 1) and an isotropic photon background $n_\gamma(\epsilon, z)$ ($\text{GeV}^{-1} \text{cm}^{-3}$), is calculated following Eqs. (13) and (14) of Ref. [120]:

$$b_{e^+e^-}(E, z) \equiv \frac{dE}{dt} = -\alpha r_0^2 Z^2 (m_e c^2)^2 c \int_2^\infty d\xi n_\gamma\left(\frac{\xi m_e c^2}{2\gamma}, z\right) \frac{\phi(\xi)}{\xi^2} , \quad (3.16)$$

where $\alpha \approx 1/137$ is the fine-structure constant, $r_0 = 2.817940 \cdot 10^{-13}$ cm is the classical electron radius, and

$$\phi(\xi) = \int_2^\xi dk \int_1^{k-1} dE_- A(k, E_-) , \quad (3.17)$$

²In the routine `ncoComputeCoolEscRate`.

Constant	Value
c_1	0.8048
c_2	0.1459
c_3	$1.137 \cdot 10^{-3}$
c_4	$-3.879 \cdot 10^{-6}$
d_0	$-170 + 84 \ln 2 - 16 \ln^2 2 + \frac{\pi^2}{3} (10 - 4 \ln 2) + 8\zeta(3) \approx -86.07$
d_1	$88 - 40 \ln 2 + 8 \ln^2 2 - \frac{4}{3}\pi^2 \approx 50.96$
d_2	$-20 + 8 \ln 2 \approx -14.45$
d_3	$\frac{8}{3}$
f_1	2.910
f_2	78.35
f_3	1837

Table 3.2: Constants used in the calculation of the $\phi(\xi)$ function, according to Eq. (3.19). Values taken from Ref. [134].

with ξ the photon energy in units of $m_e c^2$, E_- the energy of the secondary positron, and $k = \epsilon / (m_e c^2)$ the photon energy (in the nucleus rest frame) in units of the electron mass. The adimensional function $A(k, E_-)$ is defined in Eq. (8) of Ref. [120]. The exact value of the function $\phi(\xi)$, calculated through Eq. (3.17), is plotted in Fig. 2 of Ref. [120]. Since we are assuming that cosmic rays have a purely proton composition, we set $Z = 1$; and, given that the proton energy $E = \gamma m_p c^2$, we can rewrite the energy loss rate as

$$b_{e^+e^-}(E, z) = -\alpha r_0^2 (m_e c^2)^2 c \int_2^\infty d\xi n_\gamma \left(\frac{\xi (m_e c^2) (m_p c^2)}{2E}, z \right) \frac{\phi(\xi)}{\xi^2}, \quad (3.18)$$

In the same reference, an approximate expression (Eq. (16)) in the extreme relativistic regime ($\xi \gg 1$) is given for $\phi(\xi)$. However, an improved approximate expression is given in Ref. [134], for the whole range³ of ξ :

$$\phi(\xi) \simeq \begin{cases} \frac{\pi}{12} \frac{(\xi - 2)^4}{1 + \sum_{i=1}^4 c_i (\xi - 2)^i} & , \quad \xi < 25 \\ \frac{\xi \sum_{i=0}^3 d_i \ln^i \xi}{1 - \sum_{i=1}^3 f_i \xi^{-i}} & , \quad \xi \geq 25 \end{cases}, \quad (3.19)$$

with the constants c_i , d_i , and f_i given in Table 3.2. The relative error in the lower branch is reported to be less than $1.3 \cdot 10^{-3}$, while in the higher branch it is less than $1.5 \cdot 10^{-3}$. Fig. 3.1 compares the two different approximations of $\phi(\xi)$, from Refs. [120] and [134], with its exact value, *i.e.*, Eq. (3.17). Since the exact computation and the improved approximate computation by Chodorowski *et al.* which we have presented here (Eq. (3.19)) are almost indistinguishable, we have adopted the latter in the code.

³Note that, in the notation of Ref. [134], ξ is called κ instead.

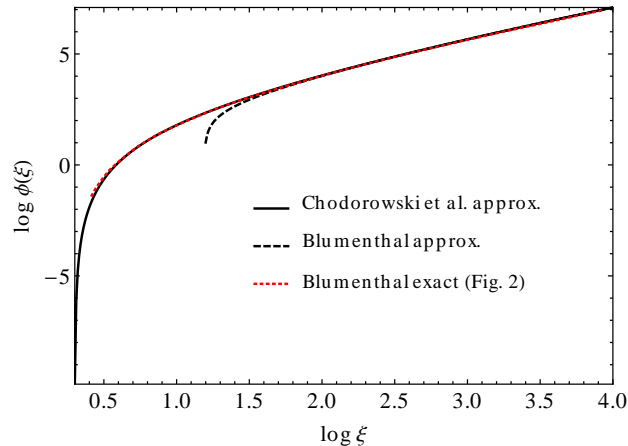


Figure 3.1: Comparison between calculations of the $\phi(\xi)$ function: approximation by Chodorowski *et al.* [134], Eq. (3.19) in this work; relativistic approximation by Blumenthal [120]; and exact solution, Eq. (3.17) in this work (taken from Fig. 2 in Ref. [120]).

3.2.4 Scaling of the cosmological photon backgrounds

Interactions with the CMB photons

The CMB photon spectrum is assumed to be isotropic, as in Ref. [96], so that $n_\gamma(\epsilon, z, c_\theta) = n_\gamma(\epsilon, z)$, and the photon number density ($\text{GeV}^{-1} \text{cm}^{-3}$) is given by

$$n_\gamma^{\text{CMB}}(\epsilon, z=0) = \frac{1}{\pi^2} \frac{1}{(\hbar c)^3} \frac{\epsilon^2}{e^{\epsilon/(k_B T)} - 1}, \quad (3.20)$$

where the present-day CMB temperature $T = 2.725 \text{ K}$ (*i.e.*, $k_B T \approx 0.23 \text{ meV}$). Since the CMB does not receive injection from sources, its transport equation consists of only the adiabatic term, $Y_\gamma^{\text{CMB}} = \partial_\epsilon (H \epsilon Y_\gamma^{\text{CMB}})$, so that $Y_\gamma^{\text{CMB}}(\epsilon, z) = a^3(z) n_\gamma^{\text{CMB}}(\epsilon, z)$. From this, the CMB spectrum scales with redshift as⁴

$$n_\gamma^{\text{CMB}}(\epsilon, z) = (1+z)^2 n_\gamma^{\text{CMB}}(\epsilon/(1+z), z=0). \quad (3.21)$$

The energy loss rates on the CMB due to photohadronic interactions and pair production, $b_{p\gamma}^{\text{CMB}}$ and $b_{e^+e^-}^{\text{CMB}}$, are calculated, respectively, from Eqs. (3.15) and (3.18), with $n_\gamma = n_\gamma^{\text{CMB}}$.

Interactions with the CIB photons

The CIB spectrum at redshift z , $n_\gamma^{\text{CIB}}(\epsilon, z)$ ($\text{GeV}^{-1} \text{cm}^{-3}$), is made up of contributions from higher redshifts and so is obtained by integrating the comoving injection spectrum $\mathcal{L}_\gamma^{\text{CIB}}(\epsilon, z)$ ($\text{GeV}^{-1} \text{Mpc}^{-3} \text{s}^{-1}$) from z upwards⁵ (see appendix C in Ref. [122] or Eqs. (8)–(9) in Ref. [135]), *i.e.*,

$$n_\gamma^{\text{CIB}}(\epsilon(1+z), z) = (1+z)^2 \int_z^{z_{\text{max}}^{\text{CIB}}} dz' \frac{\mathcal{L}_\gamma^{\text{CIB}}(\epsilon(1+z'), z')}{H(z')}, \quad (3.22)$$

⁴Appendix A in Ref. [122] claims that the scaling goes as $\sim (1+z)^3$; however, see subsection 3.2.6 in this work for a justification of why the $\sim (1+z)^2$ scaling follows from the transport equation. For a more intuitive justification, consider the individual scalings of the number density of particles (cm^{-3}), $N/V \propto (1+z)^3$ and of the energy, $E \propto 1+z$. Therefore, the photon spectrum $n_\gamma \equiv dN/dV/dE$ scales as $\sim (1+z)^2$.

⁵However, the definitions in Refs. [122] and [135] have extra factors of $(1+z)$ compared to ours; it is not absolutely clear at this point what is the correct definition of $n_\gamma^{\text{CIB}}(\epsilon, z)$, but we have used Eq. (3.22) in our calculations.

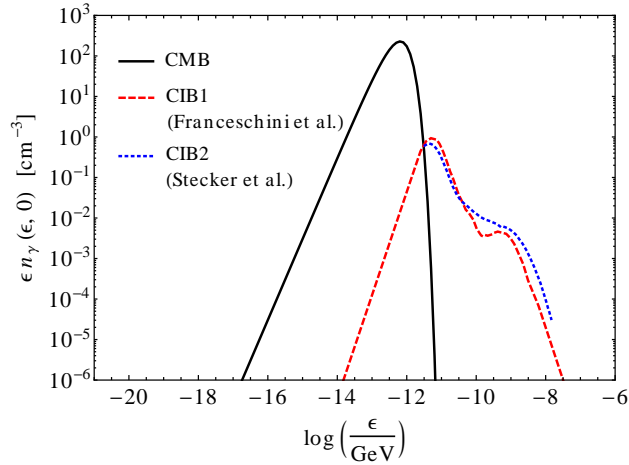


Figure 3.2: Local ($z = 0$) CMB and CIB spectra. The CIB1 model is taken from Ref. [135] and the CIB2 model, from Ref. [136]. Compare to Fig. A.6 in Ref. [87].

where ϵ is the photon energy (in the comoving frame) and $z_{\text{max}}^{\text{CIB}} \geq 6$ is fixed.

Ref. [135] calculated the CIB photon spectrum up to $z = 2$. Appendix C of Ref. [122] parametrised the comoving injection spectrum as

$$\mathcal{L}_{\text{CIB}}(\epsilon, z) \propto \mathcal{H}_{\text{CIB}}(z) \mathcal{L}_{\text{CIB}}(\epsilon, 0) , \quad (3.23)$$

obtained by scaling the local injection rate $\mathcal{L}_{\text{CIB}}(\epsilon, 0)$ by the adimensional function \mathcal{H}_{CIB} which describes the redshift evolution of the sources (see subsection 3.2.5). Denoting by $N_{\text{CIB}}(z)$ the number of IR photons per proper volume at redshift z , the bolometric evolution is found to follow

$$\frac{N_{\text{CIB}}(z)}{N_{\text{CIB}}(0)} = (1+z)^3 \frac{\int_z^\infty dz' \mathcal{H}_{\text{CIB}}(z') / (H(z')(1+z'))}{\int_0^\infty dz' \mathcal{H}_{\text{CIB}}(z') / (H(z')(1+z'))} . \quad (3.24)$$

With this, the CIB spectrum can be approximated as

$$n_\gamma^{\text{CIB}}(\epsilon, z) \simeq \frac{1}{1+z} \frac{N_{\text{CIB}}(z)}{N_{\text{CIB}}(0)} n_\gamma^{\text{CIB}}(\epsilon/(1+z), 0) . \quad (3.25)$$

Hence, the redshift evolution of the CIB spectrum depends on the redshift evolution of the sources that contribute to it, via the factor $N_{\text{CIB}}(z)/N_{\text{CIB}}(0)$, which is calculated by our code from Eq. (3.24), for a specified model of source redshift evolution, \mathcal{H}_{CIB} . The energy loss rates on the CIB due to photohadronic interactions and pair production, $b_{p\gamma}^{\text{CIB}}$ and $b_{e^+e^-}^{\text{CIB}}$, are calculated, respectively, from Eqs. (3.15) and (3.18), with $n_\gamma = n_\gamma^{\text{CIB}}$.

There are different competing parametrisations of the local CIB spectrum, $n_\gamma^{\text{CIB}}(\epsilon, 0)$. So far, we have used the ones by Franceschini *et al.* [135] (which we have labeled CIB1) and by Stecker *et al.* [136] (CIB2). Fig. 3.2 shows the local spectrum for these two models, compared to the local CMB spectrum.

The comoving injection rate of IR photons can be further complicated by writing it instead as

$$\mathcal{L}_{\text{CIB}}(\epsilon, z) = \mathcal{H}_{\text{CIB}}(z) Q_{\text{CIB}}(\epsilon, z) , \quad (3.26)$$

where $Q_{\text{CIB}}(\epsilon, z)$ is now the injection spectrum of photons ($\text{GeV}^{-1} \text{cm}^{-3} \text{s}^{-1}$) at a source with redshift z . This may correspond, for instance, to a situation where different star populations

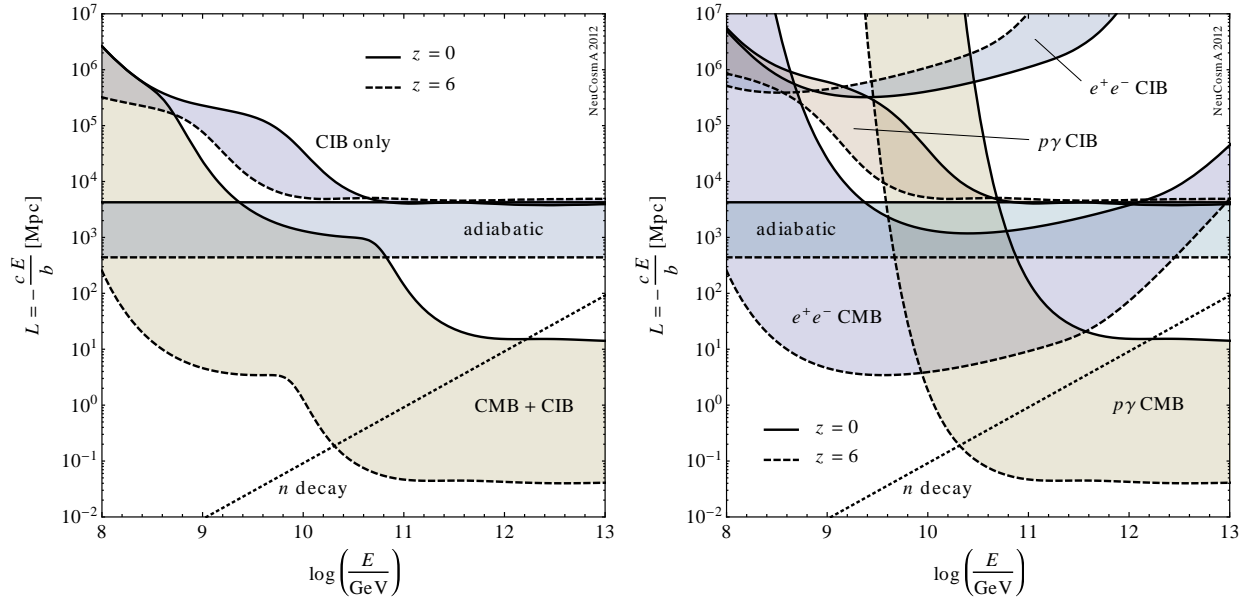


Figure 3.3: *Left:* Interaction length $L = -cE/b$ for the adiabatic losses, and for photohadronic + pair-production losses on the CIB only and on the CMB+CIB. *Right:* Interaction length taking into account, independently, pair production on the CMB and on the CIB, and photohadronic interactions on the CMB and on the CIB. In both panels, the CIB1 local spectrum (see subsection 3.2.4) and SFR evolution of the CIB sources were assumed. Compare to Fig. 3 in Ref. [129], Fig. 1 in Ref. [137], and Fig. 7 in Ref. [126].

contribute to the CIB at different redshifts, each one with a different injection spectrum. Evidently, this injection rate should match the local rate $\mathcal{L}_{\text{CIB}}(\epsilon, 0)$ and its observed evolution, which is known up to $z \approx 2$ [135]. Using Eq. (3.26), the ratio $N_{\text{CIB}}(z)/N_{\text{CIB}}(0)$ becomes energy-dependent, namely,

$$\frac{N_{\text{CIB}}(\epsilon, z)}{N_{\text{CIB}}(\epsilon, 0)} = (1+z)^3 \frac{\int_z^\infty dz' \mathcal{H}_{\text{CIB}}(z') Q_{\text{CIB}}(\epsilon(1+z'), z') / (H(z')(1+z'))}{\int_0^\infty dz' \mathcal{H}_{\text{CIB}}(z') Q_{\text{CIB}}(\epsilon(1+z'), z') / (H(z')(1+z'))}. \quad (3.27)$$

This ratio can be plugged into the approximate expression, Eq. (3.25), as before; alternatively, the exact CIB spectrum at any redshift can be calculated from its definition using Eq. (3.22).

Scaling of the energy loss rate

The total interaction rate which enters Eq. (3.5), either due to photohadronic or pair production interactions, receives contributions from interactions on the CMB and CIB, *i.e.*,

$$b^{\text{tot}}(E, z) = b^{\text{CMB}}(E, z) + b^{\text{CIB}}(E, z). \quad (3.28)$$

Following appendix A of Ref. [122], due the adiabatic redshift scaling of the CMB spectrum, Eq. (3.21), the associated energy loss rate scales as

$$b^{\text{CMB}}(E, z) = (1+z)^2 b^{\text{CMB}}((1+z)E, 0). \quad (3.29)$$

This scaling is exact for the loss rate on the CMB spectrum. By default⁶, the code calculates $b_{p\gamma}^{\text{CMB}}(E, 0)$ and $b_{e^+e^-}^{\text{CMB}}(E, 0)$ during initialisation, and uses Eq. (3.29) to scale it to different redshifts, instead of computing them, at each redshift, from their definitions, Eqs. (3.15) and (3.18). The result is a sizable gain in computing speed⁷.

As seen in the previous subsection, however, the redshift scaling of the CIB is not merely adiabatic, but more complicated, and therefore so is the scaling of the corresponding energy loss rate, b^{CIB} . The code has been written to allow for any arbitrary redshift evolution of the CIB spectrum, \mathcal{H}_{CIB} , to be used.

The interaction length can be calculated from the energy loss rate as $L = -cE/b$. Fig. 3.3 shows the attenuation length corresponding to adiabatic losses only (in this case, $b_{\text{adiabatic}} = -cH(z)$), and the interaction lengths due to photohadronic plus pair-production losses on the CIB and on the CMB+CIB. The local parametrisation CIB1 and the SFR source evolution of the CIB sources have been assumed. Note that, at low energies, the interaction length is dominated by the interactions with the CIB (though adiabatic losses dominate at lower redshifts): since IR photons are more energetic than microwave photons, lower proton energies are needed to achieve equal energy loss rates. At around $E \sim 10^{8.5}$ GeV, the CMB interactions start to become dominant, and the interaction length decreases due to the total energy loss rate $b^{\text{tot}} = b^{\text{CMB}} + b^{\text{CIB}}$ becoming larger. Note also that, since the photon densities grow with redshift, the interaction lengths are shorter for $z = 6$ than for $z = 0$. For comparison, the neutron decay length has been included in Fig. 3.3, *i.e.*,

$$L_n(E) = c\tau = c(E/m_n)\tau_0, \quad (3.30)$$

with $m_n = 940$ MeV the neutron mass and $\tau_0 = 885.7$ s its lifetime in the rest frame.

We have said already that (by default in our code) $b_{p\gamma}^{\text{CMB}}$ and $b_{e^+e^-}^{\text{CMB}}$ are calculated from their definitions only once, at $z = 0$, and afterward rescaled to any z ; hence, calculating these loss rates at arbitrary z entails little computational cost. For the CIB, however, the scaling might not be so computationally cheap, especially if Eq. (3.27) is used.

One can take advantage of the fact that, even when interactions on the CIB are dominating (at $E \lesssim 10^{8.5}$ GeV), the corresponding interaction length is ~ 4 Gpc or larger, to speed up the numerical evaluation of the CR propagation by calculating the energy loss rates on the CIB at more spaced redshift intervals than for the CMB. We have done so in our code; see subsection A.4.3 for implementation details.

3.2.5 CR injection rate

Like for the CIB (see Eq. (3.26)), we can write the CR injection rate in Eq. (3.2) as⁸

$$\mathcal{L}_{\text{CR}}(E, z) = \mathcal{H}_{\text{CR}}(z) Q_{\text{CR}}(E, z), \quad (3.31)$$

where Q_{CR} is the injection spectrum at the source ($\text{GeV}^{-1} \text{Mpc}^{-3} \text{s}^{-1}$) and \mathcal{H} is an adimensional function of z that accounts for the redshift evolution of the cosmological sources. It is defined [138]

⁶Setting `NCO_CRPROP_CMB_SCALING = 1`.

⁷With the CMB scaling, protons can be propagated from $z = 6$ to $z = 0$ in ~ 120 s; without scaling, the same computation takes ~ 40 minutes. These execution times were obtained on an Intel Core i7-2600 CPU running at 3.40 GHz, with 8 GB of RAM.

⁸In general, the injected CR spectrum can depend on both energy and redshift, where the latter could be used to calculate the spectrum normalisation.

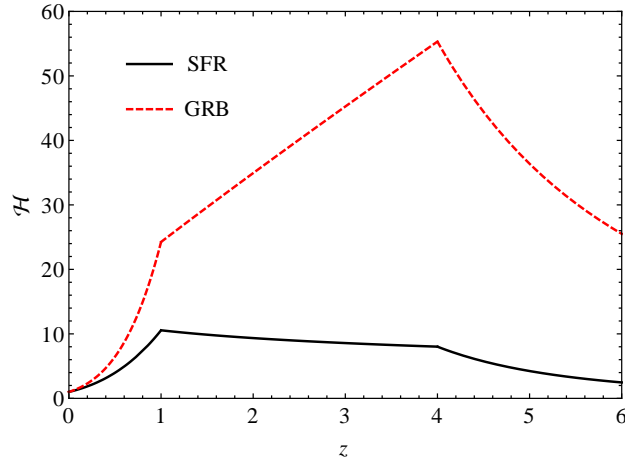


Figure 3.4: Star formation rate \mathcal{H}_{SFR} , Eq. (3.32), and GRB redshift evolution \mathcal{H}_{GRB} , Eq. (3.33).

as the comoving number of density of CR sources, $\dot{\rho}_{\text{CR}}(z)$ ($\text{Mpc}^{-3} \text{ yr}^{-1}$), normalised to the local rate, i.e, $\mathcal{H}(z) \equiv \dot{\rho}_{\text{CR}}(z) / \dot{\rho}_{\text{CR}}(0)$.

For instance, the star formation rate (SFR) is assumed to follow [139, 140]

$$\mathcal{H}_{\text{SFR}}(z) = \begin{cases} (1+z)^{3.4} & , z < 1, \\ N_1 (1+z)^{-0.3} & , 1 \leq z < 4, \\ N_1 N_4 (1+z)^{-3.5} & , z \geq 4 \end{cases} , \quad (3.32)$$

with $N_1 = 2^{3.7}$ and $N_4 = 5^{3.2}$. As shown in Refs. [140, 141, 138], the comoving GRB rate ($\text{Mpc}^{-3} \text{ yr}^{-1}$) is obtained by multiplying the star formation density $\dot{\rho}_{\text{SFR}} (M_{\odot} \text{ Mpc}^{-3} \text{ yr}^{-1})$ by a correction factor $\varepsilon(z) = \varepsilon_0 (1+z)^{\alpha}$ (ε_0 in units of M_{\odot}^{-1}) to account for the observation that the GRB population appears to be higher in the past than what the SFR yields. The normalised GRB comoving rate is therefore

$$\mathcal{H}_{\text{GRB}}(z) = (1+z)^{\alpha} \mathcal{H}_{\text{SFR}}(z) , \quad (3.33)$$

with, typically, $\alpha = 1.2$ (we have assumed this value to produce Fig. 3.4 and the plots in section 3.3). Fig. 3.4 shows \mathcal{H}_{SFR} and \mathcal{H}_{GRB} as functions of redshift.

Note that CR injection occurs from z_{max} only down to z_{hom} , the redshift below which the universe becomes inhomogeneous. It should be approximately $z_{\text{hom}} = 0.02$, corresponding to ~ 77 Mpc.

3.2.6 Solving the transport equation under adiabatic expansion only

If we consider solely adiabatic losses due to cosmological expansion, then only the first term in the r.h.s. of Eq. (3.5) survives, *i.e.*,

$$\partial_z Y(E, z) = -\frac{1}{1+z} \partial_E [EY(E, z)] . \quad (3.34)$$

Setting a generic boundary condition $Y(E, z_{\text{max}}) = f(E, z_{\text{max}})$ allows us to write down the solution as

$$Y(E, z) = \frac{1+z_{\text{max}}}{1+z} f\left(\frac{1+z_{\text{max}}}{1+z} E, z_{\text{max}}\right) . \quad (3.35)$$

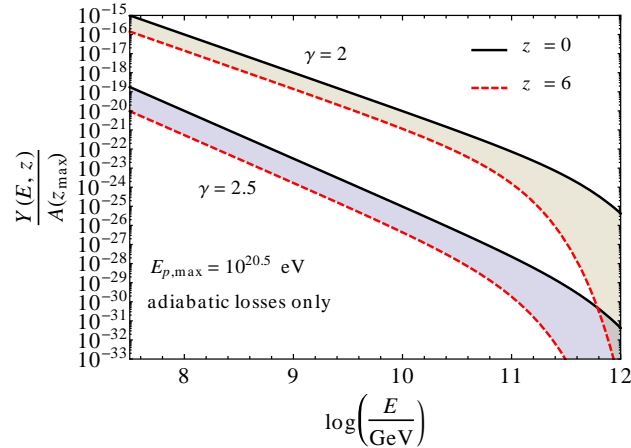


Figure 3.5: Comoving proton density at $z = 0$ and $z = 6$ in the simplified scenario where the only losses are due to the adiabatic cosmological expansion, Eq. (3.36), with γ the spectral index of the proton spectrum at $z = z_{\max} = 6$ (see text for details).

(Since neutrinos can be assumed not to interact with the photon backgrounds, when calculating the contribution to the total neutrino flux at Earth coming from neutrinos created at a redshift z , Eq. (3.35) is used, with the replacements $z_{\max} \rightarrow z$ and $z \rightarrow z_{\min} = 0$.)

Using the particular choice $f(E, z_{\max}) = A(z_{\max}) E^{-\gamma} e^{-E/E_{\max}}$, with $A(z_{\max})$ the normalisation of the comoving density at $z = z_{\max}$, this becomes

$$Y(E, z) = \left(\frac{1 + z_{\max}}{1 + z} \right)^{1-\gamma} A(z_{\max}) E^{-\gamma} \exp\left(-\frac{1 + z_{\max}}{1 + z} \frac{E}{E_{\max}} \right). \quad (3.36)$$

Fig. 3.5 shows the redshift evolution of $Y(E, z)$ in this simplified scenario, for different choices of the spectral index γ .

We can also use Eq. (3.35) to justify the scaling of the CMB density ($\text{GeV}^{-1} \text{cm}^{-3}$), Eq. (3.21). Setting $Y \rightarrow Y_\gamma$, $z \rightarrow 0$, and $z_{\max} \rightarrow z$, Eq. (3.35) becomes

$$Y_\gamma(\epsilon, 0) = (1 + z) Y_\gamma((1 + z)\epsilon, z). \quad (3.37)$$

This can be rewritten to find the spectrum at redshift z in terms of the local spectrum, *i.e.*,

$$Y_\gamma(\epsilon, z) = (1 + z)^{-1} Y_\gamma(\epsilon/(1 + z), 0). \quad (3.38)$$

The proper spectrum, n_γ , can be obtained from the comoving spectrum through $Y_\gamma = n_\gamma/(1 + z)^3$, which, after replacing in the last equation, yields

$$n_\gamma(\epsilon, z) = (1 + z)^2 n_\gamma(\epsilon/(1 + z), 0), \quad (3.39)$$

for the CMB scaling, as was shown in Eq. (3.35).

3.2.7 Cosmogenic neutrinos

Cosmogenic neutrinos may come from two different sources: the decay of pions, muons, and kaons⁹, and the decay of neutrons. One needs the *actual* (not comoving) proton and photon

⁹In NeuCosmA, only K^+ production from protons is included. In the coupled pneutron system, K^- should be produced from neutrons with a comparable rate, by isospin symmetry arguments, see also Ref. [142]. This is automatically included if `ParticleIn = NCO_PROTON` is used for the K^+ production.

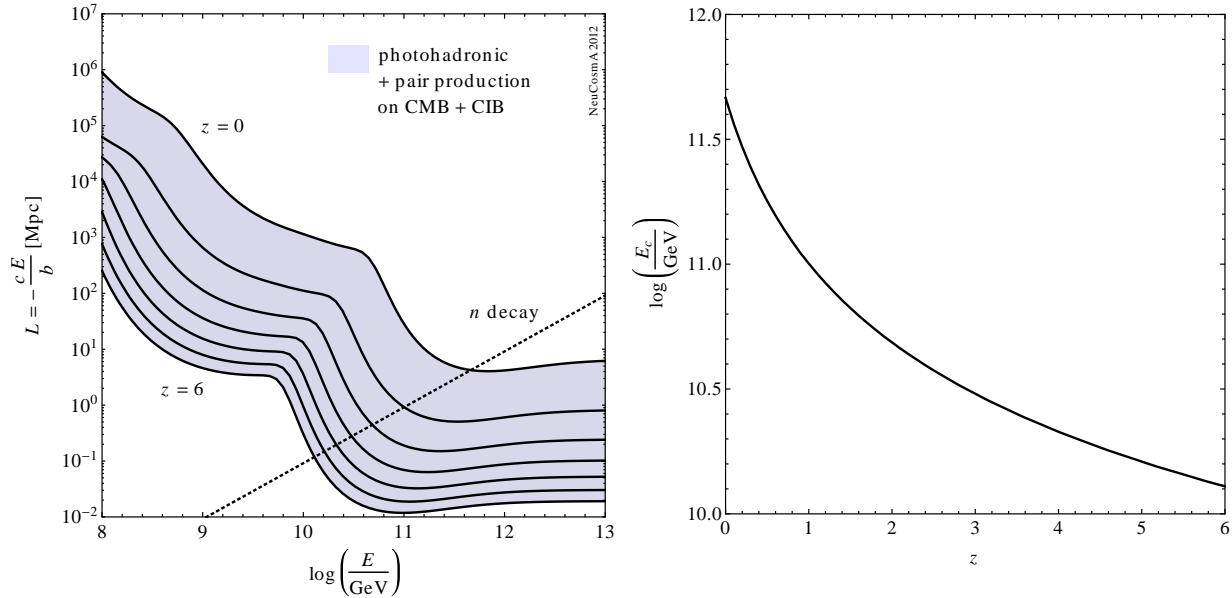


Figure 3.6: *Left:* Proton/neutron interaction length at different redshifts, from $z = 0$ (top solid curve) to $z = 6$ (bottom solid curve), in steps of $\delta z = 1$. The neutron decay length, Eq. (3.30), is shown as a dotted line. *Right:* Critical energy $E_c(z)$ above which neutrons interact before decaying; it is obtained by intersecting the proton/neutron interaction length and the neutron decay length, as shown in the left panel. Compare to Fig. 5 in Ref. [124] for $z = 0$, where $E_c(0) \approx 4 \cdot 10^{11}$ GeV.

densities ($\text{GeV}^{-1} \text{cm}^{-3}$) to compute the interactions, *i.e.*, especially the proton density has to be computed from the comoving one. The output is the secondary injection ($\text{GeV}^{-1} \text{cm}^{-3} \text{s}^{-1}$), which one may want to translate back into a comoving one (to let it evolve just like Y). Another complication is the time-dependence: in order to obtain the comoving number density, one has to integrate over time. In practice, one will add the injection to the total result by multiplying with the redshift stepsize Δz ($\Delta t = \Delta t / \Delta z \cdot \Delta z$). Note that the final result cannot depend on the number of integration (Δz) steps.

Here one simplification may be that we do not need the steady state if we assume that the magnetic fields and adiabatic expansion are small compared to the decay rate. In this case, we can treat them as the neutron decays (see below) and just let them decay. Watch the difference between an injection (per time frame) and steady spectrum (needed for the decays), which are related by the decay rate – see neutrons in the above files for how that works. Finally, we obtain the (unoscillated) neutrino injection spectra per energy, volume, and time, as usual. These ought to be translated into the flux at the Earth by the usual flavor mixing and the *same* transformation as the cosmic ray protons, *i.e.*,

$$J_{\nu_\alpha}(E_0) = \frac{c}{4\pi} n_{\nu_\alpha}(E, 0) . \quad (3.40)$$

For the neutrinos from neutron decays, we assume that only protons interact, and neutrons decay before they interact. This is a good assumption for energies below a certain critical energy E_c , which is obtained by intersecting the neutron/proton interaction length¹⁰, at a redshift z , with the neutron decay length, Eq. (3.30). The left panel of Fig. 3.6 shows curves of the neutron/proton interaction length for redshifts $z = 0$ up to $z = 6$ (solid lines) and the neutron decay length (dotted

¹⁰Obtained from the `ncComputeInteractionRate` routine in NeuCosmA.

line). The critical energy $E_c(z)$, determined at the intersections for different z , is shown in the right panel of Fig. 3.6. If protons are injected at significantly higher energies¹¹, we have an actually mixed proton-neutron system (approaching roughly 50:50 very quickly) because neutrons interact before they decay. In this case, neutrons are only produced in 50% of all interactions, and these neutrons do not contribute to the neutrino flux.

NeuCosmA computes neutron injection¹² lets all neutrons below E_c decay into neutrinos directly in the usual way, and ignores all neutrons above E_c . This is done by introducing an exponential cutoff $\propto e^{-E^2/E_c^2(z)}$ after the neutron injection, *i.e.*, by multiplying the neutron injection spectrum by this factor. Note that the critical energy at any redshift is determined by the intersection of the neutron interaction length (on the CIB and CMB) and the neutron decay length. Of course, one cannot include a possible pile-up effect that way (the neutrons may cool by photohadronics to below E_c , where they pile up), but such pile-ups only happen for soft enough spectra. Note that in most cases there will be no effect of this cutoff since the sources really need to inject at extremely high energies for it to be noticeable (the high- E tail may be somewhat reduced).

3.2.8 Energy density of electromagnetic cascades

In addition to neutrinos, cosmic ray interactions with the photon backgrounds produce photons, through the decay of the secondary neutral pions, *i.e.*, $\pi^0 \rightarrow \gamma\gamma$, and electrons and positrons, through the decay of the secondary π^\pm . Electromagnetic cascades are then driven by pair production, $\gamma\gamma_b \rightarrow e^+e^-$, and inverse Compton scattering, $e^\pm\gamma_b \rightarrow e^\pm\gamma$, on the background photons γ_b [87, 143].

Following Ref. [87], we calculate the electromagnetic cascade energy density (GeV cm^{-3}) at $z = 0$ as

$$\omega_{\text{cas}} = \int dt \int dE \frac{b_{\text{cas}}(E, z)}{(1+z)^4} n_p(E, z) , \quad (3.41)$$

with the continuous energy loss rate of protons into the e.m. cascade given by

$$b_{\text{cas}}(E, z) = b_{e^+e^-}(E, z) + \frac{5}{8} b_{p\gamma}(E, z) . \quad (3.42)$$

The factor 5/8 accounts for the fact that five out of the eight decay products of the charged pions are electrons and photons. From this definition, it is evident that ω_{cas} receives contributions from all redshifts; this becomes clearer if we rewrite the integral in t as an integral in z , using $|dt/dz|$ from Eq. (3.4), namely

$$\omega_{\text{cas}} = \int_0^z \left| \frac{dt}{dz'} \right| dz' \int dE \frac{b_{\text{cas}}(E, z')}{(1+z')^4} n_p(E, z') = \int_0^z dz' \int dE \frac{b_{\text{cas}}(E, z')}{(1+z')^2 H(z')} Y_p(E, z') , \quad (3.43)$$

where we have replaced the real proton spectrum $n_p(E, z)$ by the comoving spectrum $Y_p(E, z) = (1+z)^{-3} n_p(E, z)$.

Ref. [143] found that the *Fermi*-LAT bound data [144] impose an upper bound on the e.m. cascade energy density of

$$\omega_{\text{cas}} \leq 5.8 \cdot 10^{-16} \text{ GeV cm}^{-3} . \quad (3.44)$$

¹¹Since, according to the right plot of Fig. 3.6, $E_c(z) \gtrsim 10^{10.1}$ GeV, we could have instead used a redshift-independent suppression $\propto e^{-E^2/E_c^2(0)}$, with $E_c(0) \approx 4 \cdot 10^{11}$ GeV, and the calculated neutrino flux at Earth would have been the same.

¹²With the routine `ncoComputeSecondarySpectrum`, using `ParticleIn = NCO_PROTON` and `ParticleOut = NCO_NEUTRON`

This bound was found by propagating the secondary electrons, positrons, and photons in the CMB and CIB¹³, calculating the resulting photon flux at Earth, J_{cas} (Eq. (3) in Ref. [143]), and, with this, the e.m. cascade energy density, $\omega_{\text{cas}} = (4\pi/c) \int dE E J_{\text{cas}}(E)$. (Note that, like in our code, the normalisation of the primary proton injection spectrum was indirectly set by fitting the proton flux at Earth to the HiRes data.) The maximum allowed photon flux was determined by requiring that the J_{cas} curve just touches the lower end of the error bars of the *Fermi*-LAT data (see Fig. 1 in Ref. [143]), which imposes the upper bound on the e.m. cascade energy density, Eq. (3.44). Of course, to every set of values of the CR propagation parameters (*e.g.*, proton spectral index, CR source evolution, etc.) will correspond a photon flux with a different spectral shape. However, Ref. [143] proved that the shape of J_{cas} is universal, *i.e.*, it is approximately the same for a large choice of parameter values; the main effect of choosing a set of values is to fix the flux normalisation. Therefore, it makes sense to use the integrated flux, *i.e.*, the energy density ω_{cas} , which is a computationally more efficient method, compared to tracking the evolution of the e.m. cascade, of taking into account the *Fermi*-LAT bounds.

Finally, while the *Fermi*-LAT data spans the approximate energy range 1 GeV - 100 GeV, note that the energy integration in Eq. (3.43) covers the much larger and higher range of proton energies, typically 10^7 GeV - 10^{12} GeV. However, the e^\pm and γ generated at these much higher energies eventually cascade down to the *Fermi*-LAT range, which makes the application of the bound in Eq. (3.44) valid.

3.3 Selected results

The plots in this section have been produced using $z_{\text{hom}} = 10^{-3}$ (see subsection A.2), which corresponds to ~ 39 Mpc. The appropriate value, however, should be $z_{\text{hom}} = 0.02$, corresponding to ~ 77 Mpc. Since the plots presented here already match those found in the references, we can safely say that the fluxes would not be greatly affected by this change in z_{hom} .

3.3.1 The UHE proton flux at Earth

For test purposes (see subsection A.2), we have assumed a proton injection spectrum of the form

$$Q_{\text{CR}}(E) \propto E^{-\gamma} e^{-E/E_{p,\text{max}}} , \quad (3.45)$$

with γ and $E_{p,\text{max}}$ free parameters. For Figs. 3.7–3.11, the normalisation of Q_{CR} was determined by matching –by visual inspection only¹⁴– the calculated flux at Earth, $J_p(E_0)$ in Eq. (3.3), to the flux observed by HiRes [44]. The same normalisation was used to produce the plots of the cosmogenic neutrino flux in Figs. 3.14– 3.18.

As explained in Ref. [121], the first bump in the proton flux, at $\sim 10^{8.8}$ GeV in Fig. 3.7, is due to the pile-up of higher-energy protons that have lost energy through pair-production on the CMB. This can be inferred from the right panel of Fig. 3.3: at low energies, the shortest interaction length is due to pair production on the CMB (though adiabatic losses dominate at low redshifts). As a result of this pile-up, a dip is formed after the bump, while, to the left of the bump, adiabatic losses dominate. At higher energies, the same behaviour is repeated due to the photohadronic

¹³The CIB spectrum was assumed to follow that of Ref. [145].

¹⁴The fits of the UHECR protons in the present chapter are not rigorous and should not be taken at face value; they have been chosen in order to facilitate the comparison between different parameter choices. In chapter 4, however, we have performed numerical fits to the experimental data; see appendix C for details.

interactions on the CMB, with a bump appearing at $\sim 10^{10.7}$ GeV, and a cut-off afterwards (with a much steeper slope, since $|b_{p\gamma}| \gg |b_{e+e-}|$ at these energies). The model in which the appearance of said bumps and dips are due only to the proton interactions with the photon backgrounds is known as the *dip model*.

Fig. 3.8 shows the effect of varying the maximum proton energy $E_{p,\max}$: the higher it is, the larger the enhancement of the high energy peak around $10^{10.5}$ GeV, since there will be more protons at the tail of the distribution. On the other hand, we see in Fig. 3.9 the effect of varying the spectral index of the proton injection spectrum: for low values of γ , it is possible to closely fit only the high-energy peak in the experimental data. This corresponds to a *transition model*, where only the highest-energy part of the data, above the pair-production dip, is attributed to extragalactic contributions. A higher value of γ , notably, 2.5 allows the fit to cover also the dip; hence, spectral indices close to this value correspond to dip models.

Fig. 3.10 compares the UHECR proton flux under two possibilities for the source redshift evolution: SFR (Eq. (3.32) vs. GRB (Eq. (3.33)). Towards the high-energy end of the spectrum, the curve corresponding to the GRB evolution lies below the one for SFR evolution, while the opposite is true towards the low-energy end. This is because the normalised comoving GRB rate is enhanced at high redshifts compared to the SFR rate: due to the energy losses during propagation, however, the contributions of these high-redshift sources, however, will not show up in the high-energy tail of the final local flux, but they will rather pile up towards the low-energy end of the flux.

So far, our results have been generated under the assumption that the local CIB photon spectrum follows the model by [135] *et al.* (CIB1 in our convention). Fig. 3.11 shows the resulting flux for different choices of the local CIB spectrum, including its absence. Clearly, including the CIB losses in the propagation of the UHECR protons depletes the high-energy peak of the spectrum, while leaving the pair-production dip and lower energies unmodified. This is because the $p\gamma$ interactions on the CIB are mainly photohadronic, not pair-producing – otherwise they would contribute to the pair-production dip. Furthermore, it becomes evident that the choice of local CIB model (Franceschini *et al.* [135] or Stecker *et al.* (2005) [136]) does not affect the local UHECR flux; it will, however, affect the cosmogenic neutrino flux.

3.3.2 Modification factor

The modification factor, η , was introduced in Ref. [121] as the ratio of modified to unmodified spectrum, *i.e.*,

$$\eta(E, z) = \frac{Y(E, z; \text{with adiabatic, pair-production, and photohadronic losses})}{Y(E, z; \text{with adiabatic losses only})}. \quad (3.46)$$

(Note, however, that, in Ref. [121], only the modification factor at $z = 0$ was calculated.) Since protons are injected by sources from z_{\max} down to z_{hom} , the modification factor depends on the redshift evolution of the number density of sources. Fig. 3.12 shows the modification factor assuming a spectral index $\gamma = 2$ and no source evolution ($\mathcal{H}_{\text{CR}} = \mathcal{H}_{\text{CIB}} = 1$); it matches, for $z = 0$, the results in Ref. [125]. This should be compared to Fig. 3.13, where SFR evolution has been assumed instead. Clearly, including the photohadronic interactions depletes the flux at high energies.

Note that the low-energy bump due to pair production on the CMB appears early in the evolution and is visible down to $z \approx 4$. However, adiabatic losses subsequently make the bump less pronounced at lower redshifts. These losses are also responsible for making the dip shallower with redshift.

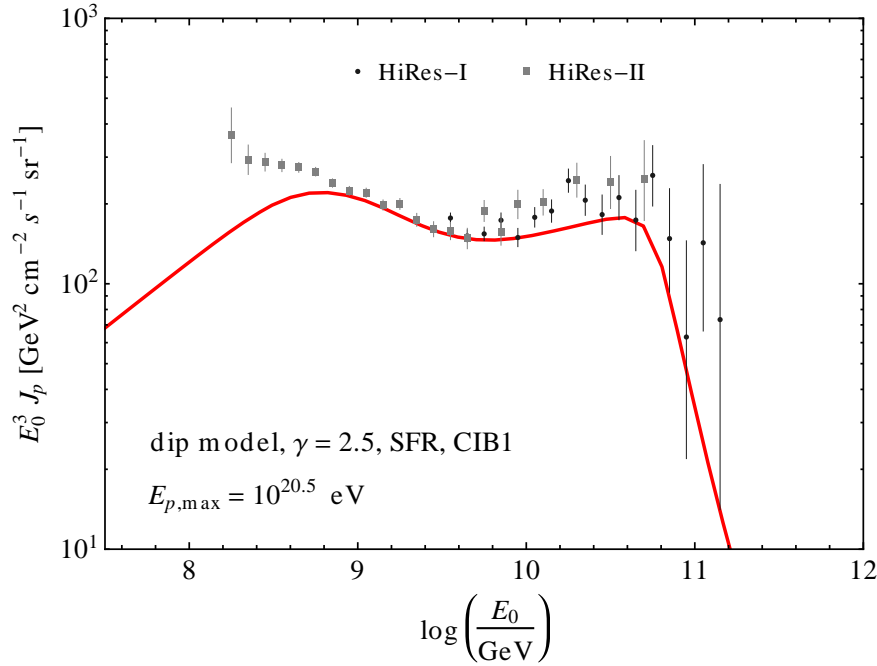


Figure 3.7: The proton flux at Earth, normalised to HiRes data.

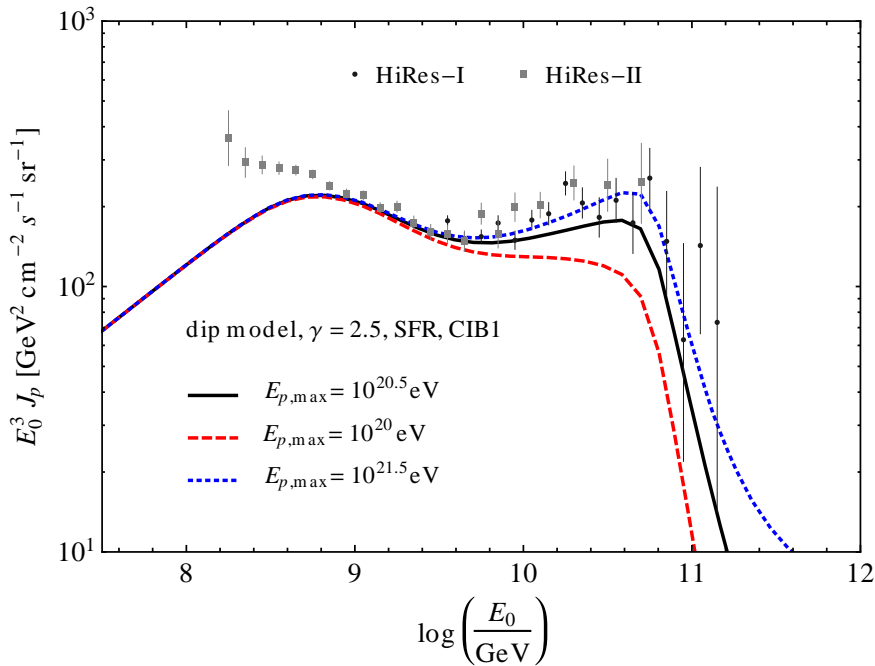


Figure 3.8: The proton flux at Earth, normalised to HiRes data, for three different choices of maximum proton energy, $E_{p,\max} = 10^{20}$, $10^{20.5}$, and $10^{21.5}$ eV.

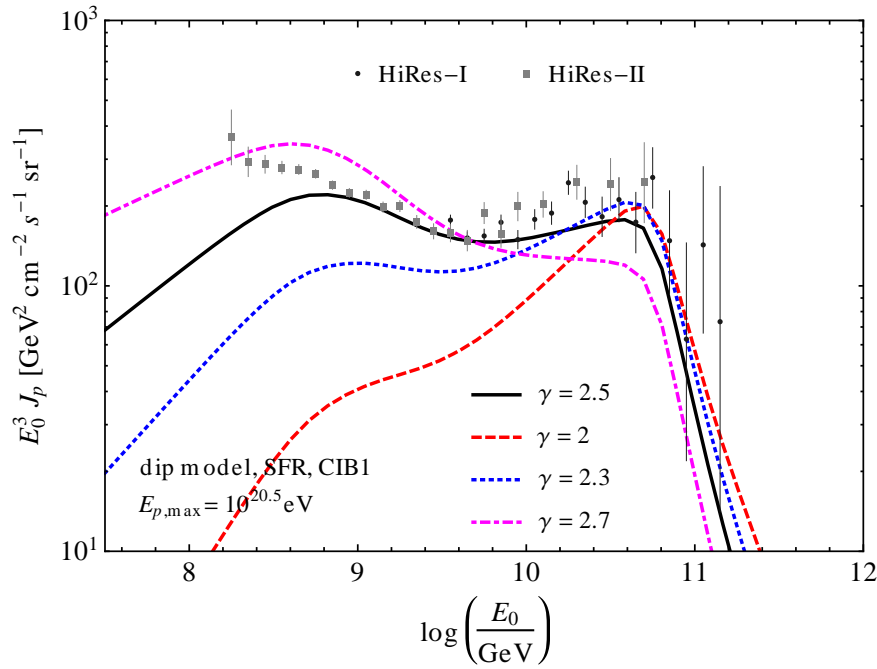


Figure 3.9: The proton flux at Earth, normalised to HiRes data, for four different choices of the proton spectral index $\gamma = 2.0, 2.3, 2.5,$ and 2.7 .

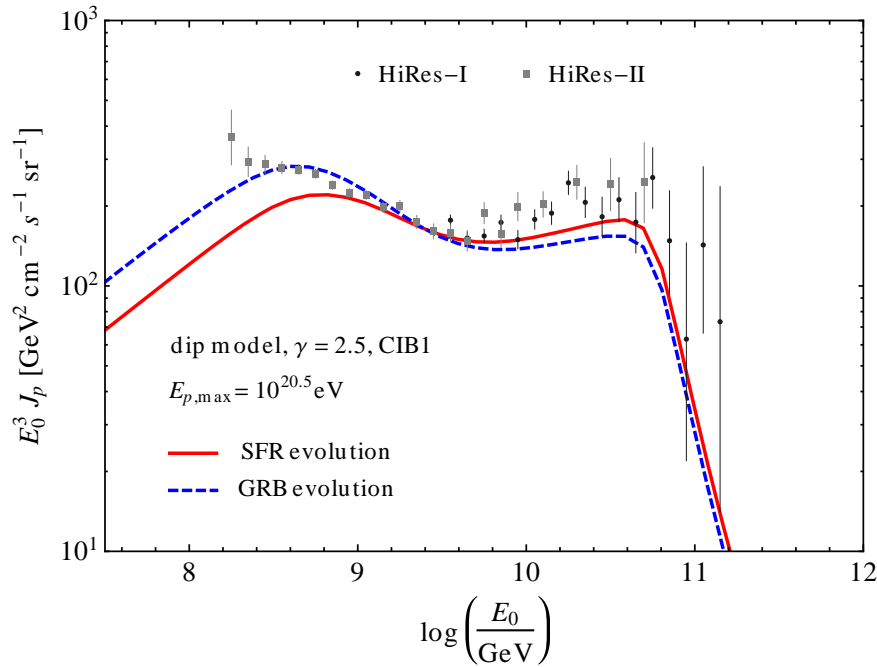


Figure 3.10: The proton flux at Earth, normalised to HiRes data, for two different source evolution models: SFR vs. GRB evolution.

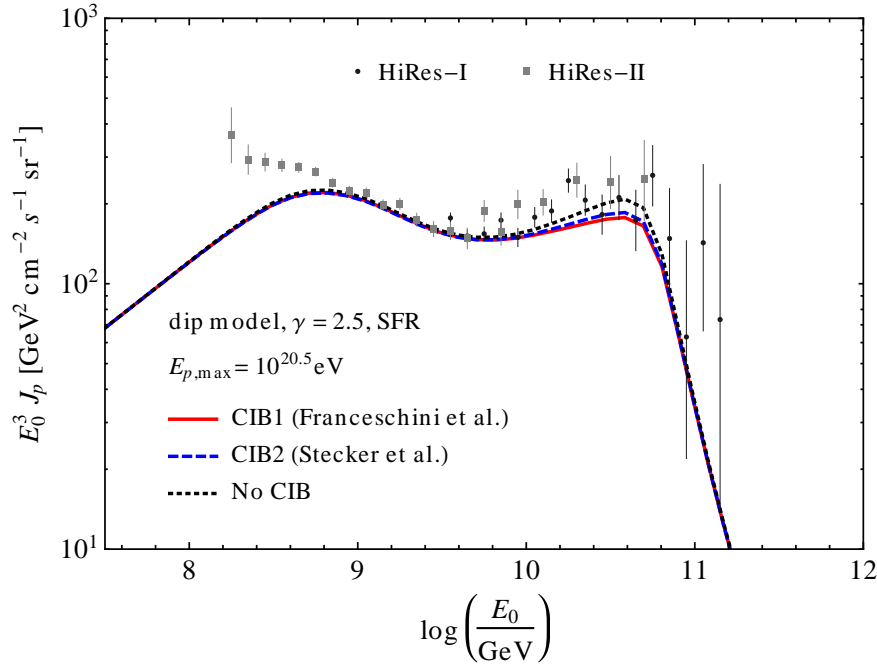


Figure 3.11: The proton flux at Earth, normalised to HiRes data, for two different models of the local ($z = 0$) CIB: CIB1, by Franceschini *et al.* [135] and CIB2, by Stecker *et al.* [136].

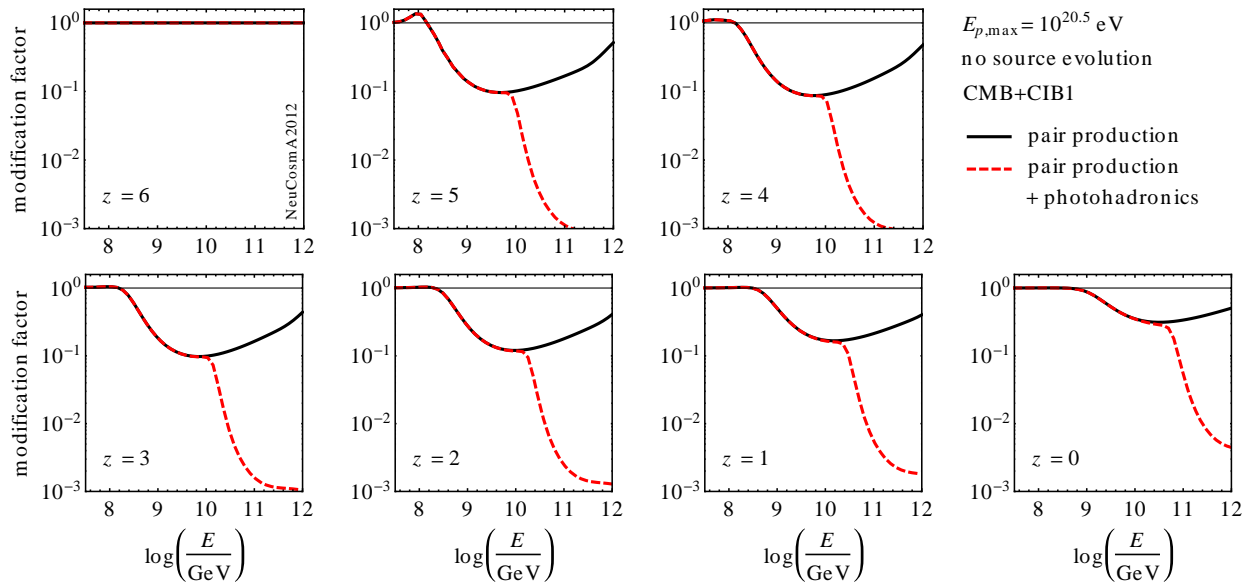


Figure 3.12: Modification factor, Eq. (3.46), assuming $\gamma = 2$ and no source evolution with redshift.

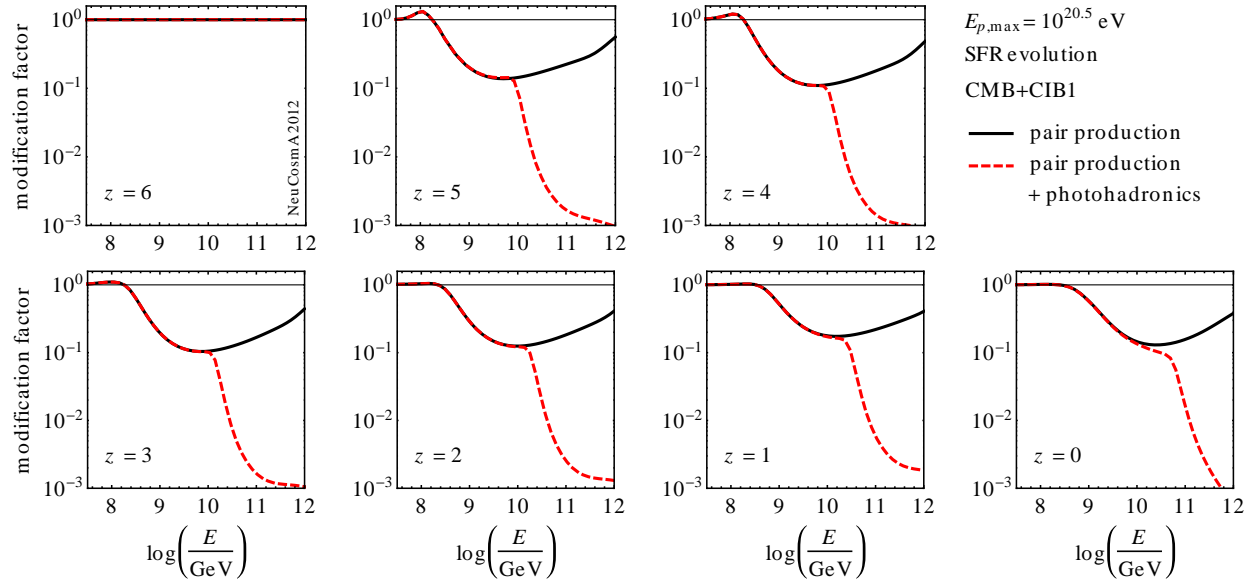


Figure 3.13: Modification factor, Eq. (3.46), assuming $\gamma = 2$ and SFR source evolution.

At $z = 0$, the dip in the modification factor calculated under the assumption of SFR evolution (Fig. 3.12) is deeper than the corresponding one under the no-evolution assumption (Fig. 3.13). From Fig. 3.4, we know that the maximum difference between \mathcal{H}_{SFR} and a uniform source density of $\mathcal{H} = 1$ occurs around $z \lesssim 1$, which, according to the right panel of Fig. 3.3 is precisely the redshift region in which, for large energies ($E \gtrsim 10^{8.8}$ GeV), losses through photohadronic interactions on the CMB dominate over adiabatic losses by more than two orders of magnitude. In other words, in the SFR evolution case, more protons are injected just at the right redshift where they are prone to lose more energy through photohadronic interactions than adiabatically. Therefore, the dip in the modification factor becomes deeper.

3.3.3 The cosmogenic neutrino flux at Earth

The cosmogenic neutrino flux at Earth, $J_\nu(E_0)$ in Eq. (3.40), is calculated as explained in subsection 3.2.7; see also section 3.1. Note that due to the high energies and very long baselines, the flavour-transition probability is no longer oscillatory, but averaged-out.

To generate Figs. 3.14–3.17, we used the best-fit values of the mixing parameters from Ref. [105], assuming a normal mass hierarchy:

$$\sin^2(\theta_{12}) = 0.307 \quad , \quad \sin^2(\theta_{13}) = 0.0245 \quad , \quad \sin^2(\theta_{23}) = 0.398 \quad , \quad \delta_{CP} = 0.89\pi \quad . \quad (3.47)$$

The IceCube 2010–2012 sensitivity curve shown in the plots was extracted from Ref. [146]. Fig. 3.14 shows the different contributions that make up the all-flavour cosmogenic neutrino flux: the $\bar{\nu}_e$ coming from the β -decay of the neutrons that escape the source, and the neutrinos+antineutrinos generated in the photohadronic interactions of the protons and the cosmological photon backgrounds. The peak at $E_\nu \approx 10^{6.8}$ GeV is due to interactions on the CIB, while the peak at $\sim 10^9$ GeV is due to interactions on the CMB. Since neutrinos in photohadronic interactions carry a fraction 1/20 of the energy of the parent proton, neutrinos at the peak were created by protons of

energies $20 \cdot 10^{6.8} \text{ GeV} \approx 1.3 \cdot 10^8 \text{ GeV}$ (for interactions on the CIB) and $20 \cdot 10^9 \text{ GeV} = 2 \cdot 10^{10} \text{ GeV}$ (for interactions on the CMB).

The left and right panels of Fig. 3.15 show, respectively, the effect on the cosmogenic neutrino flux of varying the maximum proton energy and the spectral index of the injected proton spectrum, for the same values that we explored in Figs. 3.8 and 3.9. As expected, higher values of $E_{p,\text{max}}$ result in enhanced fluxes at high energies, due to the higher abundance of high energy protons that can interact with the CMB. Note also that larger values of the spectral index γ will deplete the high-energy neutrino peak that comes from CMB interactions, but will increase the relative contribution of the lower-energy peak that comes from CIB interactions.

Furthermore, the left panel of Fig. 3.16 shows the cosmogenic neutrino flux under the two assumptions of source evolution: SFR and GRB. In comparison to the effect that the source evolution has on the UHECR flux, which is rather mild at high energies (see Fig. 3.10), the effect on the cosmogenic neutrinos is markedly stronger: this is because, while for the UHECR protons the enhancement of the number of sources at high redshifts is counteracted by the energy losses during the longer propagation, for the cosmogenic neutrinos no energy losses apart from the adiabatic one exist, and so neutrinos from all redshifts effectively contribute to the local flux. The right panel of Fig. 3.16 shows, on the other hand, the effect of the choice of the local CIB photon spectrum; since the CIB2 spectrum is slightly higher than the CIB1 spectrum (see Fig. 3.2), the low-energy peak of the cosmogenic neutrino flux is correspondingly higher under the CIB2 model.

It is interesting to study how different redshift ranges contribute to the total cosmogenic neutrino flux: Fig. 3.17 shows that while most of the flux comes from $0.5 \leq z \leq 1.5$, contributions from even the highest redshifts are not at all negligible, with the band $2.5 \leq z \leq 4.0$ only approximately a factor of five lower. We are also able to calculate the flux per flavour, for neutrinos and antineutrinos, as shown in the left panel of Fig. 3.18. Due to flavour transitions, we expect an approximately equal flux of neutrinos+antineutrinos of each flavour, and we find that the curves are consistent with this expectation. The central panel shows the ratio of neutrinos to antineutrinos for the different flavours, where we see that there are markedly more ν_e than $\bar{\nu}_e$, with the ratio varying between 2 and 3, while for muon- and tau-flavour the ratio oscillates around 1.1. Around 10^4 GeV the ratio drops to almost zero, since at this energy the only contribution comes from the β -decay of neutrons into exclusively $\bar{\nu}_e$. Finally, the right panel of Fig. 3.18 shows the ratio of each flavour to the total number of neutrinos, antineutrinos, and their sum. As expected, starting from $\sim 10^{5.5} \text{ GeV}$, *i.e.*, once most of the neutrinos come from photohadronic interactions and not from neutron decay, the ratios lie around 0.3, in agreement with the left panel of the figure.

3.4 The effect of the CIB on cosmogenic neutrinos

Our motivation here is to find ways to enhance the peak in the predicted cosmogenic neutrino flux at $E_\nu \sim 10^7 \text{ GeV}$, which is due to photohadronic interactions of UHE protons with the CIB. In order to achieve this, we have explored the effects of adding an extra component to the CIB photon spectrum, properly tuned in order for its effect to be to increase the number of photohadronic interactions on the CIB at higher redshifts¹⁵.

¹⁵The results in section 3.4 were obtained by using a value of the Hubble constant of $H_0 = 74.3 \text{ km s}^{-1} \text{ Mpc}^{-1} = 2.4095 \cdot 10^{-18} \text{ s}^{-1}$ [147]

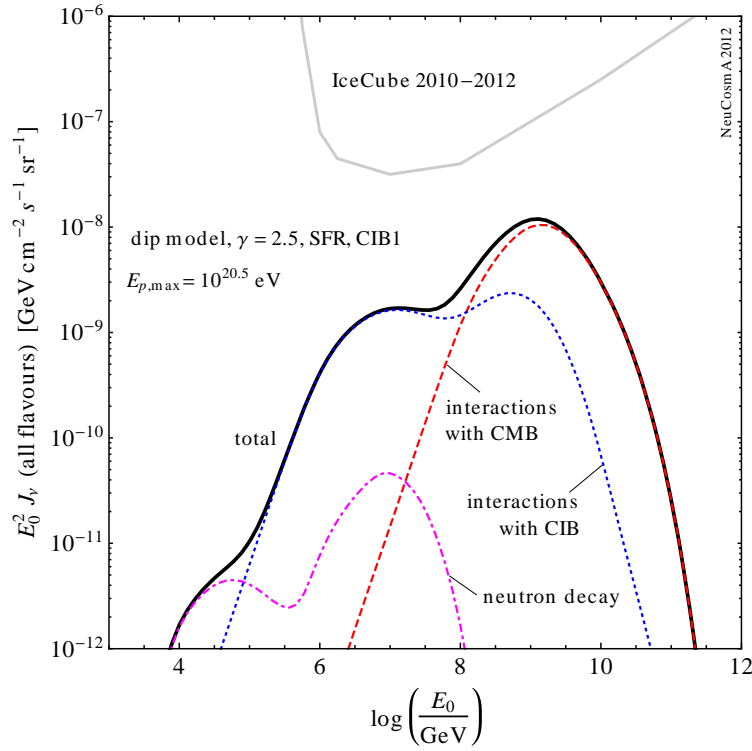


Figure 3.14: Cosmogenic neutrino flux at Earth, assuming SFR source evolution. Individual contributions from neutron decay, interactions (photohadronic and pair-production) on the CMB, and interactions on the CIB are shown separately.

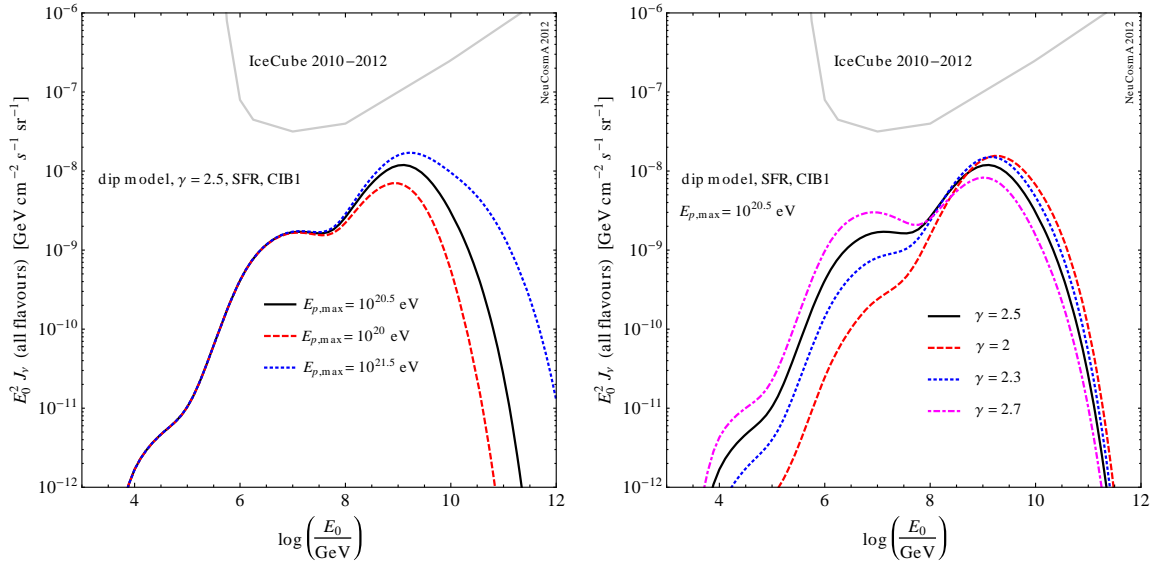


Figure 3.15: *Left:* cosmogenic neutrino flux at Earth, assuming SFR source evolution, for three different choices of maximum proton energy, $E_{p,\max} = 10^{20}$, $10^{20.5}$, and $10^{21.5}$ eV. *Right:* flux for four different choices of the proton spectral index $\gamma = 2.0, 2.3, 2.5$, and 2.7 .

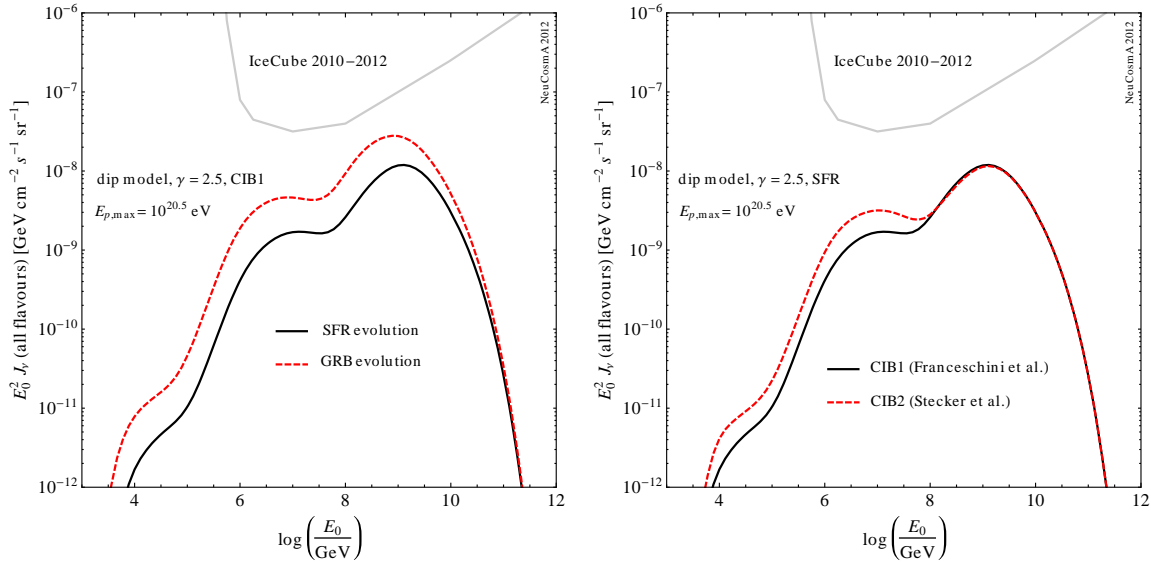


Figure 3.16: *Left:* cosmogenic neutrino flux at Earth, for two different source evolution models, SFR vs. GRB evolution. *Right:* flux for two different models of the local ($z = 0$) CIB: CIB1, by Franceschini *et al.* [135] and CIB2, by Stecker *et al.* [136].

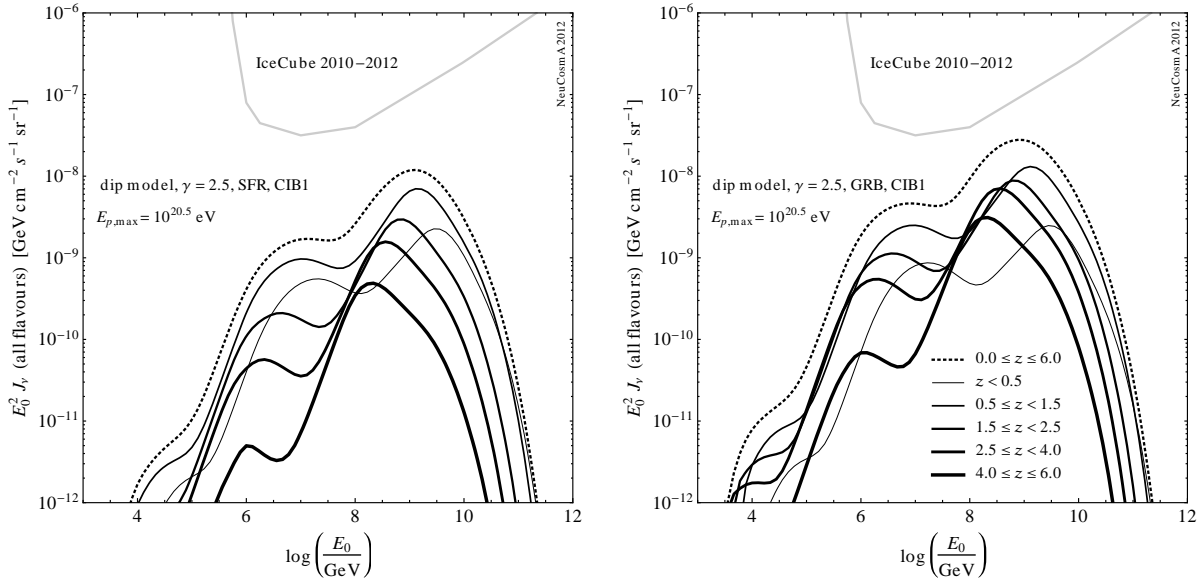


Figure 3.17: Cosmogenic neutrino flux at Earth coming from different redshift ranges, assuming that the CR and CIB source evolution both follow the SFR (left panel) or the GRB rate (right panel). Compare to Fig. 4 in Ref. [130].

3.4.1 Adding an extra component to the CIB photon spectrum

Our aim is to explore possible enhancements of the peak at $E_{\nu, \text{peak}}^0 \approx 10^{6.81}$ GeV in the local ($z = 0$) cosmogenic neutrino flux that is due to interactions with the CIB. The most straightforward way

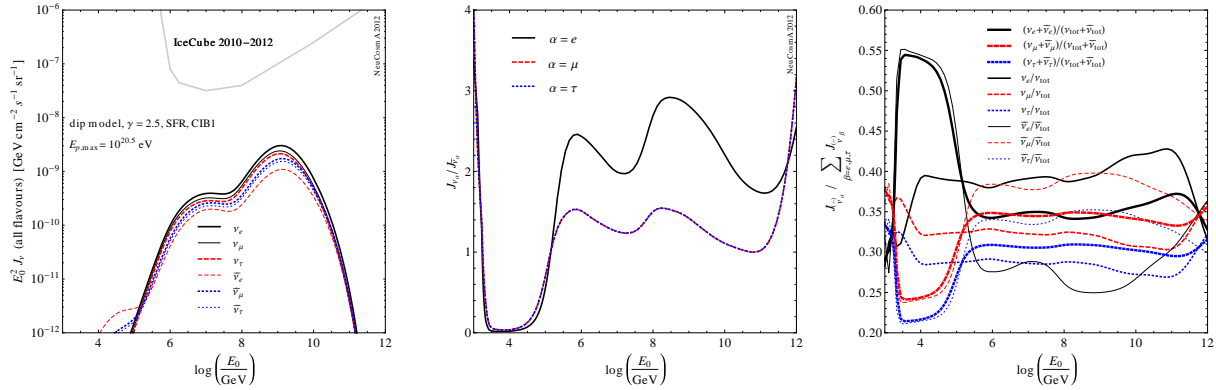


Figure 3.18: *Left:* Cosmogenic ν_α and $\bar{\nu}_\alpha$ fluxes at Earth shown separately, and per flavour. *Center:* Ratio $J_{\nu_\alpha}/J_{\bar{\nu}_\alpha}$ of cosmogenic neutrinos to antineutrinos, per flavour. *Right:* Ratio of each flavour of neutrino and antineutrino to the total, all-flavour, flux, $J_{\nu_\alpha}/\sum_\beta J_{\nu_\beta}$ and $J_{\bar{\nu}_\alpha}/\sum_\beta J_{\bar{\nu}_\beta}$, respectively.

to achieve this is to add a suitably-chosen extra component to the CIB photon spectrum, so that the total spectrum is computed as

$$n_\gamma^{\text{CIB}}(\epsilon, z) = n_{\gamma, \text{base}}^{\text{CIB}}(\epsilon, z) + n_{\gamma, \text{extra}}^{\text{CIB}}(\epsilon, z), \quad (3.48)$$

where $n_{\gamma, \text{base}}^{\text{CIB}}$ is the base spectrum, given by one of the available models in the literature (*e.g.*, Stecker *et al.* [136, 148], Franceschini *et al.* [135], Inoue *et al.* [149], *etc.*), and $n_{\gamma, \text{extra}}^{\text{CIB}}$ is the extra component.

The size of this extra component will be limited by three different pieces of observational data:

The UHECR observations. Cosmogenic neutrinos are created in the interactions of UHE protons –injected by cosmological sources– with the cosmological photon backgrounds. The proton spectrum that is assumed to be injected by the sources and that is propagated down to Earth, while taking into account energy losses, must be able to fit the observed local UHECR spectrum (*e.g.*, as measured by HiRes), and to yield values of the local energy injection rate in CRs that are in agreement with the one derived from the observations ($\sim 5 \cdot 10^{44} \text{ erg Mpc}^{-3} \text{ yr}^{-1}$).

The UHE neutrino bounds. After the addition of the CIB extra component, the resulting cosmogenic neutrino flux must still lie below the UHE neutrino bound from IceCube [146].

The model uncertainties on the CIB at low redshifts. Different models of the CIB give different (though mostly compatible) results for the local photon spectrum and its uncertainty, both of which are better estimated at lower redshifts. Hence, as an additional requirement of our analysis, we demand that the addition of the extra component to the CIB spectrum does not exceed the base model uncertainty at low redshifts. At higher redshifts, where the predictions of the spectrum and the uncertainty estimates are much less well-known, the size of the extra component may be larger.

An extra component $n_{\gamma,\text{extra}}^{\text{CIB}}$ that satisfies these three requirements could therefore potentially enhance the cosmogenic neutrino flux at $E_{\nu,\text{peak}}^0$ without disrupting the UHECR and low- z CIB predictions, and respecting the UHE neutrino upper bound.

We will assume that the extra component has a Gaussian shape. In order for it to enhance the cosmogenic neutrino flux in as much as possible, we will see that it is sufficient to make its central value satisfy the Δ -resonance energy condition at every value of redshift. In the CM frame, the neutrino energy $E_\nu \approx 0.05E_p$. On the other hand, the threshold for the Δ -resonance to occur is give by $E_p\epsilon \approx 0.2 \text{ GeV}^2$. Since neutrinos only lose energy adiabatically, their energy at production is simply a factor $(1+z)$ higher than their energy at detection, *i.e.*, $E_\nu = (1+z)E_\nu^0$. Therefore,

$$E_\nu = (1+z)E_\nu^0 \approx 0.05E_p, \quad (3.49)$$

and, with this, the threshold condition can be rewritten as

$$\epsilon \approx \frac{0.2 \text{ GeV}^2}{E_p} \approx \frac{0.2 \text{ GeV}^2}{\frac{(1+z)E_\nu^0}{0.05}} = \frac{0.01}{(1+z)E_\nu^0} \text{ GeV}. \quad (3.50)$$

Therefore, from this relation, we find that if we wish to enhance the local neutrino peak at $E_{\nu,\text{peak}}^0 \approx 10^{6.8125} \text{ GeV}$, then the extra component of the CIB spectrum must be centered at

$$\epsilon_{\text{peak}}^{\text{CIB}}(z) \approx \frac{1.54 \text{ eV}}{1+z}. \quad (3.51)$$

We then set, at every redshift, the central height and standard deviation of the Gaussian extra component of the CIB spectrum to be proportional to the value of the base spectrum evaluated at $\epsilon_{\text{peak}}^{\text{CIB}}(z)$. The extra component can thus be written as

$$n_{\gamma,\text{extra}}^{\text{CIB}}(\epsilon, z) = e^{z-z^*} \left[\kappa_1 n_{\gamma,\text{base}}^{\text{CIB}}(\epsilon_{\text{peak}}^{\text{CIB}}(z), z) \right] \exp \left[-\frac{\left(\epsilon - \epsilon_{\text{peak}}^{\text{CIB}}(z) \right)^2}{2 \left(\kappa_2 \epsilon_{\text{peak}}^{\text{CIB}}(z) \right)^2} \right], \quad (3.52)$$

with κ_1 and κ_2 free proportionality constants of the model. The damping factor e^{z-z^*} ensures that, below z^* , the extra component is small, so that it does not exceed the uncertainty bands of the CIB spectrum at low redshifts (typically, $2 \leq z^* \leq 3$), where they are better modeled. See, *e.g.*, Fig. 3.19, which shows the uncertainty bands for the Stecker *et al.* (2012) model [148].

At this point we should mention that the shape of the CIB extra component, Eq. (3.52), is purely phenomenological: by definition, the CIB spectrum $n_\gamma^{\text{CIB}}(\epsilon, z)$ is obtained from integrating in z the photon injection spectrum $\mathcal{L}_\gamma^{\text{CIB}}(\epsilon, z)$ (see Eq. (3.22)); hence, adding an extra component $n_{\gamma,\text{extra}}^{\text{CIB}}(\epsilon, z)$ to the CIB spectrum implies adding an extra component $\mathcal{L}_{\gamma,\text{extra}}^{\text{CIB}}$ to the injection function, *i.e.*,

$$\mathcal{L}_\gamma^{\text{CIB}}(\epsilon, z) = \mathcal{L}_{\gamma,\text{base}}^{\text{CIB}}(\epsilon, z) + \mathcal{L}_{\gamma,\text{extra}}^{\text{CIB}}(\epsilon, z). \quad (3.53)$$

Due to the added difficulty in finding a form of $\mathcal{L}_{\gamma,\text{extra}}^{\text{CIB}}$ that yields $n_{\gamma,\text{extra}}^{\text{CIB}}$ in Eq. (3.52), we have first concerned ourselves with adding the extra component directly on the CIB spectrum, while leaving for section 3.4.2 the issue of what is the corresponding extra injection component. For the redshift evolution of the base CIB spectrum, we have used Eq. 3.25 (see also appendix C of Ref. [122]), $n_\gamma^{\text{CIB}}(\epsilon, z) \rightarrow n_{\gamma,\text{base}}^{\text{CIB}}(\epsilon, z)$. To produce the results in the present section, we have assumed that the base CIB model is given by the local Stecker (2005) *et al.* calculation [136] and that $\mathcal{H}_{\text{CIB}}(z)$ is the SFR evolution.

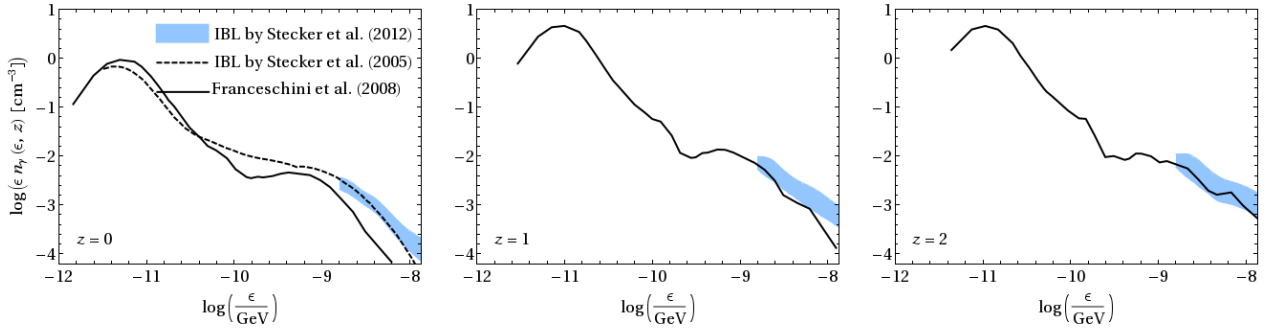


Figure 3.19: Three different models of the CIB at low redshifts. The shaded band shows the 68% uncertainty on the Stecker *et al.* (2012) model [148].

Fig. 3.20 shows the evolution of the CIB spectrum with redshift. We include a rough estimate of the uncertainty of the base model as a blue shaded band covering from half to twice the value of the base spectrum (black solid line) at each energy value, approximately reproducing the uncertainty of the Stecker *et al.* (2012) model shown in Fig. 3.19. The base spectrum should be compared to the three enhanced CIB models (Eq. (3.48)) that we have included: two conservative models with $(\kappa_1, \kappa_2, z^*) = (2, 1, 2)$ (red dashed lines) and $(2, 1, 3)$ (blue dotted), and an extreme model with $(6, 1, 2)$ (magenta dot-dashed). Note that, for the latter, the uncertainty band is exceeded already at $z = 2$.

As the next step, we have calculated the cosmogenic neutrino flux, using each of the different CIB spectra from Fig. 3.20. In order to do this, we have assumed a distribution of extragalactic UHECR pure-proton sources that follow the GRB rate, Eq. (3.33), and an injection spectrum of $Q_{\text{CR}} \propto E^{-\alpha_p} \exp(-E/E_{p,\text{max}})$ for each source, with a fixed maximum proton energy of $E_{p,\text{max}} = 10^{11.5}$ GeV for the present analysis. As before, we have normalised our generated UHECR proton flux to the HiRes experimental data, which fixes also the cosmogenic neutrino flux normalisation.

Fig. 3.21, left panel, shows the calculated local cosmogenic neutrino flux for a proton injection spectral index of $\alpha_p = 2$, and using for the CIB spectrum the base model and the enhanced models depicted in Fig. 3.20. It is evident that, even when using the extreme CIB enhanced model with $(\kappa_1, \kappa_2, z^*) = (6, 1, 2)$, the enhancement is not nearly high enough to bring the peak at $E_{\nu,\text{peak}}^0 \approx 10^{6.81}$ GeV close to the IceCube sensitivity. The situation is better for a spectral index of $\alpha_p = 2.5$, shown in the right panel of Fig. 3.21. In this case, when using the extreme CIB enhanced model, the peak at $E_{\nu,\text{peak}}^0$ reaches the same level as the highest-energy peak at $\sim 10^9$ GeV which is due to interactions with the CMB, and lies considerably closer to the IceCube sensitivity.

However, since the CIB spectrum slightly exceeds the uncertainty of the CIB models already at $z = 2$, it will probably be a better choice to use a Gaussian extra component with $\kappa_1 \approx 5$ instead (see Eq. (3.52)). Nevertheless, it is clear that the phenomenological form of the extra component in the CIB spectrum that we have adopted, $n_{\gamma,\text{extra}}^{\text{CIB}}$, is able to achieve what we sought: it enhances the peak in the cosmogenic neutrino flux at $E_{\nu,\text{peak}}^0 \approx 10^{6.81}$ GeV.

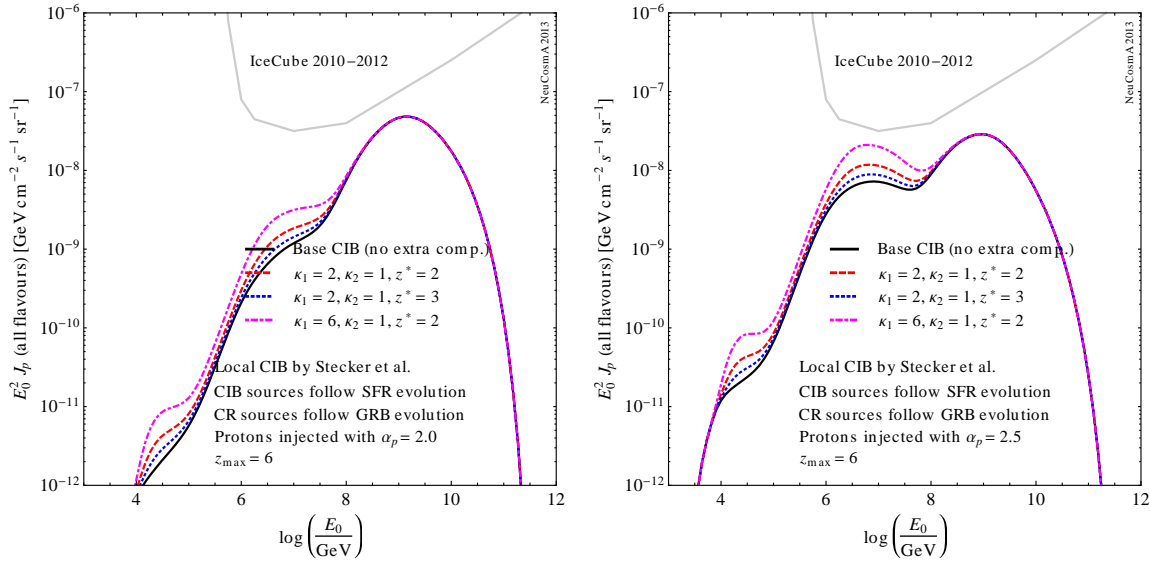


Figure 3.21: Cosmogenic neutrino flux assuming a proton injection spectral index of $\alpha_p = 2.0$ (left panel) and $\alpha_p = 2.5$ (right panel). The base CIB spectrum at $z = 0$ has been assumed to be the one by Stecker *et al.* (2005) [148], and the density of the CIB sources follows the SRF evolution (see Eq. (3.22)). The same three enhanced CIB spectra (see Eqs. (3.48) and (3.52)) used in Fig. 3.20 are included.

3.4.2 A simple model of the CIB injection function

In this section, we propose a simple model of the CIB injection function which reproduces existing models in the literature, with the aim that it could later be used as a basis to explore how to add the required extra component $\mathcal{L}_{\gamma,\text{extra}}^{\text{CIB}}$ introduced in section 3.4.1.

We have modeled the logarithm of the injection function as the addition of two Gaussians with (initially) free parameters that are allowed to evolve with redshift¹⁶:

$$\log \mathcal{L}_{\gamma}^{\text{CIB}}(x, z) = \frac{N_l(z)}{\sqrt{2\pi}\sigma_l(z)} \exp\left[-\frac{(x - \mu_l(z))^2}{2\sigma_l^2(z)}\right] + \frac{N_h(z)}{\sqrt{2\pi}\sigma_h(z)} \exp\left[-\frac{(x - \mu_h(z))^2}{2\sigma_h^2(z)}\right], \quad (3.54)$$

with $x \equiv \log \epsilon$. We have parametrised the redshift dependence as follows:

$$\sigma_l(z) = \sigma_{l0} (1+z)^n \quad (3.55)$$

$$\sigma_h(z) = \sigma_{h0} (1+z)^m \quad (3.56)$$

$$\mu_l(z) = \mu_{l0} (1+z)^p \quad (3.57)$$

$$\mu_h(z) = \mu_{h0} (1+z)^q \quad (3.58)$$

$$N_l(z) = N_{l0} (1+z)^r \quad (3.59)$$

$$N_h(z) = N_{h0} (1+z)^s \quad (3.60)$$

There are twelve free parameters in this model: σ_{l0} , σ_{h0} , μ_{l0} , μ_{h0} , N_{l0} , N_{h0} , n , m , p , q , r , and s . The motivation behind using a two-Gaussian model of the CIB injection function is that, by fitting

¹⁶In the current implementation, the factors $\sqrt{2\pi}\sigma_l(z)$ and $\sqrt{2\pi}\sigma_h(z)$ appear in the normalisation. However, these are unnecessary and may be removed as a refinement.

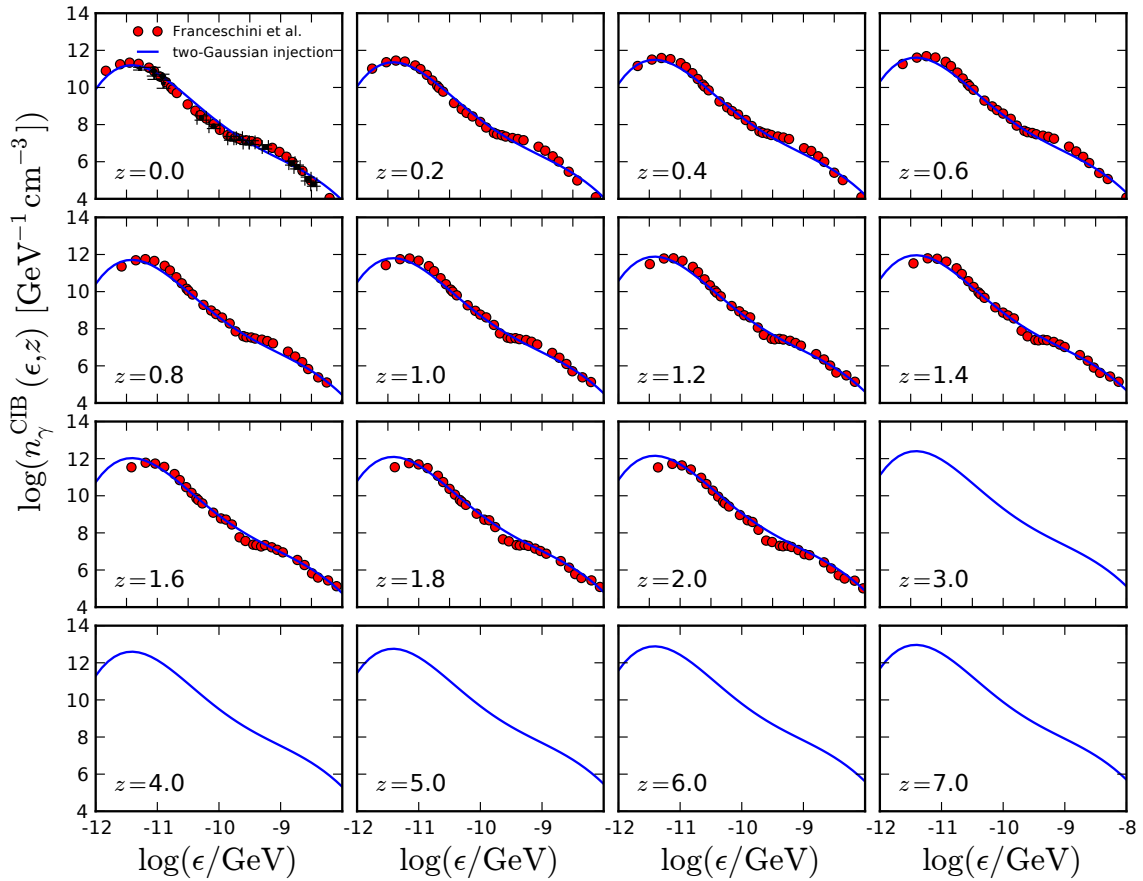


Figure 3.22: CIB spectrum at different redshifts. Data from the model by Franceschini *et al.* [135] is shown as red circles. The blue line is the best-fit CIB spectrum calculated under the assumption of a two-Gaussian injection spectrum, whose parameters were fit to the data. At $z = 0$, the experimental data points and (very small) error bars are shown. See the text for details.

its parameter values to observations of the local ($z = 0$) CIB spectrum or to existing models of the CIB spectrum at $z \geq 0$, one could gain insight as to what the redshift behaviour of the injection function should be in order to maximise the cosmogenic neutrino flux, in particular, as we said, what the extra component $\mathcal{L}_{\gamma, \text{extra}}^{\text{CIB}}$ should be.

The directly measurable quantity is the local CIB spectrum, $n_{\gamma}^{\text{CIB}}(\epsilon, 0)$. The injection function $\mathcal{L}_{\gamma}^{\text{CIB}}$ is not an experimentally accessible quantity. The CIB spectrum at $z > 0$ can be inferred through the use of the luminosity functions of sources which are expected to contribute to the CIB. This has been done by several groups and using different source samples and luminosity functions; in the present note, we have adopted the CIB spectrum constructed by Franceschini *et al.* [135], which extends up to $z = 2$.

To find the values of the free parameters of our model, we have constructed a simple χ^2 function

$$\chi^2(\sigma_{l0}, \sigma_{h0}, \mu_{l0}, \mu_{h0}, N_{l0}, N_{h0}, n, m, p, q, r, s)$$

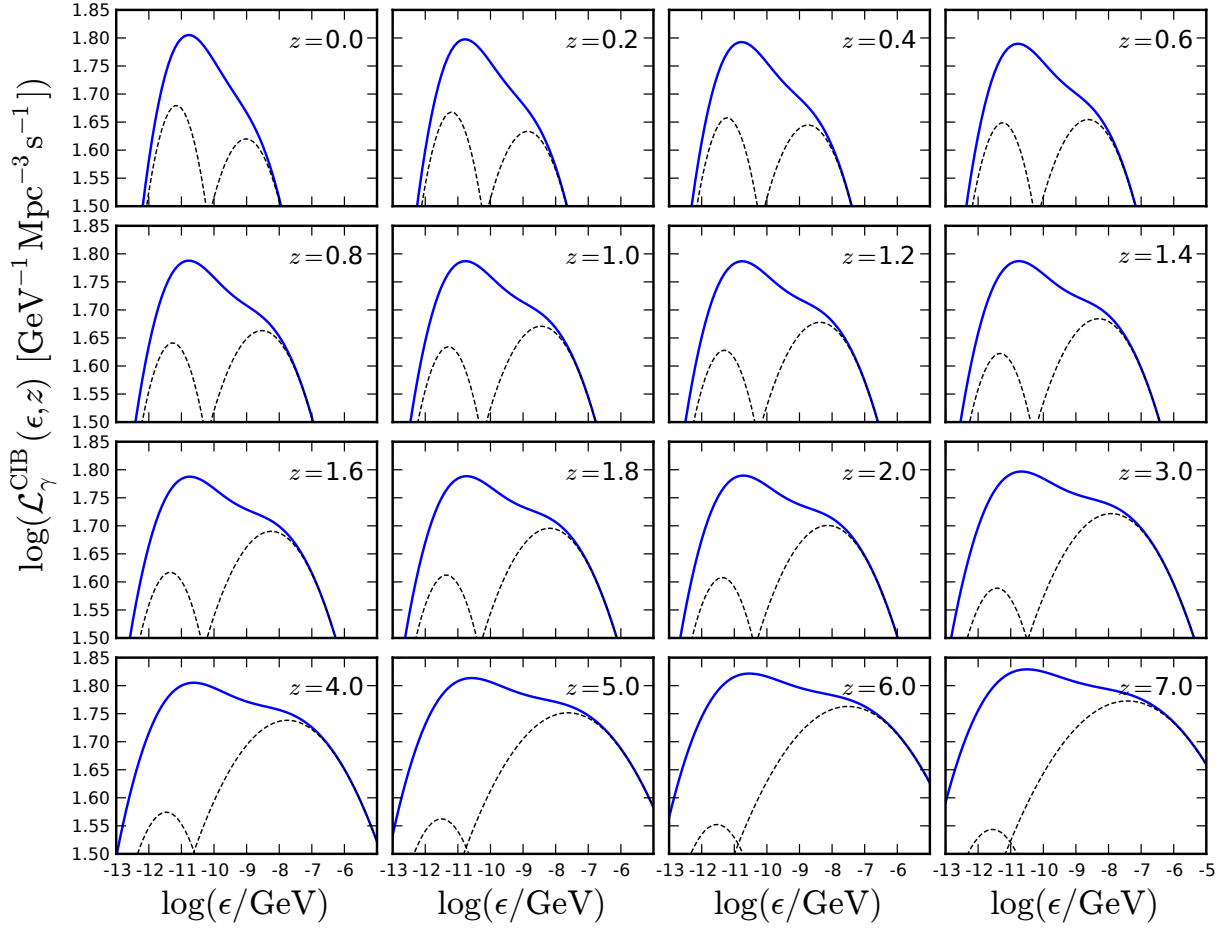


Figure 3.23: CIB injection function composed of two Gaussian functions whose parameters have been found by fitting the associated CIB spectrum (see Eq. (3.22)) to the model by Franceschini *et al.* [135].

$$= \sum_z \sum_x \left[\frac{n_\gamma^{\text{CIB}}(\sigma_{l0}, \sigma_{h0}, \mu_{l0}, \mu_{h0}, N_{l0}, N_{h0}, n, m, p, q, r, s; x, z) - n_\gamma^{\text{CIB-data}}(x, z)}{n_\gamma^{\text{CIB}}(\sigma_{l0}, \sigma_{h0}, \mu_{l0}, \mu_{h0}, N_{l0}, N_{h0}, n, m, p, q, r, s; x, z)} \right]^2 \quad (3.61)$$

with $n_\gamma^{\text{CIB-data}}(x, z)$ the data points from the particular model selected, and scanned the twelve-dimensional parameter space in order to find a minimum¹⁷ of χ^2 . We can choose either to fit to the observed CIB spectrum at $z = 0$ only, or to fit to the inferred CIB spectra in all of the range $0 \leq z \leq z^*$ ($z^* = 2$ in the Franceschini *et al.* model). In the present note we have followed the latter option as an initial step, in order to try to reproduce what is a widely accepted model of the CIB spectrum.

Fig. 3.22 shows the result of such minimisation procedure¹⁸: the red dots are the data from Tables 1 and 2 of Ref. [135] (covering the range $0 \leq z \leq 2$ in steps of 0.2), while the blue line is the best fit to the data assuming the two-Gaussian injection function, Eq. (3.54). We show also the

¹⁷One should be aware that there might be degeneracies among the parameters, and several minima of comparable magnitude.

¹⁸The Python library `pyminuit` was used.

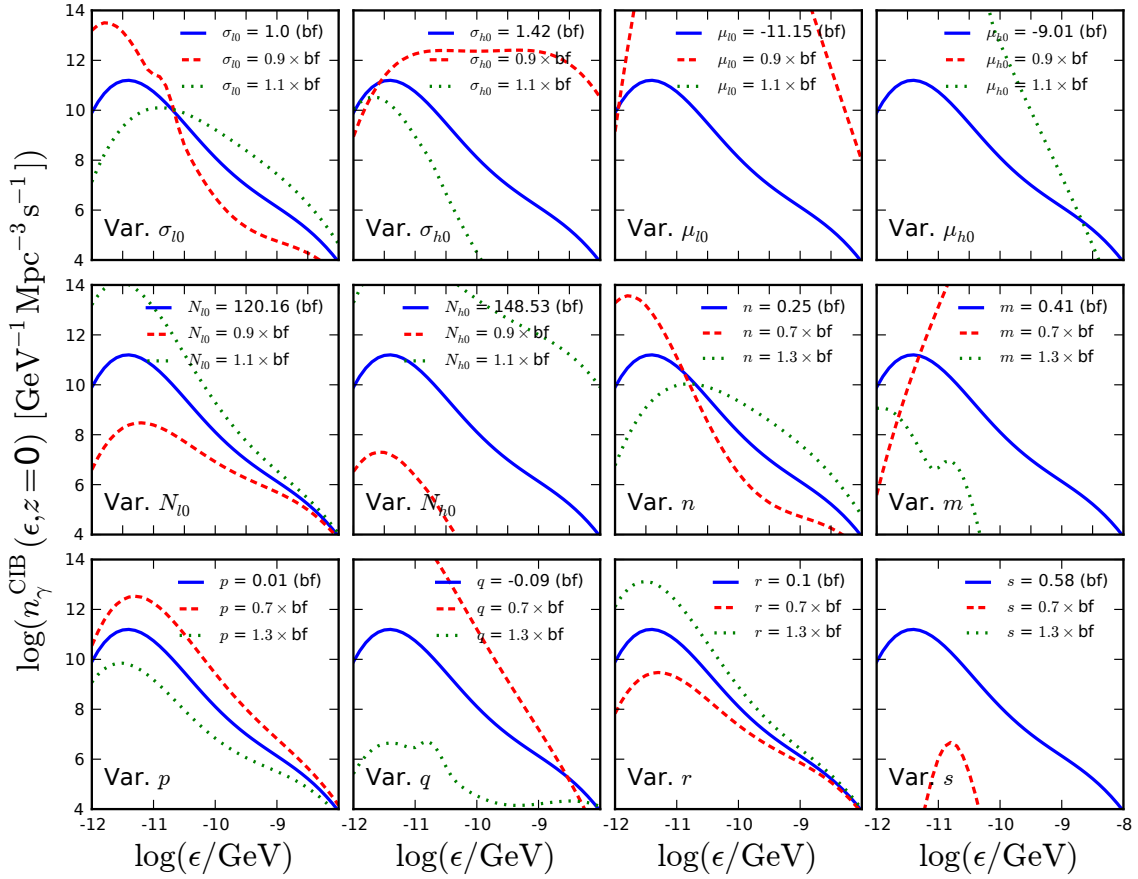


Figure 3.24: Effect on the CIB spectrum at $z = 0$ of varying one parameter of the two-Gaussian model at a time (bf = best-fit).

calculated spectrum at $z > 2$, where there are no more data points calculated within the model by Franceschini *et al.*. At $z = 0$, we have included the experimental points and error bars shown in Fig. 1 from Ref. [135]. Fig. 3.23 shows the underlying CIB injection function, where the evolution of the two Gaussians is clearer.

In order to understand how each parameter affects the CIB spectrum, we have varied them one at a time, while keeping the remaining ones at their best-fit values. Figs. 3.24 and 3.25 show the effect of such a parameter-by-parameter variation on the CIB spectrum and injection function at $z = 0$, respectively.

Fig. 3.26 compares three different treatments of the CIB spectrum based on the model by Franceschini *et al.* [135]:

- CIB spectrum tabulated from the tables in Ref. [135] (red dashed lines)
- CIB spectrum at $z = 0$ fixed to the Franceschini *et al.* model, and scaled to $z > 0$ following the approximation in Eq. (3.22). For this plot, we have assumed that the sources follow the star formation rate.

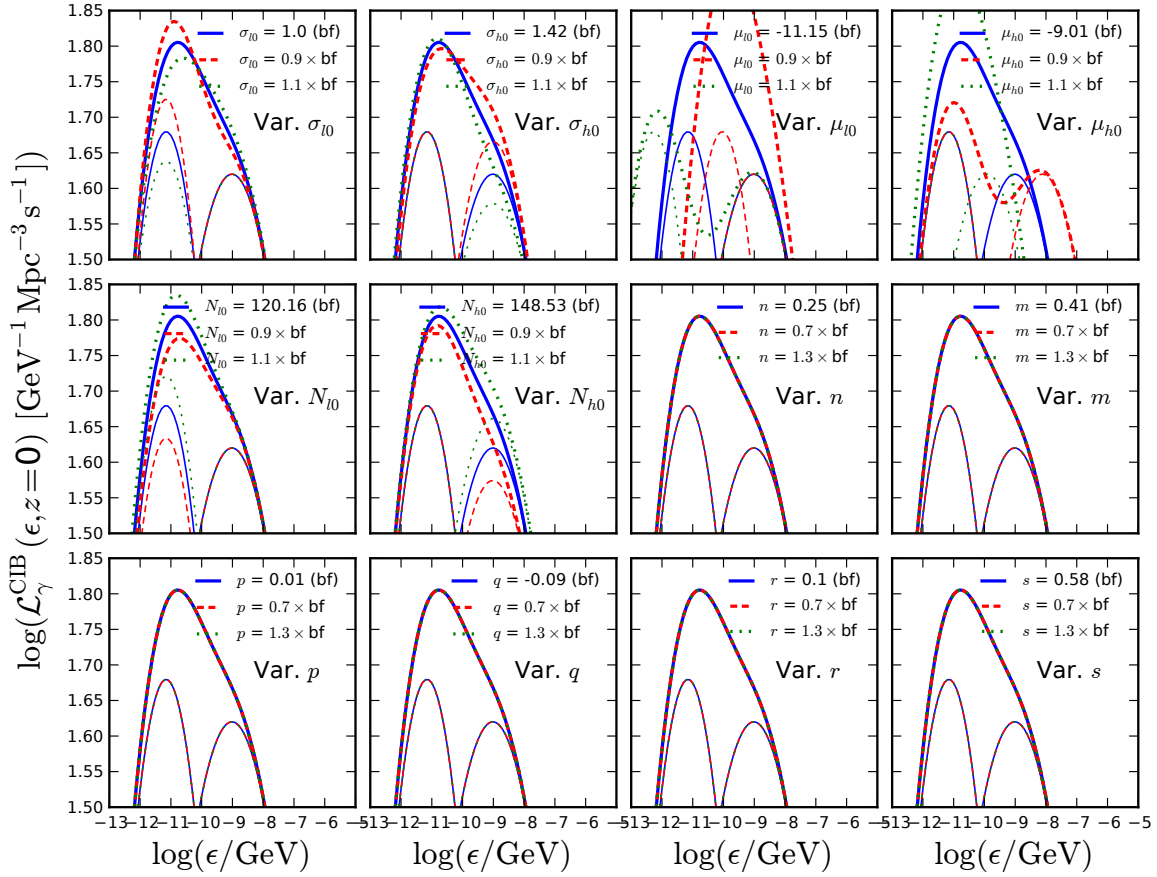


Figure 3.25: Effect on the CIB injection function at $z = 0$ of varying one parameter of the two-Gaussian model at a time (bf = best-fit).

- CIB spectrum calculated in the two-Gaussian model introduced in the present note (blue dotted lines)

One can see from Fig. 3.26 that the low-energy slope of the CIB spectrum calculated with the two-Gaussian model is much steeper than that of the redshift-scaled spectrum. However, this occurs at energies in which the CIB is already subdominant with respect to the CMB, and therefore it will not affect the cosmogenic neutrino flux. It is also evident that the high-energy peak of the CIB spectrum in the two-Gaussian model is not sufficiently pronounced (compared to the tabulated CIB), a problem that could be solved by improving the quality of the fit.

The left and right panels of Fig. 3.27 show, respectively, the cosmogenic neutrino flux, integrated up to $z_{\max} = 2$ and $z_{\max} = 6$, comparing the results obtained with the different parametrisations of the CIB that were used in Fig. 3.26. Note that, with the current best-fit values of the parameters, the two-Gaussian model yields a lower cosmogenic neutrino flux. This could presumably be solved, again, by improving the quality of the fit.

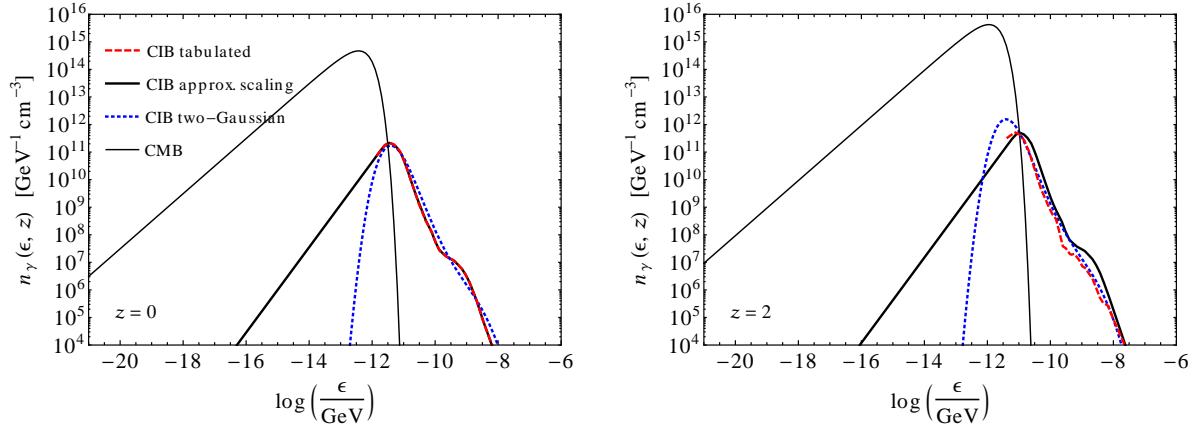


Figure 3.26: Comparison between different treatments of the CIB based on the model by Franceschini *et al.* [135], at $z = 0$ and $z = 2$. See text for details.

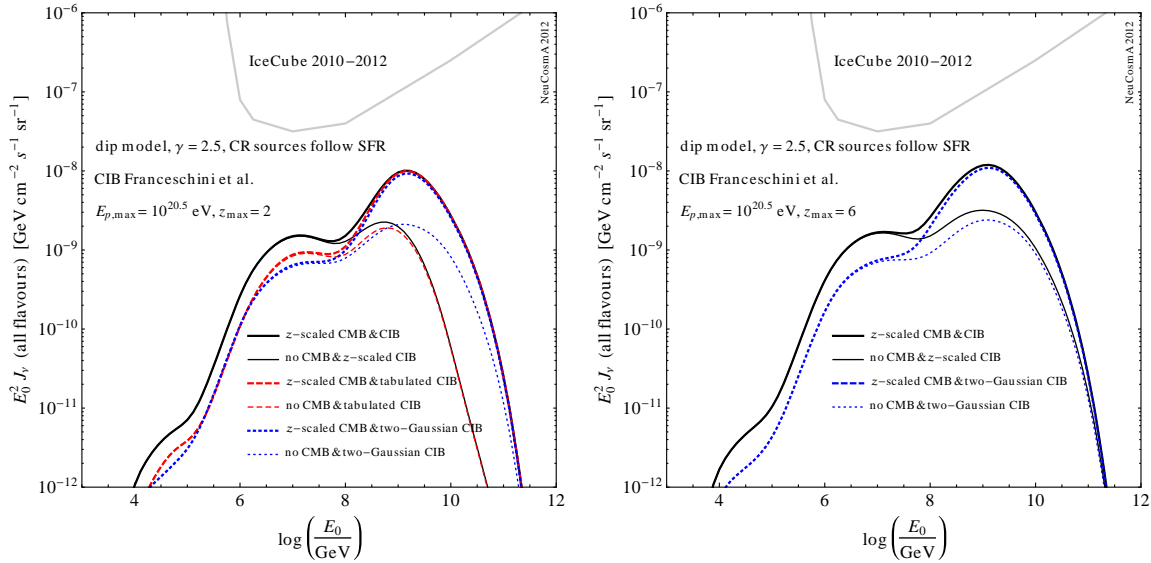


Figure 3.27: Cosmogenic neutrino+antineutrino flux at Earth (summed over all flavours) calculated assuming different treatments of the CIB. The flux receives contributions of neutrinos produced up to $z_{\max} = 2$ (left panel) or $z_{\max} = 6$ (right panel). The dip model with a proton-only composition for the UHECRs has been assumed, with proton spectral index of $\gamma = 2.5$. Cosmic ray sources (which may be AGNs, GRBs, etc.) are assumed to follow the same redshift evolution as the star formation rate.

Chapter 4

Constraining joint UHECR-neutrino production in GRBs

In this chapter we combine the two-component UHECR and neutrino source model from chapter 2 with the UHECR propagation scheme from chapter 3: by normalising the obtained UHECR proton flux to the current UHECR observations by the HiRes, Telescope Array, and Pierre Auger experiments, we obtain also a prediction for the prompt GRB neutrino flux and the cosmogenic neutrino flux at Earth. A comparison of the neutrino fluxes thus calculated against the upper bounds obtained by IceCube allows to strongly constrain the regions of parameter space in which GRBs could be the main source of both UHECRs and UHE neutrinos.

4.1 Introduction

Though several transition models have been proposed to explain the UHECR spectrum (see, *e.g.*, Refs. [150, 151, 152, 153] and Ref. [154] for a recent review), we will focus here on only two: the **ankle model**, which assumes the transition between a Galactic or extragalactic component below the ankle (~ 40 EeV) and an extragalactic component above it; and the **dip model**, which assumes that a single extragalactic component extends to lower energies (~ 1 EeV) and generates the pair-production dip seen in the UHECR spectrum via interactions with the CMB. For the ankle model, the required injection spectrum index is $\alpha_p \simeq 2.5$, whereas for the dip model a steeper spectrum is necessary, with $\alpha_p \simeq 2.5 - 2.7$. Such a steep spectrum can be taken as an *ad hoc* assumption, but can also be generated from a distribution of the maximal proton energies [155].

Proposed connections between the three UHE messengers –gamma-rays, UHECRs, and neutrinos– have led to diverse approaches to the prediction of the neutrino flux which have been explored in the literature, notably:

- estimating the neutrino flux from the measured local UHECR energy injection rate, by requiring that GRBs are also the sources of the UHECRs [89];
- normalising the neutrino flux of a source to its observed gamma-ray signal [2, 90, 91]; or
- assuming that UHECRs and neutrinos are produced in the same processes, usually when only neutrons are able to leave the source (“neutron model” in chapter 2) [86, 100].

Let us briefly describe the connections between pairs of messengers:

Gamma-ray–neutrino connection. Recently, the IceCube Collaboration published upper bounds on the flux of UHE neutrinos from a catalogue of observed GRBs using the 40-string configuration of the detector and assuming an analytical neutron model for the production of neutrinos, whose prediction exceeded the upper bound [3]. However, revised numerical predictions [4, 98, 5] (see also the earlier model in Ref. [94]) yield a neutrino flux that is one order of magnitude lower than the analytical prediction, thus relaxing the tension. The normalisation of the quasi-diffuse flux in these models is directly proportional to the baryonic loading, whose value is chosen somewhat arbitrarily to be 10, whereas the number of observable (long) bursts per year is chosen to be 667 in Refs. [91, 92].

Cosmic ray–neutrino connection. While the connection is very stringent in the neutron model [100] (*i.e.*, each UHECR observed should be accompanied by one neutrino of each flavour), the connection is more loose in our two-component model (see Ref. [106] and chapter 2), since at the highest energies protons are able to escape from the source without producing neutrinos. The neutron model, however, predicts neutrino fluxes that are substantially above the current bounds, which motivates a reassessment of either the baryonic loading or the pion production efficiency, which, as we will show, have been underestimated. In addition, the original computation [89] relies on the pion production efficiency, which implies that some of the corrections found in Refs. [4, 98] apply, and on the energy injected into cosmic rays, which has to be re-evaluated in view of more recent results from experiments such as HiRes [44], the Telescope Array [156] and the Pierre Auger Observatory [157, 51].

Gamma-ray–UHECR connection. This has been heavily debated (see, *e.g.*, Refs. [158, 159]) and depends on several *fudge factors*, which we will introduce later. Clearly, the neutrino and UHECR fluxes predicted from the gamma-ray observations will depend on common factors, such as the baryonic loading, which, as we will show, should include a bolometric correction [160, 158].

In order to clarify these issues, we have adopted a self-consistent approach that consists in normalising the predicted cosmic ray flux to the experimental observations, as a result of which one can derive a value for the baryonic loading that is in turn used to normalise the neutrino flux. We will see that such an approach does not only allow us to constrain the parameter space of common models –by comparison of the predicted neutrino fluxes to the IceCube bounds–, but also to obtain information on the cosmic energy budget as a spin-off.

4.2 Cosmic energy budget and observables for GRBs

In this section, we review the multi-messenger picture among gamma-rays, neutrinos, and cosmic rays in a model-independent, analytical way; the detailed derivations can be found in appendix B.

The gamma-ray energy output from GRBs can be characterised by a number of observables, namely, the isotropic equivalent energy $E_{\gamma,\text{iso}}$ per GRB; the number of observable GRBs per year \dot{N} , which, from observations is ~ 1000 bursts per year; and the redshift distribution of the GRBs¹. We use the redshift distribution by Kistler *et al.* [138], in which GRBs follow the star formation

¹For the sake of simplicity and technical feasibility, we do not consider a luminosity distribution here. As detailed in Ref. [138], it is possible to assume a threshold luminosity which is visible in the whole chosen redshift range. Hence, it is possible to calculate an average luminosity per burst which represents the distributed result well. Our results in this paper need to be interpreted as such appropriately averaged bursts. We have included this potential development as part of the outlook in chapter 8.

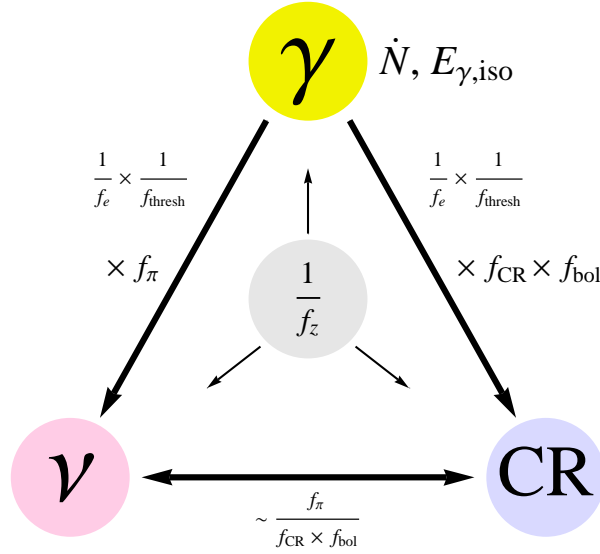


Figure 4.1: Result for the multi-messenger connection (illustration). Here “CR” refers to UHECRs in the energy range between 10^{10} GeV and 10^{12} GeV. The different labels refer to the number of observable GRBs per year (\dot{N}), the isotropic equivalent energy in gamma-rays ($E_{\gamma, \text{iso}}$), the cosmic evolution factor ($f_z > 1$), the baryonic loading ($f_e^{-1} \geq 10$), the instrument threshold correction ($f_{\text{thresh}} \simeq 0.2 - 0.5$), the fraction of baryonic energy going into cosmic ray production (f_{CR}), the fraction of baryonic energy going into pion production (f_{π}), and a bolometric correction factor ($f_{\text{bol}} \ll 1$). Figure taken from Ref. [161].

rate, Eq. (3.32), modified by an evolution factor $(1+z)^\alpha$ which, for $\alpha > 0$, implies an increase in the number of high-redshift ($z > 2$) sources.

A distinction must be made between the number of observable GRBs per year, \dot{N} , and the total number of bursts in the observable Universe per year, \dot{N}_{tot} . The latter includes bursts whose gamma-ray emission is too faint to be detected, but that nevertheless contribute to the neutrino flux. Therefore, to estimate the quasi-diffuse neutrino flux (as in, *e.g.*, Refs. [91, 92]), one must use \dot{N}_{tot} , not \dot{N} . Thus, we define a **threshold correction** factor

$$f_{\text{thresh}} \equiv \frac{\dot{N}}{\dot{N}_{\text{tot}}} \leq 1, \quad (4.1)$$

whose value will depend on detector characteristics. For a simulation following Refs. [138, 162], we have found $f_{\text{thresh}} \sim 0.3 - 0.5$; see appendix B. From a recent study that uses *Swift* data [163], we can estimate $f_{\text{thresh}} \simeq 1000/4568 \simeq 0.22$, which is close. Hence, we will use $f_{\text{thresh}} = 0.3$ in the following as a default value.

Another relevant quantity for the normalisation of the fluxes is the local GRB rate² [$\text{Gpc}^{-3} \text{yr}^{-1}$] [165, 166, 167, 168, 169, 170, 162, 163] $\dot{n}_{\text{GRB}}|_{z=0}$, defined as

$$\dot{n}_{\text{GRB}}|_{z=0} \simeq \frac{1}{\text{Gpc}^3 \text{yr}} \cdot \frac{\dot{N} [\text{yr}^{-1}]}{968} \cdot f_{\text{thresh}}^{-1} \cdot f_z^{-1}. \quad (4.2)$$

²Here we use the local GRB rate $\dot{n}_{\text{GRB}}|_{z=0}$ related to observations, while the actual GRB rate \dot{n}_{GRB} is higher due to correcting for the beaming factor of the GRBs; $\dot{n}_{\text{GRB}} \equiv \dot{n}_{\text{GRB}} / \langle f_{\text{beam}} \rangle$. See appendix B for a more detailed discussion.

SFR model	α	f_z	$\dot{n}_{\text{GRB}} _{z=0}$ [Gpc ⁻³ yr ⁻¹]	$E_{\text{CR}}^{[10^{10},10^{12}]}$ [10 ⁵³ erg]	References
Hopkins & Beacom (2006)	1.2	25.15	0.13	11.0	[139, 138]
	0.0	5.65	0.58	2.5	[139]
Wanderman & Piran (2010)	0.0	7.70	0.43	3.4	[162]
Madau & Porciani (2000)					[164]
SF1	0.0	9.89	0.35	4.3	
SF2	0.0	14.42	0.23	6.3	
SF3	0.0	14.36	0.23	6.2	

Table 4.1: Cosmic evolution factor f_z , local GRB rate (without beaming correction), and required energy per GRB in UHECRs for different SFR histories and source evolution factors α (the star formation rate is corrected by a factor of $(1+z)^\alpha$). The results for f_z are obtained using Eq. (B.8), with the integration running from $z=0$ to $z=6$. The local GRB rate is obtained from Eq. (4.2) and the cosmic ray energy per bursts in the range 10^{10} to 10^{12} GeV is obtained from Eq. (4.3), both by assuming $\dot{N} = 1000 \text{ yr}^{-1}$ and $f_{\text{thresh}} = 0.3$. Table taken from Ref. [161].

A **cosmic evolution factor** f_z connects the local ($z=0$) quantity, $\dot{n}_{\text{GRB}}|_{z=0}$, to \dot{N} , which accounts for the whole GRB sample and implicitly incorporates the redshift evolution³. In other words, the cosmic evolution factor describes how representative the local GRB rate is for the whole sample: the stronger the evolution of the GRB rate in redshift (larger α) is, the larger the values of this correction factor. Table 4.1 shows typical values of f_z , which range from 5 to 25, for different SFR models and values of the evolution factor α , as well as the corresponding values of $\dot{n}_{\text{GRB}}|_{z=0}$, obtained by assuming $\dot{N} = 1000 \text{ yr}^{-1}$ and $f_{\text{thresh}} = 0.3$. From the table, it is evident that stronger source redshift evolution implies smaller local GRB rates.

If GRBs are to be the sources of UHECRs, we can estimate the required energy output per GRB by deriving the local energy injection rate in the range 10^{10} – 10^{12} GeV that is required to reproduce the observations. The calculation by Waxman [171], based on the UHECR data available at that time, which were sparse above $8 \cdot 10^{10}$ eV (see Ref. [172] for an update using Auger data), yielded $\dot{\epsilon}_{\text{CR}}^{[10^{10},10^{12}]} = 4.5 \cdot 10^{44} \text{ erg Mpc}^{-3} \text{ yr}^{-1}$, with little sensitivity to variations of the spectral injection index in the range $1.8 < \alpha_p < 2.8$. Using the data from several experiments recently compiled by Gaisser, Stanev, and Tilav [54], we obtain $1.5 \cdot 10^{44} \text{ erg Mpc}^{-3} \text{ yr}^{-1}$, which is compatible with the original result. The required energy per GRB is then (see appendix B)

$$E_{\text{CR}}^{[10^{10},10^{12}]} = 10^{53} \text{ erg} \cdot \frac{\dot{\epsilon}_{\text{CR}}^{[10^{10},10^{12}]}}{10^{44} \text{ erg Mpc}^{-3} \text{ yr}^{-1}} \cdot \frac{968 \text{ yr}^{-1}}{\dot{N}} \cdot f_{\text{thresh}} \cdot f_z. \quad (4.3)$$

Table 4.1 includes the required energies per GRB to reach $\dot{\epsilon}_{\text{CR}}^{[10^{10},10^{12}]} = 1.5 \cdot 10^{44} \text{ erg Mpc}^{-3} \text{ yr}^{-1}$, which lie in the range $10^{53} - 10^{54}$ erg. Strong source evolution requires larger injected energy per burst, on account of the few local bursts.

A key point regarding the **baryonic loading** f_e^{-1} is that it relates the total energy in protons *in the entire energy range* to the kinetic energy in electrons, which we assume to be in equipartition with the energy in gamma-rays. While we maintain this definition of f_e^{-1} in our treatment, we stress that, for the connection between gamma-ray and UHECR observations, only the CR energy range between 10^{10} and 10^{12} GeV is relevant. Therefore, the baryonic loading is modified by a

³Note that our definition of f_z in Eq. (B.9) of appendix B is different from ξ_z in Waxman and Bahcall [113], and includes the description of the Λ CDM cosmology.

bolometric correction factor $f_{\text{bol}} < 1$ defined as the ratio of energy in protons between 10^{10} and 10^{12} GeV to the energy in the total energy range considered; see the definition, Eq. (B.16), in appendix B. For a power-law injection spectrum without cutoff and the full proton energy range⁴, we find f_{bol} between about 0.2 (for $\alpha_p = 2.0$) and $1.6 \cdot 10^{-4}$ (for $\alpha_p = 2.5$). Larger values are obtained for larger minimal proton energies, and somewhat smaller values for a (model-dependent) maximal proton energy significantly below 10^{12} GeV.

An alternative way to estimate the required energy per burst in the UHECR range is through the connection to the energy output by the burst as gamma-rays, *i.e.*,

$$E_{\text{CR}}^{[10^{10}, 10^{12}]} = f_{\text{CR}} \frac{f_{\text{bol}}}{f_e} E_{\gamma, \text{iso}}, \quad (4.4)$$

where f_{CR} is the **fraction of baryonic energy going into cosmic ray production**, analogous to the fraction f_{π} of **baryonic energy going into pion production** (pion production efficiency) as defined in Refs. [89, 2]. Note that f_{π} is the *total* energy that goes into neutral plus charged pions, and not the average energy lost to pions in a single interaction. The value of f_{π} depends on what is the cosmic ray emission mechanism: if they escape as neutrons, then typically $f_{\text{CR}} \simeq 2 \cdot f_{\pi} \simeq 0.4$ and $f_{\pi} \sim 0.2$, since neutrons on average receive four times as much energy as the pions while twice the number of pions than of neutrons is produced in $p\gamma$ interactions; whereas if they mainly leak out as protons, then typically $f_{\pi} \ll 1$ and $f_{\text{CR}} \gg f_{\pi}$.

Assuming $E_{\gamma, \text{iso}} \simeq 10^{53}$ erg, Hopkins & Beacom SFR without source evolution (conservative case, $\alpha = 0$), and $f_{\text{thresh}} = 0.3$, we can see from Eq. (4.3) that in order to match the required energy injection per GRB that a value of $f_{\text{CR}} \cdot f_{\text{bol}} \cdot f_e^{-1} \simeq 2.5$ is required. If neutron escape dominates ($f_{\text{CR}} \simeq 0.4$), the baryonic loading obtained is $f_e^{-1} \simeq 30$ for a proton spectral index of $\alpha_p = 2.0$ (where $f_{\text{bol}} \simeq 0.2$), and even larger values for f_e^{-1} if a source evolution is included. Here the difference between the usual baryonic loading f_e^{-1} and the UHE baryonic loading $f_{\text{bol}} f_e^{-1}$ which enters in Eq. (4.4) becomes relevant [160, 158]: it is not sufficient to have a large enough baryonic loading in total, one needs a large enough baryonic loading at the UHE. Therefore, if the baryonic loading is (implicitly) defined for the whole energy range (see Eq. (B.15)), as in most neutrino calculations, it has to be significantly larger than 10 to describe the UHECR observations. This is also the reason why the predicted neutrino fluxes in Ref. [100] are relatively high: the implied baryonic loading \times pion production efficiency, which is not explicitly considered therein, is very high.

Fig. 4.1 shows that f_z is an overall scaling factor, needed to infer the local GRB rate from the observed \dot{N} . Moreover, if gamma-ray observations are used as the basis to predict the UHECR and neutrino injection, then the baryonic loading and the threshold correction affect UHECRs and neutrinos in the same way, whereas if the UHECR flux is instead used to normalise the neutrino flux [100], these factors drop out from the calculation. Furthermore, it is clear that some of the scaling factors are dependent on the model and its input parameters (f_{π} , f_{CR} , $E_{\gamma, \text{iso}}$, f_{bol}), whereas the remaining relevant parameter combination scaling the neutrino and cosmic ray fluxes is $\dot{N} \cdot f_e^{-1} \cdot f_{\text{thresh}}^{-1}$. Assuming the value $\dot{N} \simeq 1000 \text{ yr}^{-1}$ from observations and $f_{\text{thresh}} \simeq 0.3$, the UHECR observations can be directly used to deduce the baryonic loading. In the following, we will fix these values and measure f_e^{-1} for the sake of simplicity and readability. However, note that f_e^{-1} is to be interpreted as the product of these quantities in the following, *i.e.*, a higher instrument threshold correction or a larger number of observed bursts per year will reduce the

⁴Technically, the full energy range is defined in the SRF in our calculations, the comparison of the energies, however, needs to be done in the source frame. Hence, the limits need to be boosted to the source frame for the actual calculation, leading to a range from $\Gamma \cdot 1 \text{ GeV}$ (from the proton rest mass) to $\Gamma \cdot 10^{10} \text{ GeV}$.

required baryonic loading. The actual baryonic loading can be derived then from the values of f_e^{-1} given in our figures as

$$f_{e,\text{actual}}^{-1} = \frac{1000 \text{ yr}^{-1}}{\dot{N}} \cdot \frac{f_{\text{thresh}}}{0.3} \cdot f_e^{-1} \quad (4.5)$$

for different choices of \dot{N} or f_{thresh} . The baryonic loading in the UHE range can be obtained as $f_{\text{bol}} f_e^{-1}$, where f_{bol} depends on the spectral proton index and on the minimal and maximal proton energies.

4.3 Combined production and propagation model

Our GRB two-component UHECR emission model has been introduced in chapter 2; the photohadronic interactions, and the production of neutrinos, make use of NeuCosmA [99]. For the cosmic ray propagation, we use the deterministic Boltzmann equation solver presented in detail in chapter 3. For the mixing parameters we have used the best-fit values from the global analysis in Ref. [105], under the assumption of a normal mass hierarchy: $\sin^2 \theta_{12} = 3.07 \cdot 10^{-1}$, $\sin^2 \theta_{13} = 2.41 \cdot 10^{-2}$, $\sin^2 \theta_{23} = 3.86 \cdot 10^{-1}$, and $\delta_{\text{CP}} = 1.08 \cdot \pi$.

For the sake of simplicity, we assume that all sources are alike in the cosmologically comoving frame, *i.e.*, the source frame. By this choice, we imply that the cosmic ray injection factorises into a redshift- and an energy-dependent part. If, for instance, the observables were fixed in the observer’s frame, the maximal proton energy would depend on redshift and subtle spectral features would appear: for a fixed luminosity, high-redshift bursts would have a lower variability timescale (in the source frame) due to the redshift correction, and, consequently, the particle densities would be higher, photohadronic interactions would become more frequent, and this would introduce an artificial pull on the maximal proton energy. If, on the other hand, a luminosity distribution function were used, only few bursts would contribute to the maximal proton energies, which again would introduce spectral features and subtleties in the interpretation. For the “standard” GRB parameters, we use, unless noted otherwise, $\alpha_\gamma = 1$, $\beta_\gamma = 2$, $\epsilon'_\gamma = 1 \text{ keV}$ (in the SRF), $\Gamma = 300$, $T_{90} = 10 \text{ s}$, $t_v = 10^{-2} \text{ s}$, and a luminosity $L_{\text{iso}} = 10^{52} \text{ erg s}^{-1}$. These parameters are given in the source frame in order to guarantee similar properties in that frame, which means that $L_{\text{iso}} \simeq E_{\gamma,\text{iso}}/T_{90}$. We use an acceleration efficiency $\eta = 1.0$, unless noted otherwise. The normalisation of the photon spectrum and the calculation of the maximum proton energy follows the procedure outlined in section 1.4, but in contrast here we keep the baryonic loading as a free parameter and only fix it later by fitting the UHECR observations.

The cosmic ray injection function is given by Eq. (B.17) in appendix B (for details, see Eq. (B.12)), built up from the individual source spectrum. The sources are assumed to be distributed following the chosen SFR, corrected by an evolution factor $(1+z)^\alpha$, down to very small redshifts. In order to test the statistical significance of a model, we fit our UHECR flux prediction to the Telescope Array data [156] (see appendix C for details). For a comparison to data from the Pierre Auger and HiRes experiments, see appendix E of Ref. [161]. The best-fit normalisation and energy calibration translate into the baryonic loading f_e^{-1} of the model – assuming that $\dot{N} \simeq 1000 \text{ yr}^{-1}$ and $f_{\text{thresh}} \simeq 0.3$, as discussed in section 4.2.

4.3.1 Ankle model for cosmic ray transition

We focus first on the ankle model; to describe the extragalactic component we restrict our analysis to the range from 10^{10} to 10^{12} GeV , which coincides with the analytical considerations in

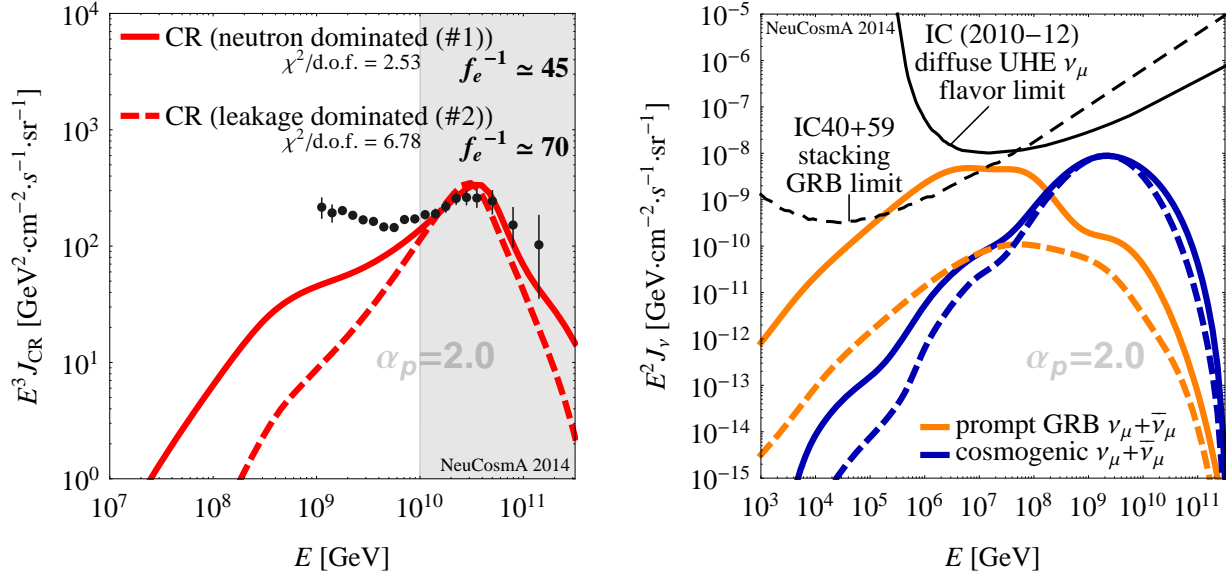


Figure 4.2: Best-fit cosmic ray (left panel) and neutrino (right panel) fluxes as a function of energy for $\alpha_p = 2$, the Hopkins & Beacom star formation rate [139], and no cosmic evolution correction ($\alpha = 0$). In the left panel, the observed UHECR data from the Telescope Array [156] is depicted as black circles together with our cosmic ray flux predictions (red curves). Additionally, the fit range is gray-shaded, and the $\chi^2/\text{d.o.f.}$ and obtained f_e^{-1} are given. In the right panel, the prompt (PeV) and cosmogenic (EeV) muon neutrino fluxes are given, together with the current bounds (see appendix C). The solid curves (neutron dominated (#1)) correspond to our standard burst parameters with $\Gamma = 300$ (see main text) and the neutron model; the dashed curves (leakage dominated (#2)) use a higher $\Gamma = 800$, leading to direct proton escape dominating at the highest energies. Figure taken from Ref. [161].

section 4.2. Fig. 4.2 shows the fits to TA data for two extreme UHECR models: one dominated by neutron escape (#1) and another one dominated by direct proton escape (#2), in both cases assuming a proton injection spectrum with $\alpha_p = 2$, the Hopkins & Beacom star formation rate, and no cosmic evolution correction ($\alpha = 0$). The fitted UHECR fluxes are shown in the left panel, while the GRB prompt and cosmogenic neutrino fluxes are shown in the right panel. The fit to the UHECR data yields baryonic loading values between 45 and 70, consistent with our analytical estimates from the previous section. The normalisation of the neutrino fluxes follows from that of the UHECRs. Clearly, the cosmogenic neutrino flux is barely affected by the choice of model; this is because only the total number of protons emitted from the source, regardless of the emission mechanism, is important for cosmogenic neutrinos. In contrast, the prompt neutrino prediction strongly depends on the UHECR escape mechanism: while the neutron model (#1) is basically ruled out, in consistency with Ref. [100], the direct escape model (#2) flux is significantly below the current bounds (with a poorer $\chi^2/\text{d.o.f.}$, though).

In Fig. 4.3 we show the single-collision source spectra for the two models (sans propagation effects), with the different components (initial injection, cosmic rays from neutrons, cosmic rays from direct proton escape, and neutrinos) presented separately. The two emission models are obtained from our underlying two-component emission model (see Ref. [106] and chapter 2) for two different choices of parameter set values: the model reduces to the conventional neutron escape model

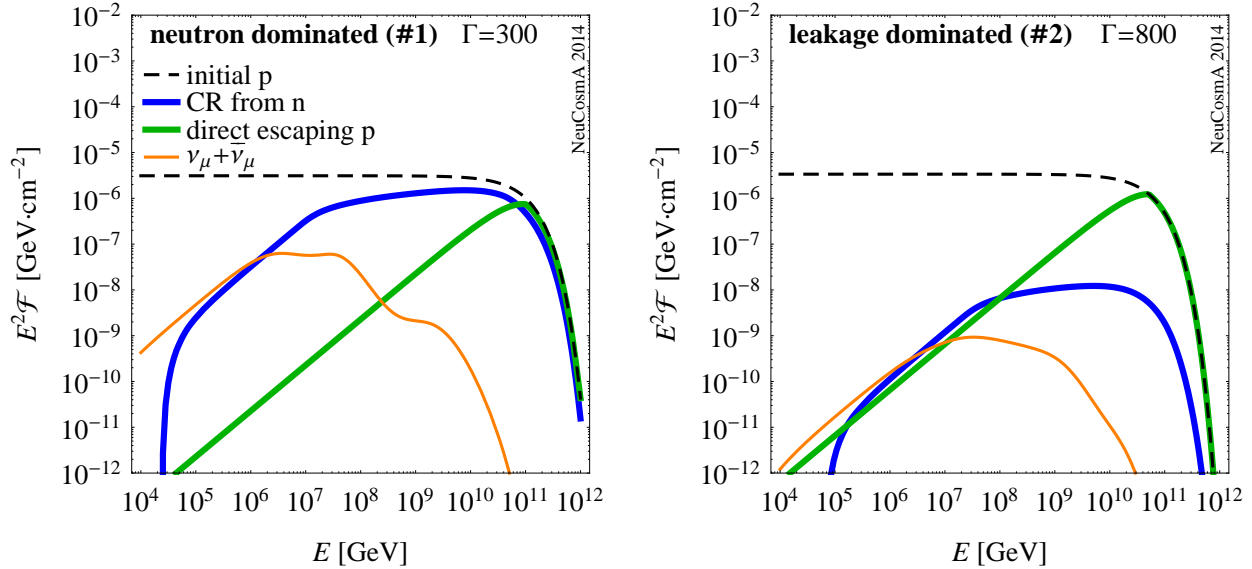


Figure 4.3: Expected spectra from a single collision for our standard GRB parameters and $\Gamma = 300$ (left panel) and $\Gamma = 800$ (right panel), respectively ($z = 2$). The spectra are shown in the observer’s frame, including only adiabatic losses due to the cosmic expansion, as in Ref. [106]. Depicted are the input proton spectrum (in case all protons would just escape; thin dashed curve), the CR from neutron escape (thick blue/black curve), the contribution of directly escaping protons to the CR flux (thick green/gray curve), and the muon neutrino flux (after flavor mixing; thin orange/light gray curve). Figure taken from Ref. [161].

for high enough pion production efficiencies (left panel), whereas the direct escape component dominates if the pion production efficiency is low (right panel), *i.e.*, different models are obtained for different sets of parameters.⁵ The direct escape component is harder than the neutron escape component, which is why the corresponding UHECR flux in Fig. 4.2, left panel, dashed curve, becomes harder as well. Therefore, while larger α_p can produce a better fit of the shape (the $\chi^2/\text{d.o.f.}$ is significantly smaller), they do so at the expense of a larger f_e^{-1} (see Eq. (4.4), where f_{bol} is smaller then). Furthermore, a diffusive escape component could look closer to the neutron model, especially if Kolmogorov-like diffusion is assumed. Thus, we anticipate that both options are, in principle, possible.

If the strong evolution case ($\alpha = 1.2$) with more high-redshift bursts is used instead, the UHECR fit is equally good, with somewhat larger predicted cosmogenic neutrino fluxes and a more clearly excluded prompt neutrino flux in the neutron model (#1). However, the required baryonic loading is larger, around 200, due to the larger value of f_z ; see, *e.g.*, Eq. (B.18). Hence, SFR turns out to be the most conservative assumption to obtain the baryonic loading, *i.e.*, it will yield the lowest values of f_e^{-1} .

⁵Note that the neutron component is slightly harder than the input proton spectrum as a result of the high-energy (multi- π) processes.

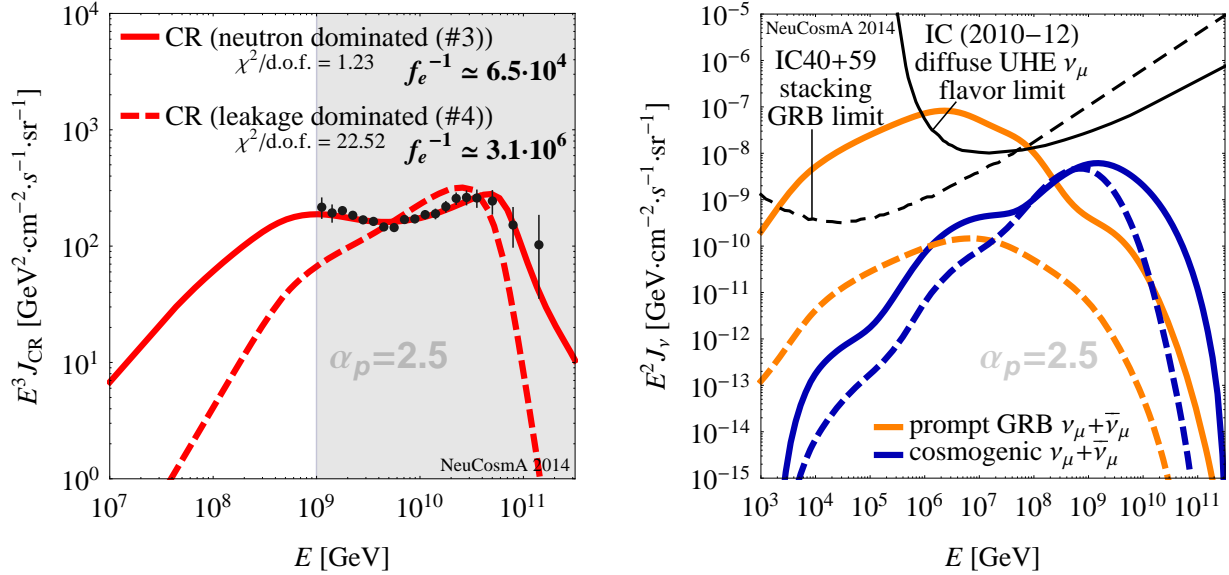


Figure 4.4: Best-fit cosmic ray (left panel) and neutrino (right panel) fluxes as a function of energy for $\alpha_p = 2.5$, the Hopkins & Beacom star formation rate [139], and no cosmic evolution correction ($\alpha = 0$). In the left panel, the observed UHECR data from the Telescope Array [156] is depicted as black circles together with our cosmic ray flux predictions (red curves). Additionally, the fit range is gray-shaded, and the $\chi^2/\text{d.o.f.}$ and obtained f_e^{-1} are given. In the right panel, the prompt (PeV) and cosmogenic (EeV) muon neutrino fluxes are given, together with the current bounds (see appendix C). The solid curves (neutron dominated (#3)) correspond to our standard burst parameters with $\Gamma = 300$ (see main text) and the neutron model; the dashed curves (leakage dominated (#4)) use a higher $\Gamma = 600$ and lower $L_{\text{iso}} = 10^{50.5} \text{ erg s}^{-1}$, leading to direct proton escape dominating at the highest energies. Figure taken from Ref. [161].

4.3.2 Dip model for cosmic ray transition

To study the dip model, we use a larger energy range in our fits, between 10^9 and 10^{12} GeV, which covers the pair-production dip, but still lies above the energy at which diffusion effects on the intergalactic magnetic fields might affect the spectral shape [173, 55, 174].

Fig. 4.4 focuses again on two extreme models: a neutron-escape dominated case (#3) and a direct escape-dominated case (#4), both generated with $\alpha_p = 2.5$. Fig. 4.5 shows the corresponding single-collision spectra, to be compared to Fig. 4.3. Contrasting the neutrino results with the ankle model, the difference between the two emission cases is more marked, with the neutron model clearly excluded and the direct escape model located significantly below the current bounds (right panel of Fig. 4.4). To understand this behaviour, consider the peak of the prompt neutrino spectrum at, say, 10 PeV; these neutrinos were created by protons with energies a factor of 20 higher, *i.e.*, 200 PeV. At this energy, as seen in the left panels of Figs. 4.2 and 4.4, the dip model fits the UHECR data more closely than the ankle model, which implies that the cosmic ray flux is higher for the dip model than for the ankle model, and so, as a result, the same occurs for the prompt neutrino flux, which overshoots the upper bound. In the direct escape case this can be avoided, since protons manage to escape without producing neutrinos; however, the spectral fit is

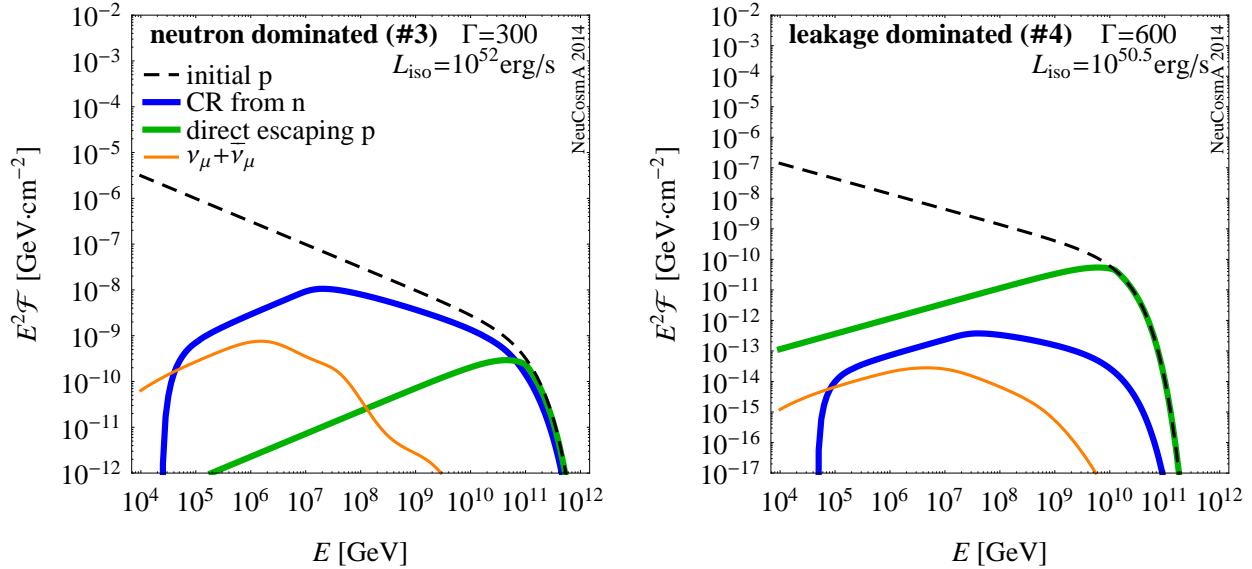


Figure 4.5: Expected spectra from a single collision for our standard GRB parameters and $\Gamma = 300$, $L_{\text{iso}} = 10^{52} \text{ erg s}^{-1}$ (left panel) and $\Gamma = 600$, $L_{\text{iso}} = 10^{50.5} \text{ erg s}^{-1}$ (right panel), respectively ($\alpha_p = 2.5$, $z = 2$). The spectra are shown in the observer’s frame, including only adiabatic losses due to the cosmic expansion, as in Ref. [106]. Depicted are the input proton spectrum (in case all protons would just escape; thin dashed curve), the CR from neutron escape (thick blue/black curve), the contribution of directly escaping protons to the CR flux (thick green/gray curve), and the muon neutrino flux (after flavor mixing; thin orange/light gray curve). Figure taken from Ref. [161].

not as good as for the neutron escape case due to the harder spectrum⁶.

The required baryonic loadings in the dip model are of the order of $f_e^{-1} \simeq 10^5$, several orders of magnitude larger than for the ankle model. The difference comes from the bolometric correction factor f_{bol} , which is smaller the steeper the spectrum is. Of course, f_{bol} depends on the minimal proton energy as well, especially for $\alpha_p > 2$, but it is nevertheless clear that the conventional assumptions for the baryonic loading of GRBs are challenged in that model. Note that the UHECR baryonic loading $f_{\text{bol}} f_e^{-1} \sim 10$, as for the ankle model.

Though here we do not explore in detail potential mechanisms to generate the spectral injection indices $\alpha_p \simeq 2.5 - 2.7$, required for the dip model from the normally anticipated injection indices for Fermi shock acceleration $\alpha_p \simeq 2.0 - 2.2$, it is interesting to mention two possibilities. First, the turbulences in Fermi shock acceleration, which reduce the effectiveness of the acceleration and changes the expected spectral index to $\alpha_p \geq 2.3$ [175]. Second, it has been proposed for AGNs to use a distribution function on the maximal proton energy in combination with an injection index $\alpha_p \simeq 2$ to generate this steep spectrum [155]; a similar distribution could be induced for GRBs through an appropriate luminosity function.

Based on these observations, we conclude that the combined production-propagation GRB internal

⁶One could change the spectral index to improve the fit here, but at the expense of the baryonic loading. Changing the spectral index from $\alpha_p = 2.5$ to $\alpha_p = 2.7$ decreases the bolometric correction f_{bol} by a factor of 30, which leads to an increase of the needed baryonic loading f_e^{-1} by the same factor.

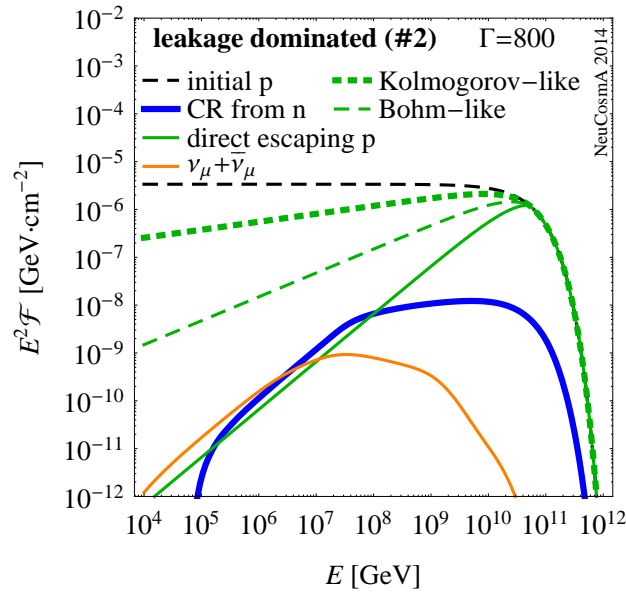


Figure 4.6: Different assumptions for additional escape components (in a single collision), together with neutrino and neutron escape spectra. Figure corresponds to the example in the right panel of Fig. 4.3. Figure taken from Ref. [161].

shock model is challenged in the context of the dip cosmic ray transition model, because a) very high baryonic loadings are required, and b) the prompt neutrino flux easily overshoots the neutrino flux bound in the neutron model case. We therefore focus on the ankle model in the following.

4.4 Statistical analysis of the cosmic ray ankle model

We saw in the previous section that the ankle model is capable of explaining the UHECR observations while keeping in agreement with the current UHE neutrino upper bounds. Hence, we will now focus on the ankle model only and find in what parts of the parameter space this statement holds, and how it is affected by the escape model.

4.4.1 Impact of cosmic ray escape model

Using our two-component escape model, we consider three different possible escape regimes, illustrated for one set of parameters in the single-collision spectra in Fig. 4.6 (see Ref. [106] and chapter 2 for details):

Neutron model. The cosmic rays escape as neutrons and the protons are magnetically confined. This is the assumption frequently used in the literature. In Fig. 4.6, it corresponds to the thick dark/blue curve.

Direct escape. All protons from the edges of the shells will escape over a width of R'_L .

Diffusive escape. A less conservative estimate for the escape of the protons is that a fraction $\lambda'/\Delta d'$ can escape, where $\lambda' = \sqrt{D' t'_{\text{dyn}}}$ is the diffusion length over the dynamical timescale

t'_{dyn} , and D' is the (spatial) diffusion coefficient. For Bohm diffusion, $D' \propto R'_L \propto E'$; for Kolmogorov diffusion, $D' \propto (E')^{1/3}$; and the fraction of escaping particles is proportional to the square root of that. Note that, since diffusion length and shell width scale differently, the treatment here is only a rough approximation. For details, see appendix A of Ref. [106].

We have performed a scan of the parameter space: at each point in parameter space, we have assessed whether or not the UHECR observations and the neutrino upper bounds are satisfied. Our main results are presented as scans in the $L_{\text{iso}} - \Gamma$ plane in Fig. 4.7, together with Fig. 4.8, which shows cosmic ray, prompt neutrino, and cosmogenic neutrino spectra for selected points from Fig. 4.7. The different rows in Fig. 4.7 correspond to the three different assumptions for the UHECR escape discussed above; the different columns, to two different acceleration efficiencies ($\eta = 1.0$ on the left, $\eta = 0.1$ on the right). The different emission regimes (optically thick/thin to neutron escape, direct escape) that we identified in the parameter scans of chapter 2 (Fig. 2.4, central column) appear here in Fig. 4.7. Notably, the red dashed line in Fig. 4.7 separates the region dominated by neutron escape (below) from the one dominated by direct proton escape (above). The different rows in Fig. 4.8 correspond to different panels in Fig. 4.7, as indicated.

The methodology that we have used to scan the parameter space is the following: at each point in parameter space, we compute the neutrino and cosmic rays coming from a population of GRBs distributed in redshift, all of them alike in the cosmologically comoving frame. The parameter values at each parameter space point will determine what is the dominant emission mechanism. Cosmic rays are propagated from the sources down to the local Universe using the method presented in chapter 3, which takes into account energy losses due to interactions with the cosmological photon backgrounds and the production of cosmogenic neutrinos. The predicted local UHECR flux obtained in such a manner is then fitted to Telescope Array surface detector data [156] between 10^{10} and 10^{12} GeV, using a χ^2 function (see appendix C). This determines its normalisation and also the energy recalibration necessary to fit the data, within the systematic uncertainty of the experiment.

In Fig. 4.7, the best-fit point in each panel is shown as a diamond, with the best-fit parameters given in the upper left corners. The filled coloured regions represent the 90% (red), 95% (yellow), and 99% C.L. (blue) regions around the best fit. The baryonic loading can be deduced from the normalisation, and we show the values of $\log_{10} f_e^{-1}$ as (black) contour lines in Fig. 4.7. The normalisation of the UHECR also fixes that of the neutrinos; thus, we are able to compare the neutrino flux predictions to the current upper bounds from IceCube. Fig. 4.7 shows the excluded regions where the prompt neutrinos exceed the GRB stacking bound [92] as filled gray areas: light gray for the currently available data and dark gray for 15 yr of full detector exposure. Similarly, the excluded region due to 15 yr of cosmogenic neutrino data⁷ exceeding the IceCube cosmogenic upper bound is shown as green filled areas (the current exposure is too small for cosmogenic neutrinos to be presently capable of excluding any part of the parameter space shown). Note that the GRB source model determines the pion production efficiency and the shapes of the prompt neutrino and ejected cosmic ray spectra, while the cosmic ray propagation model determines the shape of the cosmogenic neutrino spectrum and observed cosmic ray spectrum.

Fig. 4.7, top row, demonstrates that the neutron model provides an excellent fit to UHECR data, for reasonable parameter values, if only cosmic rays –and not also neutrinos– are considered. For instance, the best fit for $\eta = 1$ (left panel) is at $\Gamma \approx 302$ and $L_{\text{iso}} \approx 10^{53} \text{ erg s}^{-1}$, and corresponds to $f_e^{-1} \approx 10$, while the best fit for $\eta = 0.1$ (right panel) is at a higher Γ , as a consequence of the less effective particle acceleration, which is also responsible for the slight worsening of the quality

⁷Calculating using the effective area from Ref. [7]; see appendix C.

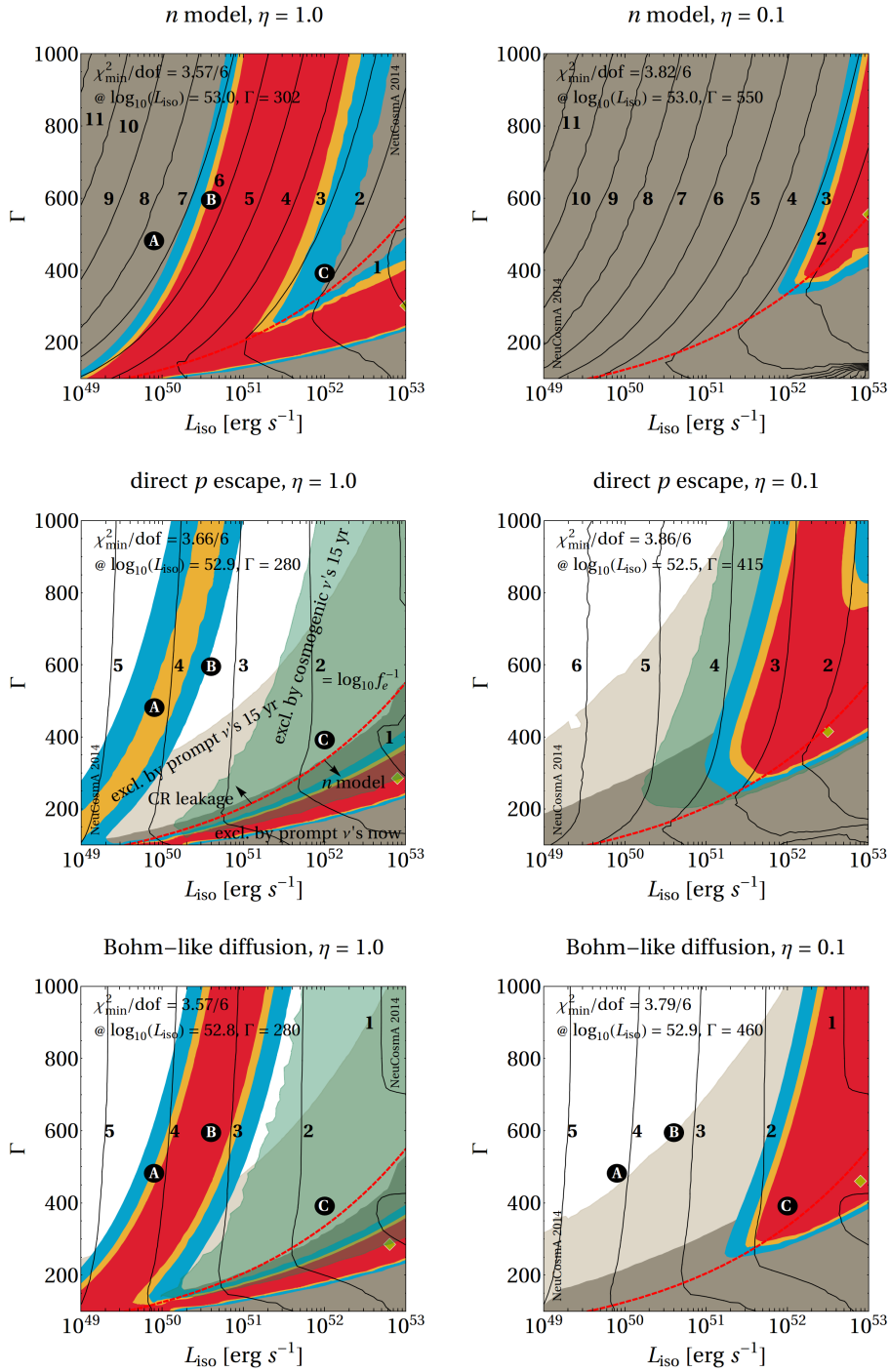


Figure 4.7: Filled contours: allowed regions (red/darkest gray: 90% C.L., yellow/light gray: 95% C.L., blue/darker gray: 99% C.L.) as a function of L_{iso} and Γ for the fit to cosmic ray data from the Telescope Array [156], in the energy range $10^{10} - 10^{12}$ GeV. In the left (right) column, $\eta = 1.0(0.1)$. Rows correspond to different UHECR escape models: neutron escape (top), direct proton escape (middle), and Bohm-diffusive escape (bottom). The red-dashed curve separates the “direct escape dominated” region (above curve) and the “neutron model” region. The dark and light gray shading, respectively, mark the IceCube-excluded region from the GRB analysis using the current and expected exclusion after 15 years; and the green shading, the expected exclusion from the cosmogenic neutrino analysis after 15 years (in the top left panel, contained within the prompt neutrino exclusion). The iso-baryonic loading contours (numbers are $\log_{10} f_e^{-1}$) are shown also. Here $\alpha_p = 2.0$, $t_v = 0.01$ s (in the source frame), and SFR evolution of the sources by Hopkins & Beacom ($\alpha = 0$) have been chosen. Figure taken from Ref. [161].

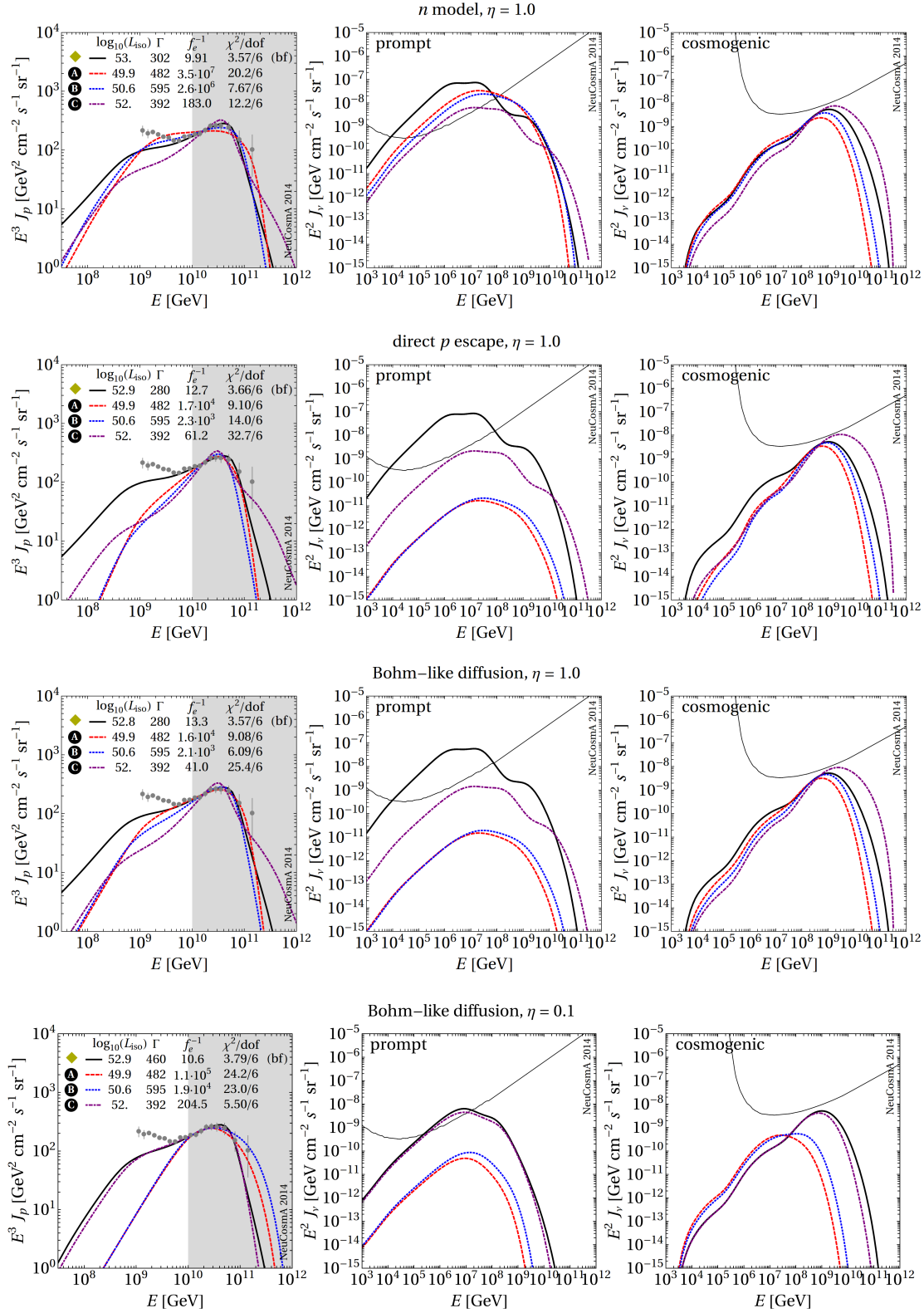


Figure 4.8: Cosmic ray, prompt neutrino, and cosmogenic neutrino spectra (in columns) from GRBs in the range $z = 0$ to 6, for selected points in the parameter space plane Γ vs. L_{iso} , corresponding to the markers in Fig. 4.7. The different rows correspond to the upper left, middle left, lower left, and lower right panels in Fig. 4.7. The fit range is gray-shaded. Figure taken from Ref. [161].

of the fit, represented by the χ^2 per degree of freedom, $\chi^2/\text{d.o.f.}$ For a more detailed discussion of the dependence on η and its impact on the conclusions, see appendix D of Ref. [161].

Up to this point, due to the plausible ranges of the best-fit parameter values, the neutron model for cosmic ray escape was widely regarded as a good description of UHECR production in GRBs. However, Refs. [100, 92] rejected this hypothesis by relating the cosmic ray and neutrino spectra, and comparing the latter to the current neutrino bounds, as we have also done here. Indeed, we show in the top row of Fig. 4.7, corresponding to the neutron model, that the gray shading depicting the region excluded by the absence of GRB neutrinos with the current IceCube exposure spans all of the parameter space. Hence, the neutron model is excluded everywhere. Compared to earlier references, we have the source model prediction for the baryonic loading as well, which increases tremendously above the red (dashed) curve. The reason is that the pion production efficiency drops there, and in fact it turns out that above this curve other escape mechanisms become important, whereas below this curve neutron escape dominates in all of our models.

Note that we allow for arbitrarily high baryonic loadings here derived from the normalization, and the required baryonic loadings for this model have to be extremely high in the upper left corner. In practice, depending on the minimal proton energy at injection, it can be estimated that baryonic loadings $\gtrsim 10^4$ could mean that pp self-interactions among the protons become important, an effect which we do not consider. In addition, gamma-rays from π^0 decays produced by $p\gamma$ interactions or proton synchrotron radiation could violate the *Fermi* bound [143], if they can escape.⁸

Several sample spectra corresponding to selected points from the upper left panel in Fig. 4.7 are shown in the first row of Fig. 4.8, marked by the diamond (best-fit) and dots. Good fits are obtained for the best-fit point and point B, bad fits for point A (requires an upscaling of the energy) and C (too high proton energy, leading to a strong spectral peak). However, one can clearly see that all prompt neutrino fluxes overshoot the current bounds. At point C, the cosmogenic neutrino flux will eventually become larger because of the larger $E'_{p,\text{max}}$.

Allowing for direct (middle row of Fig. 4.7) or diffusive escape (lower row of Fig. 4.7) of protons at the highest energies changes the results completely. Below the red dashed curve all models are still similar, since neutron escape dominates in this region. Above that curve, however, where either direct or diffuse escape dominates, there are two important differences: the required baryonic loadings are significantly smaller, and the neutrino spectra does not anymore exceed the upper bounds, since the pion production efficiency is lower. In fact, for $\eta = 1.0$ (left panels), the cosmogenic neutrinos are able to probe parts of the parameter space that the prompt neutrinos are unable to probe; this is because the former do not care about what the cosmic ray escape mechanism is. From these plots (taking into account intermediate values of η , as discussed in appendix D of Ref. [161]), it is clear that

1. There are parts of the parameter space with moderate $\Gamma \gtrsim 400$ and baryonic loadings $10 \lesssim f_e^{-1} \lesssim 100$ which are still allowed (at present) if cosmic rays can efficiently escape by diffusion (see lower right panel), which however can be tested by future IceCube data.
2. There are parts of the parameter space with either extremely large Γ or extremely large f_e^{-1} which are inaccessible by future IceCube bounds; see also appendix D in Ref. [161] for more details. These parts will have to be probed elsewhere; for example, the branch in the middle left panel will disappear if the energy calibration of the cosmic ray measurements can be improved (see appendix D in Ref. [161]).

⁸For a more detailed discussion on the impact of the gamma-ray bounds for efficient pion production, see Ref. [100].

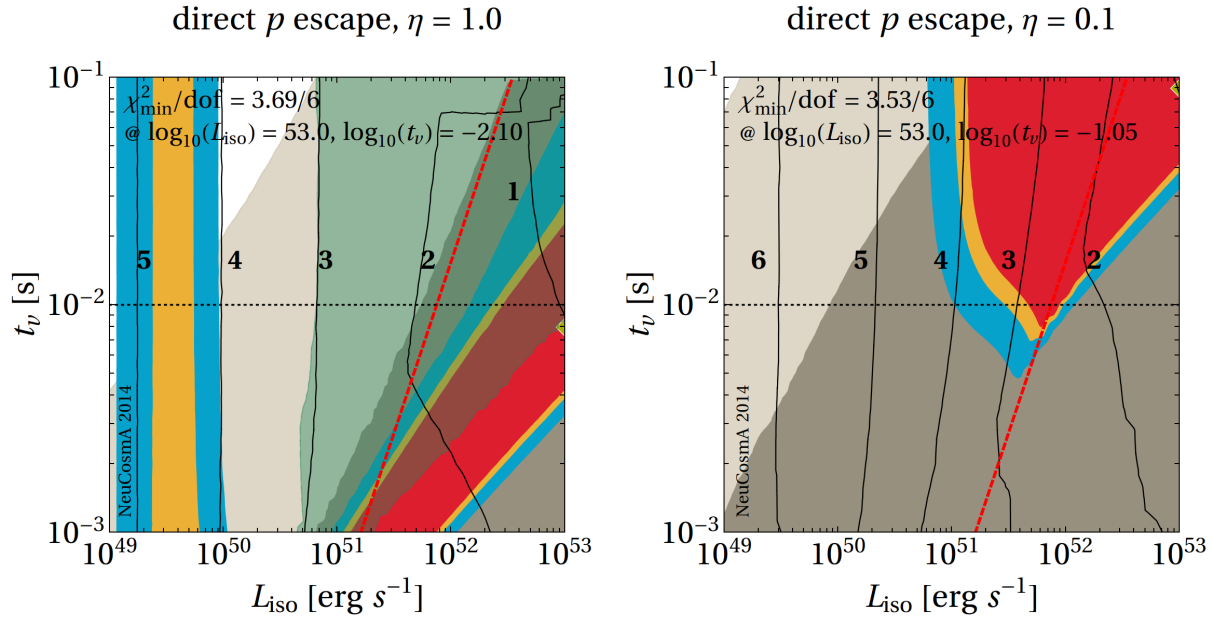


Figure 4.9: Same as Fig. 4.7, middle panels (direct escape), as a function of L_{iso} and t_ν for a fixed $\Gamma = 300$. The left (right) panel corresponds to an acceleration efficiency of $\eta = 1.0$ (0.1). The horizontal dotted lines mark the standard value of $t_\nu = 10^{-2}$ s. Figure taken from Ref. [161].

Therefore, if cosmic rays can escape by mechanisms other than neutron production, it is clear that the current neutrino bounds are not yet strong enough to disqualify GRBs as the sources of UHECRs in the internal shock model. However, if IceCube fails to find high-energy neutrinos from GRBs after ~ 15 yr, it will be very difficult to maintain this hypothesis.

We also show the spectra for several points in Fig. 4.8. Comparing the middle two rows (direct escape versus diffusion), it is clear that the cosmic ray spectra for direct escape are harder, and therefore provide worse fits. While the cosmic ray spectra in the second row (direct escape) appear to be similar for points A and B, the fit for point B is still much worse because the energy recalibration is penalised. In all cases, the best-fit prompt neutrino fluxes overshoot the current bound for the prompt neutrino flux. For $\eta = 1.0$ (upper three rows), the maximal proton energy for point C is high, and therefore the cosmogenic neutrino flux is high, too. Comparing the lower two rows ($\eta = 1.0$ and $\eta = 0.1$ for diffusive escape), one can easily see that lower acceleration efficiencies help for the shape, but too low proton energies (points A and B) are penalized because of the energy calibration error.

So far, we have fixed several of the parameters and have shown the dependence as a function of L_{iso} and Γ . In Fig. 4.9, we instead fix Γ and vary t_ν . While the result looks qualitatively different, it does not reveal any new allowed regions. This is expected, since the pion production efficiency roughly scales $\propto L_{\text{iso}}/(\Gamma^4 t_\nu \epsilon'_\gamma)$ [89, 2], with ϵ'_γ chosen to be the photon break energy in the SRF, and the neutron model and prompt neutrino production follow the pion production efficiency. That is, there is a degeneracy among L_{iso} , Γ^4 , t_ν , and ϵ'_γ , which means that the relevant features will be visible in any of the relevant parameter combinations. The other regions follow, more or less, the maximal proton energy; see Fig. 2.5.

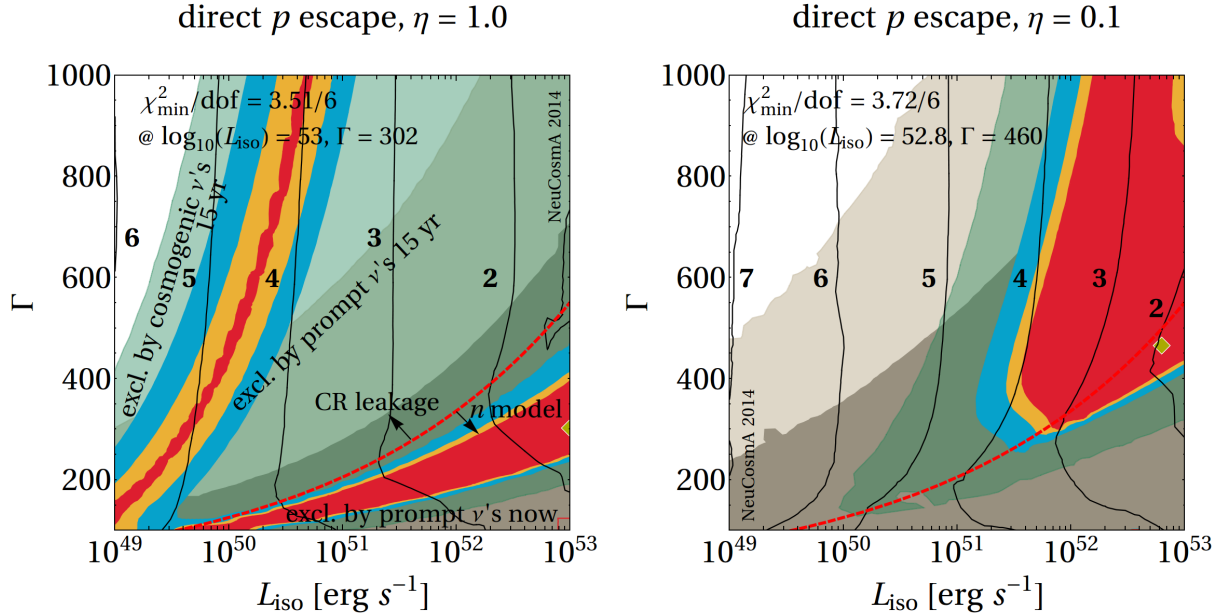


Figure 4.10: Same as Fig. 4.7, middle panels (direct escape), but assuming GRB evolution of the sources. Figure taken from Ref. [161].

4.4.2 Effect of cosmological source evolution

Our results so far have been obtained under the assumption of SFR evolution of the sources. We now show in Fig. 4.10 the fits as in Fig. 4.7, middle panels (direct escape), but for GRB evolution of the sources (SFR times $(1+z)^{1.2}$ [138]). A comparison to Fig. 4.7 reveals two important differences: first, the required baryonic loading is higher everywhere, as a consequence of the higher evolution factor f_z in Eq. (4.3); and, second, the cosmogenic neutrino bound has a much larger impact than in the SFR case, since a strong evolution entails a higher cosmogenic neutrino flux.

A different possibility is that the GRB rate deviates from the SFR locally, *i.e.*, that it exhibits either a fluctuation upwards or downwards. The GRB observations would be left mostly unchanged because they are dominated by larger redshifts $z \approx 1$. In contrast, the UHECR spectrum, and the associated baryonic loading predictions, would be affected, since the mean free path of UHECRs is only about 1 Gpc ($z \simeq 0.25$) at 10^{10} GeV, and 100 Mpc ($z \simeq 0.024$) at 10^{11} GeV; see Fig. 3.3 in chapter 3.

We illustrate a local deviation (below redshift 0.25) in Fig. 4.11; here the unchanged version of the dimensionless distribution of sources in redshift $\mathcal{H}(z)$ is defined in Eq. (B.5) (see appendix B). We have estimated the local deviation from statistics: distributing 1000 bursts over redshift, only about six will be in the range $z \lesssim 0.25$.⁹ The 1σ relative (Gaussian) error is therefore roughly $1/\sqrt{6} \simeq 0.41$, and the 3σ range can be estimated as $-1 \lesssim \Delta\mathcal{H} \lesssim +1.2$.

The effect of two such local deviations, $\Delta\mathcal{H} = -1$ and $\Delta\mathcal{H} = 1.2$, is illustrated in Fig. 4.12 for

⁹One can also estimate this from the local GRB rate of $\sim 1 \text{ Gpc}^{-3} \text{ yr}^{-1}$, since $z \simeq 0.25$ corresponds to a mean free path of the protons of $R \simeq 1 \text{ Gpc}$ at 10^{10} GeV. The average GRB rate between $z = 0$ and $z = 0.25$ is roughly 1.5 (see Fig. 4.11), which leads to $4\pi R^3/3 \cdot 1.5 \cdot 1 \text{ Gpc}^{-3} \text{ yr} \simeq 6 \text{ yr}^{-1}$.

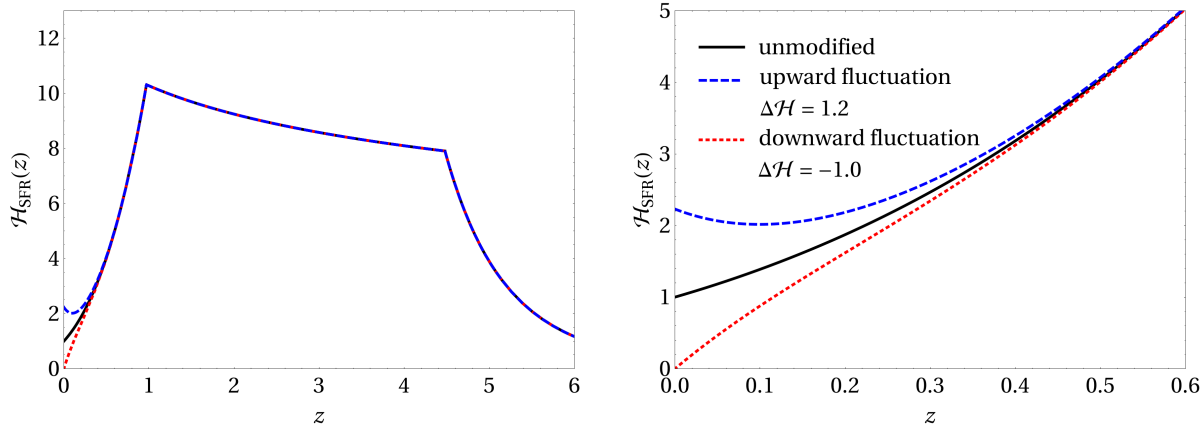


Figure 4.11: *Left:* Unmodified SFR evolution with redshift (black, solid line), and SFR with a local upwards (blue, dotted line) and downwards fluctuation (red, dashed line). *Right:* Magnification for low redshifts. Figure taken from Ref. [161].

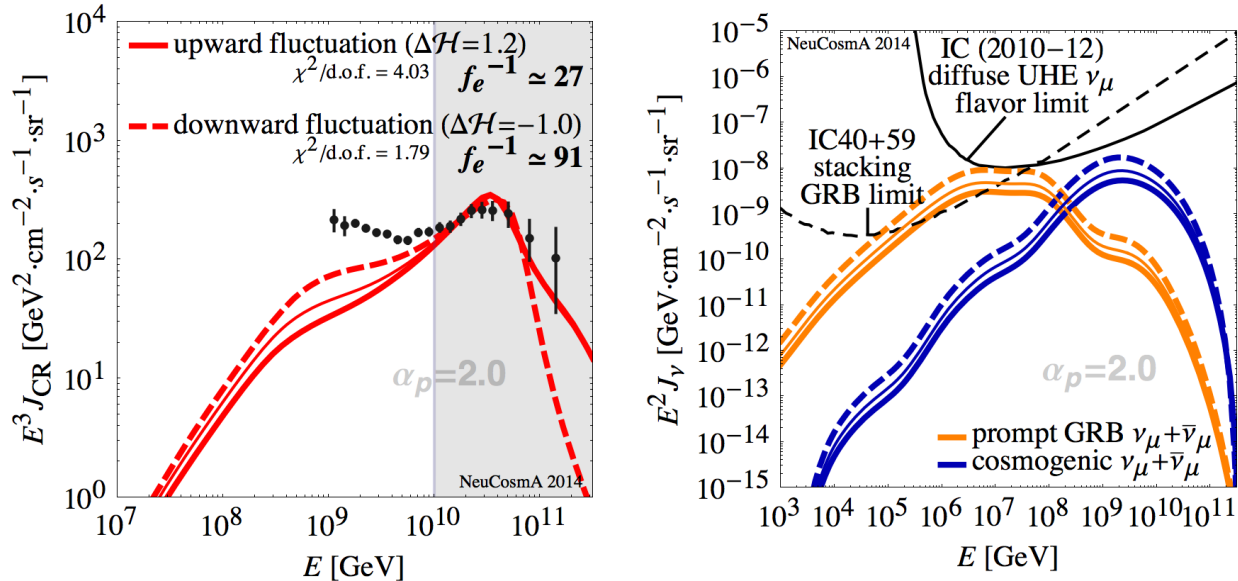


Figure 4.12: The effect of ensemble fluctuations on the CR (left column) and neutrino spectra (right column), for model #1 in Fig. 4.2. The original results obtained in the absence of fluctuations are included as thin lines for comparison. Figure taken from Ref. [161].

model #1 of Fig. 4.2. A local upward fluctuation of the GRB rate clearly reduces the required baryonic loading, and, at the same time, the prompt and cosmogenic neutrino fluxes. The reduction of f_e^{-1} is a consequence of the lower normalisation needed to fit the UHECR observations: since more GRBs are local, a higher proportion of UHECR protons experience little energy losses and therefore are already enough to fit the UHE region. Therefore, a local upward fluctuation of the

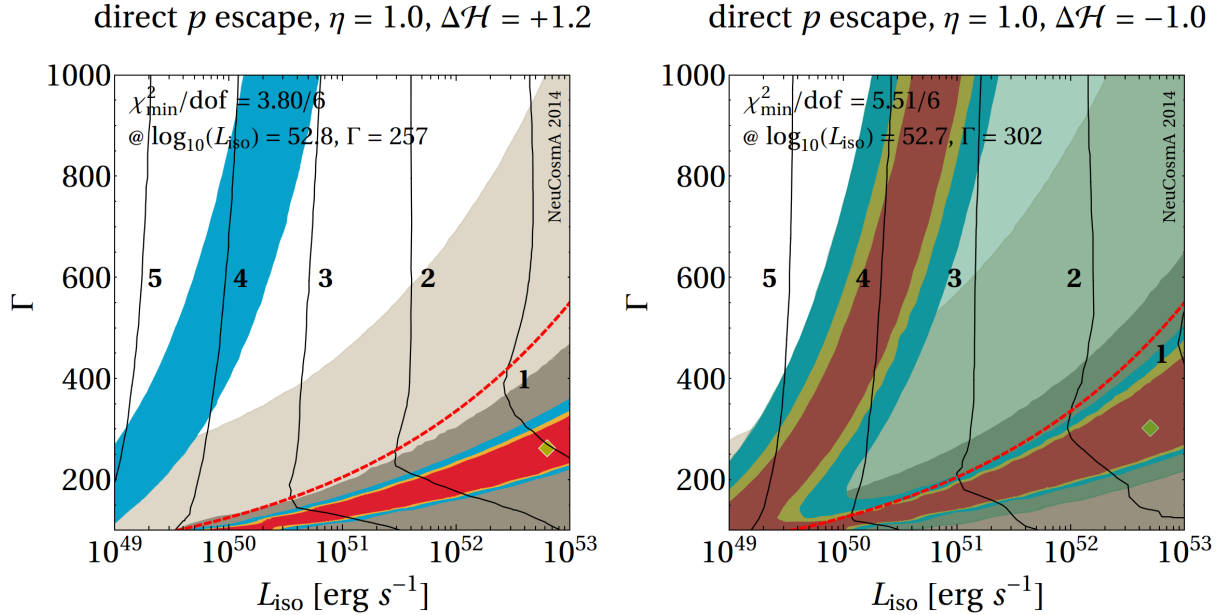


Figure 4.13: Same as Fig. 4.7, middle left panel (direct escape with $\eta = 1.0$), but assuming a local upward (left panel) and downward (right panel) fluctuation of the SFR of $\Delta\mathcal{H} = 1.2$ and -1.0 , respectively. Note that, in the right panel, the left border of the exclusion region from cosmogenic neutrinos (in green) coincides with the left border of the 99% C.L. allowed region (in blue). Figure taken from Ref. [161].

GRB rate may be a plausible explanation for the non-observation of neutrinos from GRBs, while allowing for reasonable values of f_e^{-1} . However, the goodness of fit is slightly reduced, because the local enhancement relatively increases the high-energy part of the cosmic ray spectrum. A local downward fluctuation of the GRB rate causes the opposite effect: a better fit, at the expense of higher neutrino fluxes and baryonic loadings.

The results of a parameter scan for the same two values of the local fluctuation $\Delta\mathcal{H}$ are presented in Fig. 4.13, assuming a direct escape-dominated scenario. As expected, the upward fluctuation (left panel) is capable of reducing the required values of baryonic loadings enough to make the cosmogenic neutrino exclusion (after 15 years of exposure) disappear, at the expense of the spectral shape change, which makes the left fit branch vanish. The corresponding downward fluctuation increases the cosmogenic neutrino flux, which means that the future cosmogenic bound can even partially exclude the left branch of the fit.

4.5 Limitations of the analysis

We have shown that it is possible to use current UHECR observations and neutrino upper bounds to assess in what regions of parameter space a joint UHECR and neutrino emission model from GRBs is still viable. In accordance with Refs. [100, 92], we have found that a scenario where only neutrons can escape is ruled out by current bounds on the GRB neutrino flux from IceCube. Using our two-component emission model (chapter 2) it becomes clear that, by allowing protons to either directly escape or diffuse out of the sources at the highest energies, the UHECR data can still be

closely fitted, while also conforming to the neutrino bounds. As a result of our parameter scan, we are in addition able to deduce a value for the baryonic loading at every point in parameter space, instead of having to use an external *ad hoc* value for it. Under the constraints of the neutrino bounds, the baryonic loadings thus found can be very high ($\gtrsim 10^4$).

One limitation of our present analysis is that the GRB model that we have adopted assumes that the proton, neutrino, and photon emissions all originate in internal collisionless shocks that occur at a single representative, average radius $R_C = 2\Gamma^2 ct_v$ from the central emitter, *i.e.*, the calculations are performed within the “static burst” approximation (see chapter 1). In chapter 5 we will study a dynamical burst, where the internal collisions occur at different radii, and the emission of the different particle species peak at different values of R_C . In this model, most of the neutrino emission will come from the innermost collisions, where photohadronic interactions are more common on account of the higher proton and photon densities, whereas, the gamma-rays and heavier nuclei with the highest energies [176, 160] may come from large collision radii, as shown in chapter 5 and appendix F.

A second limitation of our analysis is that UHECRs are assumed to be exclusively protons (included as a potential development in chapter 8). Including heavier nuclei in the UHECRs may allow for higher CR energies, as nuclei can be accelerated more efficiently due to their larger electrical charges. However, under the static burst approximation, the nuclei can escape without being photodisintegrated only for parameter sets for which the photon densities are low enough; see Refs. [176, 160]. In fact, the disintegration and pion production efficiencies are proportional to each other [177], which means that the UHECR nuclei escape without disintegration in our direct/diffusive escape regimes, and that we anticipate that our results do not qualitatively change there. For higher photon densities, however, photodisintegration can become efficient (see appendix F) and the neutrino and neutron production will be reduced, which has to be compensated by higher baryonic loadings.

Chapter 5

A dynamical GRB evolution model

In the literature on gamma-ray bursts (GRBs), it is typical to simplify the calculations of the prompt radiation phase by considering a “static burst”, where the gamma-ray, cosmic-ray, and neutrino fluxes are generated by $T_{90}/t_v \sim 100\text{--}1000$ identical internal shocks, all of them occurring at the same, fixed collision radius, with identical parameters (see Fig. 1.8). In a more realistic scenario, however, the collisions will occur at different radii, as the fireball expands. We have studied the collision radius dependence of the cosmic ray and neutrino production.

We work in the framework of the internal shock model for GRB fireballs. As before, we assume that the target photon spectrum is a broken power law, as motivated by gamma-ray observations, and we do not discuss the origin of that spectrum. For the cosmic ray and neutrino production, we follow Ref. [106], so that the UHECR proton emission is made up of two components: one coming from neutron escape and another one coming from the direct proton escape from the source (see chapter 2). We allow matter shells to propagate and collisions to occur at different radii, and we follow the time profile of the collisions (see Sec. 5.1). This is what we refer to as “evolution of the fireball”.

5.1 Fireball evolution and collision model

5.1.1 General description and fireball parameters

A central engine or emitter (*e.g.*, a collapsing massive star) is assumed to emit collimated jets of beamed, highly-accelerated matter carrying a considerable baryonic loading. As before, we consider the isotropically-equivalent scenario, where the matter ejecta are radially-expanding spherical shells. The burst simulation described here covers only the “coasting phase” of the GRB, at the start of which it is assumed that the shells have been already accelerated to their maximum speeds, which the shells maintain during their one-dimensional propagation. The earlier acceleration phase and the later deceleration phase –when the shells run into the surrounding interstellar environment– are not part of the simulation.

We consider contributions from collision at various radii. Collisions among shells are numerically calculated using a simplified one-dimensional model [178, 179]. The model assumes an initial number N_{sh} of shells, each labeled by an index k , where inner shells are labeled by larger numbers. By running numerical simulations of the propagation and collision of the expanding shells, one can calculate the final number of pairwise collisions between them, N_{coll} .

At any time during the simulation, the k -th shell is characterised by the following four basic parameters:

- r_k : the shell radius, as measured from the emitter
- l_k : the shell width
- Γ_k : bulk Lorentz factor of the shell, assumed to be highly relativistic ($\Gamma_k \gg 1$). It remains constant during the propagation of the shell¹ (it will change only when a collision occurs, as we will see later).
- m_k : total mass of particles in the shell, which also remains constant, except during collisions

For convenience, we also keep track of the following shell parameters, which can be derived from the previous ones:

- $V_{\text{iso},k}$: volume of the isotropically-equivalent spherical shell. We assume that, during propagation, the shell width is kept constant (it will change only when a collision occurs); hence, the volume is given by

$$V_{\text{iso},k} = 4\pi r_k^2 l_k . \quad (5.1)$$

- $E_{\text{kin},k}^{\text{iso}}$: bulk kinetic energy of the shell, given by

$$E_{\text{kin},k}^{\text{iso}} = \Gamma_k m_k c^2 . \quad (5.2)$$

- ρ_k : mass density of the shell, calculated as

$$\rho_k = m_k / V_{\text{iso},k} . \quad (5.3)$$

Table 5.1 lists these and other simulation parameters, with their respective units. Unless otherwise noted, all quantities are expressed in the source reference frame; quantities expressed in the observer’s frame will be indicated as such. As before, primed quantities are expressed in the shock rest frame (SRF). For convenience, we have included in appendix D the burst evolution algorithms that were implemented, following Refs. [178, 179].

5.1.2 Fireball initialisation

Before starting the simulation, the fireball is initialised; see Fig. 5.1 for an illustration. This consists of creating N_{sh} shells, each one described by the initial tuple $(r_{k,0}, l_{k,0}, \Gamma_{k,0}, E_{\text{kin},0}^{\text{iso}})$; see table 5.1. In order to do this, the emitter is characterised by two timescales: an “uptime”, δt , during which it emits one spherical matter shell, followed by a “downtime”, Δt , where the emitter is inactive. These two timescales determine the initial shell width, $l = c\delta t$, which we assume to be common for all shells (*i.e.*, $l_k|_{t=0} = l$), and the initial separation between consecutive shells is $d = c\Delta t$, common for all pairs of neighbouring shell pairs. Thus, each of the initial N_{sh} shells is located at position $r_{k,0} = r_{N_{\text{sh}}} + (N_{\text{sh}} - k)(l + d)$, where $r_{N_{\text{sh}}}$ is the distance from the innermost shell to the emitter, which is an input parameter of the simulation². At initialisation time, therefore, we assume that

¹Once the shell reaches the external shock region, of course, it will decelerate; however, as we said before, we will not consider this stage of the fireball evolution.

²Results will not depend on $r_{N_{\text{sh}}}$ much, unless its value is too large; see table 5.1.

Parameter	Description	Type	Units	Notes
Fireball initialisation				
N_{sh}	initial number of shells	input	–	
δt	uptime of the emitter, or duration of emission of one shell	input	s	
Δt	downtime of the emitter, or initial time separation between shells	input	s	
$r_{N_{\text{sh}}}$	distance from the innermost shell to the emitter	input	km	set to $r_{N_{\text{sh}}} = 10^3$ km by default
r_{dec}	deceleration radius, where external shocks start	input	km	set to $r_{\text{dec}} = 5.5 \cdot 10^{11}$ km by default
A_{Γ}	fluctuation factor of the $\Gamma_{k,0}$ distribution	input	–	
$E_{\text{kin},0}^{\text{iso}}$	initial bulk kinetic energy of the shells	input	erg	initial shells are assumed to have a common $E_{\text{kin},k}^{\text{iso}} = E_{\text{kin},0}^{\text{iso}}$
z	redshift of the emitter	input	–	used to calculate t_{obs} , Eq. (5.13)
l	initial shell width	internal	km	set to $l = c\delta t$
d	initial separation between consecutive shells	internal	km	common for all initial shells set proportional to l , <i>i.e.</i> , $d \propto l$
$r_{k,0}$	initial radius of the k -th shell, measured from the emitter	internal	km	common for all initial shells $r_{k,0} = r_{N_{\text{sh}}} + (N_{\text{sh}} - k)(l + d)$
$\Gamma_{k,0}$	initial Lorentz factor of the k -th shell	internal	–	sampled from a log-normal distribution
$m_{k,0}$	initial mass of the k -th shell	internal	GeV	$m_{k,0} = E_{\text{kin},0}^{\text{iso}} / (\Gamma_{k,0} c^2)$
Fireball evolution				
t	time in the source frame	internal	s	
r_k	radius of the shell, measured from the emitter	internal	km	initially set to $r_{k,0}$; grows as $r_k = r_{k,0} + c\beta_k t$
l_k	width of the shell	internal	km	initially set to l ; changes only in collisions
Γ_k	bulk Lorentz factor of the shell	internal	–	initially set to $\Gamma_{k,0}$; changes only in collisions
m_k	mass of the shell	internal	GeV	initially set to $m_{k,0}$; changes only in collisions
β_k	bulk speed of the shell	internal	–	$\beta_k = \sqrt{1 - \Gamma_k^{-2}}$
$V_{\text{iso},k}$	volume of the shell	internal	km ³	$V_{\text{iso},k} = 4\pi r_k^2 l_k$
$E_{\text{kin},k}^{\text{iso}}$	bulk kinetic energy of the shell	internal	erg	initially set to $E_{\text{kin},0}^{\text{iso}}$; changes only in collisions
ρ_k	mass density of the shell	internal	GeV km ⁻³	$\rho_k = m_k / V_{\text{iso},k}$
Shell collisions				
$m_{r(s)}$	mass of the rapid (slow) shell	internal	GeV	
$\Gamma_{r(s)}$	bulk Lorentz factor of the rapid (slow) colliding shell	internal	–	
$\Gamma_{fs(rs)}$	bulk Lorentz factor of the forward (reverse) shock	internal	–	See Eq. (5.17)
$\beta_{fs(rs)}$	bulk speed of the forward (reverse) shock	internal	–	$\beta_{fs(rs)} = \sqrt{1 - \Gamma_{fs(rs)}^{-2}}$
β_m	bulk speed of the merged shell	internal	–	$\beta_m = \sqrt{1 - \Gamma_m^{-2}}$
ρ_m	mass density of the merged shell	internal	GeV km ⁻³	See Eq. (5.19)
t_{coll}	time at which the collision occurs, in the source frame	internal	s	
N_{coll}	total number of collisions that occurred in the burst	output	–	
t_{obs}	time at which the collision occurs, in the observer's frame	output	s	See Eq. (5.13)
$E_{\text{coll}}^{\text{iso}}$	internal energy liberated in the collision	output	erg	See Eq. (5.14)
Γ_m	bulk Lorentz factor of the merged shell	output	–	See Eq. (5.15)
l_m	width of the merged shell	output	km	See Eq. (5.16)
R_C	radius at which the collision occurs	output	km	
δt_e	time at which the reverse shock crosses the rapid shell	output	s	$\delta t_e = l_m / [c(\beta_r - \beta_{rs})]$

Table 5.1: Main parameters of the fireball evolution simulation and their units. All of them are expressed in the source frame, except for t_{obs} , which is in the observer's frame.

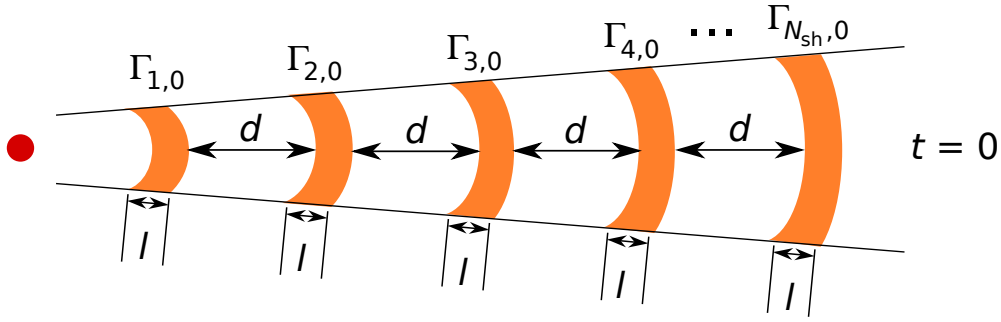


Figure 5.1: Diagram depicting the initial state of the simulated burst.

the emitter has already output N_{sh} pulses (spherical shells) of duration δt , at a frequency $1/\Delta t$. Note that our simplified treatment assumes that the shells do not widen during propagation, so that l_k remains constant for each of them, except, as we will see, when shells collide. However, because the bulk Lorentz factors are different, the separations between them will change over time.

An estimate of the values of l and d can be obtained by comparison with observations [180]: from the measured GRB light curves, we expect that roughly $l \approx ct_v$ and $d \approx ct_q$ (e.g., [178, 181]), where t_v is the GRB variability time, *i.e.*, the characteristic duration of the peaks in the light curve, and t_q –where q stands for “quiescent”– is the characteristic time between consecutive peaks. Note that d should be comparable to l in the internal shock model, and the simulations in Ref. [178] set $d = l$, while Ref. [181] sets $d = 5l$, based on the fact that the observed time separation between peaks and the total duration of the burst are much longer than the variability time. However, we stress that the variability timescale of the burst, t_v , is **not** an input parameter of the fireball simulation, but a result of it. Only the uptime of the emitter, δt , *i.e.*, the duration of the ejection of one shell by the emitter, is an input. One finds that for certain choices of the burst simulation parameters, the estimated value of the variability time (t_v), which is obtained from the light curve built after running the simulation, is close to δt (see section 5.3). We therefore set δt to a value close to the desired variability time.

We assume the initial values of the bulk Lorentz factor of the shells, $\Gamma_{k,0}$, to be randomly sampled from a log-normal distribution defined by the characteristic Lorentz factor Γ_0 and the amplitude of the fluctuations A_Γ as follows:

$$\ln \left(\frac{\Gamma_{k,0} - 1}{\Gamma_0 - 1} \right) = A_\Gamma x, \quad (5.4)$$

where x follows a Gaussian distribution,

$$P(x)dx = \frac{e^{-x^2/2}}{\sqrt{2\pi}} dx. \quad (5.5)$$

When $A_\Gamma < 1$, the mean value becomes $\langle \Gamma \rangle \approx \Gamma_0$ and the variance becomes $\Delta \Gamma \approx A_\Gamma \Gamma_0$. When $A_\Gamma > 1$, both the mean value and variance are largely affected by fluctuations. Too large values of A_Γ result in too many collisions occurring close to the central emitter. Values of $A_\Gamma \approx 1$ are required in order to achieve high efficiencies in the conversion of kinetic to radiated energy [182]. See Fig. 5.2 for an illustration of the probability density function (pdf) of the initial Lorentz factors, for different values of A_Γ .

Finally, we have to decide on how to assign the masses m_k to the initial shells. There are two typical assumptions: one is the equal-mass assumption, *i.e.*, $m_{k,0} = m$ for all k ; the other is the

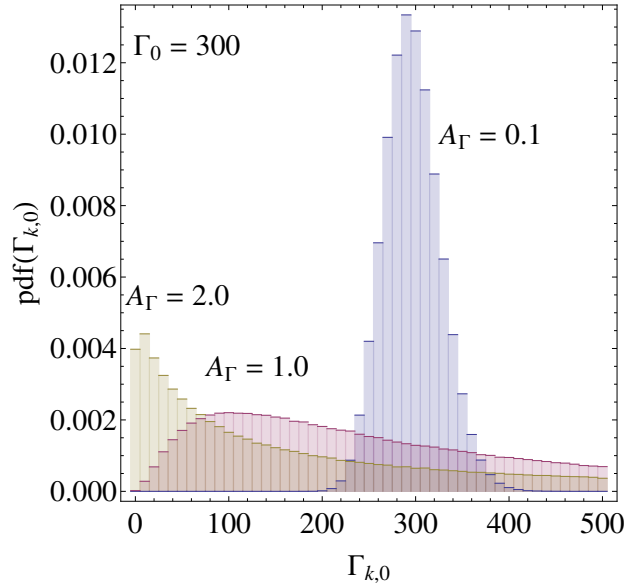


Figure 5.2: Probability density functions (pdf) of the initial value of the Lorentz factors, for a central value of $\Gamma = 300$ and three different choices of the spread: $A_\Gamma = 0.1$ (blue), 1 (purple), and 2 (brown).

equal-energy assumption, *i.e.*, $m_{k,0} = E_{\text{kin},0}^{\text{iso}} / (\Gamma_{k,0} c^2)$, with $E_{\text{kin},0}^{\text{iso}}$ the initial bulk kinetic energy common to all shells. We have adopted the latter assumption since it appears that it could be better to explain observations³ [180].

5.1.3 Fireball evolution

The spherical shells are assumed to expand radially with highly relativistic speed. Fig. 5.3 shows an illustration of the burst expansion and an internal collision. We consider the simplified case in which the shell width $l_k = l$ remains constant during propagation⁴. The width will only change when shells collide; we will see that the merged shell that results from a two-shell collision is squeezed. At any time during the propagation, the shell volume, assuming isotropic emission, can be calculated as

$$V_{\text{iso},k} = 4\pi r_k^2 l_k . \quad (5.6)$$

The mass of a shell is also assumed to remain constant during propagation (again, except when collisions occur). Therefore, its mass density

$$\rho_k = m_k / V_{\text{iso},k} \quad (5.7)$$

decreases like $\sim r^{-2}$ as the fireball expands. Given that we are simulating the coasting phase of the fireball only, the shell speeds, or, equivalently, their Lorentz factors, are unchanged during propagation (except in collisions). Hence, since both the mass and Lorentz factor of the shell remain unchanged, its kinetic energy,

$$E_{\text{kin},k}^{\text{iso}} = \Gamma_k m_k c^2 , \quad (5.8)$$

³Also, even in simulations that use the equal-energy assumption, dedicated analyses of the time-evolution of the internal energy of individual shells show that the dissipated energy varies even at the same collision radius, since it cannot be expressed only by the kinetic energy of shells [183].

⁴Depending on the internal energy, the shell spreading is important especially after collisions. Recent dedicated simulations take into account this effect, but it is neglected in the simplest versions, like the one we have adopted [181].

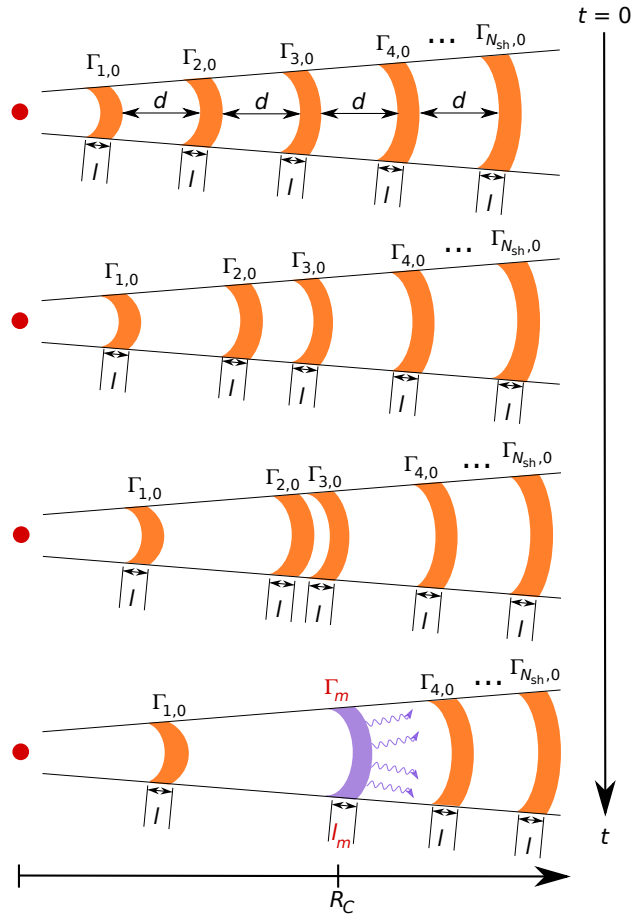


Figure 5.3: Diagram depicting the time evolution of the simulated burst.

remains constant as well.

Now, the general relation between the total free, or internal, energy of a gas, $E_{\text{int-tot}}^{\text{iso}}$, and its volume is

$$E_{\text{int-tot}}^{\text{iso}} \propto V_{\text{iso}}^{-(\gamma-1)} \propto r^{-2(\gamma-1)}, \quad (5.9)$$

where γ is the adiabatic index. For a relativistic gas, $\gamma = 4/3$, and so we expect the available internal energy of the fireball to evolve as

$$E_{\text{int-tot}}^{\text{iso}} \propto r^{-2/3} \quad (5.10)$$

as it expands. We will see later (Fig. 5.7) that this scaling is clearly visible in the results of our simulations; it is not put in by hand, but is rather a direct consequence of the growth of the volume as $\propto r^2$. Note the distinction between a shell's bulk kinetic energy, $E_{\text{kin},k}^{\text{iso}}$, and its internal energy, $E_{\text{int-sh},k}^{\text{iso}}$: while the former is related to the shell speed as measured in the source rest frame, the latter measures the kinetic energy of the particles moving randomly inside the shell, as measured in the shock rest frame. We will see later that when two shells collide and a new merged shell is created, part of the kinetic energy of the colliding shells is converted into the internal energy of the new one; this will be promptly radiated away in the form of energetic particles (photons, protons, neutrons, neutrinos).

As a result of the expansion, occasionally a rapid shell catches up with a slower one and they collide, leading to internal shocks. In the source frame, among N_{sh} shells, one can calculate the

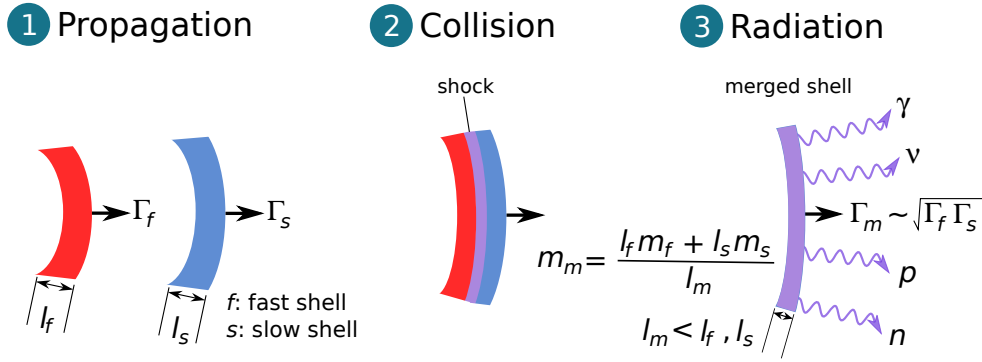


Figure 5.4: Diagram depicting the collision of two shells.

collision time for all pairs of neighbouring shells by

$$\Delta t_{k,k+1} = \frac{d_{k,k+1}}{c(\beta_{k+1} - \beta_k)}, \quad (5.11)$$

where $d_{k,k+1} \equiv r_k - r_{k+1} - l_{k+1}$ is the separation between shells k and $k+1$. The time until the next collision is the minimum of the collision times, *i.e.*,

$$\Delta t_{\text{next}} = \min[\Delta t_{k,k+1}]. \quad (5.12)$$

Then, one can increase the simulation time to $t \rightarrow t + \Delta t_{\text{next}}$, and the collision radius is correspondingly determined, *i.e.*, $R_C = r_{k'}$, with k' the index of the innermost shell of the colliding pair. The emission of light associated to this collision will be detected by a distant observer at time⁵

$$t_{\text{obs}} = \left(\frac{D(z) - R_C}{c} + t \right) (1 + z), \quad (5.13)$$

with $D(z)$ the light-travel, or lookback, distance to the emitter with redshift z .

At this point, having determined the time of the next collision, all of the shells in the fireball are propagated to their new positions $r_k \rightarrow r_k + c\beta_k \Delta t_{\text{next}}$. If one of the shells reaches the radius at which the external shock starts becoming important, *i.e.*, where the fireball starts decelerating, this shell is removed from the simulation. Following Ref. [73], we have assumed $r_{\text{dec}} = 5.5 \cdot 10^{11}$ km for the deceleration radius (see, *e.g.*, Eq. (15) in Ref. [72]).

We still have to decide the fate of the two colliding shells. Our treatment contemplates that when two shells collide they merge into a new one: the kinetic energy of the initial two shells is used partly as bulk kinetic energy for the new shell and partly as its internal energy; see Fig. 5.4. We assume that the new shell immediately cools by prompt emission of particles, *i.e.*, that its internal energy is immediately radiated away by gamma-rays, cosmic rays, and neutrinos⁶. However, more detailed treatments (including, *e.g.*, reflections) are also possible (*e.g.*, Ref. [182]). While the details on how two shells collide depend on the modeling of hydrodynamical properties (see, *e.g.*, Ref. [184]), we can use the simple collision model in the relativistic limit introduced in Ref. [178] to calculate the internal energy dissipated by a collision.

⁵Note however that the term $D(z)/c$ is just an offset: it will be discarded when, in the output of the simulation, the first emission is set to start at $t_{\text{obs}} = 0$.

⁶Realistically, some internal energy should still remain in the shell, and it is recovered into the kinetic energy via adiabatic expansion, where the Lorentz factor is increased. Also, treating this is related to the efficiency problem, pulse structure, and so on (*e.g.*, [182]).

In the collision of a slow (s) and a rapid (r) shell, the internal energy of the resulting merged shell is equal to the difference in bulk kinetic energy before and after the collision, *i.e.*,

$$E_{\text{coll}}^{\text{iso}} = (\Gamma_r - \Gamma_m)m_r c^2 + (\Gamma_s - \Gamma_m)m_s c^2 . \quad (5.14)$$

Considering momentum and energy conservation, its Lorentz factor is found to be

$$\Gamma_m \simeq \sqrt{\frac{\Gamma_r m_r + \Gamma_s m_s}{m_r/\Gamma_r + m_s/\Gamma_s}} , \quad (5.15)$$

when $\Gamma_r, \Gamma_s \gg 1$. The merged shell is assumed to cool down instantly by prompt emission of its internal energy.

The width of the merged shell (m) is determined by [178, 181]

$$l_m \simeq l_k \frac{\beta_{\text{fs}} - \beta_m}{\beta_{\text{fs}} - \beta_k} + l_{k+1} \frac{\beta_m - \beta_{\text{rs}}}{\beta_{k+1} - \beta_{\text{rs}}} , \quad (5.16)$$

where $\beta_{fs(rs)} = \sqrt{1 - \Gamma_{fs(rs)}^{-2}}$ is the speed of the forward (reverse) shock, whose Lorentz factor is given by

$$\Gamma_{fs(rs)} = \Gamma_m \sqrt{\frac{1 + 2\Gamma_m/\Gamma_{s(r)}}{2 + \Gamma_m/\Gamma_{s(r)}}} . \quad (5.17)$$

Since the collision occurs at $r = R_C$, the volume of the new shell is

$$V_{\text{iso-}m} = 4\pi R_C^2 l_m . \quad (5.18)$$

The density is different between the shocked faster shell and shocked slower shell. For simplicity, we assume that the merged shell achieves the average density

$$\rho_m \simeq \frac{l_{k+1}\rho_{k+1} + l_k\rho_k}{l_m} , \quad (5.19)$$

and thus its mass is

$$m_m = V_{\text{iso-}m}\rho_m . \quad (5.20)$$

Therefore, the kinetic energy of the new shell is

$$E_{\text{kin-}m}^{\text{iso}} = \Gamma_m m_m c^2 . \quad (5.21)$$

After the collision, the $(k + 1)$ -th shell is eliminated from the simulation, and the new merged shell replaces the former k -th shell, which is then propagated alongside the rest of the remaining shells in the fireball.

Having defined what occurs in an individual two-shell collision, we can track how all of the shells undergo subsequent collisions and dissipate their kinetic energy. The simulation, consisting of shell propagation and collision, continues until either a single shell is left, or all shells are ordered outwards with increasing Lorentz factor, so that no further collisions are possible. The output will be in terms of the collisions (not of the initial shells):

- 1 : $(t_{\text{obs},1}, R_{C,1}, l_{m,1}, \Gamma_{m,1}, E_{\text{coll},1}^{\text{iso}})$
- 2 : $(t_{\text{obs},2}, R_{C,2}, l_{m,2}, \Gamma_{m,2}, E_{\text{coll},2}^{\text{iso}})$

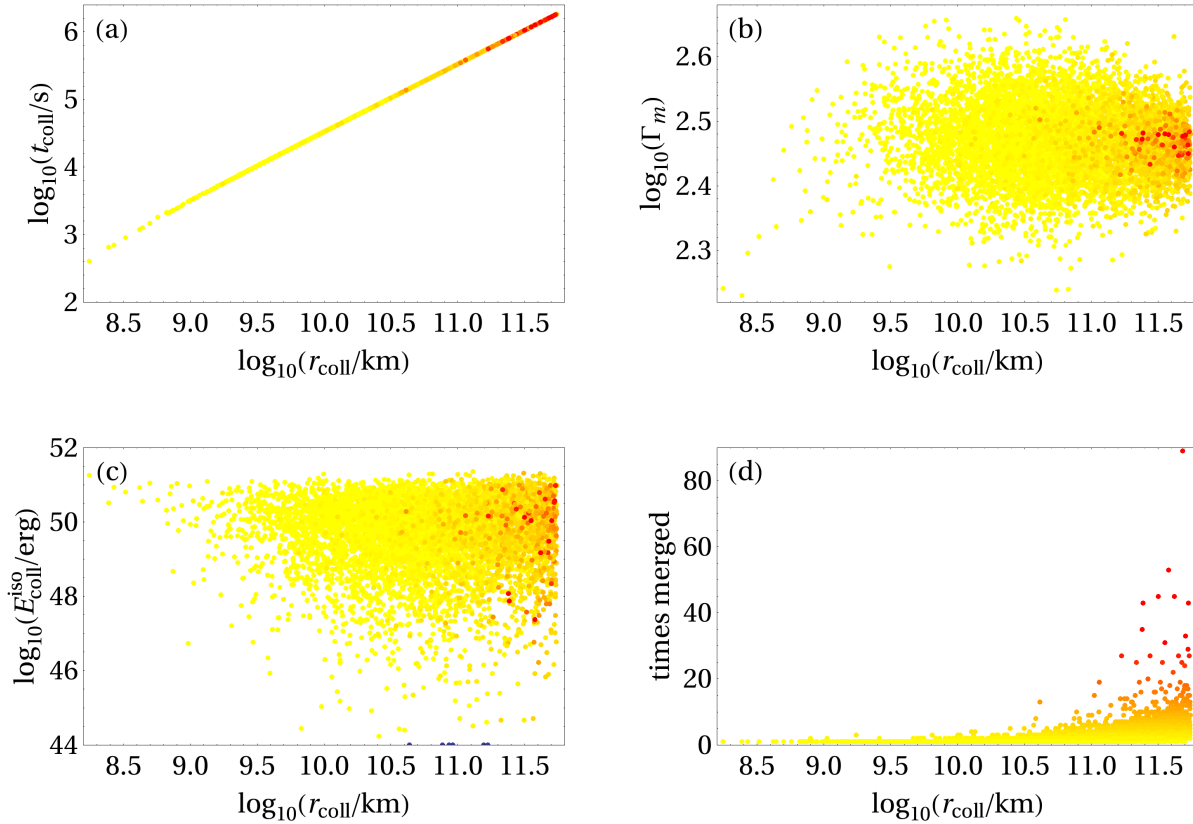


Figure 5.5: Resulting correlations for a single simulation with the following parameters: $N_{\text{sh}} = 10000$, $\Gamma_0 = 300$, $A_\Gamma = 0.2$, $\delta t = 0.01$ s, $d = l$, $z = 2$, and $E_{\text{kin},0}^{\text{iso}} = 10^{52}$ erg. The number of collisions was $N_{\text{coll}} = 7694$. In yellow, we indicate collisions in which the resulting merged shell was created by two shells that had not collided before; as the number of times that the colliding shells have merged increases, the colour of the collision tends to red.

$$\begin{aligned}
 & \vdots \\
 N_{\text{coll}} & : (t_{\text{obs},N_{\text{coll}}}, R_{C,N_{\text{coll}}}, l_{m,N_{\text{coll}}}, \Gamma_{m,N_{\text{coll}}}, E_{\text{coll},N_{\text{coll}}}^{\text{iso}}) \quad (5.22)
 \end{aligned}$$

for N_{coll} collisions. Here, $t_{\text{obs},k}$ is the start time, in the observer's frame, of the emission from the k -th collision, $r_{\text{coll},k}$ is the radius at which the collision happens, $l_{m,k}$ is the width of the merged shell, $\Gamma_{m,k}$ is its Lorentz factor, and $E_{\text{coll},k}^{\text{iso}}$ is its internal energy. Note that we have to set the minimum of t_{obs} to be the origin of the observer's time before we can depict light curves [178, 179] (see section 5.3). After doing this, the final form of the simulation output is given, with the collision numbering set by $t_{\text{obs},1} = 0 \leq t_{\text{obs},2} \leq \dots \leq t_{\text{obs},N_{\text{coll}}}$.

5.2 A few results and correlations

Fig. 5.5 shows correlations between the collision parameters R_C , t_{coll} , Γ_m , and $E_{\text{coll}}^{\text{iso}}$. To obtain these results, a simulation was run with an unusually high number of initial shells ($N_{\text{sh}} = 10000$) so that the correlations can be more clearly appreciated. During the fireball evolution, we have also kept track of the age of each shell, measured as the cumulative number of collisions that have

led to the creation of the shell (at initialisation, the age of all shells is set to zero). The redder the point in Fig. 5.5, the “older” the corresponding merged shell, *i.e.*, the more times it has been involved in collisions.

From Fig. 5.5a, we see that early in the fireball evolution collisions necessarily occur at low radii, since the fireball is still small in size. As the fireball evolves, its expansion allows collisions to occur at increasingly larger radii. There is a sharp cut-off at $\log_{10} r_{\text{dec}} \simeq 11.74$, where shells are removed from the simulation (see section 5.1.3). A tendency for late collisions to occur at larger radii is clearly visible: it is simply the result of the fireball expansion. As indicated by the colour code, late collisions occur predominantly among “old” shells, *i.e.*, shells that are the result of numerous collisions.

Fig. 5.5b shows that the first collisions are the ones where the merged shells have the lowest Lorentz factors. This can be easily explained by recalling that the first collisions occur between those neighbouring shells traveling at speeds that are disparate enough for the faster shell to be able to quickly catch up to the slower one, *i.e.*, where Γ_r is considerably larger than Γ_s . For these first merged shells, then, Eq. (5.15) yields $\Gamma_m \simeq \sqrt{\Gamma_r \Gamma_s m_r / m_s}$. Since the shells involved in these first collisions have not collided before, their masses still have their initial values, *i.e.*, $m_{r(s)} = E_{\text{kin},0}^{\text{iso}} / (\Gamma_{r(s)} c^2)$, so that $\Gamma_m \simeq \Gamma_s$, which is why the first few collisions in Fig. 5.5b are so below the characteristic Lorentz factor. Later in the fireball evolution, collisions between pairs of shells with more similar Lorentz factors become possible. As a result, the central value in the distribution of Γ_m matches the fireball’s characteristic Lorentz factor Γ_0 ($300 \approx 10^{2.5}$ in the plot shown), and the spread in Γ_m grows to reflect the underlying spread in the distribution of Lorentz factors with which the fireball was initialised. Towards the end of the fireball simulation, the spread is reduced as a result of the many collisions –note that many late collisions are among old shells– among shells moving at increasingly similar speeds (in other words, due to the repeated application of Eq. (5.15) with increasingly similar values of Γ_r and Γ_s).

The evolution with collision radius (or, equivalently, time) of the internal energy dissipated in collisions, $E_{\text{coll}}^{\text{iso}}$, is shown in Fig. 5.5c. We see that the first few collisions are all very energetic, with $E_{\text{coll}}^{\text{iso}} \gtrsim 10^{51}$ erg. This is to be expected because, as we have seen, these collisions occur among shell pairs with Γ_r as higher than Γ_s as possible, and they create shells with Lorentz factors $\Gamma_m \simeq \Gamma_s$, so that, according to Eq. (5.14), the internal energy liberated in them is $E_{\text{coll}}^{\text{iso}} \simeq E_{\text{kin},0}^{\text{iso}} (1 - \Gamma_s / \Gamma_r)$. For $A_\Gamma < 1$, the shell population has a mean value of the Lorentz factor $\langle \Gamma \rangle = \Gamma_0$, and a variance $\Delta\Gamma = A_\Gamma \Gamma_0$ (see subsection 5.1.2). In such a case, we can estimate the Lorentz factors of the first colliding shells to be $\Gamma_{r(s)} \simeq \langle \Gamma \rangle \pm \Delta\Gamma = (1 \pm A_\Gamma) \Gamma_0$, with which the ratio $\Gamma_s / \Gamma_r \simeq (1 - A_\Gamma) / (1 + A_\Gamma)$ (this is strictly valid only for the collisions that occur early to about half way through the fireball evolution). For Fig. 5.5c, $A_\Gamma = 0.2$ was used, which entails $\Gamma_s / \Gamma_r \approx 0.67$; hence, the first collisions are expected to liberate $E_{\text{coll}}^{\text{iso}} \approx 0.67 \cdot E_{\text{kin},0}^{\text{iso}} \approx 10^{51.8}$ erg, which roughly agrees with what Fig. 5.5c shows.

As the fireball evolves and collisions between shells moving at similar speeds become possible (*i.e.*, $\Gamma_r \approx \Gamma_s$), the spread in $E_{\text{coll}}^{\text{iso}}$ grows and the liberated energy may be lower, as shown when replacing $\Gamma_m \approx \Gamma_r \approx \Gamma_s$ in Eq. (5.14). The trend towards lower energies agrees with the dilution of total available internal energy $E_{\text{int-tot}}^{\text{iso}} \propto r^{-2/3}$ expected from just the expansion of the fireball (see section 5.1.3 and Fig. 5.7). Finally, late in the fireball evolution, when only a few very massive shells remain, the spread in $E_{\text{coll}}^{\text{iso}}$ is again reduced and most collisions are very energetic, on account of the large masses compensating the small differences $\Gamma_{r(s)} - \Gamma_m$ in Eq. (5.14). Fig. 5.5d clearly shows that collisions among the oldest shells –those with up to 70 previous mergings, for the simulation shown – occur in the outskirts of the fireball, which is to be expected, since, in order for the shells to have been involved in a large number of previous collisions, they must have had

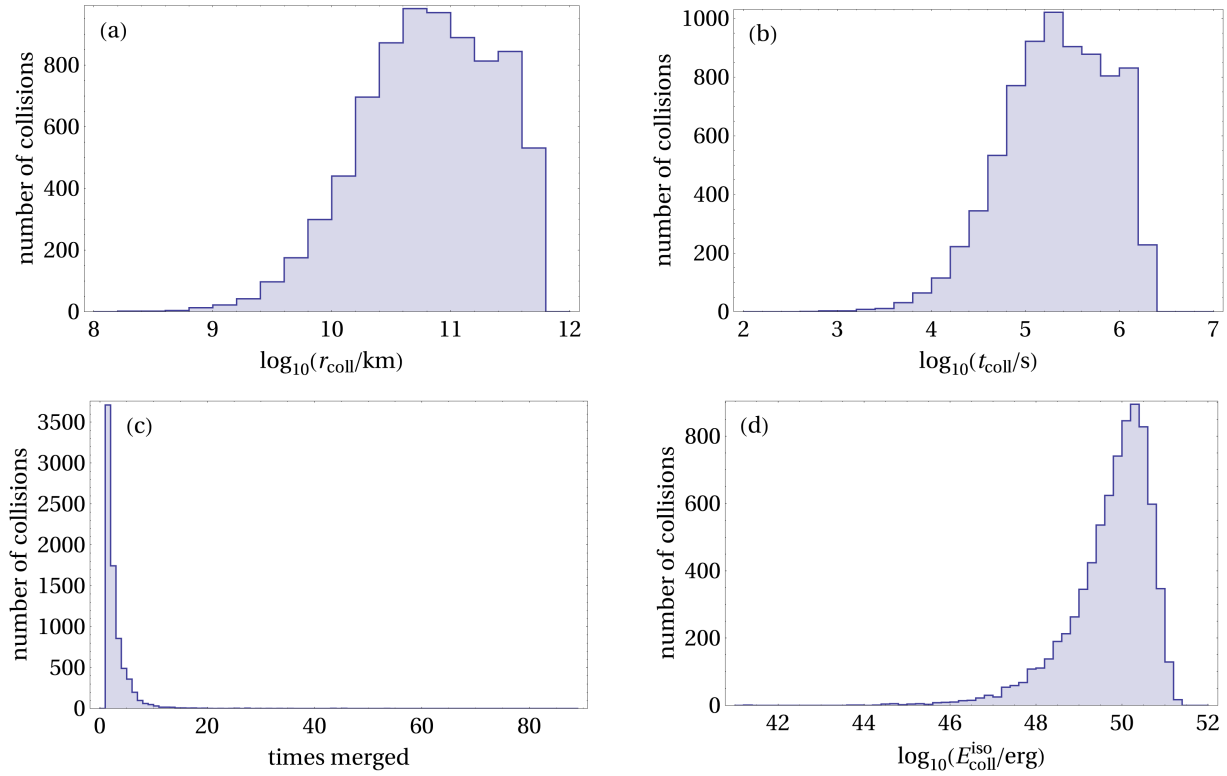


Figure 5.6: Distributions of number of collisions with collision radius, collision time, times merged (“age”), and internal energy of the merged shells. The histograms were produced using the same simulation data as in Fig. 5.5.

traversed most of the fireball.

As a complement to Fig. 5.5 and in agreement with it, Fig. 5.24 depicts the binned distribution of number of collisions in terms of collision radius, collision time, number of previous collisions (“times merged”, or “age”), and internal energy liberated in the collisions for the same test parameter set as in Fig. 5.5. Fig. 5.24a clearly shows that the vast majority of collisions occurs at $R_C \gtrsim 10^{10.5}$ km. There are only few collisions at low radii. This is explained by Fig. 5.24b: except in the uncommon cases in which two neighbouring shells have, at initialisation time, sufficiently different Lorentz factors (with the outer shell being slower) to quickly catch up and merge, it is necessary for some time to pass in order for the first pair of neighbouring shells with similar Lorentz factors to collide. We see this gradual increase in the number of collisions as the fireball evolves, with most collisions occurring after $t_{\text{coll}} \approx 10^5$ s. If a higher value of the Lorentz factor fluctuation A_Γ is used, one expects a faster rise in the number of collisions, since it will be more likely for neighbouring shells to have disparate Lorentz factors. Furthermore, Fig. 5.24c shows that most collisions take place among young shells; the number of collisions among old shells that have merged ten or more times is about two orders of magnitude lower than first-time collisions. Finally, Fig. 5.24d shows that most collisions liberate an internal energy of $E_{\text{coll}}^{\text{iso}} \approx 10^{50.3}$ erg, about two orders of magnitude below the initial bulk kinetic energy of the shells $E_{\text{kin},0}^{\text{iso}} = 10^{52}$ erg.

Fig. 5.7 shows the time evolution of a few macroscopic parameters of the fireball: average shell mass $\langle m \rangle / \langle m_0 \rangle$ (quantities with a zero subscript or superscript denote values at initialisation time), root mean square of the Lorentz factor $\Gamma_{\text{rms}} / \Gamma_{\text{rms}}^0$, and total available internal energy of the fireball

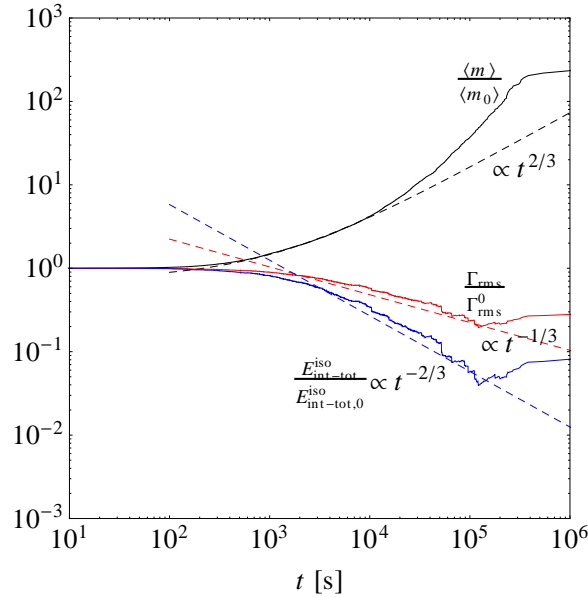


Figure 5.7: Evolution of the average shell mass $\langle m \rangle / \langle m_0 \rangle$, the Lorentz factor rms (root mean square value) $\Gamma_{\text{rms}} / \Gamma_{\text{rms}}^0$, and the total internal energy of the shells, $E_{\text{int-tot}}^{\text{iso}} / E_{\text{int-tot},0}^{\text{iso}}$. The time t is in the source frame. Solid lines are the numerical results from a simulation run with the parameter values $N_{\text{sh}} = 3000$, $\Gamma_0 = 300$, $A_{\Gamma} = 0.2$, $\delta t = 0.001$ s, $d = l$, $z = 2$, and $E_{\text{kin},0}^{\text{iso}} = 10^{52}$ erg, while dashed lines are the power laws predicted analytically in Ref. [185] (compare to Fig. 1 therein).

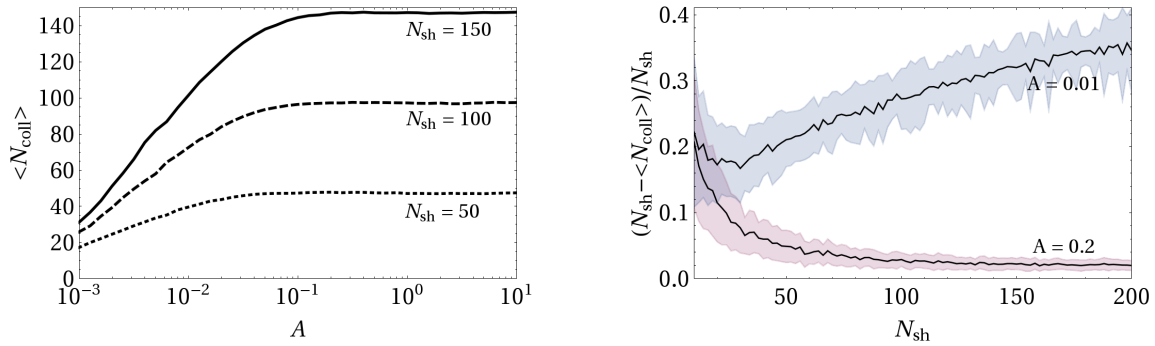


Figure 5.8: *Left:* average number of collisions $\langle N_{\text{coll}} \rangle$ for fireballs with $N_{\text{sh}} = 50, 100$, and 150 initial shells, and varying fluctuation of the Lorentz factor, A_{Γ} . The rest of the parameters are fixed at the same values as in Fig. 5.5. The average number of collisions was obtained by running 100 fireball simulations for each value of A_{Γ} . *Right:* average fraction of remaining shells, $(N_{\text{sh}} - \langle N_{\text{coll}} \rangle) / N_{\text{sh}}$, as a function of N_{sh} . The top and bottom curves correspond to a fixed value of $A_{\Gamma} = 0.01$ and $A_{\Gamma} = 0.2$, respectively. The coloured bands represent the 1σ uncertainty, coming from running 100 simulations at each value of N_{sh} to obtain $\langle N_{\text{coll}} \rangle$.

$E_{\text{int-tot}}^{\text{iso}} / E_{\text{int-tot},0}^{\text{iso}}$. The latter is calculated using Eq. (6) in Ref. [185]:

$$\frac{E_{\text{int-tot}}^{\text{iso}}}{E_{\text{int-tot},0}^{\text{iso}}} \simeq M c^2 \frac{\Gamma_{\text{rms}}^2}{2\Gamma_{\text{CM}}}, \quad (5.23)$$

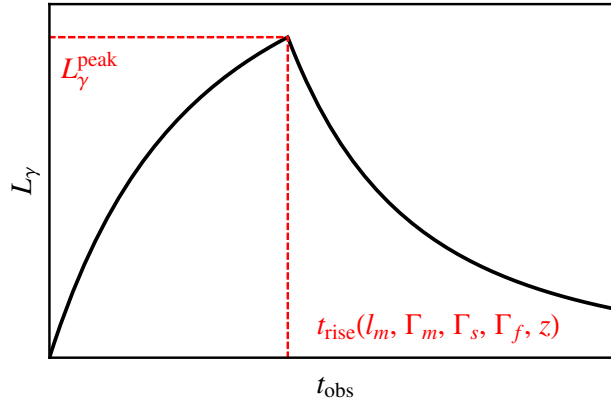


Figure 5.9: A fast-rise-exponential-decay pulse associated to the collision of two shells.

with M the total mass of the fireball and Γ_{CM} the Lorentz factor of its center of mass. Solid lines in Fig. 5.7 are numerical results obtained from running the simulation, while dashed lines are the analytical power-law predictions from Ref. [185]. We see that the fit of the numerical results to these predictions is good; deviations occur at late times, owing to the fact that the remaining number of shells drops and the power-law predictions are no longer applicable.

The left plot of Fig. 5.8 shows that the average number of collisions (obtained from running many simulations, see the figure caption), $\langle N_{\text{coll}} \rangle$, for a fireball with fixed number N_{sh} of initial shells grows with the value of the fluctuation of the Lorentz factor, A_Γ . This can be explained as follows: if A_Γ is low, then all of the shells in the fireball have approximately the same Lorentz factor, which means that only a few of them will catch up with another shell and collide before reaching the deceleration radius r_{dec} and being removed from the simulation. As A_Γ grows, the chance of early collisions increases, since the shells have more disparate speeds and are more likely to bump into each other. For $A_\Gamma \gtrsim 0.1$, a limiting value of $\langle N_{\text{coll}} \rangle$ is reached which is close to the number of initial shells, *e.g.*, $\langle N_{\text{coll}} \rangle \approx 97.5$ for $N_{\text{sh}} = 100$. This means that, for high A_Γ , the halting condition of having a single shell left in the simulation will be satisfied in a larger number of runs.

The related right plot of Fig. 5.8 shows how the average fraction of remaining shells in a fireball, *i.e.*, the number of shells that are left when the simulation stops, varies with N_{sh} , for a fixed value of A_Γ . The top and bottom curves correspond to fireballs with fluctuation parameters $A_\Gamma = 0.01$ and $A_\Gamma = 0.2$, respectively. To understand the behaviour of the curves, it is useful to write the average number of collisions as $\langle N_{\text{coll}} \rangle \simeq N_{\text{sh}} - N_r$, with N_r , the number of remaining shells at halting time, dependent on A_Γ , so that the average fraction of remaining shells can be written as $(N_{\text{sh}} - \langle N_{\text{coll}} \rangle)/N_{\text{sh}} \simeq N_r/N_{\text{sh}}$. From the left plot, we saw that for $A_\Gamma = 0.2$, we obtained $N_r \ll N_{\text{sh}}$ regardless of the value of N_{sh} ; therefore, in this case, $N_r/N_{\text{sh}} \sim 1/N_{\text{sh}}$, as shown by the lower curve in the right plot. In comparison, for lower values of A_Γ , the remaining number of shells N_r is a sizable fraction of N_{sh} ; for $A_\Gamma = 0.01$, in fact, N_r grows faster than linearly with N_{sh} , so that the remaining fraction of shells N_r/N_{sh} grows with N_{sh} . **In conclusion, we see that, in order for the fireball to be efficient (in the sense of colliding as many shells as possible), a fluctuation value of $A_\Gamma \gtrsim 0.1$ is required.**

5.3 Light curves and burst duration

In each internal collision, part of the initial bulk kinetic energy of the colliding shells is radiated away as particles. To each collision we can therefore assign a gamma-ray pulse. Following Ref. [178], we parametrise the time dependence of the observed luminosity pulse (at Earth, *i.e.*, in the observer’s frame) coming from the k -th collision as

$$L_{\gamma,k}(t_{\text{obs}}) = \begin{cases} 0 & , t_{\text{obs}} < 0 \\ h \left[1 - \frac{1}{(1+ct/R_{C,k})^2} \right] & , 0 \leq t_{\text{obs}} < t_{\text{rise}} \\ h \left\{ \frac{1}{[1+(t-\delta t_{e,k})c/R_{C,k}]^2} - \frac{1}{(1+ct/R_{C,k})^2} \right\} & , t_{\text{obs}} \geq t_{\text{rise}} \end{cases} , \quad (5.24)$$

with

$$\delta t_{e,k} \equiv \frac{l_{m,k}}{c(\beta_r - \beta_{rs})} \quad (5.25)$$

the emission timescale of the collision, *i.e.*, the time at which the reverse shock crosses the rapid shell. Eq. (5.24) describes a peaked profile, with a fast rise and exponential decay (“FRED”); see Fig. 5.9 for an illustration. The “rise time”,

$$t_{\text{rise}} \equiv \frac{\delta t_{e,k}}{2\Gamma_{m,k}^2} (1+z) , \quad (5.26)$$

is the time elapsed since the start of the emission until the peak luminosity $L_{\gamma,k}^{\text{peak}} \equiv L_{\gamma,k}(t_{\text{rise}})$ is reached, measured in the observer’s frame (for an illustration, see Fig. 1 in Ref. [178]). The peak value of the luminosity is determined by

$$h = \frac{E_{\gamma\text{-sh},k}^{\text{iso}}}{1+z} \frac{1}{t_{\text{rise}}} = \frac{E_{\gamma\text{-sh},k}^{\text{iso}}}{(1+z)^2} \frac{2\Gamma_{m,k}^2}{\delta t_{e,k}} , \quad (5.27)$$

where $E_{\gamma\text{-sh},k}^{\text{iso}}$ is the energy emitted as photons in the k -th collision (see section 5.3.1). Note that the time t in the source frame is related to t_{obs} through

$$t = \frac{2\Gamma_{m,k}^2 t_{\text{obs}}}{1+z} . \quad (5.28)$$

The “light curve” for a particular burst is thus computed by adding up all the individual luminosity peaks of the N_{coll} collisions, *i.e.*,

$$L_{\gamma}(t_{\text{obs}}) = \sum_{k=1}^{N_{\text{coll}}} L_{\gamma,k}(t_{\text{obs}}) . \quad (5.29)$$

Fig. 5.10 shows results for four simulated bursts; each column corresponds to a different burst (see the caption for the parameter values). From top to bottom, the rows show: temporal distribution (t_{obs}) of internal energy liberated in collisions ($E_{\text{coll}}^{\text{iso}}$), of the rise time of the luminosity peaks (t_{rise}), of peak luminosity ($L_{\gamma,k}^{\text{peak}}$), and light curve of the simulated burst. For this plot, we have unrealistically assumed that all of the liberated energy of the collision is emitted as photons, *i.e.*, $E_{\gamma\text{-sh},k}^{\text{iso}} = E_{\text{coll},k}^{\text{iso}}$.

Experimentally, for a detected GRB, the burst duration T_{90} is defined as the time window during which 90% of the total photon count from a burst is detected, a conventional definition introduced

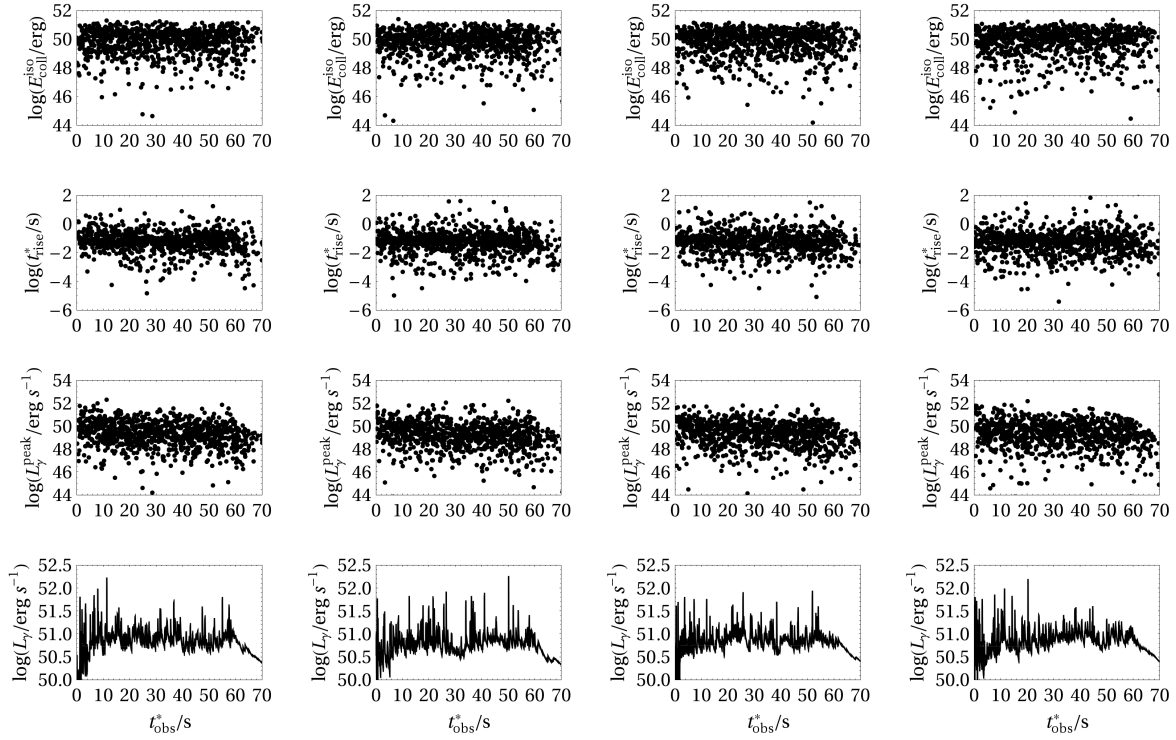


Figure 5.10: Results for four simulated bursts with the parameters $N_{\text{sh}} = 1000$, $\Gamma_0 = 300$, $A_\Gamma = 0.2$, $\delta t = 0.01$ s, $d = l$, $z = 2$, and $E_{\text{kin},0}^{\text{iso}} = 10^{52}$ erg; each column corresponds to a different burst. Rows from top to bottom depict the temporal distribution (t_{obs} is time in the observer’s frame) of internal energy liberated in collisions ($E_{\text{coll}}^{\text{iso}}$), of the rise time of the luminosity peaks (t_{rise}^*), of peak luminosity (L_γ^{peak}), and light curve of the simulated burst. To produce this plot, we have unrealistically assumed that all of the liberated energy of the collision is emitted as photons, *i.e.*, $E_{\gamma\text{-sh},k}^{\text{iso}} = E_{\text{coll},k}^{\text{iso}}$.

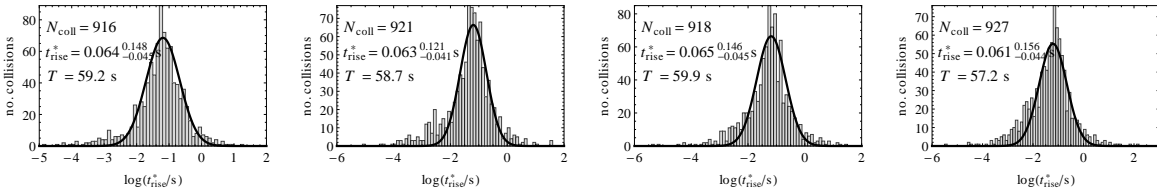


Figure 5.11: Distribution of rise time for the collisions of the four bursts shown in Fig. 5.10. The fit to a Gaussian distribution (thick black line), its mean value, and the standard deviation are shown for each. The variability time is estimated as $t_v = \bar{t}_{\text{rise}}$ (Eq. (5.30)), and the burst duration, as $T = \bar{t}_{\text{rise}} N_{\text{coll}}$ (Eq. (5.31)). See the main text for details.

by the BATSE experiment, which defined T_{90} as the time between which 5% and 95% of the photon count was detected [186]. In our simulated bursts, we do not count individual photons, so we need to fashion an alternative measure of burst duration that resembles the experimental, “real” T_{90} as closely as possible.

In Fig. 5.11 we show the frequency distribution of t_{rise} values (in logarithmic scale) for the collisions of the same four simulated bursts from Fig. 5.10. As a result of fitting to each a Gaussian distribution (thick black curve), we have found the central value \bar{t}_{rise} for each simulated burst, and its standard deviation⁷. We can use the central value as an estimate of the variability time of our simulated bursts, *i.e.*,

$$t_v = \bar{t}_{\text{rise}} . \quad (5.30)$$

From here, we can estimate the burst duration as

$$T = \bar{t}_{\text{rise}} N_{\text{coll}} . \quad (5.31)$$

For the bursts shown in Fig. 5.11, we obtain a value of $t_{v,1} \approx 0.06$ s and of T between 52 s and 60 s. By comparison to the corresponding light curves (bottom row of Fig. 5.10), we see that it is precisely at $t_{\text{obs}} = T$ when the quick succession of luminosity peaks characteristic of a GRB light curve ceases, and a final exponential fall sets in, with only a few final low-energy collisions. Therefore, Eq. (5.31) seems initially to be a good estimator for the burst duration (see, however, Fig. 5.12 and the associated comments). Furthermore, notice that the estimated values of t_v and T lie close to the “standard assumptions” for these bursts, $t_v^{\text{std}} = (1+z)(l+d)/c = 2\delta t(1+z) = 0.06$ and $T^{\text{std}} = N_{\text{coll}} t_v^{\text{std}} \approx 55 - 56$ s.

In Fig. 5.12, we show light curves for different values of the Lorentz factor fluctuation A_Γ . Two features are salient: first, that the normalisation of the light curve grows with A_Γ and, second, that the estimated burst duration, T , decreases with A_Γ (except for $A_\Gamma = 5$, where our predictions break down). Both observations are in agreement with what was detailed in the previous section (see Fig. 5.8 and the corresponding text): in bursts with low A_Γ , all the shells have similar speeds, and a long time is needed for neighbouring shells to catch up to each other and collide, *i.e.*, T is larger and collisions occur only after shells have lost a sizable fraction of their available internal energy during propagation (recall that the total internal energy of the burst falls as $r^{-2/3}$). Conversely, in bursts with higher A_Γ , shell speeds are more disparate, collisions occur early, while the shells still have high internal energy, and so T is smaller. Notice, however, that when $A_\Gamma \lesssim 0.1$ or $A_\Gamma \gtrsim 0.5$, the calculated value of T no longer corresponds to the end of the multi-peaked emission phase of the light curve; *e.g.*, for $A_\Gamma = 0.5$, we see that this phase lasts until $t_{\text{obs}} \approx 60$ s, while the estimated $T \approx 112$ s. The disparity worsens for $A_\Gamma > 1$. This reflects the fact that, as A_Γ rises, the distribution of rise times t_{rise} of the burst’s collisions widens, *i.e.*, the standard deviation of the estimated t_{rise} grows. Since T is estimated using only the mean value \bar{t}_{rise} (Eq. (5.31)), it therefore becomes less representative of the true burst duration as A_Γ grows.

We have found, however, that the estimator T defined in Eq. (5.31) accurately estimates the duration of our simulated bursts *only* for low values of A_Γ , close to 0.2. For higher values of A_Γ , it grossly underestimates the burst duration. We have therefore introduced an alternative duration estimator, T_{90} , defined as the time that elapses between the times t_5 and t_{95} at which, respectively, 5% and 95% of the total radiated gamma-ray energy has been emitted, *i.e.*,

$$T_{90} = t_{95} - t_5 , \quad (5.32)$$

⁷Notice that the errors in \bar{t}_{rise} are asymmetric because the Gaussian is fit to the distribution of t_{rise}^* on a logarithmic scale. A symmetric error could be obtained by fitting the Gaussian instead to the distribution on a linear scale.

with⁸

$$\int_0^{t_5} L_\gamma(t_{\text{obs}}) dt_{\text{obs}} = 0.05 \frac{E_{\gamma\text{-tot}}^{\text{iso}}}{1+z}, \quad \int_0^{t_{95}} L_\gamma(t_{\text{obs}}) dt_{\text{obs}} = 0.95 \frac{E_{\gamma\text{-tot}}^{\text{iso}}}{1+z}. \quad (5.33)$$

Here, the total radiated energy in photons is calculated as

$$E_{\gamma\text{-tot}}^{\text{iso}} = \sum_{k=1}^{N_{\text{coll}}} E_{\gamma\text{-sh},k}^{\text{iso}} \quad (5.34)$$

and $E_{\gamma\text{-sh},k}^{\text{iso}} = \epsilon_e E_{\text{coll},k}^{\text{iso}}$ is the energy emitted as photons in the k -th collision, with ϵ_e the fraction of the total energy made up of photons. The variability timescale can then be simply computed as

$$t_v = T_{90}/N_{\text{coll}}. \quad (5.35)$$

We have tested that the values of T_{90} and t_v thus calculated for several simulated bursts closely match the values obtained from the “standard relations” of the internal shock model (Eqs. (5.40) and (5.41)), and accurately approximate the duration of the light curves by visual inspection.

Fig. 5.13 shows light curves for different values of the ratio between the initial width (l) and separation (d) of the shells. In this case, the duration of the multi-peaked emission phase grows with d/l , since, as the initial separation grows, shells need to travel longer before they collide. For the largest ratios ($d/l = 5, 10$), a drop in the normalisation of the light curve is evident: shells have lost a large part of their internal energy by the time they collide.

Finally, for completeness, Fig. 5.14 shows light curves for six different values of the emitter uptime, $\delta t = 0.001, 0.005, 0.01, 0.1, 1$, and 10 s. As expected, the burst duration, and its estimation by means of T_{90} , grow with δt , since we have set the initial separation between shells to be $d \propto l = c\delta t$. This occurs because in our simulations we have fixed the initial number of shells to a set value, which limits the maximum possible number of collisions. By removing this fixed constraint, however, for a given value of δt , we could of course find a value of N_{sh} that will yield a desired burst duration.

5.3.1 Normalising the photon spectrum

As a result of the simulation, we know the distribution of gamma-ray energy $E_{\gamma\text{-sh},k}^{\text{iso}} \approx \epsilon_e E_{\text{coll},k}^{\text{iso}}$ of the burst, where $E_{\gamma\text{-sh},k}^{\text{iso}}$ is the energy radiated as gamma-rays by the k -th collision⁹. One possibility is to assume energy equipartition between electrons and photons, magnetic field, and protons, *i.e.*, $\epsilon_e = \epsilon_B = \epsilon_p = 1/3$, with ϵ_e , ϵ_B , and ϵ_p , respectively, the fraction of liberated energy carried by electrons, the magnetic field, and protons. **We have instead used $\epsilon_e = \epsilon_B = 1/12$ and**

⁸For the numerical computation of t_5 and t_{95} , we have actually used the following:

$$k_5 = \operatorname{argmin}_k \left[\left(\sum_{j=1}^k \frac{E_{\gamma\text{-sh},j}^{\text{iso}}}{1+z} \right) - 0.05 \frac{E_{\gamma\text{-tot}}^{\text{iso}}}{1+z} \right], \quad t_5 = t_{\text{obs},k_5},$$

$$k_{95} = \operatorname{argmin}_k \left[\left(\sum_{j=1}^k \frac{E_{\gamma\text{-sh},j}^{\text{iso}}}{1+z} \right) - 0.95 \frac{E_{\gamma\text{-tot}}^{\text{iso}}}{1+z} \right], \quad t_{95} = t_{\text{obs},k_{95}}.$$

⁹Note that when producing the sample light curves in Figs. 5.10, 5.12, 5.13, and 5.14 we have unrealistically assumed $\epsilon_e = 1$, so that all of the emitted energy is in photons. For our main results, however, we have used $\epsilon_e = \epsilon_B = 1/12$, $\epsilon_p = 5/6$, as explained in the main text.

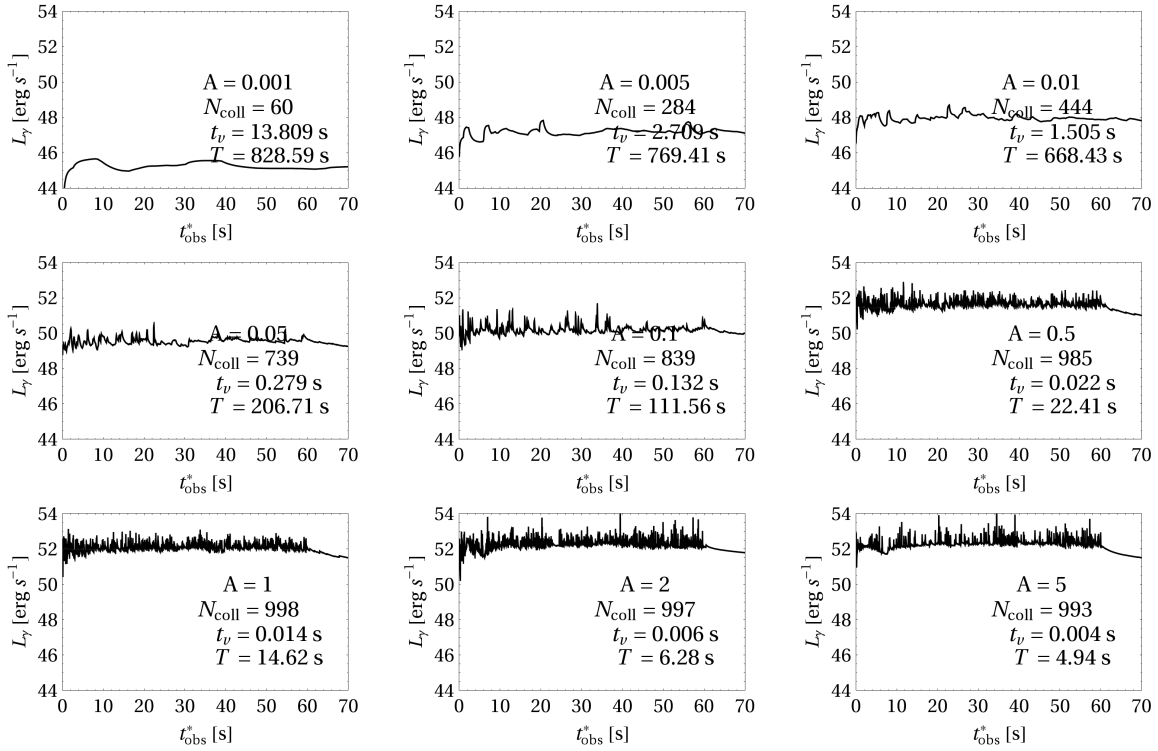


Figure 5.12: Simulated light curves for different values of the fluctuation of the Lorentz factor, A_Γ . The following values for the remaining fireball parameters were used: $N_{\text{sh}} = 1000$, $\Gamma_0 = 300$, $\delta t = 0.01$ s, $d = l$, $z = 2$, and $E_{\text{kin},0}^{\text{iso}} = 10^{52}$ erg. For this plot, we have unrealistically assumed that all of the liberated energy of the collision is emitted as photons, *i.e.*, $E_{\gamma\text{-sh},k}^{\text{iso}} = E_{\text{coll},k}^{\text{iso}}$. The values of t_v and T were calculated using Eqs. (5.31) and (5.30), and *not* the correct ones, Eqs. (5.32) and (5.35), and are included here only for illustration.

$\epsilon_p = 5/6$, since this yields the standard value of the baryonic loading, $1/f_e = \epsilon_p/\epsilon_e = 10$. Then, the normalisation of the $E_{\gamma\text{-sh},k}^{\text{iso}}$ distribution is determined by

$$\sum_{k=1}^{N_{\text{coll}}} E_{\gamma\text{-sh},k}^{\text{iso}} \equiv E_{\gamma\text{-tot}}^{\text{iso}} = \epsilon_e E_{\text{tot}}^{\text{iso}}, \quad (5.36)$$

where the total (isotropic) energy in gamma-rays, $E_{\gamma\text{-tot}}^{\text{iso}}$, is an experimentally accessible quantity and the total liberated energy of the burst, $E_{\text{tot}}^{\text{iso}}$, is calculated from the individual liberated energies of each collision in our simulated burst. The cosmic-ray energy is also introduced by $E_{\text{cr-sh},k}^{\text{iso}} \approx (1/f_e) E_{\gamma\text{-sh},k}^{\text{iso}}$.

Following Ref. [181], we can assume that the distribution of photons in the shock rest frame (SRF) is given by a broken power law function, *i.e.*,

$$n'_\gamma(\epsilon') \equiv \frac{dn'_\gamma}{d\epsilon'} = C'_\gamma \begin{cases} \left(\epsilon'/\epsilon'_{\gamma,\text{break}}\right)^{-\alpha_\gamma} & , \quad \epsilon' < \epsilon'_{\gamma,\text{break}} \\ \left(\epsilon'/\epsilon'_{\gamma,\text{break}}\right)^{-\beta_\gamma} & , \quad \epsilon' \geq \epsilon'_{\gamma,\text{break}} \end{cases}, \quad (5.37)$$

where C'_γ is a normalisation constant to be determined for each collision. The input required for the calculation following Ref. [106] is $E_{\text{coll},k}^{\text{iso}}$, $\Gamma_{\text{coll},k}$, $R_{C,k}$, *etc.* For instance, Eq. (15) in Ref. [106]

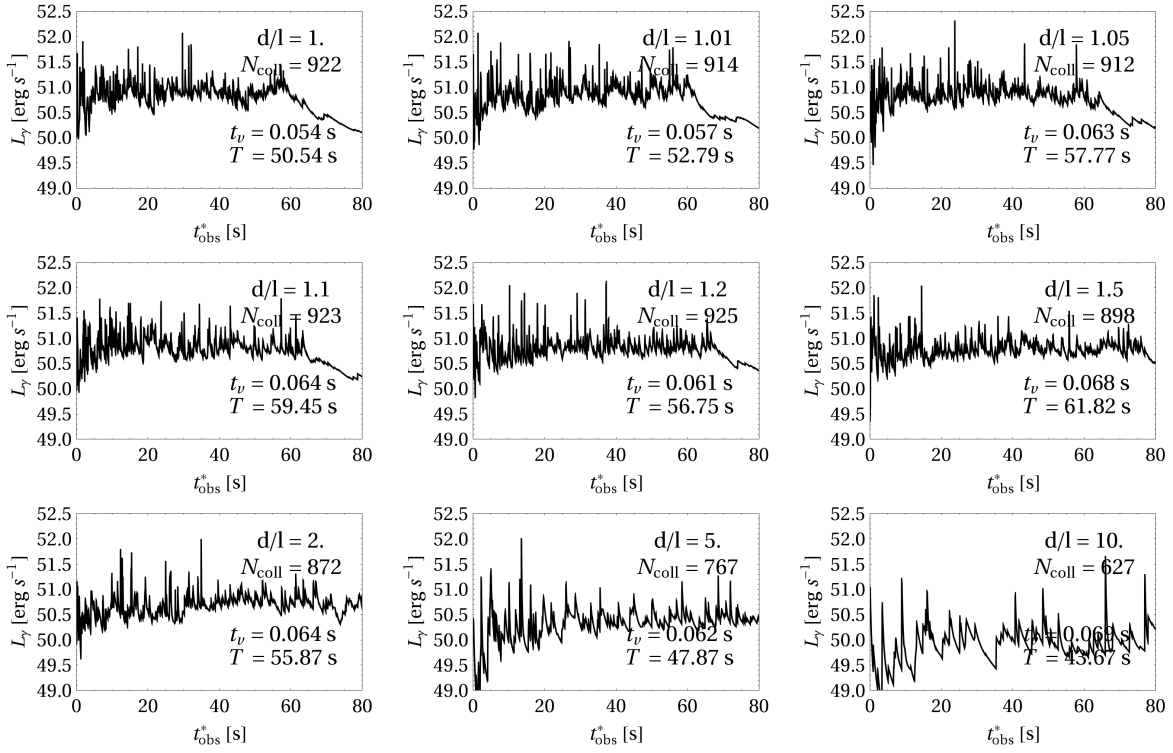


Figure 5.13: Simulated light curves for different values of the ratio between the initial width (l) and separation (d) of the shells. For the rest of the parameters, the same values as in Fig. 5.12 were used, with fixed $A_{\text{r}} = 0.2$.

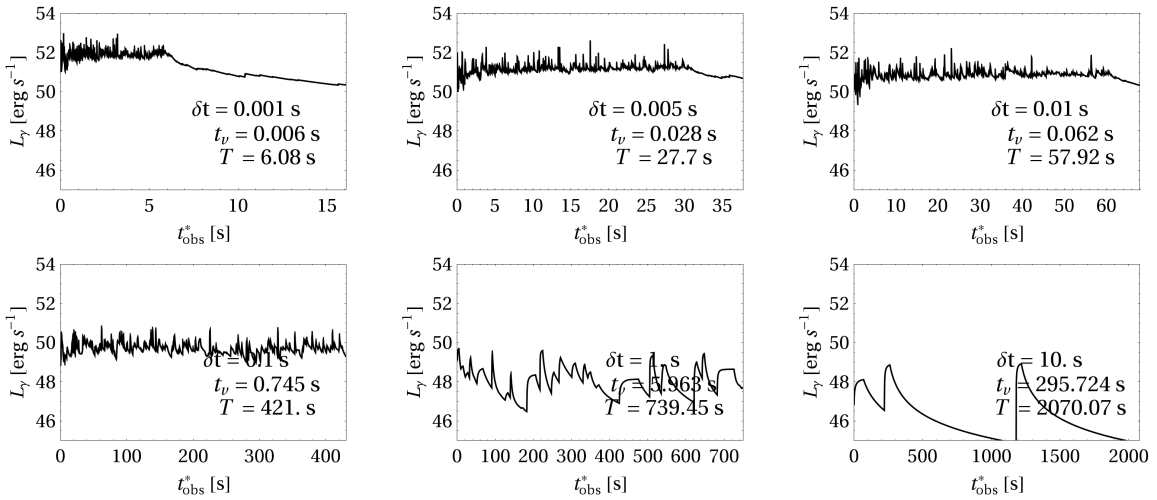


Figure 5.14: Simulated light curves for different values of the emitter uptime, δt . For the rest of the parameters, the same values as in Fig. 5.12 were used, with fixed $A_{\text{r}} = 0.2$.

changes into (primed quantities are in the shock rest frame)

$$\int \varepsilon' n'_\gamma(\varepsilon') d\varepsilon' = \frac{\epsilon_e E'_{\text{coll},k}}{V'_{\text{iso},k}}, \quad \int E'_p n'_p(E'_p) dE'_p = \frac{\epsilon_p E'_{\text{coll},k}}{V'_{\text{iso},k}} = \frac{1}{f_e} \frac{E'_{\gamma\text{-sh},k}}{V'_{\text{iso},k}}, \quad (5.38)$$

where $V'_{\text{iso},k}$ is given by

$$V'_{\text{iso},k} = 4\pi R_{C,k}^2 l'_{m,k} = 4\pi R_{C,k}^2 \Gamma_{m,k} l_{m,k} . \quad (5.39)$$

This normalisation procedure is carried out separately for each collision, using its particular parameter values. Using the formalism in Ref. [106], one can then easily calculate the neutrino or neutron fluence (or the injection into the interstellar medium) per collision and time.

The spectral indices α and β remain fixed at, *e.g.*, $\alpha_\gamma = 1$ and $\beta_\gamma = 2.2$. The minimum and maximum energies are set to $\varepsilon'_{\gamma,\text{min}} = 0.2 \text{ eV}$ and $\varepsilon'_{\gamma,\text{max}} = 1 \text{ PeV}$, respectively, in accordance with [181]. However, pair production, through the processes $\gamma\gamma \rightarrow e^+e^-$ and $e\gamma \rightarrow ee^+e^-$, will damp the photon spectrum and drive down the maximum energy (see appendix E). The break energy¹⁰ is set at $\varepsilon'_{\gamma,\text{break}} = 1 \text{ keV}$.

5.4 Detailed study of a simulated burst

In this section, we will focus on one simulated bursts and study the gamma-ray, UHECR, and neutrino emission coming from it. Table 5.2 shows the run parameters and results for our selected model including, for the latter, the number of collisions, burst duration (Eq. (5.32)), variability time (Eq. (5.35)), total radiated energy *in photons*, $E_{\gamma\text{-tot}}^{\text{iso}}$, and total radiated energy *in all particles*, $E_{\text{tot}}^{\text{iso}}$. The gamma-ray energy $E_{\gamma\text{-sh},k}^{\text{iso}}$ radiated in each collision was calculated by assuming the energy fractions $\epsilon_e = \epsilon_B = 1/12$, $\epsilon_p = 5/6$, which yield a baryonic loading of $1/f_e = \epsilon_p/\epsilon_e = 10$ (see section 5.3.1). For the calculation of the UHECR and neutrino spectra, we have assumed an acceleration efficiency of $\eta = 1$.

The table also shows the expected values of some of the burst parameters that are predicted by the standard relations of the internal shock model, namely¹¹,

$$t_v^{\text{std}} = \frac{d+l}{c} (1+z) \quad (5.40)$$

$$T^{\text{std}} = N_{\text{coll}} t_v^{\text{std}} \quad (5.41)$$

$$\Gamma_m^{\text{std}} = \langle \Gamma_m \rangle \quad (5.42)$$

$$R_C^{\text{std}} = 2 \left(\Gamma_m^{\text{std}} \right)^2 \frac{ct_v^{\text{std}}}{1+z} \quad (5.43)$$

$$E_{\gamma\text{-sh}}^{\text{iso,std}} = E_{\gamma\text{-tot}}^{\text{iso}} / N_{\text{coll}} . \quad (5.44)$$

We have kept track of the different parameters of the burst during its evolution and we show them here, in Fig. 5.15, with respect to time in the observer's frame; in Fig. 5.16, with respect to collision radius; and in Fig. 5.17, as the distributions. For illustration purposes, in Fig. 5.18 here we show the light curve, taking into account superphotospheric collisions only, *i.e.*, those from which the gamma-rays are able to escape (see below).

Once the simulation has been run, we can calculate the UHECR and neutrino spectra for each collision, using its own particular set of parameters, and assuming the two-component emission

¹⁰It is uncertain how $\varepsilon'_{\gamma,\text{break}}$ changes with R_C , since the scaling expected in the internal shock model has a problem [184]. Probably, we could introduce the temporal behavior phenomenologically by a power law.

¹¹An alternative definition of t_v^{std} is $t_v^{\text{std}} = \delta t (1+z)$, which, for $l = d = c\delta t$, would reduce the values of t_v^{std} and T^{std} by a factor of 2, worsening the agreement with our numerical estimations. We keep the definition as is, so that our numerical results agree nicely with what we have defined as ‘‘standard relations’’.

Parameter	Value
Fireball initialisation	
N_{sh}	1000
δt [s]	0.01
A_{Γ}	1.0
$\log_{10} \left(E_{\text{kin},0}^{\text{iso}} / \text{erg} \right)$	51.59
Γ_0	300
d/l	1
Simulation results	
N_{coll}	990
T_{90} [s]	58.85
t_v [s]	$5.94 \cdot 10^{-2}$
$\log_{10} \left(E_{\gamma\text{-tot}}^{\text{iso}} / \text{erg} \right)$	53
$\log_{10} \left(E_{\text{tot}}^{\text{iso}} / \text{erg} \right)$	54.08
Standard expectation	
$\log_{10} \left(R_C^{\text{std}} / \text{km} \right)$	9.21
$\log_{10} \left(E_{\gamma\text{-sh}}^{\text{iso,std}} / \text{erg} \right)$	50.00
Γ_m^{std}	368.6
t_v^{std} [s]	$6.00 \cdot 10^{-2}$
T^{std} [s]	59.40

Table 5.2: Parameters and simulation results for our chosen simulated burst. We have fixed $l = c\delta t$, $r_{N_{\text{sh}}} = 10^3$ km, $z = 2$, $r_{\text{dec}} = 5.5 \cdot 10^{11}$ km, $\epsilon_e = \epsilon_B = 1/12$, and $\epsilon_p = 5/6$. The total initial kinetic energy of the burst is $E_{\text{kin},0}^{\text{iso}} \cdot N_{\text{sh}} = 10^{54.59}$ erg.

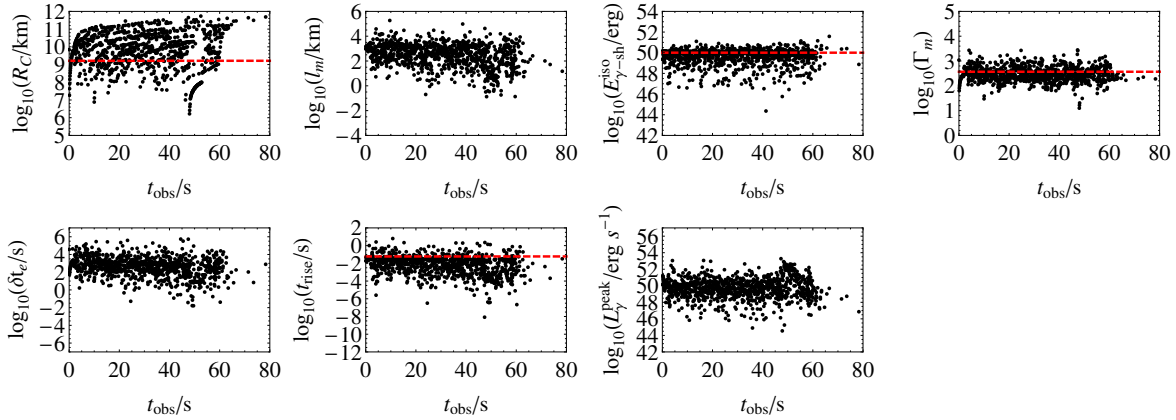


Figure 5.15: Evolution with t_{obs} , the time in the observer's frame, of the parameters of our simulated burst.

model from chapter 2. Fig. 5.19 shows the neutrino fluence (left panel), the maximum proton energy (central panel), and the maximum photon energy (right panel) for each collision of our model. Three different types of collisions are distinguished: depending on the dominant UHECR component, collisions can be dominated by neutron escape (red filled circles) or by direct proton escape (blue empty circles). In our model, 48 collisions are neutron escape-dominated, and 861 are direct proton escape-dominated. Additionally, we distinguish subphotospheric collisions (black

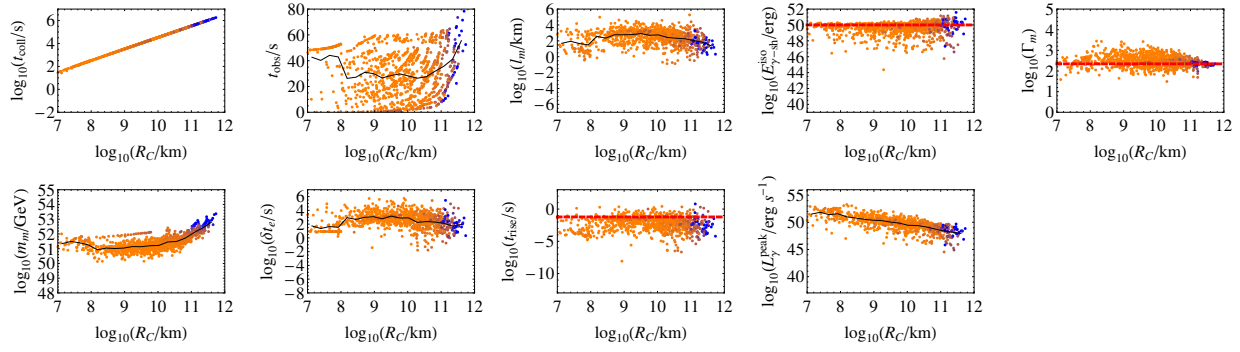


Figure 5.16: Evolution with R_C , collision radius, of the parameters of our simulated burst.

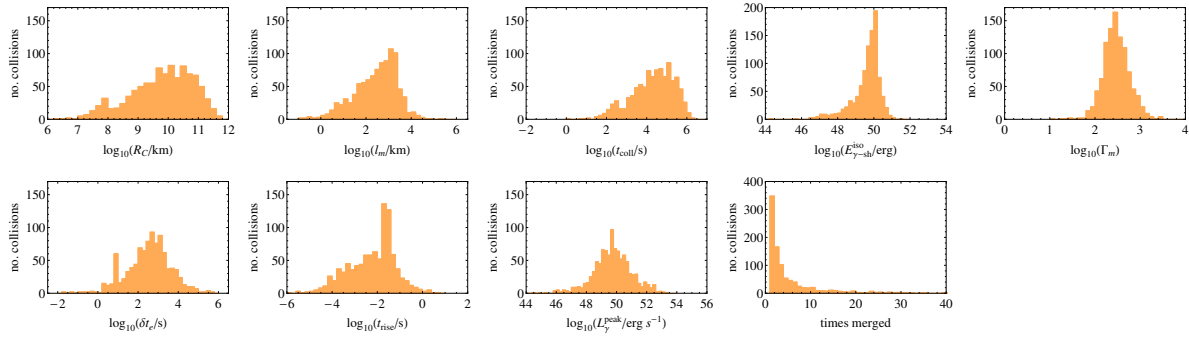


Figure 5.17: Distribution of the different GRB parameters of our simulated burst.

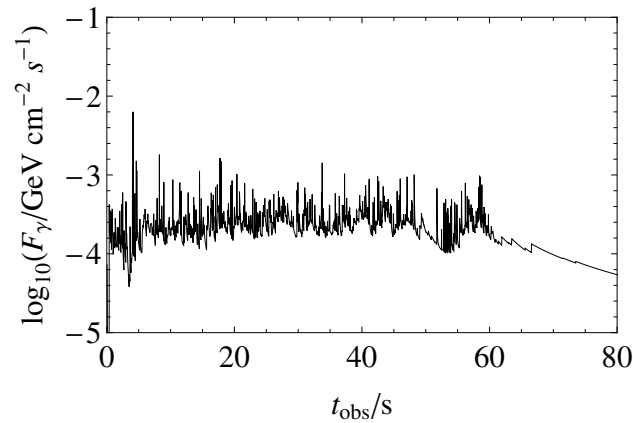


Figure 5.18: Simulated light curve from (superphotospheric) collision of shells in our simulated burst (model G'). A redshift of $z = 2$ was assumed to produce this light curve.

squares). In these, the Thomson optical depth for $e\gamma$ scattering is larger than unity and, as a consequence, photons are not able to escape the newly formed shell after the collision. The

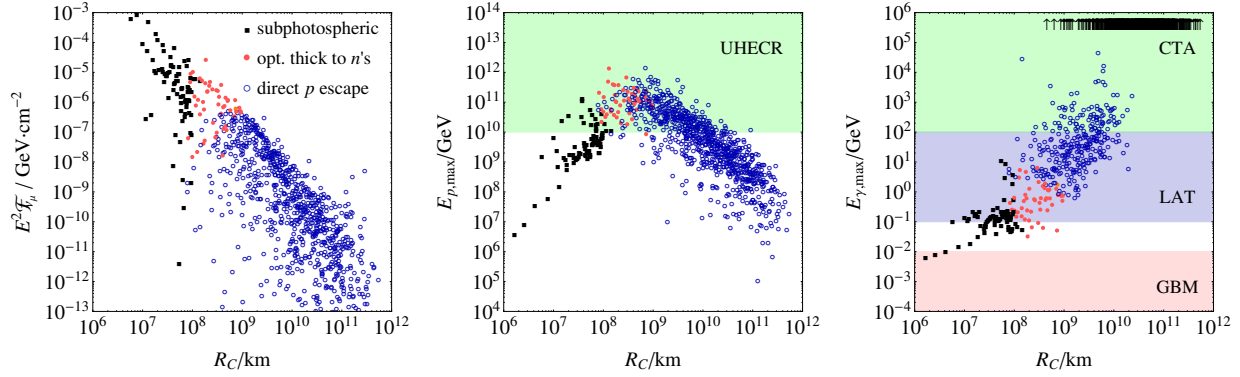


Figure 5.19: From left to right: muon-neutrino fluence (in the observer’s frame), maximal proton energy (in the source frame), and maximally allowed gamma-ray energy (in the source frame, where $\tau_{\gamma\gamma}(E_{\gamma,\max}) = 1$) as a function of the collision radius. Each dot represents one collision: red filled dots represent collisions where cosmic rays protons escape as neutrons, blue empty circles represent collisions where cosmic ray leakage dominates over the neutron model, and black boxes denote subphotospheric collisions or collisions where this picture cannot be maintained (*i.e.*, where the Thomson optical depth is large). In the right panel, the energy ranges which can be reached by the *Fermi*-GBM, *Fermi*-LAT, and Cerenkov Telescope Array (CTA) instruments are illustrated as colored bands. Collisions in which photons are able to escape with energies above 10^6 GeV are marked as upward-pointing arrows.

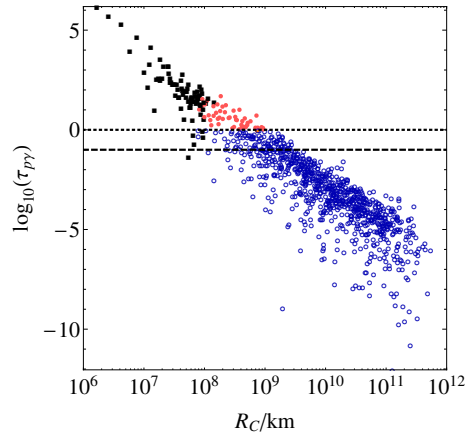


Figure 5.20: Evolution of the photohadronic ($p\gamma$) optical depth for the different collisions, as a function of collision radius R_C .

Thomson optical depth for the k -th merged shell is calculated as

$$\tau_{T,k} = \sigma_T n'_{e,k} l'_{m,k}, \quad (5.45)$$

with $\sigma_T \approx 6.65 \cdot 10^{-25}$ cm² the Thomson cross section and $n'_{e,k}$ the electron density (cm⁻³). We have estimated the latter by assuming that the shell is, on the whole, electrically neutral, so that

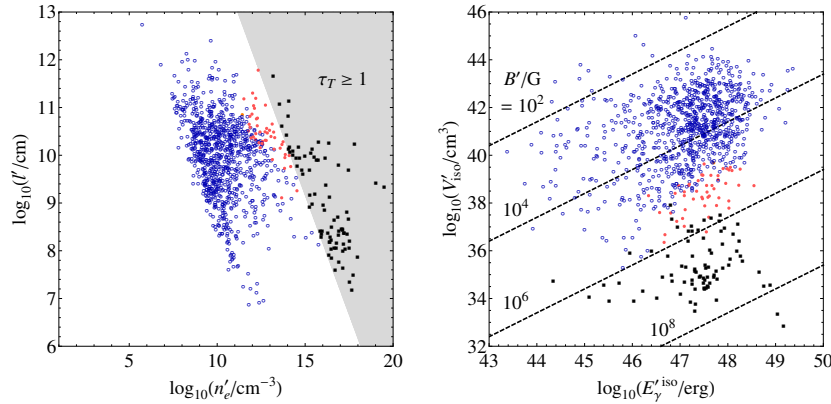


Figure 5.21: *Left:* Collisions arranged in the n'_e vs. l' plane. Within the region coloured gray, the Thomson optical depth is larger than 1 and, accordingly, the collisions within it are marked as subphotospheric. *Right:* Collisions arranged in the $E_{\gamma\text{-sh}}^{\text{iso}}$ plane, showing that, at the photosphere, merged shells have magnetic fields of around 10^6 G.

electron and proton densities are roughly equal, *i.e.*, $n'_e \approx n'_p$. From this, and from the expression for the mass of the shell, $m_k = m_p n'_p V'_{\text{iso}-m,k} + m_e n'_e V'_{\text{iso}-m,k}$, we can write the electron density as

$$n'_e \simeq \frac{m_k}{m_p + m_e} \frac{1}{V'_{\text{iso}-m,k}} \simeq \frac{m_k}{m_p} \frac{1}{V'_{\text{iso}-m,k}}. \quad (5.46)$$

The photosphere is defined as the radius at which the Thomson optical depth is one. In our chosen model, 80 out of the 990 collisions are subphotospheric, that is, they have $\tau_{T,k} > 1$ and photons scatter within the shell rather than escape out of it. Clearly, they occur at low collision radii, since it is here where the shell masses are higher and the shell volumes are smaller. Our neutrino calculations break down below the photosphere; therefore, when we later calculate the neutrino spectra from our simulated burst, we will consider only subphotospheric collisions.

The left panel of Fig. 5.19 clearly shows that most of the neutrino signal comes from low radii, where usually the energy liberated in the collision is higher (see the $E_{\text{coll}}^{\text{iso}}$ vs. R_C scatter plot in Fig. 5.16) and where the proton and photon densities are larger, which leads to the occurrence of many neutrino-producing photohadronic interactions, within the neutron escape regime. The densities decrease with collision radius, and the collisions eventually reach the direct proton escape regime. This is precisely what is shown in Fig. 5.20, where it is clear that the optical depth to photohadronic interactions, $\tau_{p\gamma}$, falls with collision radii, and where the transition from neutron escape-dominated collisions to direct proton escape-dominated collisions at $\tau_{p\gamma} = 1$ can be appreciated. For comparison, the value of $\tau_{p\gamma} = 0.1$ used in the standard calculations has been included (dashed line). Fig. 5.20 reveals that all of the neutron escape-dominated collisions have higher values of $\tau_{p\gamma}$, with eighteen of them having $\tau_{p\gamma} > 5$. The highest optical depth for a superphotospheric collision is close to 50, and it turns out that this will be the single most dominant collision for neutrino production.

The behaviour of $E_{p,\text{max}}$ in the central panel of Fig. 5.19 shows that it initially grows, up to $R_C \approx 10^{8.5}$ km, and then decreases. The kink coincides with the transition from neutron escape to direct proton escape. Below $R_C \approx 10^{8.5}$ km, most of the collisions are limited by synchrotron losses, while adiabatic losses limit the collisions at larger radii. It is possible to derive this change

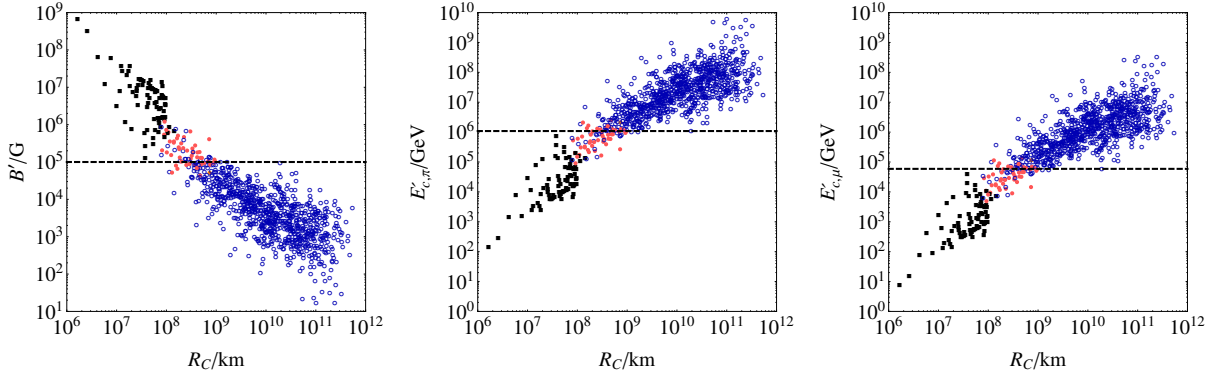


Figure 5.22: Evolution in R_C of the magnetic field (left), synchrotron critical energy of pions (center), and of muons (right). The dashed lines mark the standard values commonly employed within the static burst approximation: $B' = 10^5$ G, $E'_{c,\pi} \approx 10^6$ GeV, and $E'_{c,\pi} \approx 6 \cdot 10^4$ GeV.

in behavior from analytical considerations. The magnetic field in a merged shell can be written as (similar to Eq. (16) in Ref. [106])

$$B'_m = \sqrt{8\pi \frac{\epsilon_B}{\epsilon_e} \frac{E'_{\gamma\text{-sh}}{}^{\text{iso}}}{V'_{\text{iso}-m}}} \propto \frac{\sqrt{E'_{\gamma\text{-sh}}{}^{\text{iso}}}}{R_C}. \quad (5.47)$$

With this, we can approximate the timescales associated to the acceleration and energy loss processes as [106]

$$t'_{\text{acc}}(E'_p) = \frac{E'_p}{\eta c e B'} \propto \frac{E'_p R_C}{\sqrt{E'_{\gamma\text{-sh}}{}^{\text{iso}}}} \quad (5.48)$$

$$t'_{\text{syn}}(E'_p) = \frac{9m^4}{4ce^4 B'^2 E'_p} \propto \frac{R_C^2}{E'_p E'_{\gamma\text{-sh}}{}^{\text{iso}}} \quad (5.49)$$

$$t'_{\text{ad}} = l'/c = \text{const.} \quad (5.50)$$

In the neutron escape regime, synchrotron losses are the dominant ones, so we can estimate that the maximum proton energy associated to individual shell collisions varies with collision radius as

$$t'_{\text{acc}}(E'_{p,\text{max}}) = t'_{\text{syn}}(E'_{p,\text{max}}) \Rightarrow E'_{p,\text{max}} \propto R_C^{1/2} (E'_{\gamma\text{-sh}}{}^{\text{iso}})^{-1/4} \quad (\text{neutron escape regime}). \quad (5.51)$$

On the other hand, in the direct proton escape regime, adiabatic losses are dominant, and so

$$t'_{\text{acc}}(E'_{p,\text{max}}) = t'_{\text{ad}} \Rightarrow E'_{p,\text{max}} \propto R_C^{-1} (E'_{\gamma\text{-sh}}{}^{\text{iso}})^{1/2} \quad (\text{direct proton escape regime}). \quad (5.52)$$

These overall trends for the two regimes can indeed be observed in the central panel of Fig. 5.19. The actual behavior is slightly complicated as the figure shows the maximum proton energy in the source frame and therefore also includes a dependence on Γ_m .

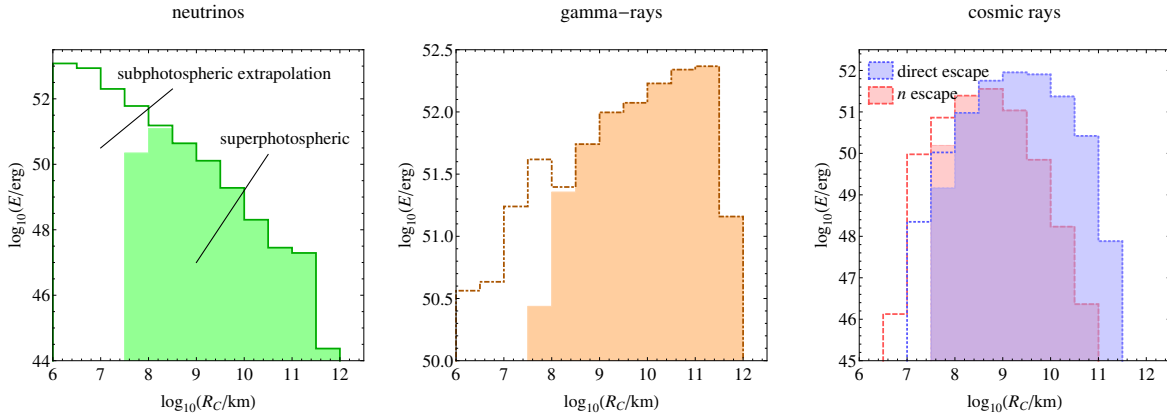


Figure 5.23: Energy histograms of neutrinos (left), gamma-rays (center), and cosmic rays (right), including both superphotospheric collisions only (shaded areas) and all collisions.

It is interesting also to look at the range of magnetic field values present in the collisions. These are shown for each collision, in the plane $E_{\gamma\text{-sh}}^{\text{iso}}$ vs. l' , in the right panel of Fig. 5.21, where we see that B' approximately spans the range $10^2 - 10^8$ G, with the subphotospheric collisions having fields in excess of 10^6 G. Additionally, the left panel of Fig. 5.22 shows its evolution with collision radius: the $\sim 1/R_C$ scaling of B' from Eq. (5.47) is evident. Notice that, while most collisions have values below the standard assumption of 10^5 G, a few have values above it, up to $\sim 10^8$ G, though superphotospheric collisions reach only up to 10^6 G. The central and right panels show the critical synchrotron energy for pions, $E'_{c,\pi}$, and for muons, $E'_{c,\mu}$, and we see that, for collisions with $B' \approx 10^6$ G, these energies lie above the standard values by about one order of magnitude. This, as we will see later, makes the peak of neutrino spectrum lie at an energy that is roughly one order of magnitude below the position calculated within the static fireball approximation.

The right panel of Fig. 5.19 shows the evolution of the maximum gamma-ray energy with collision radius. Photon escape from a particular collision radius is limited by electron-positron pair production due to photon-photon interactions. For a particular collision resulting in a merged shell of width l_m , one can calculate the optical depth to photon escape as $\tau_{\gamma\gamma} = l_{\gamma\gamma}/l_m$, where $l_{\gamma\gamma}$ is the photon-photon interaction length; see appendix E for details. Using the information on the normalised particle densities, it can be computed (numerically) using Eq. (E.2). The maximum photon energy $E_{\gamma,\text{max}}$ in Fig. 5.19 is the energy (in the source frame) at which $\tau_{\gamma\gamma} = 1$, *i.e.*, it is the maximum energy that an escaping photon can have at this particular collision radius. Note that these values are not the maximal photon energies obtained from synchrotron radiation or inverse Compton scattering, but the maximal energy value at which photons can escape before pair creation suppresses them. The sensitivity bands for three different gamma-ray experiments are included: *Fermi*-GBM (1 keV – 10 MeV), *Fermi*-LAT (100 MeV – 100 GeV), and CTA (100 GeV – 1 PeV). We can see that emission from the different regimes would be detected by different instruments: while *Fermi*-GBM is sensitive to the gamma-ray signal coming from the optically thick to neutron escape regime (*i.e.*, low radii), *Fermi*-LAT, and especially CTA, are sensitive to the signal coming mainly from the direct proton escape regime (*i.e.*, large radii), with LAT also somewhat sensitive to the neutron escape regime. Collisions in which the gamma-ray emission is not limited by pair production to energies below 10^6 GeV are shown as upward-pointing arrows.

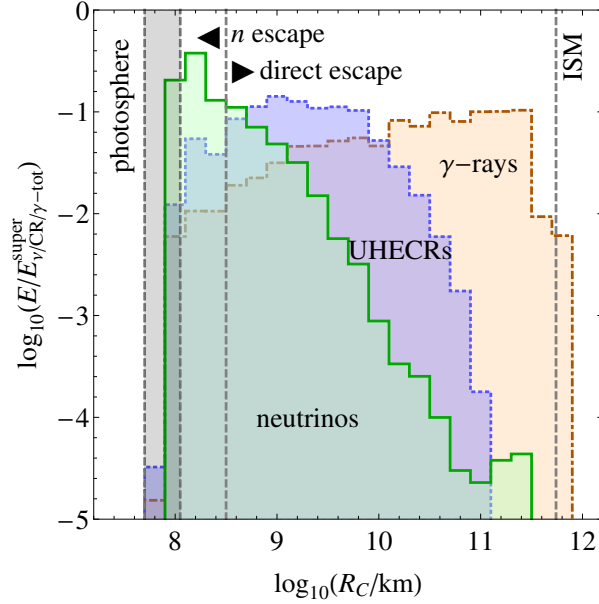


Figure 5.24: Energy dissipated in (prompt) gamma-rays, neutrinos, and CR protons (UHECRs from 10^{10} to 10^{12} GeV) beyond the photosphere, binned in the collision radius. Each bin shows the fraction of the total (superphotospheric) energy for neutrinos, cosmic rays, and gamma-rays. Neutron escape dominates the cosmic ray emission below $R_C \approx 10^{8.5}$ km, while proton escape dominates above this radius. The photosphere is marked by a gray band that spans the range $R_C \approx 10^{7.7} - 10^8$ km and we assume that the interstellar medium starts at $5.5 \cdot 10^{11}$ km.

In Fig. 5.23 we have binned, in R_C , the energy emitted as neutrinos, gamma-rays, and UHECR protons for our chosen model. The histogram contours show the distributions for all collisions, while the shaded histograms show the distributions for superphotospheric collisions only, which account for about 92% of the total number of collisions. Our earlier observation becomes more clear here: neutrino emission comes mainly from the inner radii, gamma-ray emission comes from the outer radii, and UHECR emission comes from intermediate radii, with neutron escape peaking at lower radii than direct proton escape. The comparison between the different emission regimes is easier in Fig. 5.24; here, we show instead the binned energy distribution normalised to the total emitted energy for each particle species, exclusively for superphotospheric collisions. Neutrino emission is dominated by collisions that occur below the standard collision radius $R_C^{\text{std}} \approx 10^{9.2}$ km. From Fig. 5.22 we know that in these collisions the magnetic field ranges from 10^5 G to 10^6 G, with most of the collisions occurring in the neutron escape regime, due to the high proton and photon densities in the source, and, from Fig. 5.20, we know that these collisions reach photohadronic optical depths higher than $\tau_{p\gamma} = 10$. Therefore, even though the superphotospheric neutron escape-dominated collisions are few (48 out of the total of 910 superphotospheric collisions), they account for most of the neutrino emission of the whole burst and, in fact, the emission is dominated by the ten collisions with $\tau_{p\gamma} > 10$.

This becomes evident in Fig. 5.25, where we show the quasi-diffuse flux of neutrinos, assuming that all of the 667 long-duration bursts that are observed per year behave just as our chosen model. The

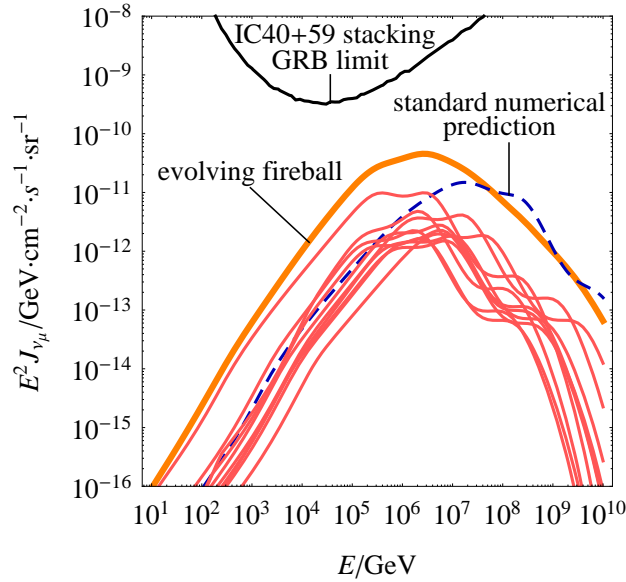


Figure 5.25: Neutrino spectra from individual (dominant) collisions (thin red curves), total spectrum (thick orange curve), and reference spectrum computed from averaged burst parameters in the conventional approach (dashed blue curve). The spectra are estimates of the diffuse flux obtained from the individual burst (or collision) results by assuming 667 long bursts per year over the whole sky. The diffuse GRB flux limit from the IC40+59 analysis [92] is shown as a thin black curve. Moreover, the recently detected flux of high energy neutrinos is at the level of $10^{-8} \text{ GeV cm}^{-2} \text{ s}^{-1} \text{ sr}^{-1}$ [8] which corresponds to the upper edge of the shown plot.

total flux (thick orange curve) is made up only of superphotospheric collisions; the contributions from the ten most prominent collisions –from the point of view neutrino-production– are included as thin lines. We also include the flux obtained in the static fireball approximation, as a dashed curve. This prediction was obtained using the standard parameters from table 5.2, for $N_{\text{coll}} = 990$ identical collisions. There are two important observations to point out:

- The flux from the evolving burst model is at a slightly higher level than the standard flux. This is in spite of the fact that the neutrino emission from the evolving burst is dominated by only around ten collisions, whereas the standard flux is made up of almost a thousand collisions. We already came across the reason earlier: these ten collisions have photohadronic optical depths that are much higher –two orders of magnitude– than the standard value of 0.1.
- The flux from the evolving burst model peaks at $\sim 10^{6.2} \text{ GeV}$, whereas the standard flux peaks at $\sim 10^7 \text{ GeV}$. The reason is that in the evolving burst the dominant neutrino-producing collisions occur at radii smaller than the standard value of $\sim 10^{9.2} \text{ km}$. We have seen (Fig. 5.22) that here the synchrotron critical energies of pions and muons are roughly one order of magnitude lower than their standard values. As a consequence, the kink in the neutrino flux that signals the onset of synchrotron losses, and which is responsible for the position of the flux peak, occurs roughly one order of magnitude below the 10^7 GeV peak of the standard flux.

Our results, most clearly Fig. 5.24, have shown that different particle species come from very distinct collision radii ranges of the expanding burst. Naturally, usually the parameters used in making the UHECR and neutrino predictions, such as the collision radius, are inferred from gamma-ray observations of the burst. Our results show that these parameters might not be good descriptors of the UHECR and neutrinos, whose emissions are generated at smaller radii. Therefore, many of the UHECR and neutrino predictions found in the literature might be more model-dependent than previously believed, since they would apply to the particular burst scenarios where all of the particle species come from collisions at the same radii.

Chapter 6

UHE astrophysical neutrino decay

Within the Standard Model, neutrinos are stable; all of our results in the previous chapters have been obtained using this implicit assumption. The possibility remains, however, that neutrinos are unstable particles, but with lifetimes long enough that we have not been able to observe the effects of their decay in the neutrino detection experiments that have so far been carried out. In this chapter we will explore the possibility of neutrino decay in UHE astrophysical neutrinos, first by re-deducing the relevant redshift-dependent expressions, and then by predicting possible signal modifications due to decay in the GRB neutrino flux.

6.1 Introduction

The absence of decay signatures allows to set bounds on the lifetimes of the different neutrino mass eigenstates. The most stringent phenomenological bound comes from the observation of $\bar{\nu}_e$ from supernova 1987A [187, 188] by the Kamiokande II, IMB, and Baksan detectors. Given the uncertainty on the supernova neutrino flux ($\sim 50\%$) and the neutrino mixing parameters, it may apply¹ to the mass eigenstate ν_1 or to ν_2 . For the sake of simplicity, and since $\sim 91\%$ of the ν_e content is accounted for by ν_1 , we assume that the bound applies to ν_1 : $\tau_1/m_1 \gtrsim 10^5$ s/eV.² The (model-independent) bounds on the other mass eigenstates are less stringent: bounds on ν_2 lifetime are imposed by solar neutrino data, yielding $\tau_2/m_2 \gtrsim 10^{-4}$ s/eV for decays into invisible daughters [189, 190, 191] and $\tau_2/m_2 \gtrsim 10^{-3}$ s/eV for decay modes with secondary $\bar{\nu}_e$ appearance [192, 193]. Furthermore, ν_3 is constrained from the analysis of atmospheric and long-baseline neutrino data, $\tau_3/m_3 \gtrsim 10^{-10}$ s/eV [194].

More stringent bounds can be derived when specific decay models are assumed (see, *e.g.*, Refs. [195, 196, 197, 198, 199, 200, 201, 202, 203, 204, 205]). In this study, we do not consider specific decay models, but focus on the phenomenology of neutrino decay, given the bounds on the lifetimes above. Especially neutrino telescopes [206, 207, 208, 209] are sensitive to neutrinos with an average energy and traveled distance many orders of magnitude larger than present accelerator, reactor, atmospheric, and solar neutrino experiments, and may be an interesting approach to probe neutrino decay.

¹In our treatment, the lifetime of the mass eigenstate ν_i and its antiparticle $\bar{\nu}_i$ are assumed to be equal.

²Neutrino lifetime is usually described by $\kappa_i^{-1} \equiv \tau_{i,0}/m_i$, where $\tau_{i,0}$ is the rest frame lifetime of the mass eigenstate ν_i . The origin of the mass dependence is the fact that decays scale as $\exp[-t/(\tau_{i,0}\gamma)] \simeq \exp[-(Lm_i)/(E\tau_{i,0})]$, *i.e.*, the rest frame lifetime $\tau_{i,0}$ is boosted by $\gamma = E/m_i$ into the observer's frame, and L (baseline source-detector) and E (neutrino energy) are quantities related to source and experiment.

We distinguish between decays into products *invisible* to the detector, such as sterile neutrinos, unparticle states, Majorons, or active neutrinos strongly degraded in energy, and decays into *visible* states, *i.e.*, active neutrino flavours. Besides, the decays can be *complete*, *i.e.*, all unstable mass eigenstates have decayed (see, *e.g.*, Ref. [210]), or *incomplete*, *i.e.*, the particular signature of decay will be visible in the spectrum. A complete classification of complete (visible or invisible) decay scenarios has been performed in Ref. [211], while incomplete invisible decay has, for instance, been studied for active galactic nuclei (AGNs) in Ref. [212, 213]. The description of incomplete visible decays is, in general, more complicated [214, 215], partially because it requires the consideration of branching ratios, which is why we focus on incomplete invisible decay in this study.

In the literature on the subject, it is often assumed that decays are always complete if the sources lie far enough away, which, in turn, allows for the test of very long neutrino lifetimes, of the order of

$$\kappa^{-1} \left[\frac{\text{s}}{\text{eV}} \right] \equiv \frac{\tau [\text{s}]}{m [\text{eV}]} \simeq 10^2 \frac{L [\text{Mpc}]}{E [\text{TeV}]} . \quad (6.1)$$

On account of this, astrophysical neutrino sources lying at high redshifts are potentially well suited to test the neutrino lifetime, and may potentially lead to bounds stronger than the one from SN 1987A. In this work we have focused on GRBs as sources, with observed redshifts as high as $z \simeq 6 - 8$. This leads to potentially strong constraints via Eq. (6.1). There is subtlety which, however, we will address here and which will turn out to be important: the connection between distance L and redshift z depends, for $z \gtrsim 0.1$ (or $L \gtrsim 360 \text{ Mpc}$), on the cosmological distance measure that is used; see Refs. [216, 217] for a discussion in the context of neutrino oscillations, and Refs. [218, 219] in the context of pseudo-Dirac neutrinos. For the neutrino flux, especially redshifts $z \simeq 1$ will dominate [99], which is a consequence of the convolution of the star formation rate (including some redshift evolution function) and the contribution to the total flux scaling as $1/d_L^2$, where d_L is the luminosity distance. This value is already significantly beyond the indicated $z \simeq 0.1$, which means that cosmological effects have to be taken into account.

As in previous chapters, we here use the NeuCosmA software to generate the neutrino spectra from GRBs³: in particular, we will use the improved nominal prediction for the quasi-diffuse flux from Ref. [4], calculated with the IC-40 bursts [3]. Note that model-specific [4] and more generic [5] astrophysical uncertainties may imply even lower neutrino flux predictions. Neutrino decay provides an alternative explanation for the continued lack of detection of neutrinos from GRBs: they may have decayed, at least partially, during their propagation between source and detector. We will investigate the impact of this hypothesis on the predicted fluxes.

Recently, the IceCube neutrino telescope detected three cascade events at PeV energies [7, 8]. Assuming that these have an extragalactic origin, it is interesting to ask why there are no accompanying muon tracks at PeV energies. One possibility is simply that this is a consequence of the IceCube search strategy: since cascades can be generated by neutral-current interactions of any neutrino flavour and by charged-current interactions of ν_e , while muon tracks can be generated only by charged-current interactions of ν_μ , then it is only natural that more cascades than muon tracks are seen. We will show here that neutrino decay can also provide an answer to that question, in line with the current constraints on neutrino lifetime; for alternative explanations, see Refs. [220, 221]. We will demonstrate that muon tracks may be strongly suppressed in the presence of neutrino decay compared to (especially electromagnetic) cascades, and that cascade measurements are much more powerful to find astrophysical neutrinos in this case. Though we will use GRBs as an example, our conclusions can be applied to AGNs and to cosmogenic neutrinos as well.

³Within the static burst approximation, not the dynamical burst from chapter 5.

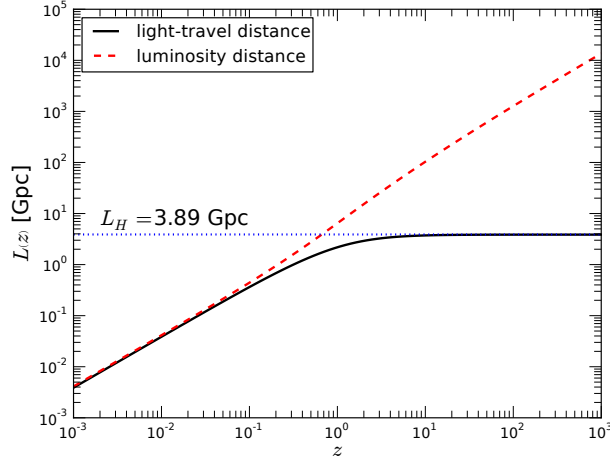


Figure 6.1: Light-travel distance as a function of redshift in a Λ CDM cosmology (solid black line). For comparison, we have also included the luminosity distance (dashed curve). Figure taken from Ref. [119].

6.2 Decay framework for cosmological neutrinos

Decay of the neutrino mass eigenstate ν_i can be described by the usual differential equation

$$\frac{dN_i}{dt} = -\lambda_i N_i, \quad (6.2)$$

where the decay rate (inverse lifetime) λ_i is given by

$$\lambda_i = \frac{m_i}{\tau_{i,0}} \frac{1}{E} \equiv \frac{\kappa_i}{E}, \quad (6.3)$$

with $\tau_{i,0}$, the rest frame lifetime, boosted by $\gamma_i = E/m_i$ into the observer's frame, $\kappa_i \equiv m_i/\tau_{i,0}$, and E the neutrino energy. Since neither $\tau_{i,0}$ nor the observed lifetime $\tau_i = \gamma_i \tau_{i,0}$ are directly observable, and since we do not know the absolute neutrino masses, we typically refer to the combination $\kappa_i^{-1} = \tau_{i,0}/m_i$ [s eV $^{-1}$] as the lifetime of the neutrino mass eigenstate ν_i .

For ultra-relativistic neutrinos, the time $t \approx L$. If the source has a redshift z , the distance must be expressed in terms of it, $L(z)$. The relationship between distance and redshift depends on the choice of cosmological distance measure [222]; for neutrino decay, the relevant quantity is the time traveled in Eq. (6.2), which is to be associated with the light-travel or look-back distance. In other words, the clock which triggers neutrino decay is directly related to the distance the neutrino has traveled since its production. By definition,

$$L(z) = L_H \int_0^z \frac{dz'}{(1+z')h(z')}, \quad (6.4)$$

with $L_H \equiv c/H_0 \approx 3.89$ Gpc the Hubble length [223], $h(z) \equiv H(z)/H_0$, $H(z)$ the Hubble factor, Eq. (3.6), and H_0 the Hubble constant. As before, we assume a flat Λ CDM cosmology, with $\Omega_m = 0.27$ and $\Omega_\Lambda = 0.73$ [133], unless explicitly noted otherwise.

Fig. 6.1 compares the light-travel distance $L(z)$ to the luminosity distance: it is limited by the Hubble length L_H , the horizon beyond which ultra-relativistic particles cannot be seen. Hence, the maximum distance relevant for the test of decay is limited. Clearly, Fig. 6.1 shows that

the extended notion that larger distances can probe longer lifetimes only holds for $z \lesssim 0.1$ (or $L \lesssim 360$ Mpc), where the cosmological distance measures are very similar, whereas for $z \gtrsim 1$, the light-travel distance is limited. For “typical” neutrino peak energies higher than about 10^2 TeV for GRBs and AGNs, one can estimate that the maximal testable lifetimes are about $\kappa^{-1} \sim 10^4 \text{ s eV}^{-1}$ from Eq. (6.1). Therefore, the bound on the lifetime of ν_1 from SN 1987A cannot be exceeded by UHE astrophysical neutrinos; instead, future Galactic supernova neutrinos should be better suited for this.

Neutrino decay modifies the flavour transition probability to

$$P_{\alpha\beta}(E_0, z) = \sum_i |U_{\alpha i}|^2 |U_{\beta i}|^2 \frac{N_i(E_0, z)}{\hat{N}_i(E_0)} = \sum_i |U_{\alpha i}|^2 |U_{\beta i}|^2 D_i(E_0, z), \quad (6.5)$$

where E_0 is the observed energy, $N_i(E_0, z)$ is the number of neutrinos left after traveling a distance $L(z)$, $\hat{N}_i(E_0)$ is the initial number of neutrinos, and $D_i(E_0, z) \equiv N_i(E_0, z)/\hat{N}_i(E_0) \leq 1$ is the corresponding damping factor [224], *i.e.*, the solution of Eq. (6.2). For the mixing angles, we use the best-fit values (for normal hierarchy) from Ref. [225], *i.e.*, $\sin^2 \theta_{12} = 0.307$, $\sin^2 \theta_{23} = 0.398$, $\sin^2 \theta_{13} = 0.0245$, and the CP-violating phase $\delta = 0.89 \cdot \pi$. As before, the flavour composition at the source is computed in a self-consistent way using NeuCosmA and including the cooling of the secondary pions, muons, and kaons, and the helicity-dependent muon decays; see, *e.g.*, Refs. [95, 111, 226, 103].

The usual way in which the decay equation, Eq. (6.2), is solved assumes that λ_i is independent of redshift to find the well-known solution

$$N_i(t) = N_i(t=0) e^{-\lambda_i t} = \hat{N}_i e^{-\lambda_i t}. \quad (6.6)$$

In terms of redshift and using Eq. (6.4), we can rewrite this as⁴

$$N_i(z) = \hat{N}_i e^{-\lambda_i L(z)}, \quad (6.7)$$

where $N_i(z)$ is the number of remaining neutrinos after⁵ traveling a distance $L(z)$. We must also take into account the effect of the adiabatic cosmological expansion on the neutrino energy: if $E(z)$ is the energy in the production epoch and E_0 is the observed energy, then $E(z) = (1+z) E_0$. With this, the decay rate in Eq. (6.3) acquires a redshift dependence, and, using that in Eq. (6.7), we can write the damping factor needed for Eq. (6.5) as

$$D_i(E_0, z) = \exp\left(-\frac{\kappa_i}{E_0} \frac{L(z)}{(1+z)}\right) \quad (6.8)$$

with the definition of $L(z)$ from Eq. (6.4). In order to isolate the redshift-dependent part of the evolution, we define the dimensionless function

$$\mathcal{Z}_1(z) \equiv \exp\left(\frac{L(z)}{L_H \cdot (1+z)}\right), \quad (6.9)$$

such that Eq. (6.8) can be re-written as

$$D_i(E_0, z) = [\mathcal{Z}_1(z)]^{-\frac{\kappa_i L_H}{E_0}}. \quad (6.10)$$

Here the exponent depends on κ_i and E_0 only, whereas the base depends on redshift only.

⁴We use natural units, *i.e.*, $\hbar = c = 1$.

⁵Note that here the redshift is measured relative to the origin z , whereas in cosmology $z = 0$ (and quantities marked with “0”) refer to the current epoch.

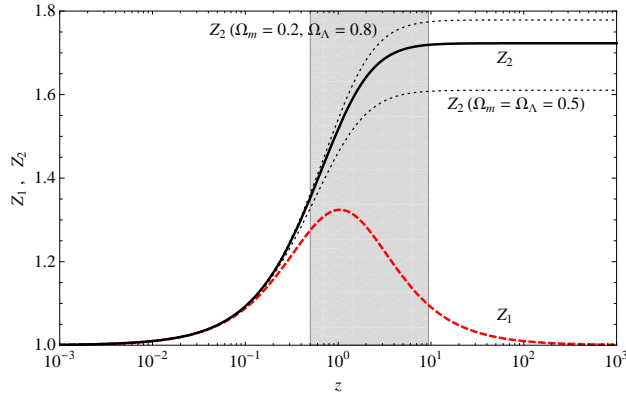


Figure 6.2: Comparison of the simplified (\mathcal{Z}_1) and proper (\mathcal{Z}_2) redshift dependencies. For $z \lesssim 0.1$ the approaches are identical. The gray-shaded region illustrates the typical redshift range populated by GRBs. Figure taken from Ref. [119].

We show the functional dependence of $\mathcal{Z}_1(z)$ in Fig. 6.2. For large z , $\mathcal{Z}_1 \rightarrow 1$, which means that the neutrinos from high redshifts are stable, and the notion of complete decays does not exist. From Eq. (6.10), they are even stable independent of the value of E_0 , which is counter-intuitive, since more energetic neutrinos should live longer than less energetic ones. The problem with this approach is that introducing the energy dependence $E(z)$ *after* the solution of Eq. (6.2) fails to take into account that the neutrinos lose energy continuously, which changes the solution of the differential equation. That is, the energy assigned to the neutrinos is chosen to be the one at the production epoch, which is on average too high, and the neutrinos are hence too long-lived. While one would naively expect that this effect is small, we have encountered a severe contradiction here. The proper solution of the decay equation, Eq. (6.2), is, of course, to re-write it in terms of redshift using the redshift-dependent connection between energies at production and detection epochs:

$$\frac{dN_i(E_0, z)}{dz} = -\frac{\kappa_i}{E_0} \frac{dL}{dz} \frac{N_i(E_0, z)}{1+z}. \quad (6.11)$$

Note that in the following, we choose $z = 0$ as the present epoch, *i.e.*, we integrate from z to 0. Therefore, from the definition of light-travel distance Eq. (6.4), we have

$$\frac{dL}{dz} = -\frac{L_H}{(1+z)h(z)}. \quad (6.12)$$

The solution is

$$D_i(E_0, z) = \exp\left(-\frac{\kappa_i L_H}{E_0} \int_0^z \frac{dz'}{(1+z')^2 h(z')}\right) = [\mathcal{Z}_2(z)]^{-\frac{\kappa_i L_H}{E_0}}, \quad (6.13)$$

where we have isolated the z -dependent part through⁶

$$I_2(z) \equiv \int_0^z \frac{dz'}{(1+z')^2 h(z')}, \quad (6.14)$$

$$\mathcal{Z}_2(z) \equiv e^{I_2(z)}. \quad (6.15)$$

⁶Note that the function $I_2(z)$ was already encountered in the context of oscillations, and corresponds to Eq. (6) in Ref. [216].

The function $\mathcal{Z}_2(z)$ is also shown in Fig. 6.2. It is now monotonously increasing with redshift, and larger than unity. This means that for large decay rates $\kappa_i \gg E_0/L_H$, one finds $D_i(E_0, z) \rightarrow 0$ (complete decays) for $z > 0$, as expected in a self-consistent framework. In addition, since the maximal distance is limited by the Hubble distance, the base \mathcal{Z}_2 in Eq. (6.13) is asymptotically limited. This has interesting implications for the notion of complete decays, which one can read off from Eq. (6.13): the condition for complete decays is $\kappa L_H/E_0 \gg 1$, or, equivalently,

$$E_0 [\text{TeV}] \ll \frac{4 \cdot 10^5}{\kappa^{-1} [\text{s eV}^{-1}]} . \quad (6.16)$$

First of all, this confirms our earlier estimates that energies considerably lower than 1 TeV are needed to test lifetimes comparable to the SN 1987A bounds. Second, it is a condition on energy, which is independent of distance (or redshift). Therefore, over cosmological distances (for $z \gtrsim 1$), “complete decays” is an energy-dependent concept, and has nothing to do with distance.

A useful analytical approximation for \mathcal{Z}_2 is

$$\mathcal{Z}_2(z) \simeq a + be^{-cz} , \quad (6.17)$$

with⁷ $a \simeq 1.71$, $b \simeq 1 - a = -0.71$, and $c \simeq 1.27$. Hence, the asymptotic value is $\mathcal{Z}_2 \rightarrow a$ for $z \rightarrow \infty$. It depends on cosmology, as it is illustrated in Fig. 6.2 for different values of Ω_m and Ω_Λ : the higher the cosmological constant contribution (for a flat universe), the more efficient neutrino decays will be for large redshifts.

6.3 Decay of neutrinos from GRBs

We now apply the decay framework developed above to GRBs; note, however, that our results can be equally applied to AGNs or other objects. We choose four benchmark bursts, for which the parameters are given in table 2.1. The standard burst “SB” is a burst for which most parameters, such as α , β , z , and L_γ^{iso} , are frequently used in the literature. In addition, three different recent GRBs detected by the *Fermi* satellite have been chosen as examples: GRB 080916C, GRB 090902B, and GRB 091024. GRB 080916C has been selected, because it is one of the brightest bursts ever seen, although at a large redshift, and one of the best studied *Fermi*-LAT bursts. The gamma-ray spectrum of GRB 090902B has a relatively steep cutoff. GRB 091024 can be regarded as a typical example representative for many *Fermi*-GBM bursts [114], except for the long duration. Note that the middle two bursts have an exceptionally large $\Gamma \gtrsim 1000$, whereas $\Gamma \simeq 200$ for the last burst.

We use the same GRB parameters that we used in chapter 2, in table 2.1, and the NeuCosmA software [4] (see Ref. [99] for details) to predict the neutrino fluxes, assuming that the baryonic loading $f_e^{-1} = 10$, energy equipartition between electrons and magnetic field energy ($\epsilon_e = \epsilon_B$) (as in Refs. [91, 3, 92]), and an acceleration efficiency of $\eta = 0.1$.

We first assume that all of the mass eigenstates have the same lifetimes: Fig. 6.3 shows the predicted muon-neutrino flux⁸ as a function of neutrino energy for the four benchmark bursts in table 2.1 for this model. Thick curves correspond to the proper decay solution, and thin curves to the simplified approach. Note that this model serves only to illustrate the effects of neutrino decay, but is otherwise unrealistic since the lifetimes are chosen such that the SN 1987A bound for one of the mass eigenstates must be violated.

⁷Actually, a and b are not independent, since $\mathcal{Z}_2(z=0) = 1$ must be satisfied. This implies that $b = 1 - a$.

⁸Here the neutrino flux is just the neutrino fluence divided by T_{90} .

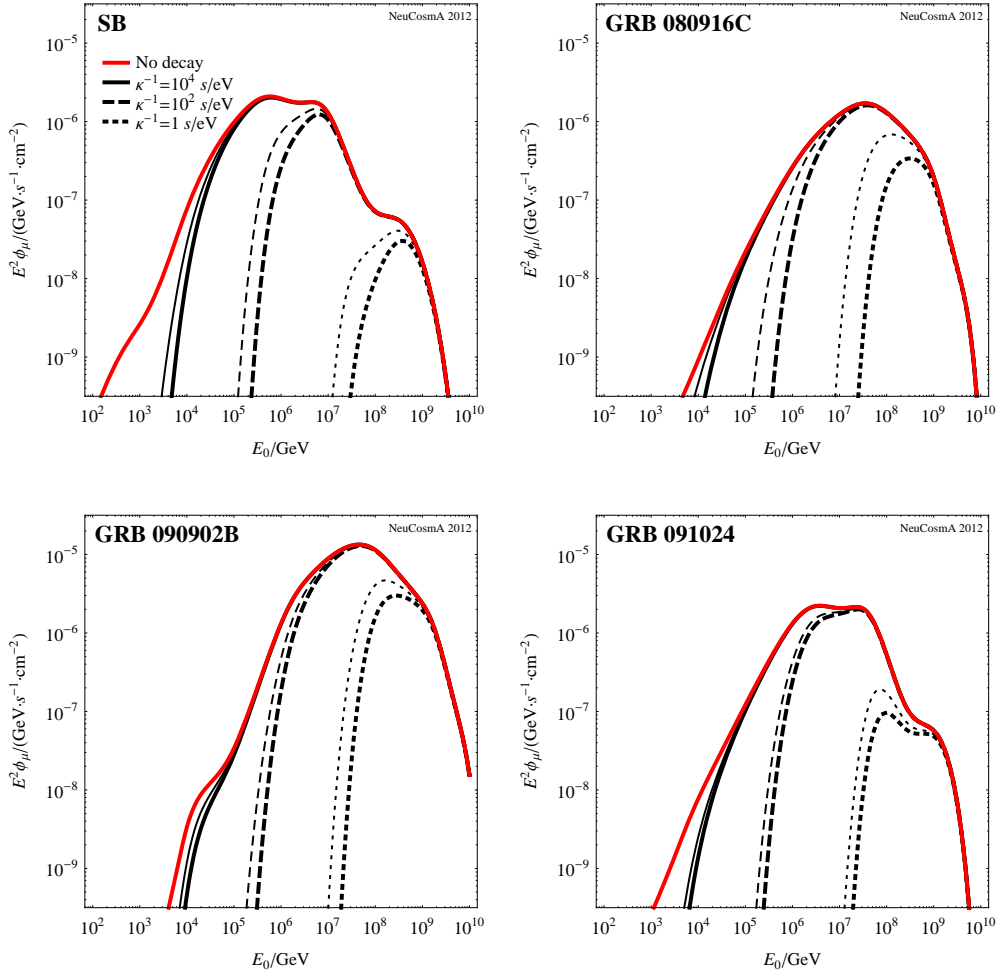


Figure 6.3: Predicted muon-neutrino flux as a function of neutrino energy for the four benchmark bursts in table 2.1 (panels). The different curves in each panel correspond to no decay (stable neutrinos) and three different lifetimes, as given in the legend. Thick curves correspond to the proper solution of the decay equation, and thin curves to the simplified approach, for comparison. Here we (hypothetically) assume that all mass eigenstates have the same lifetime, as indicated in the legend. Figure taken from Ref. [119].

We can use Eq. (6.16) to estimate at what energies the decays will be complete. For instance, in the upper left panel, the flux is suppressed below 4000 TeV for $\kappa^{-1} = 10^2 \text{ s eV}^{-1}$. This condition is the more accurate, the higher the redshift of the burst is. For instance, for GRB 091024 ($z \simeq 1.1$), the suppression is somewhat weaker (shifted to smaller energies) because the base \mathcal{Z}_2 in Fig. 6.2 has not yet reached its saturation value. Obviously the suppression in the proper decay treatment is stronger, which is expected since $\mathcal{Z}_2 \gg \mathcal{Z}_1$ for large redshifts. The difference between the curves also increases with redshift, and can be quite significant for large redshifts (*cf.*, GRB 080916C).

One can show that, in the presence of decay, and provided κ^{-1} is sufficiently large, the main contribution does not come from $z \simeq 1$ anymore, but from very low z (peaking at $z = 0$): for an energy $E_0 \simeq 10^6 \text{ GeV}$, this occurs if $\kappa^{-1} \lesssim 400 \text{ s eV}^{-1}$. This is expected, since the neutrinos from the low-redshift bursts will not have decayed yet. If, on the other hand, $\kappa^{-1} \gtrsim 400 \text{ s eV}^{-1}$, the bursts from $z \simeq 1$ will dominate, as for stable neutrinos.

Finally, comparing the lifetimes used for Fig. 6.3 with the SN 1987A bound, one can easily see

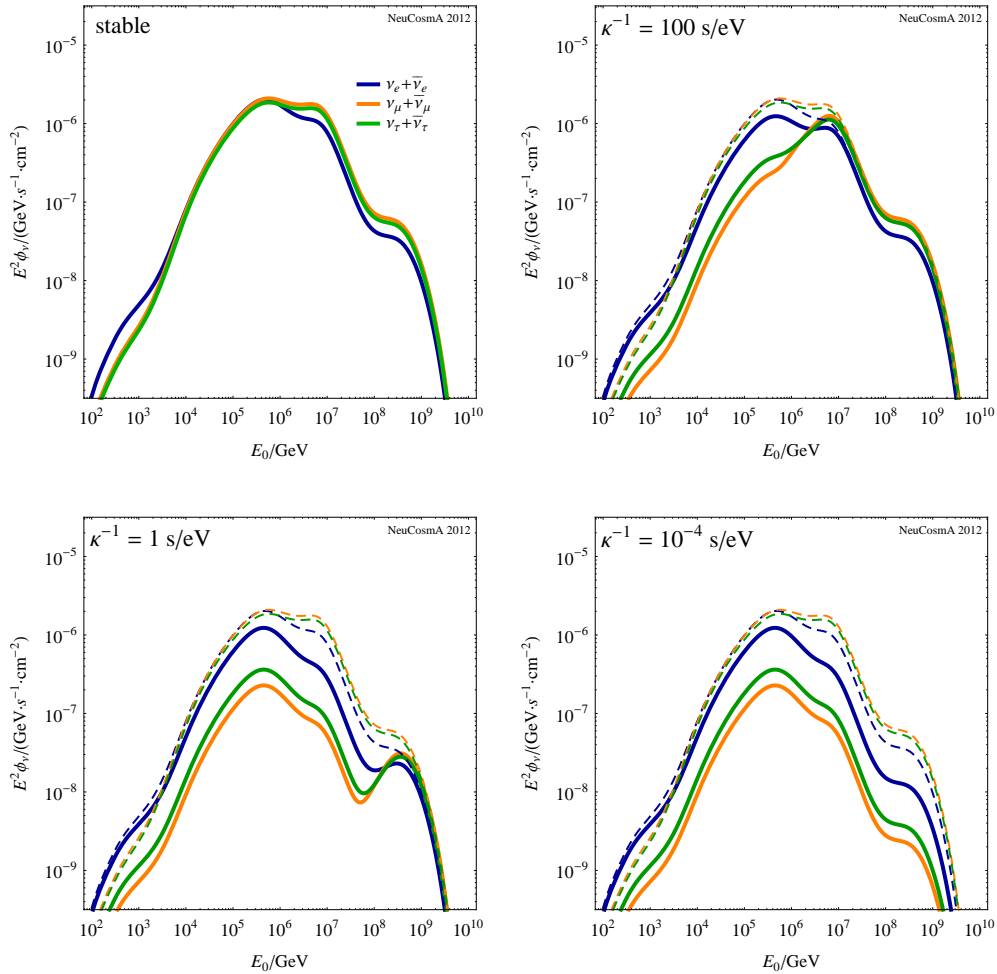


Figure 6.4: Predicted neutrino flux as a function of neutrino energy for the benchmark burst SB in table 2.1. The different panels correspond to different lifetimes, as given in the panels. The different curves correspond to different flavours (after flavour mixing), as given in the legend. Thin dashed curves shown the stable case (upper left panel) for reference. As decay model, ν_1 is assumed to be stable, whereas ν_2 and ν_3 decay with the indicated lifetime, *i.e.*, all of the panels are consistent with the SN 1987A bound. Figure taken from Ref. [119].

that no strong decay suppression can be obtained if this bound is applied to all mass eigenstates. Therefore, the neutrino lifetimes of the different mass eigenstates have to be different for a phenomenologically allowed scenario, where the most plausible case, satisfying the SN 1987A constraint, might be that ν_1 is stable. In fact, this is for the discussed GRB fluxes equivalent to saturating the SN 1987A bound on ν_1 . Therefore, we only discuss this case in the following, and we only use the proper solution of the decay equation. We assume that ν_2 and ν_3 decay with the same lifetime, for the sake of simplicity, with lifetimes satisfying the ν_2 (and, consequently, ν_3) bound. The mass eigenstate ν_2 is about an equal mixture among ν_e , ν_μ , and ν_τ , whereas ν_3 is a mixture between ν_μ and ν_τ with a small contribution of ν_e . The decay of ν_2 will affect the electron flavour somewhat, which however can be absorbed in the uncertainties of current supernova flux predictions. The decay of ν_3 will be hardly observable in the electron flavour.

We show the electron-, muon-, and tau-neutrino fluxes for this model in Fig. 6.4 for the standard burst SB and for different values of the lifetime (panels). In the stable case (upper left panel), at

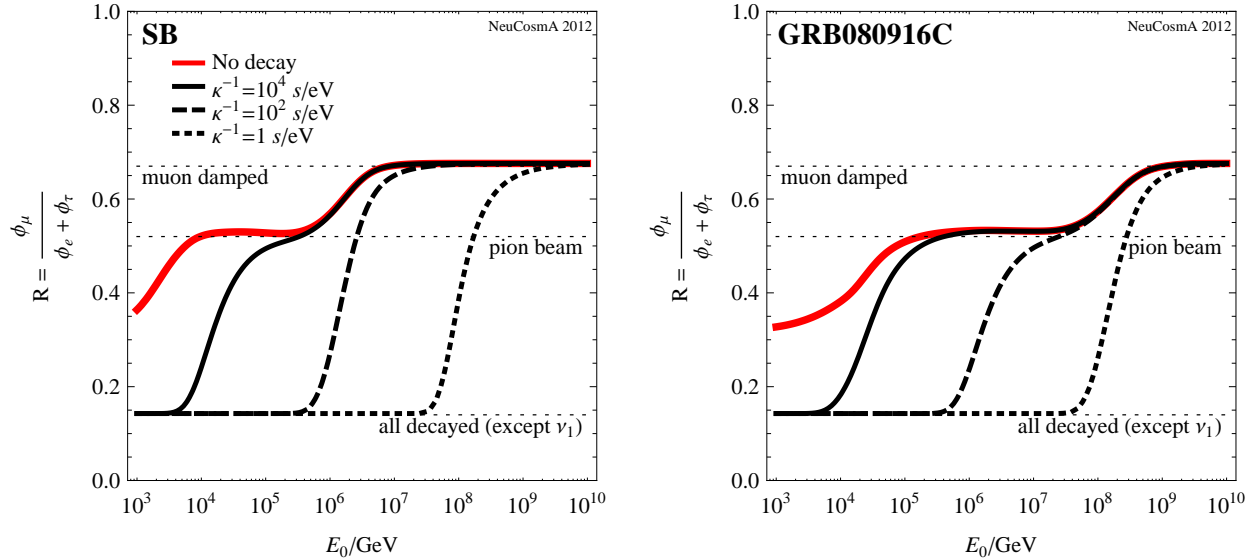


Figure 6.5: Predicted flavour ratio R (muon tracks to cascades) as a function of neutrino energy for the first two benchmark bursts in table 2.1 (panels). The different curves in each panel correspond to no decay (stable neutrinos) and three different lifetimes, as given in the legend. As decay model, ν_1 is assumed to be stable, whereas ν_2 and ν_3 decay with the indicated lifetime, *i.e.*, all of the lifetimes are consistent with the SN 1987A bound. Figure taken from Ref. [119].

the peak, where the flavour composition $\nu_e : \nu_\mu : \nu_\tau$ is approximately 1 : 2 : 0 at the source, flavour equilibration at the detector is roughly achieved. Even for larger energies, the fluxes of all flavours are roughly comparable on a logarithmic scale – we will discuss the flavour ratio below. In the most extreme decay case (lower right panel), both ν_2 and ν_3 decay with a lifetime corresponding to the current ν_2 bound: the electron-neutrino flux survives (because ν_1 is stable), whereas the muon- and tau-neutrino fluxes are suppressed. As a consequence, while electromagnetic cascades are observable at roughly the same level as in the stable case, muon tracks are suppressed by about one order of magnitude and neutral-current cascades are reduced to $\sim 1/3$ of the stable case⁹. It is therefore clear that this scenario can easily explain why only cascades have been recently observed at PeV energies, and will be dominating with increasing statistics, in spite of the effective areas comparable between muon tracks and cascades [6]. The PeV energies are exactly at the peak expected from the standard burst (SB), which means that the events may come from the diffuse GRB flux.

We show in Fig. 6.5 the flavour ratio $R = \phi_m / (\phi_e + \phi_\tau)$ (muon tracks to cascades) as a function of neutrino energy for two different bursts (panels) and different lifetimes (curves); for instances where R has been used, see, *e.g.*, Ref. [210, 95, 205, 211, 227, 228]. One can easily see the characteristic transition from a pion beam source (initial flavour composition $\nu_e : \nu_\mu : \nu_\tau$ of 1 : 2 : 0, yielding $R \approx 0.52$) to a muon damped source (initial flavour composition of 0 : 1 : 0, yielding $R \approx 0.67$) at higher energies, which comes from the energy losses of the muons in the magnetic

⁹Hadronic cascades are also strongly suppressed. The contributions of the leptonic tau decay channel into leptons can be neglected as well, since they are doubly suppressed by tau-neutrino flux and the tau branching ratios.

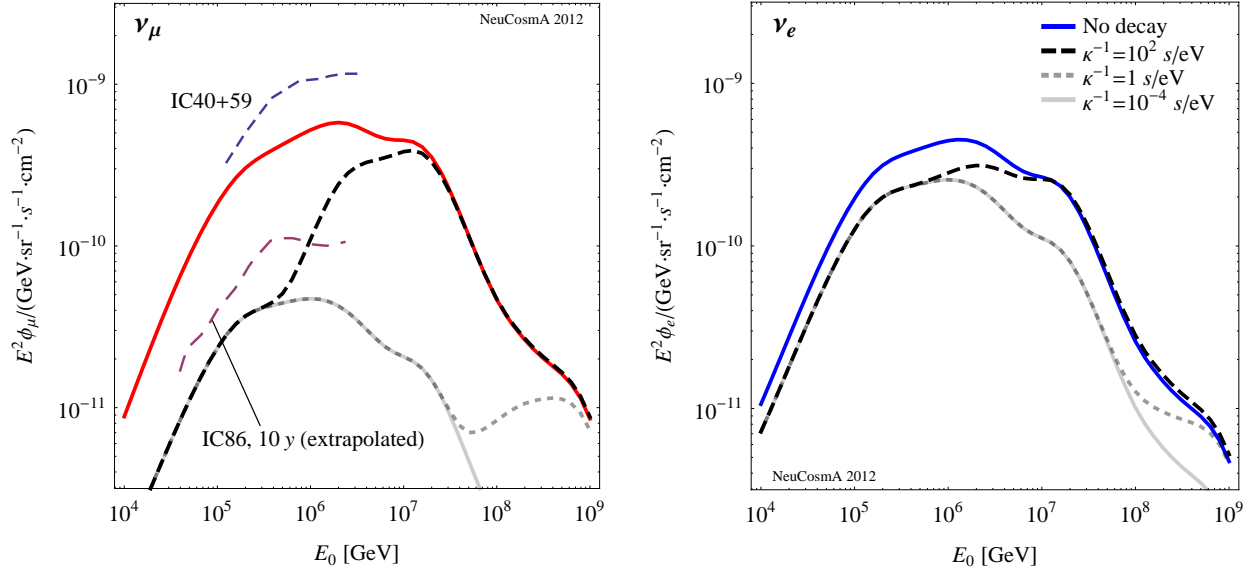


Figure 6.6: Prediction of the quasi-diffuse muon (left panel) and electron (right panel) neutrino flux from the bursts used in the IceCube stacking analysis. The different curves in each panel correspond to no decay (stable neutrinos) and three different lifetimes, as given in the legend, which are applied to each burst in the stacking sample individually. As decay model, ν_1 is assumed to be stable, whereas ν_2 and ν_3 decay with the indicated lifetime, *i.e.*, all of the lifetimes are consistent with their current bounds. The limit from IC-40+59 is shown [92], as well as an extrapolated one for IC-86 (ten years, $A_{\text{eff}}^{\text{IC86}} \simeq 3 \cdot A_{\text{eff}}^{\text{IC40}}$; see, *e.g.*, Ref. [230]). For the prediction, the 117 bursts in the IC-40 sample have been used [3], the “no decay” corresponds to the nominal prediction in Fig. 3 of Ref. [4]. Figure taken from Ref. [119].

field. It depends, apart from particle physics parameters, on the value of B' , the magnitude of the magnetic field in the shock rest frame; see Ref. [103] for a review. The different panels show two different cases for this transition.

It is easy to show that if only one mass eigenstate is stable, an asymptotic value of the ratio R is reached for complete decays which does not depend on the initial flavour composition (see, *e.g.*, Refs. [229, 211]). This asymptotic value $R \simeq 0.14$ is marked in Fig. 6.5, and it is always reached for low enough energies in the presence of decay. The low value simply reflects that muon tracks are strongly suppressed compared to the cascades. The transition towards this asymptotic curve depends on the lifetime, of course. The presence of different flavour ratios may be useful to distinguish different decay scenarios; see Refs. [211, 228].

Finally, we see the effect of decay, with only ν_1 stable, in a realistic sample of GRBs, as it has been actually used in a stacking analysis. We show in Fig. 6.6 the prediction for the quasi-diffuse muon- (left panel) and electron-neutrino (right panel) fluxes from the 117 bursts in the IC-40 stacking sample as curves labeled “no decay”. The left curve corresponds to the nominal prediction in Fig. 3 of Ref. [4], updated with the current values of the mixing angles. It uses exactly the same bursts and parameters as the original IceCube analysis, but the numerical (updated) method for the flux prediction from Ref. [4]. Note that the quasi-diffuse flux normalisation hardly depends on the burst sample used, but only the shape (*cf.*, dashed curves in Fig. 1 of Ref. [92]). This means

that the shape will be affected by the actual bursts in the sample, whereas the normalisation will remain approximately constant – modulo statistical fluctuations from the quasi-diffuse flux extrapolation; see Refs. [231, 99]. We also show in Fig. 6.6, left panel, the current stacking limit for muon tracks, as well as an extrapolation for the full-scale experiment. While the current limit does not yet exceed our nominal prediction, the full scale experiment will finally exceed it for the chosen standard values of the astrophysical parameters. Note that in the original IceCube analysis, $z = 2$ has been assigned to a burst if the redshift has not been measured, while the pion production efficiency has been computed (for long bursts) with $L_{\gamma}^{\text{iso}} = 10^{52} \text{ erg s}^{-1}$. Since we stick to these rules, most bursts will have a redshift $z > 1$, and cosmological effects will be important for decay.

In Fig. 6.6, we also show the flux predictions for different neutrino lifetimes. In the extreme cases, $\kappa^{-1} \lesssim 1 \text{ s eV}^{-1}$, the muon-neutrino predicted flux is suppressed to below the expected limit from IC-86 over ten years. However, in these cases, a substantial electron-neutrino flux is expected; see right panel. It can be read off from the figure, that GRB neutrinos should be detected with the full scale experiment in cascades if the effective area for cascades is at least 25% of the one for muon tracks at 1 PeV.¹⁰ Regardless, for the relevant search time window, we only expect 0.07 electromagnetic cascade events for the nominal (“no decay”) prediction from GRBs; therefore, the three observed events might in this case come from a strong statistical fluctuation, or a significant deviation of astrophysical parameters from their assumed mean values.

In any case, we have shown that one should keep in mind that no reliable information on astrophysical neutrino sources, such as GRBs, can be obtained from muon tracks only. In particular, it is not clear the absence of GRB neutrinos so far is due to their decay, or because the baryonic loading in GRBs is smaller than anticipated (which would make it difficult for GRBs to be the joint sources of UHECRs and neutrinos; see chapter 4). More statistics are needed from the IceCube experiment in order to be able to tell, first, whether the suppression of muon tracks at PeV energies is a physical one and, second, in case it is, whether the spectral distortion is consistent with neutrino decay.

¹⁰Unfortunately, there are no GRB cascade analyses available up to this point, which means that reliable limits in the right panel of Fig. 6.6 cannot be shown.

Chapter 7

Summary and conclusions

In this thesis we have argued for the possibility that hadronic acceleration occurs in gamma-ray bursts (GRBs), as a result of which they might be the sources of ultra-high energy cosmic rays (UHECRs) and neutrinos. We have worked under the assumption that the UHECRs are composed exclusively of protons, which are shock-accelerated to energies of $\sim 10^{12}$ GeV in the sources. Due to the high photon densities in GRBs, photohadronic ($p\gamma$) interactions are expected to dominate over proton-proton (pp) interactions [232]. Neutrinos are expected to be produced in the photohadronic interactions, *e.g.*, through the creation of resonances such as the Δ (1232) resonance (see Eq. (1.1)), which decays into pions and muons that in turn decay into neutrinos (see Eq. (1.2)). The energies of these neutrinos are expected to be about 1/20-th of the energies of the protons that produced them; since the GRB neutrino spectra typically peaks at PeV energies, this means that 20 PeV protons are responsible for these neutrinos.

As explained in **chapter 1**, we have focused on the production of UHECRs and neutrinos during the internal shock phase of long-duration GRBs (*i.e.*, those that last more than 2 s), where the plasma blobs –or, equivalently, spherical matter shells (see sections 1.3 and 1.4)– that have been ejected by the central emitter coast at constant speeds and collide with one another. In each collision, the participating shells merge into a new one, and part of their kinetic energy is radiated away as the new shell cools down, in the form of protons, neutrons, neutrinos, and gamma-rays.

For our neutrino predictions, we have used the state-of-the-art software NeuCosmA [96, 99, 4], which numerically computes the GRB neutrino spectra from photohadronic interactions, via many production channels, including higher resonances such as K , multi-pion processes, and π^- production. It also takes into account the cooling of the secondary pions and muons before their decay into neutrinos, and calculates the maximum energy that the protons can reach by comparing their acceleration timescale to the dynamical, synchrotron, and photohadronic timescales (see Eq. (1.10)). Recently, the IceCube collaboration claimed that the non-observation of neutrinos from a sample of 217 GRBs ruled out GRBs as sources of UHE neutrinos [92]: the expected neutrino flux from each source was normalised to its observed gamma-ray signal. These results, however, made use of an analytical prediction of the neutrino spectrum [2], under the assumption that only neutrons are able to escape the source and that they decay into UHECR protons outside the source (the “neutron model”). A re-analysis of the same GRB sample using instead the numerical predictions of NeuCosmA revealed that even within the pure neutron model the flux predictions lie about one order of magnitude safely below the current upper bounds from IceCube [96]. Furthermore, the ANTARES collaboration has used the NeuCosmA predictions to optimise their search for neutrinos from GRBs, and has put limits to the neutrino flux [233].

In **chapter 2** we have explicitly studied the possibility that GRBs are the sources of UHE neutrinos *and* UHECRs. In order to do this, we have built a source model [106] where UHECRs are emitted as either neutrons, which escape the source and quickly β -decay into protons, or, at higher energies, directly as protons, which leak out of the source. The latter can occur via diffusion of the protons out of the source, or, more simply, by their Larmor radius growing beyond the width of the matter shell in which the proton is contained. The relative importance of each of the two components –the neutron escape and the direct proton escape– is determined by the source’s optical thickness to neutron escape (see section 2.1): when it is below one, neutron escape will be dominant; otherwise, direct proton escape from the edges of the matter shells will dominate.

High proton acceleration efficiencies ($\eta \approx 1$ in Eq. (1.11)) are required to be able to explain the observed UHECR spectrum. Within our two-component model, we have found that a high efficiency entails that UHECRs must leave the source not only via neutron escape, but also via direct proton leakage [106]. In addition, our two-component UHECR emission model weakens the relation between UHECR and neutrino production. Whereas, in a model of where only neutrons escape, each escaping neutron entails neutrino production via the photohadronic processes that generated the neutron in the first place (*i.e.*, $p\gamma \rightarrow \Delta^+(1232) \rightarrow n\pi^0$), in a model where direct proton escape is also possible, these protons are able to leave the source without having produced neutrinos inside of it. Thus, the one-to-one correspondence between neutrino and UHECR emission is broken [106].

In order to make predictions on the observed UHECR spectrum from this two-component model, we have written original computer code that propagates the protons from the production epoch (up to a redshift $z = 6$) to the detection ($z = 0$) epoch, at Earth. The details of such treatment are shown in **chapter 3**. At each redshift step, a population of GRBs injects protons, and these are numerically propagated to smaller redshifts while taking into account the relevant energy-loss processes: adiabatic cosmological expansion, pair-creation, and photohadronic interactions with the photons of the cosmological backgrounds (see section 3.2); the latter result in the additional production of cosmogenic neutrinos, whose spectrum peaks at \sim EeV energies.

In **chapter 4** we have fitted the generated UHECR spectrum to the observations performed by the extensive air shower experiments HiRes, the Telescope Array, and the Pierre Auger Observatory. Doing this also normalises the predicted GRB neutrino spectrum and the cosmogenic neutrino spectrum, thus allowing us to compare them with the current IceCube upper bounds. Hence, while in some regions of the GRB parameter space we might be able to fit the UHECR observations, the same regions might turn out to be inviable because the corresponding neutrino expectations exceed the upper bounds [161].

Under the hypothesis that GRBs are the sources of *both* UHECRs and neutrinos, if we fit the UHECR flux prediction from our two-component emission model to the observed UHECR spectrum by extensive air shower experiments, we find that, while the regions of GRB parameter space that correspond to an emission dominated by neutron escape are able to closely fit the UHECR observations, the associated prompt neutrino fluxes already exceed the current bounds on the neutrino flux set by IceCube. These regions correspond to high gamma-ray luminosity and moderate Lorentz factors ($\lesssim 500$). The regions with higher Lorentz factors (500 – 1000) remain currently unconstrained; within these, direct proton escape is the dominant component of UHECR emission. However, after 15 yr of exposure, the non-observation of neutrinos from GRBs and of cosmogenic neutrinos by IceCube would also rule out most of the remaining parameter space [161]. As a result of fitting our UHECR predictions to the observed spectrum, we are able to find the best-fit value of the baryonic loading –the ratio of energy in UHECRs to electrons– at each point of the GRB parameter space, rather than having to use an externally fixed value for this quantity (usually,

10). We have found, however, that the region of parameter space corresponding to the neutron escape model is discarded because the associated neutrino predictions exceed the current IceCube upper bounds, in accordance to the results of Ref. [100]. These regions correspond to low values of the baryonic loading: thus, the remaining parameter space is associated to values of the baryonic loading of 1000 or higher. However, notice that these numbers are for the baryonic loading in all of the range $10^6 - 10^{12}$ GeV, while, for neutrino production, only the UHE range of $10^{10} - 10^{12}$ GeV is relevant. Within this reduced energy range, the baryonic loading is not as high.

Up to this point, our neutrino predictions have been made within a simplified scenario which is common in the literature: that of the “static burst”, described in sections 1.3 and 1.4. Within it, the gamma-ray, UHECR, and neutrino predictions from a GRB are made by assuming that all of the internal collisions among matter shells are identical, *i.e.*, they all take place at the same collision radii and under the same conditions of particle density, Lorentz factors, and other parameters that determine the particle output from the collision. In **chapter 5** we have moved beyond the static burst approximation and considered a simulated burst by tracking the individual propagation of matter shells, each with its own speed and mass, and we have built up the UHECR, neutrino, and gamma-ray signals as the sum of the spectra coming from the individual collisions among the shell, each occurring under different conditions [234].

The study of the dynamical fireball model revealed that, within the internal collision phase of the GRB evolution, UHECRs, neutrinos, and gamma-rays are emitted at different stages of the fireball expansion [234], *i.e.*, they are created by internal collisions of the matter shells that occur at different radii. As the burst expands, the particle densities fall (as $\sim r^{-2}$): as a consequence, the source becomes increasingly transparent to neutron escape. Therefore, neutrino production occurs mainly at the innermost radii, where proton and photon densities are highest and photohadronic interactions are more common; UHECR emission occurs at intermediate radii, with neutron escape peaking before direct proton escape; and gamma-ray emission comes from late in the GRB evolution, that is, from the outermost radii, where the Thomson ($e\gamma$) optical depth is low enough for photons to escape the source. Neutrino and UHECR predictions from GRBs are naturally based on the properties of the internal collisions derived from gamma-ray observations. However, we have seen that the different particle species are generated at markedly different radii; therefore the standard estimators of neutrino and UHECR emission might be more model-dependent than previously thought. We have seen that most of the neutrino emission comes from the innermost radii. In these collisions, the particle densities have higher values than the ones assumed in the static burst approximation, which is why these innermost collisions, while few, are already enough to account for most of the total neutrino signal. Since the magnetic field in these collisions is higher than the standard value ($> 10^5$ G), synchrotron losses of the secondary pions and muons are more intense, and they shift the peak of the neutrino spectrum to lower energies than in the static burst prediction.

Finally, as an additional exploration in the direction of new physics effects, in **chapter 6** we have explored the possibility of neutrino decay into invisible products, in the context of UHE neutrinos, first by working out the correct redshift-dependence of the flux damping due decay and then by introducing the damping into the NeuCosmA numerical predictions. Since neutrinos from extragalactic sources—such as GRBs and active galactic nuclei—traverse distances that might already be close to the Hubble horizon of ~ 3.8 Gpc, they become potentially powerful probes of the beyond-the-Standard-Model hypothesis that neutrinos are unstable and decay [119]: the long propagation distances allow for the possibility the neutrinos flux is depleted due to decay even if they are extremely long-lived.

A correct treatment of the redshift dependence of the decay of UHE astrophysical neutrinos shows

that, contrary to popular assumptions in the literature, unstable neutrinos that come from distant sources have not necessarily reached complete decay by the time they reach Earth [119], *i.e.*, not all of the neutrinos have decayed. We have shown that, even for neutrinos that come from the most distant source and that traverse the Hubble length, complete decay is rather an energy-dependent condition (see Eq. (6.16)).

Under the assumption that the mass eigenstate ν_1 is stable –inferred from the detection of ν_e from SN1987A–, we have shown that the instability of the mass eigenstates ν_2 and ν_3 induces a depletion of the ν_μ and ν_τ fluxes from GRBs that can reach one order of magnitude, depending on the value of the lifetime assumed, whereas the ν_e flux –which is made up mostly of ν_1 – is only slightly affected. While it is still premature to tell, such a mechanism could lead to the observed cut-off in the UHE neutrino flux at 2 PeV observed by IceCube [7, 6, 8]. More importantly, this observation further reinforces the importance of studying the flavour composition of the UHE neutrino signals.

We have thus seen that refinements over the simplest joint models of UHECR and neutrino production, which have begun to be challenged by experimental data, lead to valuable insights, be it by means of comparison with the UHECR observations and the neutrino upper bounds, or by finding a different neutrino prediction as a result of modeling the internal collisions in the GRB in a more realistic manner. Further developments, such as the ones outlined in chapter 8, are likely to reward the astroparticle community with even greater knowledge of the UHE multi-messenger picture of the Universe in the years to come.

Chapter 8

Outlook

UHE astroparticle physics is a rapidly-developing field which, thanks to the existence of the current and planned detectors, will likely continue to see important progress in the following years. As the statistical sample of UHECRs and neutrinos, and of astrophysical sources such as GRBs and AGNs, grows, our ability to discern between the competing theories of particle creation and emission will improve. As a result, it is only to be expected that many of the current theoretical models will be discarded under the growing body of experimental data. It is therefore natural to plan ahead and consider a few improvements to the various developments presented in this thesis that would perhaps make them more complete and also more competitive.

Regarding the UHECR and neutrino emission model (chapter 2):

- Consider the acceleration of nuclei up to iron in the source. For this, the destruction of the nuclei via photodisintegration on the source photon field must be taken into account; see appendix F for some initial considerations. Repeated occurrence of photodisintegration will yield progressively lighter nuclei, down to free protons. A complete treatment of nuclei in the source should consider the chain of nuclide creation, the energy losses and energy gains of each of each them.
- Implement neutrino production in the presence of UHECR nuclei. Neutrino emission will be suppressed if UHECRs have a sizable component of heavy nuclei, since each of the N nucleons of an UHECR nucleus of energy E will have an energy E/N available to produce neutrinos through photohadronic interactions, versus an UHECR proton with the same energy E .

Regarding the UHECR propagation (chapter 3):

- Include the radio photon background (see, *e.g.*, Ref. [235] and Fig. A.6 in Ref. [87]); currently photohadronic interactions during the UHECR proton propagation occur only on the CMB and CIB (see section 3.2.4).
- Implement more models of the local CIB (see, *e.g.*, Fig. 7 in Ref. [236]) into the propagation code. Currently, two of the most popular models, by Franceschini *et al.* [135] and by Stecker *et al.* [136], are implemented (see section 3.2.4).
- Include the propagation of nuclei (see, *e.g.*, Ref. [123]) in the same manner as for protons, implementing the $A\gamma$ interactions in a way similar as how the $p\gamma$ interactions are calculated

in NeuCosmA, *i.e.*, using fast, simple parametrisations of the cross sections and energy loss rates

- Include the effects of deflection on intergalactic magnetic fields, which would affect the CR flux at energies below $\sim 10^7$ GeV. The incorporation of magnetic deflections is necessary if one wishes to perform small- and large-scale anisotropy studies with potential sources of UHECRs or neutrinos. See section A.1 for a few more details on deflection by Galactic and extragalactic magnetic fields.
- Keep track of the gamma-ray flux coming from the decay of π^0 created in $p\gamma$ interactions. This amounts to implementing a Boltzmann equation for the gamma-ray flux, in the same way that one was implemented for the propagation of the UHECR protons. We currently only keep track of the integrated energy dumped into electrons and photons, but do not follow the evolution of the gamma-ray spectrum (see section 3.2.8).
- In section 3.4.2 we explored the effect of adding an extra, high-redshift component to the CIB injection function, in order to enhance the cosmogenic neutrino peak due to $p\gamma$ interactions on the CIB. While the results show that it is possible to obtain such an enhancement, they would benefit from a more careful fitting procedure to the existing CIB models and further exploration.

Regarding the constraints on the joint UHECR and neutrino production in GRBs (chapter 4):

- So far, our results have been produced under the assumption that all of the GRBs have a representative, typical gamma-ray luminosity of 10^{52} erg s⁻¹. GRBs, however, have a measured distribution in luminosity (see, *e.g.*, [138]). A more realistic, though more complex, analysis of the bounds on the joint production model would consider both a redshift and a luminosity distribution of GRBs

Regarding the dynamical GRB model (chapter 5):

- GRB light curves come in many different shapes, which is part of the reason why it is difficult to come up with a single theoretical model to generate all of the different behaviours. It would be interesting to be able to generate different light curve shapes, thereby allowing our model to make predictions of the neutrino and UHECR emission for particular observed GRBs.
- Some light curves exhibit an intermittent behaviour: periods of activity separated by periods of quiescence. One possible explanation is that the engine works also only intermittently, perhaps with matter falling into it at intervals. This could be modeled in our simulation by turning the central emitter engine on and off periodically.
- Currently, in our simulations all matter shells are initialised with the same bulk kinetic energy, $E_{\text{kin},0}^{\text{iso}}$. However, we could explore a scenario where the initial kinetic energies follow a different distribution, *e.g.*, a Gaussian distribution
- Experiments usually output GRB light curves in different energy bands (*e.g.*, *Fermi*-GBM and *Fermi*-LAT), while, so far, we have only generated bolometric light curves in a broad range covering the MeV range. It could prove useful for comparison to real measurements to come up with a way to generate synthetic light curves in different energy bands.

- Up to now, we have assumed that the photon break energy in the source photon spectrum, $\varepsilon'_{\gamma,\text{break}}$, as well as the minimal and maximal photon energies in the SRF, are fixed. We could explore the variation of $\varepsilon'_{\gamma,\text{break}}$ in different collisions by assuming that the peak photon energy is generated by synchrotron emission, which depends on the magnetic field B' , which in turn falls with collision radius.
- We might consider the growth with time of the deceleration radius, r_{dec} , where the interstellar medium starts. Also, we could calculate the effective r_{dec} for each shell, given its kinetic energy and Lorentz factor, and assuming a value for the density of the surrounding medium.

Regarding UHE neutrino decay (chapter 6):

- Use the UHE events recently detected by IceCube to deduce bounds on the neutrino lifetime.
- Explore the effect of other types of new physics –decoherence, Lorentz invariance violation, *etc.*– in the GRB UHE neutrino flux, including. Unlike decay, some of these effects may manifest more strongly at higher energies, UHE astrophysical neutrinos might constitute the only way to probe them.

This is, of course, a non-exhaustive list of potential further developments, but it is already enough to convey the richness of the research avenues that we have started to explore.

Appendix A

Description and numerical implementation of the UHECR propagation

In this appendix we show the underlying assumptions and details about the numerical implementation of the UHECR propagation scheme introduced in chapter 3.

A.1 Assumptions

Our main assumptions in modeling UHECR propagation are:

- **CRs are made up solely of protons:** lately, observations by the Pierre Auger Observatory have hinted that the composition of the most energetic CRs contains predominantly heavy nuclei, instead of protons [50]. However, it is not clear what mechanism would be able to accelerate heavy nuclei to the highest energies, while not also accelerating the protons to the same energies. In addition, the destruction of heavy nuclei by photodisintegration in nucleus-photon interactions in the source remains an unresolved problem. As a result, the heavier-composition result is still debatable and therefore in this work we have considered an exclusively proton composition of the CRs.
- **Neutrons and protons are treated as the same species:** in sources that are optically thin to neutron escape (see section chapter 2), the protons that make up the CR flux are originated in the decay of escaped neutrons from the sources. Below a critical neutron energy $E_c(z)$, the neutron decay time is shorter than its interaction time. Therefore, we treat neutrons and protons as the same species (*pneutrons*), and append a cut-off $\propto e^{E^2/E_c^2(z)}$ to the neutron injection spectrum (see section 3.2.7).

Cooling and escape rates of protons and neutrons, as well as the injection of secondaries (pions, etc.) are given in appendix B of Ref. [96]; see Eq. (B4) therein. If protons and neutrons are treated as the same species, the *pneutrons* can only cool (neutron-to-proton conversion does not change the number of *pneutrons*).¹ In our code, the *pneutron* system

¹We have added a new species to NeuCosmA, to be used in the routine `ncoComputeCoolEscRate: ParticleIn = NCO_PROTON_NEUTRON` and `ParticleOut = NCO_PROTON_NEUTRON` will give the correct cooling rate and a zero escape

does not care about what happens to the neutrons: if they decay before they interact, they will make protons with about the same energy, whereas if they interact before they decay, they will just be included in the energy loss rate.

- **There are no diffusion effects due to magnetic fields:** below $\sim 10^9$ GeV, diffusion due to the deflection of CRs on intergalactic magnetic fields kicks in. Unlike other publicly-available software for UHECR propagation², such as CRPropa [239] and SimProp [240], our code does not consider interactions with the magnetic field, and so should not be used to propagate the CRs to energies far below 10^9 GeV (10^7 GeV is probably the lowest energy that is sensible to use). Magnetic diffusion induces angular deviations in the trajectory of CRs, which makes difficult the correlation between detected CRs and potential sources. Angular deviations due the regular component of the Galactic magnetic field of magnitude $2 \mu\text{G}$ are expected to be as low as $3^\circ - 5^\circ$, for a proton of 60 EeV [241]; deviations on the turbulent component of the Galactic magnetic field are smaller, $\sim 0.5^\circ$. Available information on the extragalactic magnetic field is much scarcer than for the Galactic one, but it is expected to be more intense close to the centers of galaxy clusters and inside filaments ($\lesssim 10\mu\text{B}$) than in the void ($1 - 10$ nG, or as low as fG). The angular deviations depend on the particular trajectory followed by the UHECRs, and their estimates range from $\lesssim 0.1^\circ$ [242] to $\gtrsim 10^\circ$ for a 60 EeV proton [243].

A.2 Inputs

With the objective of making the CR propagation code as flexible as possible, we have considered the following functions and parameters as inputs:

- **Local ($z = 0$) CIB spectrum:** there are competing parametrisations of the local CIB spectrum ($\text{GeV}^{-1} \text{cm}^{-3}$), $n_\gamma^{\text{CIB}}(\epsilon, 0)$; see section 3.2.4. Currently, there are two alternatives implemented in the code: CIB1, by Franceschini *et al.* [135], and CIB2, by Stecker *et al.* [136]. Additional parametrisations can be added to the code with ease.
- **Redshift evolution of the CIB sources:** the redshift evolution of the CIB spectrum n_γ^{CIB} depends on the redshift evolution of the sources of IR photons, $\mathcal{H}_{\text{CIB}}(z)$ in Eq. (3.22). Currently, the code allows to compute the CR propagation with no source evolution (NCO_CRPROP_SOURCEDIST_CIB = 0), SFR evolution (NCO_CRPROP_SOURCEDIST_CIB = 1), GRB evolution (NCO_CRPROP_SOURCEDIST_CIB = 2), or a more general evolution of the form $(1+z)^\beta \mathcal{H}_{\text{SFR}}(z)$ (NCO_CRPROP_SOURCEDIST_CIB = 3). In the latter case, the value of the parameter β is stored in NCO_CRPROP_COSMEVOL_CIB. Note that the code is flexible enough to easily implement other forms of \mathcal{H}_{CIB} .
- **Redshift evolution of the CR sources:** $\mathcal{H}_{\text{CR}}(z)$ in Eq. (3.31). The same options as for the CIB evolution apply, but NCO_CRPROP_SOURCEDIST_CR and NCO_CRPROP_SOURCEDIST_CR are set instead.

rate. Note that this species should not work for any other function, where `ParticleIn = NCO_PROTON` is to be used in that case, and no neutrino-antineutrino distinction is to be made. Therefore, we are not sensitive to the Glashow resonance. That is, the code simply adds the finally obtained neutrino and antineutrino fluxes, since their distinction is unphysical in this case.

²There is other public software, such as GALPROP [237] and DRAGON [238], designed to propagate lower-energy CRs in the magnetic field of the Galaxy, within the diffusive regime.

- **Proton injection spectrum:** $Q_{\text{CR}}(E, z)$ in Eq. (3.31), with units $\text{GeV}^{-1} \text{Mpc}^{-3} \text{s}^{-1}$. One can either use a universal power-law spectrum with a simple exponential cut-off, *i.e.*, $Q_{\text{CR}}(E, z) \sim E^{-\gamma} e^{-E/E_{p,\text{max}}}$, implemented as the function `CRInjectionSpectrumUniversal`, or couple the source model from section 2 here.
- **Maximum proton energy, $E_{p,\text{max}}$:** this energy determines the intensity of the damping of the CR injection spectrum at high energies. The CR and cosmogenic neutrino fluxes at Earth depend strongly on the value of $E_{p,\text{max}}$. In the source model of section 2, it is determined internally by a competition between energy-gain and energy-loss processes.
- **Redshift at which the universe becomes homogenous, z_{hom} :** by default, it should be set to $z_{\text{hom}} = 2 \cdot 10^{-2}$, corresponding to $\sim 77 \text{Mpc}$. CR injection occurs down to this redshift; from z_{hom} to $z = 0$, only adiabatic energy losses are considered in their propagation.
- **Maximum redshift of contributing sources, z_{max} :** currently set to $z_{\text{max}} = 6$. It determines the initial condition $Y(E, z_{\text{max}}) = 0$; the CR flux is propagated, and the cosmogenic neutrino flux receives contributions, from z_{max} down to $z = 0$.

A.3 Limitations

Our code, of course, has limitations. Some of the assumptions in section A.1 could be seen as limitations. However, more technical limitations of our code are:

- **Cut-off of the CR injection spectrum:** when using a universal CR power-law injection spectrum, too sharp an exponential cut-off, *e.g.*, $Q_{\text{CR}}(E) \propto E^{-\gamma} e^{-E^2/E_{p,\text{max}}^2}$, occasionally yields values for the proton spectra that are below the available numerical precision, thus inducing the program to crash.
- **No composition studies possible:** since we have assumed an all-proton CR flux (see section A.1), we are not able to perform UHECR composition studies.

A.4 Numerical implementation

The UHECR propagation algorithm is implemented as C code. Its goal is to solve the kinetic equation, Eq. (3.5), and obtain the UHECR proton flux at Earth.

A.4.1 Discretised transport equation

We will denote $Y_i(E) \equiv Y(E, z_i)$. Since we are interested in the redshift evolution of the proton density, we calculate, at each value of z_i , the entire energy spectrum $Y_i(E)$ between E_{min} and E_{max} . It is useful to rewrite the derivatives w.r.t. energy in Eq. (3.5) as derivatives w.r.t. $x \equiv \log_{10} E$, by using $\partial_E = (\log_{10} e/E) \partial_x$. To solve Eq. (3.5) numerically³, we write it in terms of finite differences in the redshift direction, namely,

$$\frac{Y_{i+1}(x) - Y_i(x)}{-\Delta z} = -\frac{1}{(1+z_i)H(z_i)} \left\{ \frac{\log_{10} e}{E} [\partial_x (H(z_i) E Y_i(x))] \right.$$

³Unlike most of the publicly available codes (*e.g.*, CRProp, SimProp, GALPROP), our code does not use Monte Carlo methods to compute the propagation of CRs.

$$\begin{aligned}
 & + \partial_x (b_{e^+e^-}(x, z_i) Y_i(x)) \\
 & + \partial_x (b_{p\gamma}(x, z_i) Y_i(x)) \\
 & + \mathcal{L}_{\text{CR}}(x, z_i) \} . \tag{A.1}
 \end{aligned}$$

From this, we find an expression for the spectrum at the next redshift step, $Y_{i+1}(x)$. Notice that, since the CR spectrum is calculated from $z_{\text{max}} > 0$ down to $z = 0$, the redshift step ($-\Delta z$) must be negative.

At each redshift z_i , the spectrum $Y_i(x)$ is calculated at n_x different values of x , regularly spaced between x_{min} and x_{max} . At each of the n_x sampled values of x , the functions from the r.h.s. of Eq. (A.1),

$$H(z) E Y_i(x) \quad , \quad b_{e^+e^-}(x, z_i) Y_i(x) \quad , \quad b_{p\gamma}(x, z_i) Y_i(x) \quad , \tag{A.2}$$

are evaluated at $x - \delta x$ and $x + \delta x$, with δx a small displacement⁴. These evaluations are used to approximate the derivatives at x by

$$\partial_x f \simeq \frac{f(x + \delta x) - f(x - \delta x)}{2\delta x} \quad , \tag{A.3}$$

with f each of the functions in Eq. (A.2). The value of Y_i at any x can be obtained from the n_x sampled points by linear interpolation.

The proton spectrum is evolved from z_{max} down to the local epoch, at $z = 0$. Recall, however, that the injection term, \mathcal{L}_{CR} , is switched on only down to z_{hom} , below which the universe is no longer homogeneous (see subsections 3.2.5 and A.2). The initial condition $Y(E, z_{\text{max}}) = 0$ is translated into $Y_0(x) = 0$, and the spectrum is evolved down to $z = 0$, where the comoving spectrum, $Y_{n_z}(x)$, is automatically equal to the proper local spectrum, $n_p(x, 0)$. The proton flux at Earth is then calculated using Eq. (3.3).

The following are the main discretisation parameters in the numerical implementation of the solver:

- Δz : the step in the redshift direction, so that the total number of values of redshift at which the CR spectrum is evaluated is $n_z = 1 + (z_{\text{max}} - 0)/\Delta z$. We have found that $\Delta z = 5 \cdot 10^{-5}$ reproduces the known features of the CR spectrum (bump, dip, etc.) and matches the published results accurately. The corresponding number of values of z sampled is $n_z = 1.2 \cdot 10^6$.
- n_x : number of x values at which the spectrum $Y_i(x)$ is calculated at each redshift. For the linear interpolation of the spectrum in the whole energy range, a low value is sufficient; we have found that $n_x = 60$ reproduces published results accurately.
- $x_{\text{min}}, x_{\text{max}}$: (log of) minimum and maximum proton energies considered; at each redshift value, the proton spectrum between these energies is calculated at n_x regularly-spaced values. Typically, $x_{\text{min}} = 7$ or 7.5 and $x_{\text{max}} = 12$.
- δx : small displacement with which the numerical derivative, Eq. (A.3), is calculated. We use $\delta x = 10^{-10}$, but it is to be expected that higher values also work.

⁴One should avoid using $\delta x = (x_{\text{max}} - x_{\text{min}})/(n_x - 1)$ in order for the spectrum Y_{i+1} not to have discontinuity problems in the next step of the solver, when it is evaluated at the same n_x values as in the previous step.

A.4.2 Electromagnetic cascade energy density

The e.m. cascade energy density, ω_{cas} , receives contributions from all redshifts, as expressed by Eq. (3.43). In the implementation of our code, we have integrated instead in $x \equiv \log(E)$ at each redshift step, and approximated ω_{cas} as

$$\omega_{\text{cas}} \simeq \sum_n \left[\int dx \ln(10) E \frac{b_{\text{cas}}(x, z_n)}{(1+z_n)H(z_n)} Y_n(x) \right] \Delta z. \quad (\text{A.4})$$

Note that ω_{cas} thus calculated is returned in units of GeV Mpc^{-3} ; it needs to be multiplied by $\sim 3.4 \cdot 10^{-74}$ to convert it to GeV cm^{-3} . Since, in the current version of the code, the proton injection spectrum has not been normalised beforehand, one still needs to multiply ω_{cas} by the normalisation (fixed, *e.g.*, by fitting the proton flux at Earth to the HiRes data).

A.4.3 Tricks for speed-up

NeuCosmA already calculates the photohadronic interactions efficiently through its parametrisation of SOPHIA results as fast functions. There are, however, a few extra tricks that we have implemented to speed up the execution of the CR propagation code:

- **Protons and neutrons are treated as the same species:** as explained in sections 3.2.7 and A.1. By doing this, the code does not follow the decay of neutrons (although the decay products *are* taken into account).
- **Adiabatic scaling of the energy loss rates on the CMB:** by default (setting `NC0_CRPROP_CMB_SCALING = 1`), the pair-production and photohadronic energy loss rates on the CMB, $b_{e^+e^-}^{\text{CMB}}$ and $b_{p\gamma}^{\text{CMB}}$, are calculated once at $z = 0$, when the code is initialised, and thereafter scaled to different redshifts with the use of Eq. (3.29). This reduces the time needed to propagate the CR spectrum and calculate the cosmogenic neutrino flux from ~ 40 minutes (if the energy loss rate is calculated from definition at each redshift) to ~ 120 s.
- **CIB interactions are not calculated at each step:** since the interaction length on the CIB is much larger than the interaction length on the CMB (see Fig. 3.3), we do not calculate the CIB energy loss rate at every redshift step, but rather only every `CIBSTEPS` redshift steps. We have found that setting `CIBSTEPS $\approx 0.025/\Delta z$` correctly reproduces the desired features of the fluxes and matches published results. The plots in section 3.3 have been produced using `CIBSTEPS = 500` (*i.e.*, $\Delta z = 5 \cdot 10^{-5}$).
- **Cosmogenic neutrino spectrum is not calculated at each step:** it suffices to calculate the cosmogenic neutrino spectrum only every `NEUTRINOSTEPS = 0.05/\Delta z` steps. The plots in section 3.3 have been produced using `NEUTRINOSTEPS = 1000` (*i.e.*, $\Delta z = 5 \cdot 10^{-5}$).

Appendix B

The UHECR energy budget from GRBs

Here we show the detailed derivations leading to the conclusions in section 4.2.

B.0.4 Observation of prompt gamma-rays, and local GRB rate

For the description of the redshift distribution, we follow Ref. [138]. The comoving GRB rate [$\text{Mpc}^{-3} \text{yr}^{-1}$] is given by

$$\dot{n}_{\text{GRB}} = \mathcal{E}(z) \cdot \dot{\rho}_*(z), \quad (\text{B.1})$$

where

$$\mathcal{E}(z) = \mathcal{E}_0(1+z)^\alpha \quad (\text{B.2})$$

describes the evolution of the fraction of stars resulting in GRBs, $\alpha \simeq 1.2$, and $\rho_*(z)$ is the (comoving) star formation density [$M_\odot \text{Mpc}^{-3} \text{yr}^{-1}$]. The **observed** redshift distribution of GRBs $d\dot{N}/dz$ [yr^{-1}] can be written as [138]

$$\frac{d\dot{N}}{dz} = F(z) \frac{\dot{n}_{\text{GRB}}}{\langle f_{\text{beam}} \rangle} \frac{dV/dz}{1+z} = F(z) \frac{\mathcal{E}(z) \dot{\rho}_*(z)}{\langle f_{\text{beam}} \rangle} \frac{dV/dz}{1+z}, \quad (\text{B.3})$$

where the last factor is the comoving volume correction.¹ Note that here the beaming factor is needed to correct for the invisible GRBs beamed into different directions ($0 < \langle f_{\text{beam}} \rangle^{-1} < 1$) and $F(z)$ accounts for the ability to observe the GRB, such as the detector threshold ($0 < F(z) < 1$). In the main text, we use $\dot{\tilde{n}}_{\text{GRB}} \equiv \dot{n}_{\text{GRB}}/\langle f_{\text{beam}} \rangle$ for the sake of simplicity, which is lower than the actual GRB rate by the beaming factor.

It is useful to define the adimensional redshift evolution $\mathcal{H}(z)$ of the GRBs by normalizing the comoving GRB rate to the local rate leading to

$$\mathcal{H}(z) = \frac{\dot{n}_{\text{GRB}}}{\dot{n}_{\text{GRB}}|_0} = (1+z)^\alpha \frac{\dot{\rho}_*(z)}{\dot{\rho}_*(0)}, \quad (\text{B.5})$$

¹This correction is defined as

$$\frac{dV}{dz} = 4\pi D_H \frac{1}{h(z)} d_c^2(z), \quad \text{with } h(z) = \sqrt{\Omega_m(1+z)^3 + \Omega_\Lambda} \quad \text{and} \quad d_c(z) = D_H \int_0^z \frac{dz'}{h(z')}. \quad (\text{B.4})$$

Here $D_H = 4.255 \text{ Gpc}$, $\Omega_m = 0.27$, $\Omega_\Lambda = 0.73$, taken from Ref. [133].

such that $\mathcal{H}(z=0) = 1$. In addition, we distinguish the **total number of bursts per year in the observable universe** \dot{N}_{tot} and the **number of observable bursts per year** \dot{N} , where, from Eq. (B.3),

$$\frac{d\dot{N}}{dz} = F(z) \frac{d\dot{N}_{\text{tot}}}{dz}, \quad \dot{N} = \int_0^\infty \frac{d\dot{N}}{dz} dz, \quad \dot{N}_{\text{tot}} = \int_0^\infty \frac{d\dot{N}}{dz} \frac{1}{F(z)} dz. \quad (\text{B.6})$$

As a consequence, one can compute \dot{N}_{tot} from \dot{N} if the threshold function of the instrument is known. We define the ratio $f_{\text{thresh}} \equiv \dot{N}/\dot{N}_{\text{tot}}$ as the fraction of observable bursts because of the instrument threshold. For instance, using a power-law luminosity distribution proposed by Wanderman & Piran [162] with the redshift distribution from Kistler *et al.* [138], we obtain a ratio $f_{\text{thresh}} \simeq 0.5$ for a threshold of $1.75 \cdot 10^{-8} \text{ erg s}^{-1} \text{ cm}^{-2}$ if we assume that bursts can only have a luminosity in the range 10^{50} to $10^{54} \text{ erg s}^{-1}$, as implied in Ref. [162]. This result is of course dependent on the chosen distributions and cutoffs, *e.g.*, when we extend the distribution to lower luminosities, say, $10^{49} \text{ erg s}^{-1}$, the ratio goes down to 0.3, which is the value that we have adopted in this study. In any case, one should keep in mind that there is a factor of two to three difference between \dot{N}_{tot} and \dot{N} .

It is now useful to relate the total redshift distribution of GRBs to Eq. (B.3) by using Eq. (B.5) and Eq. (B.6) as

$$\frac{d\dot{N}_{\text{tot}}}{dz} = \frac{\dot{n}_{\text{GRB}}|_{z=0}}{\langle f_{\text{beam}} \rangle} \mathcal{H}(z) \frac{dV/dz}{1+z}, \quad (\text{B.7})$$

where $\dot{n}_{\text{GRB}}|_{z=0} = \dot{n}_{\text{GRB}}|_{z=0}/\langle f_{\text{beam}} \rangle$ is the often-quoted ‘‘local GRB rate’’, which is of the order of one burst per Gpc^3 and year; see, *e.g.*, Ref. [162]. It is reduced with respect to the actual GRB rate $\dot{n}_{\text{GRB}}|_{z=0}$, which includes the GRBs beamed in different directions which are not directly observable, by the beaming factor. We can now derive \dot{N}_{tot} as

$$\dot{N}_{\text{tot}} = \frac{\dot{n}_{\text{GRB}}|_{z=0}}{\langle f_{\text{beam}} \rangle} \cdot \int_0^\infty \mathcal{H}(z) \frac{dV/dz}{1+z} dz \equiv \frac{\dot{n}_{\text{GRB}}|_{z=0}}{\langle f_{\text{beam}} \rangle} \cdot 4\pi D_H^3 \cdot f_z, \quad (\text{B.8})$$

where we have defined

$$f_z \equiv \frac{1}{4\pi D_H^3} \int_0^\infty \mathcal{H}(z) \frac{dV/dz}{1+z} dz. \quad (\text{B.9})$$

This cosmic evolution factor describes how representative the local GRB rate is for the whole distribution, and it therefore depends on the SFR and GRB evolution. We then can derive the local GRB rate as a function of the observable \dot{N} as

$$\frac{\dot{n}_{\text{GRB}}|_{z=0}}{\langle f_{\text{beam}} \rangle} = \frac{\dot{N}}{f_{\text{thresh}}} \frac{1}{4\pi D_H^3 f_z} \simeq \frac{1}{\text{Gpc}^3 \text{ yr}} \cdot \frac{\dot{N} [\text{yr}^{-1}]}{968} \cdot f_{\text{thresh}}^{-1} \cdot f_z^{-1}, \quad (\text{B.10})$$

which contains Eq. (4.2). Note that the value 968 comes from the volume term $4\pi D_H^3 \simeq 968 \text{ Gpc}^3$. Typical values for f_z can be read off for different star formation and evolution models in Table 4.1.

B.0.5 Cosmic ray injection and observation

The cosmic-ray injection rate $\mathcal{L}_{\text{CR}}(E, z)$ [$\text{GeV}^{-1} \text{ Mpc}^{-3} \text{ s}^{-1}$] can be extrapolated from a single-source isotropic emission spectrum $dN_{\text{CR}}^{\text{iso}}/dE$ in the source frame [GeV^{-1}] as

$$\mathcal{L}_{\text{CR}}(E, z) = \frac{dN_{\text{CR}}^{\text{iso}}}{dE} \cdot \frac{1}{\langle f_{\text{beam}} \rangle} \cdot \dot{n}_{\text{GRB}}(z). \quad (\text{B.11})$$

In order to see the origin of the beaming factor, consider one GRB which ejects cosmic rays at a rate per volume $Q'_{\text{CR}}(E)$ [$\text{GeV}^{-1} \text{cm}^{-3} \text{s}^{-1}$] in the shock rest frame. Then Eq. (B.11) changes to

$$\mathcal{L}_{\text{CR}}(E, z) = \underbrace{\frac{Q'_{\text{CR}}(E) \cdot V'_{\text{iso}} \cdot T'_{90}}{\Gamma}}_{dN_{\text{CR}}^{\text{iso}}/dE \text{ source frame}} \cdot \underbrace{\frac{1}{\langle f_{\text{beam}} \rangle}}_{\text{beaming corr.}} \cdot \underbrace{\dot{n}_{\text{GRB}}(z)}_{\text{comoving GRB rate}}. \quad (\text{B.12})$$

Here the first term corresponds to the total spectrum [GeV^{-1}] released from the single GRB over the duration T'_{90} , and the next-to-last factor multiplies that times the number of GRBs per Mpc^3 and year. The actual source volume is expressed by the “isotropic volume” of the burst [99]

$$V'_{\text{iso}} = 4\pi R_C^2 \cdot \Delta d' = 4\pi R_C^2 \cdot \Gamma \cdot c \cdot t_v, \quad (\text{B.13})$$

where t_v is the variability timescale in the source frame; for details see Refs. [99, 106]. Thus the beaming factor in Eq. (B.12) enters because energy and volume V'_{iso} are computed by assuming isotropic emission, whereas only a fraction $\langle f_{\text{beam}} \rangle^{-1}$ of that energy is actually emitted by the GRB. In addition, note that Eq. (B.12) factorizes in an energy-dependent part and a redshift-dependent part, as it is often assumed in the literature.

In order to address the UHECR connection, a frequently used approach is to use the local energy injection rate between 10^{10} and 10^{12} GeV [171], which can be obtained from Eq. (B.11) as

$$\dot{\varepsilon}_{\text{CR}}^{[10^{10}, 10^{12}]} = \int_{10^{10} \text{ GeV}}^{10^{12} \text{ GeV}} \mathcal{L}_{\text{CR}}(E, 0) E \, dE = \frac{\dot{n}_{\text{GRB}}|_{z=0}}{\langle f_{\text{beam}} \rangle} \underbrace{\int_{10^{10} \text{ GeV}}^{10^{12} \text{ GeV}} \frac{dN_{\text{CR}}^{\text{iso}}}{dE} E \, dE}_{\equiv E_{\text{CR}}^{[10^{10}, 10^{12}]}}. \quad (\text{B.14})$$

which is again proportional to the local GRB rate. From Eq. (B.14), using Eq. (B.10), we can then derive Eq. (4.3).

B.0.6 Neutrinos and multi-messenger physics with GRBs

In order to include the neutrinos in the discussion, we have to take into account that they come from photohadronic interactions, for which the proton and photon densities in the source are the required input; see, *e.g.*, Ref. [96]. Typically, the energy in protons is related to the energy in electrons/photons by partition arguments, similar to the approach used in Refs. [91, 92], *i.e.*,

$$\int_0^{\infty} \frac{dN_p}{dE} E \, dE = \frac{1}{f_e} \int_0^{\infty} \frac{dN_\gamma}{d\varepsilon} \varepsilon \, d\varepsilon = \frac{1}{f_e} E_{\gamma, \text{iso}}, \quad (\text{B.15})$$

where we compute it in the source frame for this discussion. Note that minimal and maximal proton and photon energies are to be defined within dN_p/dE and $dN_\gamma/d\varepsilon$, respectively. The energy range of the gamma-rays is typically given by the instrument, such as *Fermi* GBM. The energy range of the protons spans the whole proton spectrum, from the set minimal to the set maximal energy, at least covering the energy range relevant for the neutrino production which is different from that of the UHECR.² The factor f_e^{-1} is commonly known as “baryonic loading”.

²The neutrino spectra peak at about ~ 1 PeV due to secondary cooling [97], and come from ~ 10 PeV protons.

Let us assume that a fraction $f_{\text{CR}} \leq 1$ of the protons can escape from the source as cosmic rays and define

$$f_{\text{bol}} \equiv \left(\int_{10^{10} \text{ GeV}}^{10^{12} \text{ GeV}} \frac{dN_p}{dE} E dE \right) / \left(\int_0^{\infty} \frac{dN_p}{dE} E dE \right) \quad (\text{B.16})$$

as the bolometric correction factor describing how much of the proton energy sits in the UHE range.³ This bolometric correction depends on the energy range of the proton spectrum, the proton spectral index, and the maximal proton energy, and is for all practical applications ≤ 1 . We can then derive from Eq. (B.15) and Eq. (B.16) the energy injected into UHECR from the individual burst, Eq. (4.4).

In order to see the connection between gamma-rays, cosmic rays, and neutrinos including the processes in the source, we rewrite Eq. (B.11) using Eq. (B.10):

$$\mathcal{L}_{\text{CR}}(E, z) = \frac{dN_{\text{CR}}^{\text{iso}}}{dE} \cdot \frac{\dot{N}}{f_{\text{thresh}}} \cdot \frac{1}{4\pi D_H^3 f_z} \cdot \mathcal{H}(z). \quad (\text{B.17})$$

We can then write the injected energy in the UHECR range with Eq. (4.4) as

$$\int_{10^{10} \text{ GeV}}^{10^{12} \text{ GeV}} \mathcal{L}_{\text{CR}}(E, z) E dE = f_{\text{CR}} \cdot \frac{f_{\text{bol}}}{f_e} \cdot E_{\gamma, \text{iso}} \cdot \frac{\dot{N}}{f_{\text{thresh}}} \cdot \frac{1}{4\pi D_H^3 f_z} \cdot \mathcal{H}(z), \quad (\text{B.18})$$

which shows the relationship to the gamma-ray observations.

Since neutrinos do not interact, it is straightforward to define an injection function similar to that of the cosmic rays as (*cf.*, Eq. (B.11))

$$\mathcal{L}_{\nu}(E, z) = \frac{dN_{\nu}}{dE_{\nu}} \cdot \frac{1}{\langle f_{\text{beam}} \rangle} \cdot \dot{n}_{\text{GRB}}(z), \quad (\text{B.19})$$

where the neutrinos only suffer from energy losses due to the adiabatic expansion of the universe. Note that the beaming factor can be interpreted in different ways here: either only the bursts beamed in our direction can be seen (read in combination with first factor), or only a fraction of the isotropic energy is actually injected (read in combination with last factor). In order to connect with the physics of the sources, we assume here, for the sake of simplicity, that a fraction f_{π} of the proton energy goes into pion production (pion production efficiency [89, 2]), that 50% of the pions produced in photohadronic interactions are charged pions, and each lepton in the pion decay obtains about 25% of the pion energy. Then we have from Eq. (B.19) with Eq. (B.10) and Eq. (B.15) the injected energy into neutrinos

$$\int_{E_{\nu, \text{min}}}^{E_{\nu, \text{max}}} \mathcal{L}_{\nu}(E, z) E dE \simeq \frac{f_{\pi}}{8} \cdot \frac{1}{f_e} \cdot E_{\gamma, \text{iso}} \cdot \frac{\dot{N}}{f_{\text{thresh}}} \cdot \frac{1}{4\pi D_H^3 f_z} \cdot \mathcal{H}(z). \quad (\text{B.20})$$

Of course, this simple estimate does not take into account the energy dependence of the proton interaction length and the normalization change from the cooling of secondaries [4, 98], which we fully take into account in our numerical simulations, but it can serve as a first estimate. For the gamma-rays, similar considerations can be made. However, it is straightforward to identify the common scaling factors from Eq. (B.7) using Eq. (B.10). These considerations, including Eqs. (B.18) and (B.20), are pictorially represented in Fig. 4.1.

³Note that we take the UHE range in the source frame (in principle, the energy has to be higher in the source frame to match the observed 10^{10} GeV), which is however similar to the observed UHE range because the mean free path of the protons at 10^{10} GeV is only 1 Gpc, and therefore $z \leq 0.25$.

Appendix C

Details of the statistical analysis

Here we show the details of the statistical analysis that was used to produce the results presented in chapter 3.

We fit the UHECR proton flux generated by our propagation code (see chapter 3) to the surface observation data recorded by the Telescope Array (TA) [156]. These consist of pairs $(E_i, (E^3 J_{\text{CR}})_i^{\text{TA}})$, with σ_i the uncertainty on $(E^3 J_{\text{CR}})_i^{\text{TA}}$. We define a simple two-parameter χ^2 function as

$$\chi^2(f_e^{-1}, \delta_E) = \sum_i \left(\frac{E_i'^3 J_{\text{CR}}(E_i', f_e^{-1}) - (E^3 J_{\text{CR}})_i^{\text{TA}}}{\sigma_i} \right)^2 + \left(\frac{\delta_E}{\sigma_E} \right)^2, \quad (\text{C.1})$$

with the sum performed over the data points that have energies $E_i \geq 10^{10}$ GeV for the ankle model and $E_i \geq 10^9$ GeV for the dip model. When minimized, this function yields the value of the normalization f_e^{-1} , and the energy-scale displacement δ_E , defined so that $E \rightarrow E' \equiv (1 + \delta_E) E$. Since the (Gaussian) error bars on each TA flux data point i are asymmetric, we have chosen the uncertainty σ_i for each to be the size of the upper bar, if, for given values of f_e^{-1} and δ_E , the calculated flux $E_i'^3 J_{\text{CR}}(E_i', f_e^{-1})$ lies above the central value of the data point; otherwise, we have equaled it to the size of the lower bar. For the systematic energy uncertainty of the TA experiment we have used $\sigma_E = 0.21$, following Ref. [244].

For the estimation of the number of expected neutrino events and the calculation of the limits, we use a simple approach which folds the neutrino flux prediction with the parameters of the measurement. The number of neutrino events $\#\nu$ is calculated as

$$\#\nu = \int dE J_\nu(E) \cdot A_{\text{eff}}(E) \cdot t_{\text{exp}} \cdot 4\pi, \quad (\text{C.2})$$

where $J_\nu(E)$ is the neutrino flux as function of energy (in $[\text{GeV}^{-1} \text{cm}^{-2} \text{s}^{-1} \text{sr}^{-1}]$), $A_{\text{eff}}(E)$ the energy-dependent effective area including Earth attenuation effects (in $[\text{cm}^2]$), t_{exp} the exposure (in [s]), and 4π is the factor for the full solid angle (in [sr]). The standard 90% C.L. exclusion limit by Feldman and Cousins for an arbitrary flux is obtained by choosing the normalization in Eq. (C.2) to obtain 2.44 events [245] (background-free case).

The differential limits in this study are given by

$$E^2 J_{\nu, \text{limit}}(E) = \frac{E}{2.3 \cdot A_{\text{eff}} \cdot t_{\text{exp}} \cdot 4\pi}, \quad (\text{C.3})$$

that is, a neutrino flux exactly following the differential limit over one order of magnitude in energy will yield one event. The current limit for the prompt neutrino flux is based on the model-independent solid angle-averaged effective area from the combined IC40+59 GRB stacking analysis [92] with the exposure being estimated from comparing the 215 bursts of the combined sample to the assumed 667 (long) bursts per year, *i.e.*, $t_{\text{exp}} = 215/667$ yr. For the cosmogenic neutrinos, we calculate the current limit from the average effective area for a 4π -isotropic ν_μ flux during 615.9 days lifetime with the IC79 and IC86 configurations, given in Ref. [7]. Both of these analyses are considered to be background-free, the stacking analysis because of timing and directional information, the UHE analysis because of the cut in energy.

To calculate the extrapolated neutrino upper bounds after $t_{\text{exp}} = 15$ yr of full detector exposure, for the prompt neutrinos we simply rescale the current bound by the factor $215/(15 \cdot 667)$, while for the cosmogenic neutrinos we rescale the corresponding current bound by $615.9/(15 \cdot 365)$.

Appendix D

Algorithms for the dynamical GRB model

In this appendix we include pseudocode descriptions of the algorithms used in the dynamical GRB model introduced in chapter 5.

Algorithm 1 Sample main program

Input parameters:

- ▷ N_{sh} : initial number of shells in the fireball
 - ▷ r_{min} : distance of the last shell ($i = N_{\text{sh}}$) to the emitter
 - ▷ r_{dec} : maximum distance up to which shells are propagated, *i.e.*, start of the external shock zone
 - ▷ l : initial width with which a shell is emitted ($l = ct_v$)
 - ▷ d : initial separation between consecutive shells (emitter frequency $f = c/d$)
 - ▷ $E_{\text{int-sh}}^{\text{iso}}$: initial internal energy of an emitted shell
 - ▷ Γ_0 : characteristic Lorentz boost factor
 - ▷ A : fluctuation of the Lorentz factor
 - ▷ z : redshift of the emitter
 - ▷ $\{\hat{t}_{\text{coll},k}\}, \{t_{\text{obs},k}\}, \{r_{\text{coll},k}\}, \{\Gamma_{\text{coll},k}\}, \{E_{\text{int-sh-coll},k}^{\text{iso}}\}, \{l_{\text{coll},k}\}, \{m_{\text{coll},k}\}, \{\delta t_{e,k}\}$: arrays in which the parameters for each of the simulated collisions will be returned; respectively, collision time in the source frame, collision time in the observer's frame, collision radius, Lorentz factor of the merged shell created in the collision, internal energy of the merged shell, width of the merged shell, mass of the merged shell, emission timescale of the collision
- 1: **EvolveFireball**($N_{\text{sh}}, r_{\text{min}}, r_{\text{dec}}, l, d, E_{\text{int-sh}}^{\text{iso}}, \Gamma_0, A, z, \{\hat{t}_{\text{coll},k}\}, \{t_{\text{obs},k}\}, \{r_{\text{coll},k}\}, \{\Gamma_{\text{coll},k}\}, \{E_{\text{int-sh-coll},k}^{\text{iso}}\}, \{l_{\text{coll},k}\}, \{m_{\text{coll},k}\}, \{\delta t_{e,k}\}$)
 - 2: *// This will create a fireball with, initially, N_{sh} identical shells of width l , separated by a distance d from each other, each with internal energy $E_{\text{int-sh}}^{\text{iso}}$ and a random Lorentz factor that follows a log-normal distribution. The shells will propagate, collide, and merge, until either only one shell remains or until the shells are ordered with increasing Lorentz factor. The resulting parameters of the simulated collisions will be stored in the arrays $\{\hat{t}_{\text{coll},k}\}, \{t_{\text{obs},k}\}, \{r_{\text{coll},k}\}, \{\Gamma_{\text{coll},k}\}, \{E_{\text{int-sh-coll},k}^{\text{iso}}\}, \{l_{\text{coll},k}\}, \{m_{\text{coll},k}\}, \{\delta t_{e,k}\}$.*
-

Algorithm 2

EvolveFireball(N_{sh} , r_{min} , r_{dec} , l , d , $E_{\text{int-sh}}^{\text{iso}}$, Γ_0 , A , z , $\{\hat{t}_{\text{coll},k}\}$, $\{t_{\text{obs},k}\}$, $\{r_{\text{coll},k}\}$, $\{\Gamma_{\text{coll},k}\}$, $\{E_{\text{int-sh-coll},k}^{\text{iso}}\}$, $\{l_{\text{coll},k}\}$, $\{m_{\text{coll},k}\}$, $\{\delta t_{e,k}\}$)

Input parameters:

▷ N_{sh} : initial number of shells in the fireball
 ▷ r_{min} : distance of the last shell ($i = N_{\text{sh}}$) to the emitter
 ▷ r_{dec} : maximum distance up to which shells are propagated, *i.e.*, start of the external deceleration zone
 ▷ l : initial width with which a shell is emitted ($l = ct_v$)
 ▷ d : initial separation between consecutive shells (emitter frequency $f = c/d$)
 ▷ $E_{\text{int-sh}}^{\text{iso}}$: initial internal energy of an emitted shell
 ▷ Γ_0 : characteristic Lorentz boost factor
 ▷ A : fluctuation of the Lorentz factor
 ▷ z : redshift of the emitter
 ▷ $\{\hat{t}_{\text{coll},k}\}$, $\{t_{\text{obs},k}\}$, $\{r_{\text{coll},k}\}$, $\{\Gamma_{\text{coll},k}\}$, $\{E_{\text{int-sh-coll},k}^{\text{iso}}\}$, $\{l_{\text{coll},k}\}$, $\{m_{\text{coll},k}\}$, $\{\delta t_{e,k}\}$: arrays in which the parameters for each of the simulated collisions will be returned; respectively, collision time in the source frame, collision time in the observer's frame, collision radius, Lorentz factor of the merged shell created in the collision, internal energy of the merged shell, width of the merged shell, mass of the merged shell, emission timescale of the collision

```

1:  $\hat{t} \leftarrow 0$ 
2:  $N_{\text{coll}} \leftarrow 0$  // number of collisions since  $\hat{t} = 0$ 
3: // Emit  $N_{\text{sh}}$  identical shells to initialise the fireball – the arrays  $\{r_k\}$ ,  $\{l_k\}$ ,  $\{E_{\text{int-sh},k}^{\text{iso}}\}$ ,  $\{\Gamma_k\}$ ,  $\{m_k\}$ ,  $\{\beta_k\}$  will store the
   shell parameters (see the definition of InitialiseFireball for details)
4: InitialiseFireball( $N_{\text{sh}}$ ,  $r_{\text{min}}$ ,  $l$ ,  $d$ ,  $E_{\text{int-sh}}^{\text{iso}}$ ,  $\Gamma_0$ ,  $A$ ,  $\{r_k\}$ ,  $\{l_k\}$ ,  $\{E_{\text{int-sh},k}^{\text{iso}}\}$ ,  $\{\Gamma_k\}$ ,  $\{m_k\}$ ,  $\{\beta_k\}$ )
5: // Note that the shell index grows with proximity to the emitter; the shell closest to the emitter has  $i = N_{\text{sh}}$ 
6: while  $N_{\text{sh}} > 1$  and shells not ordered with increasing values of Lorentz factor do
7:   // The next collision will occur at  $\hat{t} + \Delta\hat{t}$  between shells  $i_{\text{coll}}$  and  $i_{\text{coll}} + 1$ 
8:    $\{i_{\text{coll}}, \Delta\hat{t}, r_{\text{coll}}\} \leftarrow \text{IndexTimeRadiusNextCollision}(N_{\text{sh}}, \{r_k\}, \{l_k\}, \{\beta_k\})$ 
9:   for  $i = 1$  to  $N_{\text{sh}}$  do
10:     $r_i^0 \leftarrow r_i$  // auxiliary variable
11:     $r_i \leftarrow +c\beta_i\Delta\hat{t}$  // before the collision, propagate each existing shell for  $\Delta\hat{t}$  to its new position
12:    // We do not consider shell width growth during propagation
13:    if  $r_i > r_{\text{dec}}$  and  $i \neq i_{\text{coll}}$  then
14:      // Remove the shell if it has reached the external shock zone (if it is not a colliding shell)
15:      EliminateShell( $i$ ,  $N_{\text{sh}}$ ,  $\{r_k\}$ ,  $\{l_k\}$ ,  $\{E_{\text{int-sh},k}^{\text{iso}}\}$ ,  $\{\Gamma_k\}$ ,  $\{m_k\}$ ,  $\{\beta_k\}$ )
16:       $N_{\text{sh}} \leftarrow N_{\text{sh}} - 1$ 
17:    end if
18:   end for
19:   // Only now perform the collision and merge the colliding shells
20:    $N_{\text{sh}} \leftarrow N_{\text{sh}} - 1$ 
21:    $N_{\text{coll}} \leftarrow N_{\text{coll}} + 1$ 
22:    $\hat{t} \leftarrow \hat{t} + \Delta\hat{t}$ 
23:    $\{r_{\text{coll}}, \Gamma_m, E_{\text{int-sh},m}^{\text{iso}}, l_m, m_m, \delta t_e\}$ 
    $\leftarrow \text{ParametersOfMergedShell}(i_{\text{coll}}, i_{\text{coll}} + 1, r_{\text{coll}}, \{r_k\}, \{l_k\}, \{E_{\text{int-sh},k}^{\text{iso}}\}, \{\Gamma_k\}, \{m_k\}, \{\beta_k\})$ 
24:    $t_{\text{obs}} \leftarrow (L(z) - r_{\text{coll}})/c + \hat{t}$  // time in observer's frame;  $L(z)$  is the lookback distance to the emitter
25:   SaveCollisionData( $N_{\text{coll}}$ ,  $\hat{t}$ ,  $t_{\text{obs}}$ ,  $r_{\text{coll}}$ ,  $\Gamma_m$ ,  $E_{\text{int-sh},m}^{\text{iso}}$ ,  $l_m$ ,  $m_m$ ,  $\delta t_e$ ,  $\{\hat{t}_{\text{coll},k}\}$ ,  $\{t_{\text{obs},k}\}$ ,  $\{r_{\text{coll},k}\}$ ,  $\{\Gamma_{\text{coll},k}\}$ ,
    $\{E_{\text{int-sh-coll},k}^{\text{iso}}\}$ ,  $\{l_{\text{coll},k}\}$ ,  $\{m_{\text{coll},k}\}$ ,  $\{\delta t_{e,k}\}$ )
26:   // Eliminate the inner shell that participated in the collision
27:   EliminateShell( $i_{\text{coll}} + 1$ ,  $N_{\text{sh}}$ ,  $\{r_k\}$ ,  $\{l_k\}$ ,  $\{E_{\text{int-sh},k}^{\text{iso}}\}$ ,  $\{\Gamma_k\}$ ,  $\{m_k\}$ ,  $\{\beta_k\}$ )
28:   // Insert the new merged shell
29:   InsertShell( $i_{\text{coll}}$ ,  $r_{\text{coll}}$ ,  $l_m$ ,  $E_{\text{int-sh},m}^{\text{iso}}$ ,  $\Gamma_m$ ,  $\{r_k\}$ ,  $\{l_k\}$ ,  $\{E_{\text{int-sh},k}^{\text{iso}}\}$ ,  $\{\Gamma_k\}$ ,  $\{m_k\}$ ,  $\{\beta_k\}$ )
30: end while
31: // Now find the burst with the lowest value of  $t_{\text{obs}}$  and set it to zero, since this will be the time at which the burst starts
   to be observed.
32:  $t_{\text{obs,min}} \leftarrow \min(\{t_{\text{obs},k}\})$ 
33: for  $i = 1$  to  $N_{\text{coll}}$  do
34:    $t_{\text{obs},i} \leftarrow t_{\text{obs},i} - t_{\text{obs,min}}$ 
35: end for
36: sort the arrays  $\{\hat{t}_{\text{coll},k}\}$ ,  $\{t_{\text{obs},k}\}$ ,  $\{r_{\text{coll},k}\}$ ,  $\{\Gamma_{\text{coll},k}\}$ ,  $\{E_{\text{int-sh-coll},k}^{\text{iso}}\}$ ,  $\{l_{\text{coll},k}\}$ ,  $\{m_{\text{coll},k}\}$ ,  $\{\delta t_{e,k}\}$  in increasing order
   of  $t_{\text{obs}}$ 

```

Algorithm 3

InitialiseFireball($N_{\text{sh}}, r_{\text{min}}, l, d, E_{\text{int-sh}}^{\text{iso}}, \Gamma_0, A, \{r_i\}, \{l_i\}, \{E_{\text{int-sh},i}^{\text{iso}}\}, \{\Gamma_i\}, \{m_i\}, \{\beta_i\}$)

Input parameters:

- ▷ N_{sh} : initial number of shells in the fireball
 - ▷ r_{min} : distance of the last shell ($i = N_{\text{sh}}$) to the emitter
 - ▷ l : initial width with which a shell is emitted ($l = ct_v$)
 - ▷ d : initial separation between consecutive shells (emitter frequency $f = c/d$)
 - ▷ $E_{\text{int-sh}}^{\text{iso}}$: initial internal energy of an emitted shell
 - ▷ Γ_0 : characteristic Lorentz boost factor
 - ▷ A : fluctuation of the Lorentz factor
 - ▷ $\{r_i\}, \{l_i\}, \{E_{\text{int-sh},i}^{\text{iso}}\}, \{\Gamma_i\}, \{m_i\}, \{\beta_i\}$: arrays of shell position, width, internal energy, Lorentz factor, mass, speed
- 1: **for** $i = N_{\text{sh}}$ to 1 **do**
 - 2: $\Gamma \leftarrow \text{LogNormalDistribution}(\Gamma_0, A)$
 - 3: **InsertShell**($i, r_{\text{min}} + (N_{\text{sh}} - i)(l + d), l, E_{\text{int-sh}}^{\text{iso}}, \Gamma, \{r_k\}, \{l_k\}, \{E_{\text{int-sh},k}^{\text{iso}}\}, \{\Gamma_k\}, \{m_k\}, \{\beta_k\}$)
 - 4: **end for**
-

Algorithm 4 IndexTimeRadiusNextCollision($N_{\text{sh}}, \{r_i\}, \{l_i\}, \{\beta_i\}$)**Input parameters:**

- ▷ N_{sh} : current total number of shells in the fireball
 - ▷ $\{r_i\}, \{l_i\}, \{\beta_i\}$: arrays of shell position, width, and speed
- 1: **for** $i = 1$ to $N_{\text{sh}} - 1$ **do**
 - 2: $d_{i,i+1} \leftarrow r_i - r_{i+1} - l_{i+1}$ // separation between all consecutive pairs of shells
 - 3: $\Delta \hat{t}_{i,i+1} \leftarrow \frac{d_{i,i+1}}{c(\beta_{i+1} - \beta_i)}$ // collision time between all pairs
 - 4: **end for**
 - 5: // The next collision will occur between the pairs for which the collision time is shortest
 - 6: $i_{\text{coll}} \leftarrow \text{argmin}(\{\Delta \hat{t}_{i,i+1}\})$
 - 7: $\Delta \hat{t} \leftarrow \Delta \hat{t}_{i_{\text{coll}}, i_{\text{coll}}+1}$
 - 8: $r_{\text{coll}} \leftarrow r_{i_{\text{coll}}+1} + c\beta_{i_{\text{coll}}+1}\Delta \hat{t}$
 - 9: **return** $\{i_{\text{coll}}, \Delta \hat{t}, r_{\text{coll}}\}$
-

Algorithm 5 EliminateShell($j, N_{\text{sh}}, \{r_i\}, \{l_i\}, \{E_{\text{int-sh},i}^{\text{iso}}\}, \{\Gamma_i\}, \{m_i\}, \{\beta_i\}$)**Input parameters:**

- ▷ j : index of the shell that will be eliminated
 - ▷ N_{sh} : current total number of shells in the fireball
 - ▷ $\{r_i\}, \{l_i\}, \{E_{\text{int-sh},i}^{\text{iso}}\}, \{\Gamma_i\}, \{m_i\}, \{\beta_i\}$: arrays of shell position, width, internal energy, Lorentz factor, mass, speed
- 1: **for** $i = j$ to N_{sh} **do**
 - 2: $r_i \leftarrow r_{i+1}$
 - 3: $l_i \leftarrow l_{i+1}$
 - 4: $E_{\text{int-sh},i}^{\text{iso}} \leftarrow E_{\text{int-sh},i+1}^{\text{iso}}$
 - 5: $\Gamma_i \leftarrow \Gamma_{i+1}$
 - 6: $m_i \leftarrow m_{i+1}$
 - 7: $\beta_i \leftarrow \beta_{i+1}$
 - 8: **end for**
-

Algorithm 6 LogNormalDistribution(Γ_0, A)**Input parameters:**

- ▷ Γ_0 : characteristic Lorentz boost factor
 - ▷ A : fluctuation of the Lorentz factor
- 1: $x \leftarrow$ sample from $P(x) dx = e^{-x^2/2}/\sqrt{2\pi} dx$ // sample x from a Gaussian
 - 2: $\Gamma \leftarrow 1 + (\Gamma_0 - 1)e^{Ax}$ // distribution $\ln\left(\frac{\Gamma-1}{\Gamma_0-1}\right) = Ax$
 - 3: **return** Γ
-

Algorithm 7 InsertShell($j, r, l, E_{\text{int-sh}}^{\text{iso}}, \Gamma, \{r_i\}, \{l_i\}, \{E_{\text{int-sh},i}^{\text{iso}}\}, \{\Gamma_i\}, \{m_i\}, \{\beta_i\}$)

Input parameters:

- ▷ j : index of the new shell to be inserted
- ▷ r : position at which the new shell will be inserted ($r = 0$ to emit a new shell, next to the emitter)
- ▷ l : initial width with which a shell is inserted ($l = ct_v$)
- ▷ $E_{\text{int-sh}}^{\text{iso}}$: initial internal energy of the inserted shell
- ▷ Γ : Lorentz boost factor of the shell
- ▷ $\{r_i\}, \{l_i\}, \{E_{\text{int-sh},i}^{\text{iso}}\}, \{\Gamma_i\}, \{m_i\}, \{\beta_i\}$: arrays of shell position, width, internal energy, Lorentz factor, mass, speed

- 1: $r_j \leftarrow r$
 - 2: $l_j \leftarrow l$
 - 3: $E_{\text{int-sh},j}^{\text{iso}} \leftarrow E_{\text{int-sh}}^{\text{iso}}$
 - 4: $\Gamma_j \leftarrow \Gamma$
 - 5: $m_j \leftarrow E_{\text{int-sh},j}^{\text{iso}} / (\Gamma_j c^2)$
 - 6: $\beta_j \leftarrow \sqrt{1 - \Gamma_j^{-2}}$
-

Algorithm 8

SaveCollisionData($N_{\text{coll}}, \hat{t}, t_{\text{obs}}, r, \Gamma, E_{\text{int-sh}}^{\text{iso}}, l, m, \delta t_e, \{\hat{t}_{\text{coll},k}\}, \{t_{\text{obs},k}\}, \{r_{\text{coll},k}\}, \{\Gamma_{\text{coll},k}\}, \{E_{\text{int-sh-coll},k}^{\text{iso}}\}, \{l_{\text{coll},k}\}, \{m_{\text{coll},k}\}, \{\delta t_{e,k}\}$)

Input parameters:

- ▷ N_{coll} : current number of collisions since the start of the simulation
- ▷ $\hat{t}, t_{\text{obs}}, r, \Gamma, E_{\text{int-sh}}^{\text{iso}}, l, m, \delta t_e$: collision time in the source frame, collision time in the observer's frame, collision radius, Lorentz factor of the merged shell created in the collision, internal energy of the merged shell, width of the merged shell, mass of the merged shell, emission timescale of the collision
- ▷ $\{\hat{t}_{\text{coll},k}\}, \{t_{\text{obs},k}\}, \{r_{\text{coll},k}\}, \{\Gamma_{\text{coll},k}\}, \{E_{\text{int-sh-coll},k}^{\text{iso}}\}, \{l_{\text{coll},k}\}, \{m_{\text{coll},k}\}, \{\delta t_{e,k}\}$: arrays in which the parameters for each of the simulated collisions will be returned; respectively, collision time in the source frame, collision time in the observer's frame, collision radius, Lorentz factor of the merged shell created in the collision, internal energy of the merged shell, width of the merged shell, mass of the merged shell, emission timescale of the collision

- 1: $\hat{t}_{N_{\text{coll}}} \leftarrow \hat{t}$
 - 2: $t_{\text{obs},N_{\text{coll}}} \leftarrow t_{\text{obs}}$
 - 3: $r_{\text{coll},N_{\text{coll}}} \leftarrow r$
 - 4: $\Gamma_{\text{coll},N_{\text{coll}}} \leftarrow \Gamma$
 - 5: $E_{\text{int-sh-coll},N_{\text{coll}}}^{\text{iso}} \leftarrow E_{\text{int-sh}}^{\text{iso}}$
 - 6: $l_{\text{coll},N_{\text{coll}}} \leftarrow l$
 - 7: $m_{\text{coll},N_{\text{coll}}} \leftarrow m$
 - 8: $\delta t_{e,N_{\text{coll}}} \leftarrow \delta t_e$
-

Algorithm 9

ParametersOfMergedShell($i, j, r_{\text{coll}}, N_{\text{sh}}, \{r_i\}, \{l_i\}, \{E_{\text{int-sh},i}^{\text{iso}}\}, \{\Gamma_i\}, \{m_i\}, \{\beta_i\}$)

Input parameters:

- ▷ i, j : indices of the shells that will be merged
 - ▷ r_{coll} : collision radius
 - ▷ N_{sh} : current total number of shells in the fireball
 - ▷ $\{r_i\}, \{l_i\}, \{E_{\text{int-sh},i}^{\text{iso}}\}, \{\Gamma_i\}, \{m_i\}, \{\beta_i\}$: arrays of shell position, width, internal energy, Lorentz factor, mass, speed
- 1: **if** $\Gamma_i \geq \Gamma_j$ **then**
 - 2: $r \leftarrow i$ // r : rapid shell
 - 3: $s \leftarrow j$ // s : slow shell
 - 4: **else**
 - 5: $r \leftarrow j$
 - 6: $s \leftarrow i$
 - 7: **end if**
 - 8: $\Gamma_m \leftarrow \sqrt{\frac{\Gamma_r m_r + \Gamma_s m_s}{m_r/\Gamma_r + m_s/\Gamma_s}}$ // Lorentz factor of the merged shell
 - 9: $E_{\text{int-sh},m}^{\text{iso}} \leftarrow (\Gamma_r - \Gamma_m) m_r c^2 + (\Gamma_s - \Gamma_m) m_s c^2$ // internal energy of the merged shell
 - 10: $\Gamma_{\text{fs}} \leftarrow \Gamma_m \sqrt{\frac{1+2\Gamma_m/\Gamma_s}{2+\Gamma_m/\Gamma_s}}$ // Lorentz factor of forward shock
 - 11: $\Gamma_{\text{rs}} \leftarrow \Gamma_m \sqrt{\frac{1+2\Gamma_m/\Gamma_r}{2+\Gamma_m/\Gamma_r}}$ // Lorentz factor of reverse shock
 - 12: $\beta_r \leftarrow \sqrt{1 - \Gamma_r^{-2}}$
 - 13: $\beta_s \leftarrow \sqrt{1 - \Gamma_s^{-2}}$
 - 14: $\beta_{\text{fs}} \leftarrow \sqrt{1 - \Gamma_{\text{fs}}^{-2}}$
 - 15: $\beta_{\text{rs}} \leftarrow \sqrt{1 - \Gamma_{\text{rs}}^{-2}}$
 - 16: $l_m \leftarrow l_s \frac{\beta_{\text{fs}} - \beta_m}{\beta_{\text{fs}} - \beta_s} + l_r \frac{\beta_m - \beta_{\text{rs}}}{\beta_r - \beta_{\text{rs}}}$ // width of merged shell
 - 17: $n_r \leftarrow m_r / (4\pi r_r^2 l_r)$ // average proton densities of rapid and slow shells
 - 18: $n_s \leftarrow m_s / (4\pi r_s^2 l_s)$
 - 19: $n_m \leftarrow (n_r l_r + n_s l_s) / l_m$ // average proton density of the merged shell
 - 20: $V_{\text{iso}} \leftarrow 4\pi r_{\text{coll}}^2 l_m$ // isotropic volume of the merged shell
 - 21: $m_m \leftarrow n_m V_{\text{iso}}$ // mass of merged shell
 - 22: $\delta t_e \leftarrow \frac{l_r}{c(\beta_r - \beta_{\text{rs}})}$ // emission timescale, i.e., time at which the reverse shock crosses the rapid shell
 - 23: **return** $\{r_{\text{coll}}, \Gamma_m, E_{\text{int-sh},m}^{\text{iso}}, l_m, m_m, \delta t_e\}$
-

Appendix E

Calculation of the pair creation cut-off for photons

In our calculations, we also include a simple treatment of the pair creation cut-off in the photon spectrum. As soon as the photon energies extend beyond the threshold of $\varepsilon'_\gamma \geq 511$ keV, it is possible that two photons of sufficient energy interact and produce an electron-positron pair. Depending on the photon density, it is possible that these photon-photon interactions introduce an additional cut-off in the spectrum of the escaping photons. This effect unfortunately introduces a further subtlety in our treatment as the input spectrum in the calculations no longer is the same as the escaping photon spectrum. In the next few paragraphs, we want to detail how we determine the value of the cut-off and if it affects the photon spectrum.

The first step of this calculation consists of defining our **input photon spectrum**. For sake of simplicity, we assume that all the photon spectra from the different collisions are identical in all parameters apart from the normalization. The minimal photon energy is set to 0.2 eV, the maximal photon energy is set to 1 PeV (for numerical reasons; is assumed to be infinity), and the break energy of the spectrum is set to 1 keV; all of these energies are in the SRF. We assume that the photon spectra follow a broken power-law in energy (simplified version of the Band function). The spectral indices are assumed to be $\alpha_\gamma = 1$ and $\beta_\gamma = 2$. As stated before, the only difference in the spectra is the normalization. The normalization is calculated from the properties of an individual collision, *i.e.* we assume that the fraction of liberated energy in form of photons (with the value of said energy given in the source frame) is distributed in the energy range of the *Fermi* GBM instrument (from 0.2 keV to 30 MeV in the observer's frame). We, however, need the normalization of the photon spectrum in the rest frame of the shock (SRF), hence need to correctly boost all energies using the merged shell's Lorentz factor Γ_m . We do not discuss if such a spectrum can be obtained from the usual processes associated with non-thermal photon spectra. Conversely, we invoke the heuristic argument that these kind of spectra are similar to the ones observed in GRB observations. However, we additionally want to check what the maximal energy for the escaping photons is when we account for pair creation on the input photon spectrum. We estimate the optical thickness for $\gamma\gamma$ -interactions $\tau_{\gamma\gamma}$ to the shell thickness l'_m to the interaction length for $\gamma\gamma$ -interactions $l'_{\gamma\gamma,m}$:

$$\tau_{\gamma\gamma,m} = \frac{l'_m}{l'_{\gamma\gamma,m}} \quad . \quad (\text{E.1})$$

While l'_m is known for all our collisions, we still need to calculate the interaction length $l'_{\gamma\gamma,m}$ for the given photon spectrum. Based on the relativistic kinematics for each collision, see Ref. [246],

we can calculate said (inverse) collision length as

$$l'_{\gamma\gamma,m}{}^{-1}(\varepsilon'_t) = \int_0^\infty d\varepsilon'_\gamma n'_{\gamma,m}(\varepsilon'_\gamma) \int_{-1}^{+1} \frac{d\cos\theta}{2} (1 - \cos\theta) \sigma_{\gamma\gamma}(\varepsilon'_\gamma, \cos\theta) \quad , \quad (\text{E.2})$$

where $n'_{\gamma,m}$ is the photon spectrum released in a collision in $[\text{GeV}^{-1} \text{cm}^{-3}]$ (in SRF) and $\sigma_{\gamma\gamma}(\varepsilon'_\gamma, \cos\theta)$ is the interaction cross section for photon-photon scattering (in $[\text{cm}^2]$). For our calculation, we will use an approximated version of the interaction cross section based on the approach by Gould and Schröder [246],

$$\sigma_{\gamma\gamma}(s) \simeq 3/8 \sigma_T \cdot 4 (m_e c^2)^2 / s \left[\log \left(s / (m_e c^2)^2 - 1 \right) - 1 \right] \quad , \quad (\text{E.3})$$

with the Thomson cross section $\sigma_T = 0.665 \cdot 10^{-24} \text{cm}^2$. Note that this approximation is valid for energies high above the threshold $s \geq 4 (m_e c^2)^2$ and is basically equivalent¹ to the approximation given by Baring [247] when using $x = \sqrt{s / (m_e c^2)^2}$; for the full energy-dependent interaction cross section, see Ref. [248]. With this simplification of the interact cross section and with the assumption that the photon field is isotropic in the SRF, we can reduce Eq. (E.2) to a single integration. By substituting the integration over $\cos\theta$ into an integration over the center-of-mass energy $s = 2\varepsilon'_\gamma \varepsilon'_t (1 - \cos\theta)$ and using the threshold $s \geq 4 (m_e c^2)^2$, the calculation reduces to

$$l'_{\gamma\gamma,m}{}^{-1}(\varepsilon'_t) = \int_{\frac{(m_e c^2)^2}{\varepsilon'_t}}^\infty d\varepsilon'_\gamma \frac{3}{16} \sigma_T \cdot \frac{n'_{\gamma,m}(\varepsilon'_\gamma) (m_e c^2)^2}{\varepsilon_t'^2 \varepsilon_\gamma'^2} \cdot (m_e c^2)^2 \cdot \left[8 \left(1 - \frac{\varepsilon'_t \varepsilon'_\gamma}{(m_e c^2)^2} \right) + \left(\frac{4\varepsilon'_t \varepsilon'_\gamma}{(m_e c^2)^2} - 1 \right) \log \left(\frac{4\varepsilon'_\gamma \varepsilon'_t}{(m_e c^2)^2} - 1 \right) - 3 \log(3) \right] \quad (\text{E.4})$$

This equation can easily be implemented into a numerical code to calculate the photon-photon interaction length for a given target photon energy ε'_t . By scanning these target photon energies, we can obtain the energy at which the optical thickness $\tau_{\gamma\gamma,m} \equiv 1$. This is then considered to be our cut-off energy due to pair creation in the **escaping photon spectrum**. In the plots throughout this note, we use the energy values obtained by this method as $E_{\gamma,\text{max}}$, the maximal energy for escaping photons. Note that this is a different value from the maximal photon energy of our input photon spectrum.

The problem with this calculation is that some of the collisions are still optically thick and the aforementioned calculation gives unreasonably low values. In fact, all our calculations only apply if we are in a regime beyond the photosphere. Subphotospheric processes cannot be described by our approach and we need to ensure that we are beyond the photosphere. To obtain the correct value for the photosphere of the m th collision, we need to check if it is possible for electrons (or protons) to escape our m th shell without scattering off photons. Since the photon number density is significantly higher than the number density of leptons or baryons, interactions among the photons can lead to the production of several e^\pm -pairs, see discussion in Ref. [249]. Following said reference, we can infer that we have additional pairs, if the radiation compactness parameter $\ell' \geq 1$. The definition of the radiation compactness parameter is similar an optical thickness and can be adapted from Ref. [249] for our calculations as

$$\ell'_m \simeq l'_m \cdot n'_{\gamma,m} \sigma_T \quad . \quad (\text{E.5})$$

¹The only difference is the -1 inside the logarithm, which improves the result at low energies significantly.

Even though the calculation is a bit simplistic compared to the detailed calculation in Eq. (E.2), it is useful to estimate the total pair creation since $\gamma\gamma$ -interactions as well as $p\gamma$ -interactions can lead to pair creation. When a shell actually has such a radiation compactness $\ell'_m \geq 1$, it can be considered to be radiation-dominated and the number density of leptons n'_\pm is enhanced compared to the number density of protons n'_p . The maximal enhanced for this case is considered to be $n'_\pm \approx m_p / (2m_e) \cdot n'_p$. The other extreme case is the so called baryon-dominated plasma, with $\ell' < 1$ and $n'_\pm \simeq n'_p$. The latter relation is a consequence of charge conservation, as at least the same number of electrons is needed to counter the proton charges in a neutral plasma. Hence, with the e^\pm density known, we can now calculate the photospheric interaction length l'_{ph} with the simple formula

$$l'_{\text{ph}} \simeq \frac{1}{n'_\pm \sigma_T} \quad . \quad (\text{E.6})$$

While the calculation in the baryon-dominated is straight forward, there is still some room for interpretation in the radiation-dominated case

Appendix F

Photodisintegration of nuclei

There is indirect evidence, coming especially from the Pierre Auger Observatory, that the composition of UHECRs becomes heavier towards the highest energies. It is not yet clear whether or not it is possible for astrophysical accelerators to boost nuclei up to $\sim 10^{12}$ GeV, as nuclei will inevitably interact with the photon field at the source and break up via photodisintegration, *i.e.*, via the emission of one or more neutron or proton as a result of the interaction with the source photons. Here we will calculate the maximum proton energy that the nuclei can reach when subject to photodisintegration, for our simulated bursts. For this, we will assume that the UHECRs are entirely composed of the heaviest nuclei: iron, with $Z = 26$ and $A = 56$.

To calculate the photodisintegration interaction length for each simulated collision we will adapt the formalism of appendix B in Ref. [96]. The interaction rate [s^{-1}] in the SRF is then calculated as

$$\Gamma_{A\gamma}(E') = \int_{\frac{\varepsilon'_{\text{th}} m_p}{2E'}}^{\infty} d\varepsilon' n'_\gamma(\varepsilon') f\left(\frac{E'\varepsilon'}{m_p}\right), \quad (\text{F.1})$$

where E' and ε' are, respectively, the energy of the nucleus and of the photon in the SRF, and the response function is defined as

$$f(y) = \frac{1}{2y^2} \int_{\varepsilon'_{\text{th}}}^{2y} d\varepsilon' \varepsilon' \sigma_{A\gamma}(\varepsilon') \quad (\text{F.2})$$

with $y \equiv E'\varepsilon'/m_p$ and $\sigma_{A\gamma}$ the photodisintegration cross section.

For the photodisintegration cross section, we choose not to follow the detailed, channel-by-channel calculation in the literature developed by Puget, Stecker, and Bredekamp [250] and updated by Stecker and Salamon [251]. Instead, we adopt the simpler expression for the total cross section, in units of cm^2 , from Ref. [252] (the behaviour above ε'_1 is adopted from Ref. [253]):

$$\sigma_{A\gamma}(\varepsilon') = \begin{cases} \sigma_{\text{GDR}}(\varepsilon') & , \varepsilon'_{\text{th}} \leq \varepsilon' \leq \varepsilon'_1 \\ \max\{\sigma_{\text{GDR}}(\varepsilon'), 10^{-27} A/8\} & , \varepsilon'_1 \leq \varepsilon' \leq \varepsilon'_{\text{max}} \end{cases}, \quad (\text{F.3})$$

where $\text{GDR}(\varepsilon')$ is the approximation of the giant dipole resonance:

$$\sigma_{\text{GDR}}(\varepsilon') = \sigma_0(A) \frac{(\varepsilon'\Delta)^2}{[\varepsilon'^2 - \varepsilon_0^2(A)]^2 + (\varepsilon'\Delta)^2} \quad (\text{F.4})$$

$$\varepsilon_0(A) = 10^{-3} \text{ GeV} \cdot \begin{cases} 0.925 \cdot A^{2.433} & , A \leq 4 \\ 42.65 \cdot A^{-0.21} & , A > 4 \end{cases} \quad (\text{F.5})$$

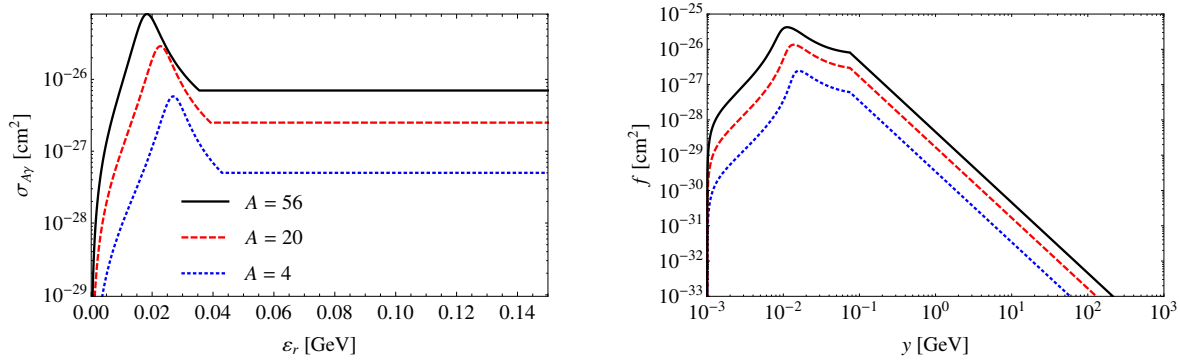


Figure F.1: *Left:* Photodisintegration cross section for helium nuclei ($A = 4$), neon nuclei ($A = 20$), and iron nuclei ($A = 56$). *Right:* Response function f for the same three nuclei, calculated using Eq. (F.2).

$$\sigma_0(A) = 1.45 \cdot A \cdot 10^{-27} \text{ cm}^2. \quad (\text{F.6})$$

Below the threshold energy ε'_{th} , the cross section is taken to be zero. Even though the value of ε'_{th} depends on the nuclide and on the particular emission process, as shown in Ref. [251], for simplicity we have set it to a fixed value $\varepsilon'_{\text{th}} = 2$ MeV, following Ref. [250]. Note that single-nucleus emission dominates below $\varepsilon'_1 = 30$ MeV, while double-nucleus emission dominates above ε'_1 . Finally, we have set the energy above which the cross section drops to zero to $\varepsilon'_{\text{max}} = 150$ MeV [252, 250]. Fig. F.1 shows the variation with energy of the photodisintegration cross section and the response function for helium nuclei ($A = 4$), neon nuclei ($A = 20$), and iron nuclei ($A = 56$).

As usual, for the photon spectrum we assume a broken power law:

$$n'_\gamma(\varepsilon') = C'_\gamma \cdot \begin{cases} \left(\varepsilon'/\varepsilon'_{\gamma,\text{break}}\right)^{-\alpha_\gamma} & , \varepsilon'_{\gamma,\text{min}} \leq \varepsilon' \leq \varepsilon'_{\gamma,\text{break}} \\ \left(\varepsilon'/\varepsilon'_{\gamma,\text{break}}\right)^{-\beta_\gamma} & , \varepsilon' > \varepsilon'_{\gamma,\text{break}} \\ 0 & , \text{otherwise} \end{cases}, \quad (\text{F.7})$$

where we have fixed $\alpha_\gamma = 1$, $\beta = 2$, $\varepsilon'_{\gamma,\text{min}} = 0.2$ eV, $\varepsilon'_{\gamma,\text{break}} = 1$ keV, $\varepsilon'_{\gamma,\text{max}} = 1$ PeV, and C'_γ is the normalisation constant, which varies for each collision of the simulated burst. For each collision, we normalise the photon spectrum in the usual way (*e.g.*, Eqs. (13) and (15) in Ref. [106]), *i.e.*,

$$\int_{1 \text{ keV}}^{10 \text{ MeV}} d\varepsilon' \varepsilon' n'_\gamma(\varepsilon') = \frac{E_{\gamma\text{-sh},m}^{\text{iso}}}{V'_{\text{iso},m}}. \quad (\text{F.8})$$

From our simulations, we have for each collision the following quantities, given in the source frame: the energy output as photons, $E_{\gamma\text{-sh},m}^{\text{iso}}$; the collision radius, R_c ; and the width of the merged shell, l_m . In the SRF, these quantities become $E_{\gamma\text{-sh},m}^{\text{iso}} = E_{\gamma\text{-sh},m}^{\text{iso}}/\Gamma$ and $V'_{\text{iso},m} = 4\pi R_c^2 l'_m = 4\pi R_c^2 (\Gamma l_m)$. From Eq. (F.8), we see that the normalisation constant N_γ therefore has a Γ^{-2} dependence.

The photodisintegration interaction length for each collision is given simply by

$$l'_{A\gamma,m} = c/\Gamma_{A\gamma}. \quad (\text{F.9})$$

As for pair creation (see appendix E), we estimate the optical depth simply as

$$\tau_{A\gamma,m} = \frac{l'_m}{l'_{A\gamma,m}}. \quad (\text{F.10})$$

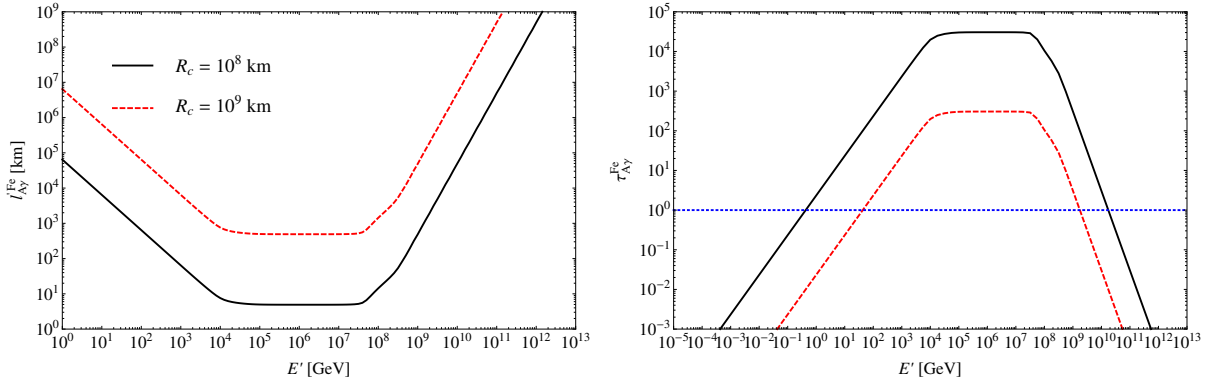


Figure F.2: *Left:* Photodisintegration interaction length for iron nuclei in a sample collision with fixed parameters $E_{\gamma\text{-sh},m}^{\text{iso}} = 10^{51}$ erg, $l_m = 1500$ km, $\Gamma_m = 100$, and two values of R_c : 10^8 km (black, solid line) and 10^9 km (red, dashed line). *Right:* Optical depth for the same two collisions. The blue, dotted line shows where $\tau_{A\gamma}^{\text{Fe}} = 1$.

Nuclei will be able to escape the source (provided no other energy-loss processes are present) as long as $\tau_{A\gamma,m} \leq 1$. Therefore, we estimate the maximum energy of the nucleus, E'_{max} , as that for which $\tau_{A\gamma}(E'_{\text{max}}) = 1$.

Fig. F.2 shows the interaction length (left panel) and optical depth (right panel) as functions of energy (in the SRF) for iron nuclei in a sample collision with fixed parameters $E_{\gamma\text{-sh},m}^{\text{iso}} = 10^{51}$ erg, $l_m = 1500$ km, $\Gamma_m = 100$, and two values of R_c : 10^8 km (black, solid line) and 10^9 km (red, dashed line) nuclei. Notice that the interaction length scales as $l'_{A\gamma,m} \sim 1/\Gamma_{A\gamma} \sim 1/C'_\gamma \sim V'_{\text{iso},m}/E'_{\gamma\text{-sh},m}$. Since $V'_{\text{iso},m} \sim R_c^2 l'_m$, the optical depth decreases with collision radius as $\tau_{A\gamma} \sim E'_{\gamma\text{-sh},m}/R_c^2$, which is consistent with Fig. F.2: the maximum energy increases with collision radius, since the photon density is lower at larger radius. On the other hand, Fig. F.2 shows that the optical depth first rises with nucleus energy, up to a kink due the break in the photon spectrum; a plateau follows, which continues up to a second break due to having reached the minimum photon energy available, after which the optical depth falls with nucleus energy. In the collisions where photodisintegration is relevant, the maximum nucleus energy $E_{\text{max}}^{\text{Fe}}$ will be determined by the first region of the optical depth curve, where it is rising with nucleus energy.

In Fig. F.3 we show the maximum nucleus energy in the presence of photodisintegration for fully-ionised iron nuclei ($A = 56$, $Z = 26$), in the source frame, for the eight simulated bursts whose parameters can be found in table F.1. For those collisions in which $E_{\text{max}}^{\text{Fe}}$ is photodisintegration-limited (black dots), we see that indeed the maximum energy increases with collision radius, as expected (see above for explanation). We have defined the fraction of collisions which are photodisintegration-limited as $f_{A\gamma\text{-lim}}$ and we show its value for each of the bursts.

Notice that it is predominantly the low-radii collisions that are photodisintegration-limited, since the photon density is higher for these collisions: nuclei from collisions occurring at higher radii are more liable to escape. The fraction $f_{A\gamma\text{-lim}}$ rises with the value of the dispersion in the distribution of the initial Lorentz factor of the shells: it is smallest for case C, which has the lowest dispersion value ($A_\Gamma = 0.2$) and highest for case I, which has the largest dispersion ($A_\Gamma = 2$). This is to be expected, since a higher value of A_Γ implies that shell speeds will be different enough for many of them to catch up to each other and collide early on in the expansion of fireball, that is, at low radii: clearly most of the collisions in case I occur at lower radii than in case C. Cases G, G', and

Parameter	C	D	D'	G	G'	G''	H	I
Fireball parameters								
N_{sh}	1000	1000	1000	1000	1000	1000	1000	1000
δt [s]	0.01	0.01	0.01	0.01	0.01	0.01	0.01	0.01
A_Γ	0.2	0.6	0.6	1.0	1.0	1.0	1.5	2.0
$\log(E_{\text{kin},0}^{\text{iso}}/\text{erg})$	52.84	51.94	51.92	51.60	51.59	51.67	51.43	51.35
Γ_0	300	300	300	300	500	1000	300	300
d/l	1	0.7	1	1	1	1	1	1
Simulation results								
N_{coll}	911	990	986	996	990	919	995	996
T_{90} [s]	60.18	51.18	58.91	55.55	58.85	52.55	55.80	54.74
t_v [10^{-2} s]	6.60	5.17	5.97	5.58	5.94	5.72	5.61	5.50
$\log(E_{\gamma\text{-tot}}^{\text{iso}}/\text{erg})$	53	53	53	53	53	53	53	53
$\log(E_{\text{tot}}^{\text{iso}}/\text{erg})$	54.08	54.08	54.08	54.08	54.08	54.08	54.08	54.08
Expected results according to standard relations								
$\log(R_C^{\text{std}}/\text{km})$	9.02	8.85	8.93	8.77	9.21	9.86	8.72	8.87
$\log(E_{\gamma\text{-sh}}^{\text{iso, std}}/\text{erg})$	50.04	50.00	50.01	50.00	50.00	50.04	50.00	50.00
Γ_m^{std}	294.5	264.7	266.3	222.1	368.6	778.6	209.3	248.3
t_v^{std} [10^{-2} s]	6.00	5.10	6.00	6.00	6.00	6.00	6.00	6.00
T^{std} [s]	54.66	50.49	59.16	59.76	59.40	55.14	59.70	59.76

Table F.1: Parameters and simulation results for eight prototypical simulated bursts. In all cases, we have fixed $l = c\delta t$, $r_{N_{\text{sh}}} = 10^3$ km, $z = 2$, $r_{\text{dec}} = 5.5 \cdot 10^{11}$ km, $\epsilon_e = \epsilon_B = 1/12$, and $\epsilon_p = 5/6$. The total initial kinetic energy of each burst is $E_{\text{kin},0}^{\text{iso}} \cdot N_{\text{sh}}$.

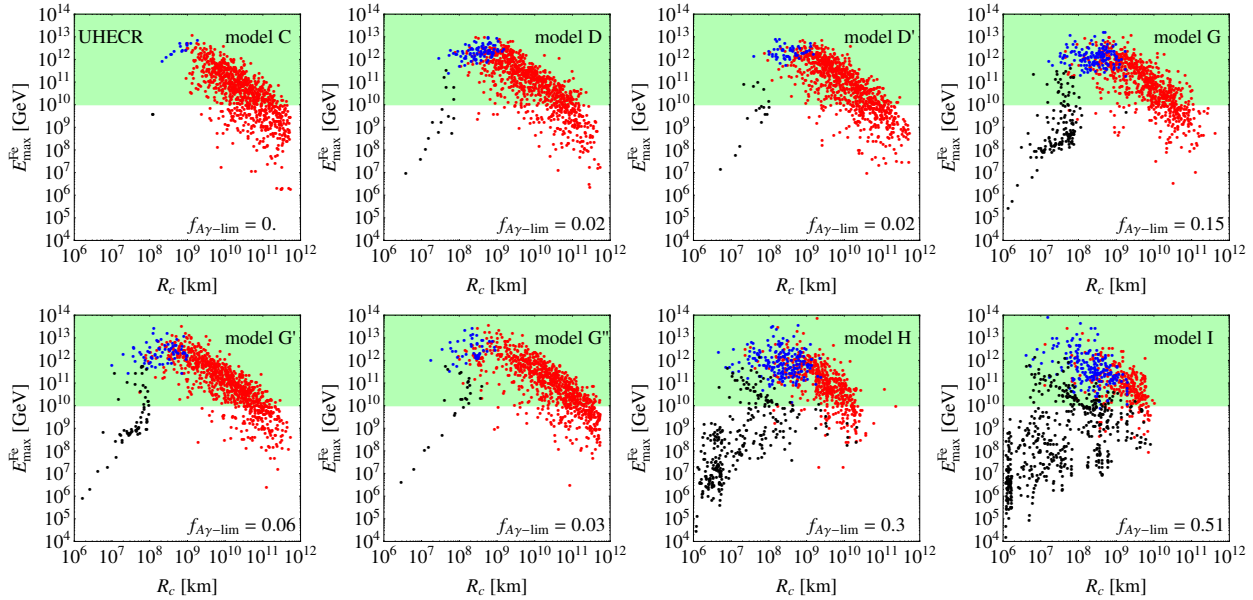


Figure F.3: Maximum energy, in the source frame, of Fe nuclei ($A = 56$, $Z = 26$), for different simulated bursts. Collisions in which the maximum energy is photodisintegration-limited are depicted as black dots; those limited by synchrotron losses are depicted in blue; and those limited by adiabatic losses, in red. The fraction of collisions in which the maximum energy is limited by photodisintegration is denoted as $f_{A\gamma\text{-lim}}$.

G'' all have a value of $A_\Gamma = 1$ (considered to be necessary for the burst to be efficient), but differ

on the mean value of the initial Lorentz factor distribution: $\Gamma_0 = 300, 500,$ and $1000,$ respectively. Fig. F.3 shows that $f_{A\gamma\text{-lim}}$ is highest for G, lower for G', and lowest for G''. The reason for this is that, for G'', due to the high $\Gamma_0 = 1000,$ shells are able to travel much farther before colliding, so that when they finally do collide, the photon density is low enough for the maximum nucleus energy not to be photodisintegration-limited. For bursts G and G', shells are slower and so more of them collide at lower radii, where the photon density is higher.

All in all, it is clear that in a simulated burst with realistic parameters ($A_\Gamma = 1, \Gamma_0 \gtrsim 300$), a sizeable fraction of nuclei will not be limited by photodisintegration and, if no other energy-process intervenes, will be able to escape.

Bibliography

- [1] D. J. Bird *et al.*, *Astrophys. J.* **441**, 144 (1995), astro-ph/9410067.
- [2] D. Guetta, D. Hooper, J. Alvarez-Muniz, F. Halzen, and E. Reuveni, *Astropart. Phys.* **20**, 429 (2004), arXiv:astro-ph/0302524.
- [3] IceCube Collaboration, R. Abbasi *et al.*, *Phys. Rev. Lett.* **106**, 141101 (2011), arXiv:1101.1448.
- [4] S. Hümmer, P. Baerwald, and W. Winter, *Phys. Rev. Lett.* **108**, 231101 (2012), arXiv:1112.1076.
- [5] H.-N. He *et al.*, *Astrophys. J.* **752**, 29 (2012), arXiv:1204.0857.
- [6] IceCube, M. Aartsen *et al.*, *Science* **342**, 1242856 (2013), arXiv:1311.5238.
- [7] IceCube Collaboration, M. Aartsen *et al.*, *Phys. Rev. Lett.* **111**, 021103 (2013), arXiv:1304.5356.
- [8] IceCube Collaboration, M. Aartsen *et al.*, (2014), arXiv:1405.5303.
- [9] R. W. Klebesadel, I. B. Strong, and R. A. Olson, *Astrophys. J. Lett.* **182**, L85 (1973).
- [10] NASA Imagine the Universe, <http://imagine.gsfc.nasa.gov/>.
- [11] BATSE webpage at NASA, <http://www.batse.msfc.nasa.gov/batse/grb/skymap/>.
- [12] G. Schilling, *Flash!: The Hunt for the Biggest Explosions in the Universe* (Cambridge University Press, 2002).
- [13] M. S. Briggs *et al.*, (1995), arXiv:astro-ph/9509078.
- [14] BATSE webpage at NASA, <http://www.batse.msfc.nasa.gov/batse/grb/duration/>.
- [15] C. Kouveliotou *et al.*, *Astrophys. J. Lett.* **413**, L101 (1993).
- [16] E. Berger, (2013), arXiv:1311.2603.
- [17] J. Hjorth and J. S. Bloom, *The Gamma-Ray Burst - Supernova Connection* (Cambridge University Press, 2012), pp. 169–190.
- [18] A. Levan *et al.*, *Astrophys. J.* **781**, 13 (2013), arXiv:1302.2352.
- [19] M. Boer, B. Gendre, and G. Stratta, (2013), arXiv:1310.4944.

- [20] L. Piro, BeppoSAX overview, in *Proceedings of the Fourth Compton Symposium*, edited by C. D. Dermer, M. S. Strickman, and J. D. Kurfess, , American Institute of Physics Conference Series Vol. 410, pp. 1485–1492, 1997.
- [21] R. L. Aptekar *et al.*, *Space Science Reviews* **71**, 265 (1995).
- [22] B. J. Teegarden and S. J. Sturmer, INTEGRAL Observations of Gamma-Ray Bursts, in *AAS/High Energy Astrophysics Division #4*, , Bulletin of the American Astronomical Society Vol. 31, p. 717, 1999.
- [23] SWIFT Collaboration, G. Chincarini, (2005), arXiv:astro-ph/0511108.
- [24] Fermi LAT Collaboration, F. de Palma, *Nuovo Cim.* **C035**, 11 (2012).
- [25] Fermi-GBM Collaborations, S. Zhu *et al.*, (2013), arXiv:1311.5623.
- [26] A. Maselli *et al.*, *GRB Coordinates Network* **14448**, 1 (2013).
- [27] Y.-Z. Fan *et al.*, *Astrophys. J.* **776**, 95 (2013), arXiv:1305.1261.
- [28] Coordinated Space Observation and Experiment Research Group, Wako, Saitama, Japan, A. Maselli *et al.*, *Science* **343**, 48 (2014), arXiv:1311.5254.
- [29] J. Paul, J. Wei, S. Basa, and S.-N. Zhang, *Comptes Rendus Physique* **12**, 298 (2011), arXiv:1104.0606.
- [30] T. Wulf, *Physikalische Zeitschrift* **5**, 152 (1910).
- [31] D. Pacini, (2010), arXiv:1002.1810.
- [32] V. F. Hess, *Z. Phys.* **13**, 1084 (1912).
- [33] J. Clay, *Proc. Amsterdam* **30**, 1115 (1927).
- [34] J. Clay, *Proc. Amsterdam* **31**, 1091 (1928).
- [35] B. Rossi, *Phys. Rev.* **36**, 606 (1930).
- [36] H. J. Bhabha and W. Heitler, *Proceedings of the Royal Society of London Series A: Mathematical, Physical & Engineering Sciences* **159**, 432 (1937).
- [37] M. Rao and B. V. Sreekantan, *Extensive air showers* (World Scientific, 1998).
- [38] P. Auger, P. Ehrenfest, R. Maze, J. Daudin, and A. F. Robley, *Rev. Mod. Phys.* **11**, 288 (1939).
- [39] J. Linsley, *Phys. Rev. Lett.* **10**, 146 (1963).
- [40] M. Lawrence, R. Reid, and A. Watson, *J. Phys.* **G17**, 733 (1991).
- [41] A. Ivanov, S. Knurenko, and I. Y. Sleptsov, *Nucl. Phys. Proc. Suppl.* **122**, 226 (2003), arXiv:astro-ph/0305053.
- [42] M. Winn, J. Ulrichs, L. Peak, C. McCusker, and L. Horton, *J. Phys.* **G12**, 653 (1986).
- [43] N. Chiba *et al.*, *Nucl. Instr. Meth. Phys. Res. Sec. A* **311**, 338 (1992).

- [44] HiRes Collaboration, R. Abbasi *et al.*, Phys. Rev. Lett. **100**, 101101 (2008), arXiv:astro-ph/0703099.
- [45] K. Greisen, Phys. Rev. Lett. **16**, 748 (1966).
- [46] G. Zatsepin and V. Kuzmin, JETP Lett. **4**, 78 (1966).
- [47] Telescope Array Collaboration, T. Abu-Zayyad *et al.*, Astropart. Phys. **48**, 16 (2013), arXiv:1305.6079.
- [48] P. Sokolsky and HiRes Collaboration, Nucl. Phys. B Proc. Suppl. **212**, 74 (2011), arXiv:1010.2690.
- [49] D. Gorbunov, P. Tinyakov, I. Tkachev, and S. V. Troitsky, JETP Lett. **87**, 461 (2008), arXiv:0711.4060.
- [50] Pierre Auger Observatory Collaboration, J. Abraham *et al.*, Phys. Rev. Lett. **104**, 091101 (2010), arXiv:1002.0699.
- [51] Pierre Auger Collaboration, P. Abreu *et al.*, J. Phys. Conf. Ser. **375**, 052006 (2012), arXiv:1107.4807.
- [52] R. Abbasi *et al.*, (2014), arXiv:1408.1726.
- [53] K.-H. Kampert and M. Unger, Astropart. Phys. **35**, 660 (2012), arXiv:1201.0018.
- [54] T. K. Gaisser, T. Stanev, and S. Tilav, Front. Phys. China **8**, 748 (2013), arXiv:1303.3565.
- [55] M. Lemoine, Phys. Rev. **D71**, 083007 (2005), arXiv:astro-ph/0411173.
- [56] F. Halzen, (2013), arXiv:1311.6350.
- [57] C. Cowan, F. Reines, F. Harrison, H. Kruse, and A. McGuire, Science **124**, 103 (1956).
- [58] C. Giunti, (2013), arXiv:1311.1335.
- [59] D. Lhuillier, PoS **EPS-HEP2013**, 522 (2013).
- [60] G. Danby *et al.*, Phys. Rev. Lett. **9**, 36 (1962).
- [61] DONUT Collaboration, K. Kodama *et al.*, Phys. Lett. **B504**, 218 (2001), arXiv:hep-ex/0012035.
- [62] T. Gaisser and M. Honda, Ann. Rev. Nucl. Part. Sci. **52**, 153 (2002), arXiv:hep-ph/0203272.
- [63] W. C. Haxton, R. G. Hamish Robertson, and A. M. Serenelli, Ann. Rev. Astron. Astrophys. **51**, 21 (2013), arXiv:1208.5723.
- [64] K. Scholberg, Ann. Rev. Nucl. Part. Sci. **62**, 81 (2012), arXiv:1205.6003.
- [65] O. Sramek, W. F. McDonough, and J. G. Learned, Adv. High Energy Phys. **2012**, 235686 (2012).
- [66] K. Nishikawa, Nucl. Instrum. Meth. **A623**, 17 (2010).
- [67] C. Mariani, Mod. Phys. Lett. **A27**, 1230010 (2012), arXiv:1201.6665.

- [68] IceCube Collaboration, M. Aartsen *et al.*, JINST **9**, P03009 (2014), arXiv:1311.4767.
- [69] IceCube Collaboration, D. Cowen, J. Phys. Conf. Ser. **60**, 227 (2007).
- [70] J. N. Bahcall and E. Waxman, Phys. Rev. **D64**, 023002 (2001), hep-ph/9902383.
- [71] T. Piran, Rev. Mod. Phys. **76**, 1143 (2004), arXiv:astro-ph/0405503.
- [72] P. Meszaros, Rept. Prog. Phys. **69**, 2259 (2006), arXiv:astro-ph/0605208.
- [73] M. Rees and P. Meszaros, Mon. Not. Roy. Astron. Soc. **258**, 41 (1992).
- [74] B. Paczynski and G. Xu, Astrophys. J. **427**, 708 (1994).
- [75] M. Rees and P. Meszaros, Astrophys. J. **430**, L93 (1994), arXiv:astro-ph/9404038.
- [76] M. Lyutikov and R. D. Blandford, (2003), arXiv:astro-ph/0312347.
- [77] B. Zhang and H. Yan, Astrophys. J. **726**, 90 (2011), arXiv:1011.1197.
- [78] B. Zhang and P. Kumar, (2012), arXiv:1210.0647.
- [79] M. Rees and P. Meszaros, Astrophys. J. **628**, 847 (2005), arXiv:astro-ph/0412702.
- [80] D. Giannios, A&A **480**, 305 (2008), arXiv:0711.2632.
- [81] K. Murase, Phys. Rev. **D78**, 101302 (2008), arXiv:0807.0919.
- [82] X.-Y. Wang and Z.-G. Dai, Astrophys. J. **691**, L67 (2009), arXiv:0807.0290.
- [83] A. M. Beloborodov, MNRAS **407**, 1033 (2010), arXiv:0907.0732.
- [84] S. Gao, K. Asano, and P. Meszaros, JCAP **1211**, 058 (2012), arXiv:1210.1186.
- [85] D. Lazzati, B. Morsony, R. Margutti, and M. Begelman, (2013), arXiv:1301.3920.
- [86] K. Mannheim, R. J. Protheroe, and J. P. Rachen, Phys. Rev. **D63**, 023003 (2001), arXiv:astro-ph/9812398.
- [87] M. Ahlers, L. Anchordoqui, M. Gonzalez-Garcia, F. Halzen, and S. Sarkar, Astropart. Phys. **34**, 106 (2010), arXiv:1005.2620.
- [88] Z. Li, (2012), arXiv:1210.6594.
- [89] E. Waxman and J. N. Bahcall, Phys. Rev. Lett. **78**, 2292 (1997), arXiv:astro-ph/9701231.
- [90] J. K. Becker, M. Stamatikos, F. Halzen, and W. Rhode, Astropart. Phys. **25**, 118 (2006), arXiv:astro-ph/0511785.
- [91] IceCube Collaboration, R. Abbasi *et al.*, Astrophys. J. **710**, 346 (2010), arXiv:0907.2227.
- [92] IceCube Collaboration, R. Abbasi *et al.*, Nature **484**, 351 (2012), arXiv:1204.4219.
- [93] T. Kashti and E. Waxman, Phys. Rev. Lett. **95**, 181101 (2005), arXiv:astro-ph/0507599.
- [94] K. Murase and S. Nagataki, Phys. Rev. **D73**, 063002 (2006), arXiv:astro-ph/0512275.
- [95] P. Lipari, M. Lusignoli, and D. Meloni, Phys. Rev. **D75**, 123005 (2007), arXiv:0704.0718.

- [96] S. Hümmer, M. Rürger, F. Spanier, and W. Winter, *Astrophys. J.* **721**, 630 (2010), arXiv:1002.1310.
- [97] P. Baerwald, S. Hummer, and W. Winter, *Phys. Rev.* **D83**, 067303 (2011), arXiv:1009.4010.
- [98] Z. Li, *Phys. Rev.* **D85**, 027301 (2012), arXiv:1112.2240.
- [99] P. Baerwald, S. Hümmer, and W. Winter, *Astropart. Phys.* **35**, 508 (2012), arXiv:1107.5583.
- [100] M. Ahlers, M. Gonzalez-Garcia, and F. Halzen, *Astropart. Phys.* **35**, 87 (2011), arXiv:1103.3421.
- [101] M. D. Kistler, T. Stanev, and H. Yuksel, (2013), arXiv:1301.1703.
- [102] E. Waxman, *Lect. Notes Phys.* **598**, 393 (2003), arXiv:astro-ph/0303517.
- [103] W. Winter, *Adv. High Energy Phys.* **2012**, 586413 (2012), arXiv:1201.5462.
- [104] A. Mücke, R. Engel, J. Rachen, R. Protheroe, and T. Stanev, *Comput. Phys. Commun.* **124**, 290 (2000), arXiv:astro-ph/9903478.
- [105] G. Fogli *et al.*, *Phys. Rev.* **D86**, 013012 (2012), arXiv:1205.5254.
- [106] P. Baerwald, M. Bustamante, and W. Winter, *Astrophys. J.* **768**, 186 (2013), arXiv:1301.6163.
- [107] H. B. Koers and R. A. Wijers, (2007), arXiv:0711.4791.
- [108] K. Murase, K. Asano, T. Terasawa, and P. Meszaros, *Astrophys. J.* **746**, 164 (2012), arXiv:1107.5575.
- [109] S. R. Klein, R. Mikkelsen, and J. K. B. Tjus, (2012), arXiv:1208.2056.
- [110] W. Winter, J. B. Tjus, and S. R. Klein, (2014), arXiv:1403.0574.
- [111] M. Kachelriess, S. Ostapchenko, and R. Tomas, *Phys. Rev.* **D77**, 023007 (2008), arXiv:0708.3047.
- [112] J. Lange and M. Pohl, (2013), arXiv:1301.2914.
- [113] E. Waxman and J. N. Bahcall, *Phys. Rev.* **D59**, 023002 (1999), arXiv:hep-ph/9807282.
- [114] L. Nava, G. Ghirlanda, G. Ghisellini, and A. Celotti, *A&A* **530**, A21 (2011), arXiv:1012.2863.
- [115] J. Greiner *et al.*, *A&A* **498**, 89 (2009), arXiv:0902.0761.
- [116] The Fermi/GBM, A. A. Abdo *et al.*, *Astrophys. J.* **706**, L138 (2009), arXiv:0909.2470.
- [117] D. Gruber *et al.*, *A&A* **528**, A15 (2011), arXiv:1101.1099.
- [118] S. Hümmer, *Neutrinos aus photohadronischen Wechselwirkungen in kosmischen Beschleunigern (in German)*, PhD thesis, Würzburg University, 2013.
- [119] P. Baerwald, M. Bustamante, and W. Winter, *JCAP* **1210**, 020 (2012), arXiv:1208.4600.
- [120] G. Blumenthal, *Phys. Rev.* **D1**, 1596 (1970).

- [121] V. Berezhinsky and S. Grigor'eva, *A&A* **199**, 1 (1988).
- [122] M. Ahlers, L. A. Anchordoqui, and S. Sarkar, *Phys. Rev.* **D79**, 083009 (2009), arXiv:0902.3993.
- [123] M. Ahlers and J. Salvado, *Phys. Rev.* **D84**, 085019 (2011), arXiv:1105.5113.
- [124] T. Stanev, eConf **C040802**, L020 (2004), arXiv:astro-ph/0411113.
- [125] R. Aloisio *et al.*, *Astropart. Phys.* **27**, 76 (2007), arXiv:astro-ph/0608219.
- [126] K. Kotera and A. V. Olinto, *Ann. Rev. Astron. Astrophys.* **49**, 119 (2011), arXiv:1101.4256.
- [127] V. Berezhinsky and G. Zatsepin, *Phys. Lett.* **B28**, 423 (1969).
- [128] F. W. Stecker, *Astrophys. J.* **228**, 919 (1979).
- [129] D. Allard *et al.*, *JCAP* **0609**, 005 (2006), arXiv:astro-ph/0605327.
- [130] K. Kotera, D. Allard, and A. Olinto, *JCAP* **1010**, 013 (2010), arXiv:1009.1382.
- [131] R. Engel, D. Seckel, and T. Stanev, *Phys. Rev.* **D64**, 093010 (2001), arXiv:astro-ph/0101216.
- [132] D. De Marco, T. Stanev, and F. Stecker, *Phys. Rev.* **D73**, 043003 (2006), arXiv:astro-ph/0512479.
- [133] WMAP Collaboration, E. Komatsu *et al.*, *Astrophys. J. Suppl.* **192**, 18 (2011), arXiv:1001.4538.
- [134] M. J. Chodorowski, A. A. Zdziarski, and M. Sikora, *Astrophys. J.* **400**, 181 (1992).
- [135] A. Franceschini, G. Rodighiero, and M. Vaccari, *A&A* **487**, 837 (2008), arXiv:0805.1841.
- [136] F. W. Stecker, M. Malkan, and S. Scully, *Astrophys. J.* **648**, 774 (2006), arXiv:astro-ph/0510449.
- [137] H. Takami, K. Murase, S. Nagataki, and K. Sato, *Astropart. Phys.* **31**, 201 (2009), arXiv:0704.0979.
- [138] M. D. Kistler, H. Yüksel, J. F. Beacom, A. M. Hopkins, and J. S. B. Wyithe, *Astrophys. J.* **705**, L104 (2009), arXiv:0906.0590.
- [139] A. M. Hopkins and J. F. Beacom, *Astrophys. J.* **651**, 142 (2006), arXiv:astro-ph/0601463.
- [140] H. Yuksel, M. D. Kistler, J. F. Beacom, and A. M. Hopkins, *Astrophys. J.* **683**, L5 (2008), arXiv:0804.4008.
- [141] M. D. Kistler, H. Yuksel, J. F. Beacom, and K. Z. Stanek, *Astrophys. J.* **673**, L119 (2008), arXiv:0709.0381.
- [142] K. Asano and S. Nagataki, *Astrophys. J.* **640**, L9 (2006), arXiv:astro-ph/0603107.
- [143] V. Berezhinsky, A. Gazizov, M. Kachelriess, and S. Ostapchenko, *Phys. Lett.* **B695**, 13 (2011), arXiv:1003.1496.
- [144] Fermi-LAT collaboration, A. Abdo *et al.*, *Phys. Rev. Lett.* **104**, 101101 (2010), arXiv:1002.3603.

- [145] T. M. Kneiske, T. Bretz, K. Mannheim, and D. Hartmann, *A&A* **413**, 807 (2004), arXiv:astro-ph/0309141.
- [146] A. Ishihara, IceCube: Ultra-high energy neutrinos, Talk at Neutrino 2012.
- [147] W. L. Freedman *et al.*, *Astrophys. J.* **758**, 24 (2012), arXiv:1208.3281.
- [148] F. W. Stecker, M. A. Malkan, and S. T. Scully, *Astrophys. J.* **761**, 128 (2012), arXiv:1205.5168.
- [149] Y. Inoue *et al.*, *Astrophys. J.* **768**, 197 (2013), arXiv:1212.1683.
- [150] C. T. Hill and D. N. Schramm, *Phys. Rev.* **D31**, 564 (1985).
- [151] S. Yoshida and M. Teshima, *Prog. Theor. Phys.* **89**, 833 (1993).
- [152] T. Wibig and A. W. Wolfendale, *J. Phys.* **G31**, 255 (2005), arXiv:astro-ph/0410624.
- [153] A. Hillas, *J. Phys.* **G31**, R95 (2005).
- [154] V. Berezhinsky, *EPJ Web Conf.* **53**, 01003 (2013), arXiv:1307.4043.
- [155] M. Kachelriess and D. V. Semikoz, *Phys. Lett.* **B634**, 143 (2006), arXiv:astro-ph/0510188.
- [156] Telescope Array Collaboration, T. Abu-Zayyad *et al.*, *Astrophys. J.* **768**, L1 (2013), arXiv:1205.5067.
- [157] Pierre Auger Collaboration, J. Abraham *et al.*, *Phys. Lett.* **B685**, 239 (2010), arXiv:1002.1975.
- [158] D. Eichler, D. Guetta, and M. Pohl, *Astrophys. J.* **722**, 543 (2010), arXiv:1007.3742.
- [159] E. Waxman, (2010), arXiv:1010.5007.
- [160] K. Murase, K. Ioka, S. Nagataki, and T. Nakamura, *Phys. Rev.* **D78**, 023005 (2008), arXiv:0801.2861.
- [161] P. Baerwald, M. Bustamante, and W. Winter, (2014), arXiv:1401.1820.
- [162] D. Wanderman and T. Piran, *Mon. Not. Roy. Astron. Soc.* **406**, 1944 (2010), arXiv:0912.0709.
- [163] A. Lien *et al.*, (2013), arXiv:1311.4567.
- [164] C. Porciani and P. Madau, *Astrophys. J.* **548**, 522 (2001), arXiv:astro-ph/0008294.
- [165] M. Schmidt, *Astrophys. J.* **523**, L117 (1999), arXiv:astro-ph/9908206.
- [166] M. Schmidt, *Astrophys. J.* **559**, L79 (2001), astro-ph/0108459.
- [167] D. Guetta, T. Piran, and E. Waxman, *Astrophys. J.* **619**, 412 (2005), arXiv:astro-ph/0311488.
- [168] D. Guetta and M. Della Valle, *Astrophys. J.* **657**, L73 (2007), arXiv:astro-ph/0612194.
- [169] E. Liang, B. Zhang, and Z. Dai, *Astrophys. J.* **662**, 1111 (2007), arXiv:astro-ph/0605200.

- [170] A. Pelangeon *et al.*, *A&A* **491**, 157 (2008), arXiv:0811.3304.
- [171] E. Waxman, *Astrophys. J.* **452**, L1 (1995), arXiv:astro-ph/9508037.
- [172] B. Katz, R. Budnik, and E. Waxman, *JCAP* **0903**, 020 (2009), arXiv:0811.3759.
- [173] V. Berezhinsky, A. Gazizov, and S. Grigorieva, *Phys. Rev.* **D74**, 043005 (2006), arXiv:hep-ph/0204357.
- [174] K. Kotera and M. Lemoine, *Phys. Rev.* **D77**, 023005 (2008), arXiv:0706.1891.
- [175] M. Lemoine, G. Pelletier, and B. Revenu, *Astrophys. J.* **645**, L129 (2006), arXiv:astro-ph/0606005.
- [176] X.-Y. Wang, S. Razzaque, and P. Meszaros, *Astrophys. J.* **677**, 432 (2008), arXiv:0711.2065.
- [177] K. Murase and J. F. Beacom, *Phys. Rev.* **D81**, 123001 (2010), arXiv:1003.4959.
- [178] S. Kobayashi, T. Piran, and R. Sari, *Astrophys. J.* **490**, 92 (1997), arXiv:astro-ph/9705013.
- [179] F. Daigne and R. Mochkovitch, (1998), arXiv:astro-ph/9801245.
- [180] E. Nakar and T. Piran, *Astrophys. J.* **572**, L139 (2002), arXiv:astro-ph/0202404.
- [181] J. Aoi, K. Murase, K. Takahashi, K. Ioka, and S. Nagataki, *Astrophys. J.* **722**, 440 (2010), arXiv:0904.4878.
- [182] S. Kobayashi and R. Sari, (2001), arXiv:astro-ph/0101006.
- [183] S. Kobayashi and R. Sari, *Astrophys. J.* **551**, 934 (2001), arXiv:astro-ph/0101006.
- [184] F. Daigne and R. Mochkovitch, *Mon. Not. Roy. Astron. Soc.* **342**, 587 (2003), arXiv:astro-ph/0303287.
- [185] A. M. Beloborodov, *Astrophys. J.* **539**, L25 (2000), arXiv:astro-ph/0004360.
- [186] W. Paciesas *et al.*, *Astrophys. J. Suppl.* **122**, 465 (1999), arXiv:astro-ph/9903205.
- [187] KAMIOKANDE-II, K. Hirata *et al.*, *Phys. Rev. Lett.* **58**, 1490 (1987).
- [188] R. Bionta *et al.*, *Phys. Rev. Lett.* **58**, 1494 (1987).
- [189] A. S. Josphipura, E. Masso, and S. Mohanty, *Phys. Rev.* **D66**, 113008 (2002), hep-ph/0203181.
- [190] A. Bandyopadhyay, S. Choubey, and S. Goswami, *Phys. Lett.* **B555**, 33 (2003), hep-ph/0204173.
- [191] J. F. Beacom and N. F. Bell, *Phys. Rev.* **D65**, 113009 (2002), arXiv:hep-ph/0204111.
- [192] KamLAND, K. Eguchi *et al.*, *Phys. Rev. Lett.* **92**, 071301 (2004), arXiv:hep-ex/0310047.
- [193] SNO, B. Aharmim *et al.*, *Phys. Rev.* **D70**, 093014 (2004), arXiv:hep-ex/0407029.
- [194] M. C. Gonzalez-Garcia and M. Maltoni, *Phys. Lett.* **B663**, 405 (2008), arXiv:0802.3699 [hep-ph].
- [195] S. Pakvasa, (2003), hep-ph/0305317.

- [196] Particle Data Group, W. M. Yao *et al.*, J. Phys. **G33**, 1 (2006).
- [197] S. Pakvasa, Mod. Phys. Lett. **A23**, 1313 (2008), arXiv:0803.1701.
- [198] G. G. Raffelt, Phys. Rev. **D31**, 3002 (1985).
- [199] G. B. Gelmini and M. Roncadelli, Phys. Lett. **B99**, 411 (1981).
- [200] Y. Chikashige, R. N. Mohapatra, and R. D. Peccei, Phys. Rev. Lett. **45**, 1926 (1980).
- [201] R. Tomas, H. Pas, and J. W. F. Valle, Phys. Rev. **D64**, 095005 (2001), hep-ph/0103017.
- [202] S.-L. Chen, X.-G. He, and H.-C. Tsai, (2007), arXiv:0707.0187 [hep-ph].
- [203] S. Zhou, (2007), arXiv:0706.0302 [hep-ph].
- [204] X.-Q. Li, Y. Liu, and Z.-T. Wei, (2007), arXiv:0707.2285 [hep-ph].
- [205] D. Majumdar, (2007), arXiv:0708.3485 [hep-ph].
- [206] ANTARES Collaboration, E. Aslanides *et al.*, (1999), astro-ph/9907432.
- [207] IceCube, J. Ahrens *et al.*, Nucl. Phys. Proc. Suppl. **118**, 388 (2003), astro-ph/0209556.
- [208] NESTOR, S. E. Tzamarias, Nucl. Instrum. Meth. **A502**, 150 (2003).
- [209] NEMO, P. Piattelli, Nucl. Phys. Proc. Suppl. **143**, 359 (2005).
- [210] J. F. Beacom, N. F. Bell, D. Hooper, S. Pakvasa, and T. J. Weiler, Phys. Rev. Lett. **90**, 181301 (2003), hep-ph/0211305.
- [211] M. Maltoni and W. Winter, JHEP **07**, 064 (2008), arXiv:0803.2050.
- [212] A. Bhattacharya, S. Choubey, R. Gandhi, and A. Watanabe, Phys. Lett. **B690**, 42 (2010), arXiv:0910.4396.
- [213] A. Bhattacharya, S. Choubey, R. Gandhi, and A. Watanabe, JCAP **1009**, 009 (2010), arXiv:1006.3082.
- [214] M. Lindner, T. Ohlsson, and W. Winter, Nucl. Phys. **B607**, 326 (2001), arXiv:hep-ph/0103170.
- [215] M. Lindner, T. Ohlsson, and W. Winter, Nucl. Phys. **B622**, 429 (2002), arXiv:astro-ph/0105309.
- [216] D. Wagner and T. Weiler, Mod. Phys. Lett. **A12**, 2497 (1997), arXiv:1101.5677.
- [217] T. J. Weiler, W. Simmons, S. Pakvasa, and J. Learned, (1994), arXiv:hep-ph/9411432.
- [218] J. F. Beacom *et al.*, Phys. Rev. Lett. **92**, 011101 (2004), arXiv:hep-ph/0307151.
- [219] A. Esmaili and Y. Farzan, (2012), arXiv:1208.6012.
- [220] V. Barger, J. Learned, and S. Pakvasa, (2012), arXiv:1207.4571.
- [221] D. Fargion, D. D'Armiento, and P. Paggi, (2012), arXiv:1208.2471.

- [222] D. W. Hogg, (1999), arXiv:astro-ph/9905116.
- [223] Particle Data Group, K. Nakamura *et al.*, J. Phys. **G37**, 075021 (2010).
- [224] M. Blennow, T. Ohlsson, and W. Winter, JHEP **06**, 049 (2005), hep-ph/0502147.
- [225] G. Fogli *et al.*, (2012), arXiv:1205.5254v2.
- [226] S. Hümmer, M. Maltoni, W. Winter, and C. Yaguna, Astropart. Phys. **34**, 205 (2010), arXiv:1007.0006.
- [227] M. Bustamante, A. Gago, and C. Pena-Garay, JHEP **1004**, 066 (2010), arXiv:1001.4878.
- [228] P. Mehta and W. Winter, JCAP **1103**, 041 (2011), arXiv:1101.2673.
- [229] S. Pakvasa, Nuovo Cim. Lett. **31**, 497 (1981).
- [230] A. Karle *et al.*, arXiv:1003.5715.
- [231] F. Halzen and D. Hooper, Astrophys. J. **527**, L93 (1999), arXiv:astro-ph/9908138.
- [232] R. Enberg, M. H. Reno, and I. Sarcevic, Phys. Rev. **D79**, 053006 (2009), arXiv:0808.2807.
- [233] ANTARES Collaboration, S. Adrian-Martinez *et al.*, A&A 559, **A9** (2013), arXiv:1307.0304.
- [234] M. Bustamante, P. Baerwald, K. Murase, and W. Winter, (in preparation).
- [235] R. Protheroe and P. Biermann, Astropart. Phys. **6**, 45 (1996), arXiv:astro-ph/9605119.
- [236] J. D. Finke, S. Razzaque, and C. D. Dermer, Astrophys. J. **712**, 238 (2010), arXiv:0905.1115.
- [237] I. V. Moskalenko, Nuovo Cim. **C034N3**, 149 (2011), arXiv:1105.4921.
- [238] <http://www.desy.de/~maccione/DRAGON/>.
- [239] K.-H. Kampert *et al.*, Astropart. Phys. **42**, 41 (2013), arXiv:1206.3132.
- [240] R. Aloisio, D. Boncioli, A. Grillo, S. Petrerera, and F. Salamida, JCAP **1210**, 007 (2012), arXiv:1204.2970.
- [241] Pierre Auger Collaboration, P. Abreu *et al.*, Astropart. Phys. **35**, 354 (2012), arXiv:1111.2472.
- [242] K. Dolag, D. Grasso, V. Springel, and I. Tkachev, JETP Lett. **79**, 583 (2004), arXiv:astro-ph/0310902.
- [243] G. Sigl, F. Miniati, and T. A. Ensslin, Phys. Rev. **D70**, 043007 (2004), arXiv:astro-ph/0401084.
- [244] M. Unger for the Pierre Auger, Yakutsk, E. Barcikowski *et al.*, EPJ Web of Conferences 53, **01006** (2013), arXiv:1306.6138.
- [245] G. J. Feldman and R. D. Cousins, Phys. Rev. **D57**, 3873 (1998), arXiv:physics/9711021.
- [246] R. J. Gould and G. P. Schreder, Phys. Rev. **155**, 1404 (1967).
- [247] M. G. Baring, Astrophys. J. **650**, 1004 (2006), arXiv:astro-ph/0606425.

-
- [248] J. M. Jauch and F. Rohrlich, *The theory of photons and electrons. The relativistic quantum field theory of charged particles with spin one-half* (Springer, 1976).
- [249] P. Meszaros and M. Rees, *Astrophys. J.* **530**, 292 (2000), arXiv:astro-ph/9908126.
- [250] J. Puget, F. Stecker, and J. Bredekamp, *Astrophys. J.* **205**, 638 (1976).
- [251] F. Stecker and M. Salamon, *Astrophys. J.* **512**, 521 (1999), arXiv:astro-ph/9808110.
- [252] S. Karakula and W. Tkaczyk, *Astropart. Phys.* **1**, 229 (1993).
- [253] L. N. Epele, S. Mollerach, and E. Roulet, *JHEP* **9903**, 017 (1999), arXiv:astro-ph/9812130.

Eidesstattliche Erklärung

Hiermit erkläre ich, Mauricio Bustamante, geboren am 13.01.1983 in Lima, Peru, an Eides statt, diese Arbeit selbstständig und ohne unlautere Hilfe angefertigt und keine anderen als die angegebenen Quellen und Hilfsmittel verwendet zu haben.

Würzburg, 20.08.2014